

PONTIFICIA UNIVERSIDAD CATÓLICA DEL PERÚ

ESCUELA DE POSGRADO



**Elemental and isotope characterization of the Lithium-rich Tuff from the Macusani
Volcanic Field, Puno, Peru**

Tesis para obtener el grado académico de Maestro en Química que presenta:

Johan Santiago Ramirez Briones

Asesor:

Dr. Lisard Torró i Abat

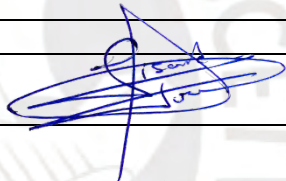
Lima, 2024

Informe de Similitud

Yo, Lisard Torr  i Abat,
docente de la Facultad de Ciencias e Ingenier a de la Pontificia Universidad Cat lica del Per , asesor de la tesis titulada “Elemental and isotope characterization of the Lithium-rich Tuff from the Macusani Volcanic Field, Puno, Peru”, del autor Johan Santiago Ramirez Briones dejo constancia de lo siguiente:

- El mencionado documento tiene un  ndice de puntuaci n de similitud de 17 %. As  lo consigna el reporte de similitud emitido por el software *Turnitin* el 03/07/2024.
- He revisado con detalle dicho reporte y la Tesis y no se advierten indicios de plagio.
- Las citas a otros autores y sus respectivas referencias cumplen con las pautas acad micas.

Lugar y fecha: Lima a 03 de julio de 2024

Apellidos y nombre del asesor: Torr� i Abat, Lisard	
DNI: 49088982	Firma 
ORCID: 0000-0002-3557-8334	

ACKNOWLEDGMENTS

This thesis is dedicated to my parents, Santiago Ramirez Lazo and Domitila Briones Yañez, who have given me their unconditional love and all the tools to reach this moment in my life.

I would also like to express my gratitude to my advisor, Lisard Torr , for his invaluable guidance and the trust he placed in me, as well as for his friendship. Likewise, I am thankful to Patrice Baby for the long conversations about geology, which sparked my profound interest in Andean tectonics.

This thesis benefited from the critical reading and constructive comments of Patrice Baby and Lu s Ortega.

Furthermore, I extend my thanks to Macusani Yellowcake – American Lithium for providing us with all the support to visit the study area, especially to Dr. Ulises Sol s and geologists Gabriel Tasayco, Miguel Cavani, Roher Huaricallo, and Henry Mamani. Also, I would like to thank to Jean Vallance for his participation in the field campaign.

Lastly, I am deeply grateful to my friends and colleagues in the Geological Engineering Program at the Pontifical Catholic University of Peru: Pablo Valverde, Mariana Segovia, Mercy Sanandres, Lorena Gomez, and Fiorela Maxi. Together, we have dedicated many years to the development of numerous undergraduate theses as part of this project. Their hard work and collaboration have been invaluable.

This study was economically supported by the Peruvian PROCIENCIA-FONDECYT project 122-2020 E041-2020-01-01.

RESUMEN

Las tecnologías ecoeficientes, en particular las baterías recargables de iones de litio, han provocado un aumento en la demanda de litio. El Proyecto de Litio Falchani, ubicado en el Campo Volcánico Neógeno de Macusani en el sureste del Perú es de tipo volcanogénico y contiene uno de los recursos de este metal más significativos a nivel mundial. El recurso de litio se aloja principalmente en la denominada Toba Rica en Litio, una lutita tobácea que se encuentra intercalada entre las unidades de Brecha Superior y Brecha Inferior, también ricas en litio. El objetivo principal de esta tesis es la caracterización geoquímica (elemental e isotópica) de la Toba Rica en Litio, con un enfoque principal en la petrogénesis del magma parental y las modificaciones post-depositacionales.

La composición de elementos mayores y traza de la Toba Rica en Litio difiere de la de las tobas de flujo piroclástico reportadas previamente en el Campo Volcánico de Macusani. En cambio, se asemeja a la composición de obsidias altamente evolucionadas y fuertemente peraluminosas conocidas como macusanita. La Toba Rica en Litio muestra la signatura geoquímica distintiva de granitos peraluminosos ricos en metales raros y pegmatitas de Li-Cs-Ta (LCT), con altos contenidos de F, Sn, W y otros metales raros como Nb, Ta, Li y Cs, además de un marcado empobrecimiento en Zr, Th, Y, tierras raras (REE) y Sr en comparación con ejemplos arquetípicos de granitos peraluminosos con moscovita (MPG).

De acuerdo a modelización geoquímica, los magmas parentales de la Toba Rica en Litio contenían aproximadamente un 15-30% de contribución de líquidos mantélicos isotópicamente similares a basaltos potásicos-ultrapotásicos del Mioceno tardío en la región. El restante 70-85% se atribuye a derivación/asimilación de paragneises proterozoicos y paleozoicos y/o metapelitas paleozoicas. El enriquecimiento temprano en elementos incompatibles en los magmas parentales de la Toba Rica en Litio se explica en parte por asimilación de metapelitas paleozoicas y cristalización fraccionada simultánea (AFC). Sin embargo, procesos metasomáticos en una etapa tardía pre-eruptiva, en presencia de fluidos exsueles de un reservorio magmático rico en volátiles y altamente fraccionado, fueron clave para el enriquecimiento extremo en Li, Be, Rb, Nb y Ta. Dicho enriquecimiento, por lo tanto, no estuvo relacionado con procesos de alteración in-situ post-depositacionales conectados a la formación de arcillas y zeolitas.

ABSTRACT

The transition to eco-efficient technology, particularly rechargeable Li-ion batteries, is causing a significant increase in the demand for lithium. The recently discovered, unconventional, volcanogenic Falchani deposit, situated within the Neogene Macusani Volcanic Field in SE Peru, represents one of the most significant global resources of lithium. The lithium ore is primarily hosted in the so-called Lithium-rich Tuff, a tuffaceous mudstone that is sandwiched between the Upper and Lower Breccia units, which are also Li-rich. The main objective of this thesis is to conduct a geochemical (elemental and isotopic) characterization of the Lithium-rich Tuff with a main focus on parental magma petrogenesis and post-depositional modifications.

The major and trace element composition of the Lithium-rich Tuff differs from that of previously reported ash-flow tuff in the Macusani Volcanic Field. Rather, it approximates the composition of highly evolved peraluminous obsidian glasses known as macusanite. The Lithium-rich Tuff shows the distinctive geochemical fingerprint of peraluminous rare metal-rich granites and Li-Cs-Ta (LCT) pegmatites, with high contents of F, Sn, W, and other rare metals such as Nb, Ta, Li, and Cs, in addition to a strong depletion in Zr, Th, Y, rare earth elements (REE), and Sr compared to archetypal muscovite-bearing peraluminous granites (MPG).

The parental magmas to the Lithium-rich Tuff have been modeled as containing ~15-30% of a mantle contribution with an isotope signature similar to that of late Miocene potassic-ultra-potassic basaltic melts. The remaining ~70-85% is attributed to Proterozoic and Paleozoic paragneiss and/or Paleozoic metapelite contributions. An early enrichment in incompatible elements in the Lithium-rich Tuff parental magmas is in part explained by assimilation of Paleozoic metapelite rocks with simultaneous fractional crystallization (AFC). However, subsequent metasomatic processes in a pre-eruptive stage in the presence of fluids exsolved from a volatile-rich, highly fractionated, crystal-rich magmatic reservoir were key to the extreme enrichment in Li, Be, Rb, Nb, and Ta. Consequently, such enrichment was not related to in-situ, post-depositional, clay and zeolite alteration processes.

Table of contents

1. INTRODUCTION	10
1.1. Lithium: a critical raw material for the global economy	10
1.2. The discovery of a major lithium resource at Falchani	14
1.3. Previous studies of the Macusani Formation	18
1.4. Conundrum	22
1.5. Objectives	23
1.6. Hypothesis	24
1.7. Justification	24
2. METHODOLOGY	25
2.1. Sampling	25
2.2. Sample preparation	30
2.3. Whole-rock element geochemistry	31
2.4. Whole-rock isotope geochemistry	33
3. GEOLOGICAL SETTING	34
3.1. Neogene ignimbrite fields in the Central Andes	34
3.2. Tectonic framework of the Eastern Cordillera in southern Peru	40
3.3. The Macusani Volcanic Field	47
3.3.1. Crucero Supergroup	48
3.3.2. Macusanite pebbles	54
3.3.3. Crucero Intrusive Supersuite	55
4. RESULTS	57
4.1. Major and minor element composition	57
4.2. Trace element composition	62
4.3. Lead, Sr, and Nd isotope ratios	68
5. DISCUSSION	74
5.1. Chemical composition of the lithium ore units within the geochemical diversity of the Macusani Formation	74
5.2. Nature of the magmatic component in the Lithium-rich Tuff	79
5.3. Source regions of parental magmas to the Lithium-rich Tuff	83
5.4. Magma differentiation and fluid-mediated controls on the composition of the Lithium-rich Tuff	89
6. CONCLUSIONS	99
7. REFERENCES	99
APPENDIX A	145
APPENDIX B	149
APPENDIX C	188
APPENDIX D	194

List of figures

Figure 1. Critical Raw Materials for the European Commission (2023) based on their supply risk and economic importance, including lithium.	11
Figure 2. Bar chart of world demand for and major uses of lithium over 2018 and forecast (f) values over 2019-2028.....	12
Figure 3. Major lithium deposits classified according to deposit type.	13
Figure 4. Geographical location of the Falchani Lithium Project.	15
Figure 5. Exploration concessions in the Macusani Volcanic Field.....	16
Figure 6. Location of the studied rock samples.	29
Figure 7. Photographs of equipment used in the QEMSCAN Laboratory at PUCP for the preparation of samples for whole-rock chemical analysis.....	30
Figure 8. Equipment used for whole-rock chemical analysis.....	31
Figure 9. Location of the Macusani Volcanic Field and other Neogene ignimbrite fields in the Central Andes.	35
Figure 10. Geological map of the Altiplano, Eastern Cordillera, and Sub Andean Zone in southern Peru.	43
Figure 11. Simplified geological map of the Macusani Volcanic Field and adjacent areas in the Eastern Cordillera.	49
Figure 12. Summary of stratigraphic units in the Macusani Volcanic Field.	50
Figure 13. Volcano-stratigraphic correlation chart of the Macusani volcanic rocks.....	52
Figure 14. Major and minor element contents in analyzed samples from the Macusani Volcanic Field according to lithotype.	58
Figure 15. Total alkalis-silica plots with analyzed samples from the Macusani Volcanic Field.....	59
Figure 16. Major elements bivariant plots with analyzed samples from the Macusani Volcanic Field.	60
Figure 17. Trace element composition of analyzed samples from the Macusani Volcanic Field.....	63
Figure 18. Upper continental crust-normalized element patterns of all analyzed volcanogenic rocks from the Macusani Volcanic Field.....	64
Figure 19. Geochemical composition of samples from the Macusani Volcanic Field in terms of (a) Nb vs. Nb/Ta, (b) Rb vs. Nb, (c) Rb vs. Ta, and (d) Rb vs. Li.	65
Figure 20. Chondrite-normalized REY patterns of all analyzed volcanogenic rocks from the Macusani Volcanic Field.....	66
Figure 21. Bivariant plots of selected elements in Lithium-rich Tuff, Upper Breccia, and Lower Breccia.....	68
Figure 22. Lead isotope compositions of volcanogenic and intrusive rocks (this and previous studies) from the Macusani Volcanic Field.....	73
Figure 23. Strontium and neodimium isotope ratios of volcanogenic and intrusive rocks (this and previous studies) from the Macusani Volcanic Field.	74
Figure 24. Major element Harker diagrams for volcanogenic units assigned to the Macusani Formation.	76
Figure 25. Bivariant plots of Ti vs. elements that behaved as incompatible in parental magmas to Macusani Formation rocks.....	77
Figure 26. Bivariant plots of Ti vs. elements that behaved as compatible in parental magmas to Macusani Formation rocks.	78

Figure 27. Bivariant plots of Ti vs. REE in Macusani Formation rocks.	78
Figure 28. Bivariant plots of Ti vs. transition metals in Macusani Formation rocks.	79
Figure 29. Composition of lithium-ore units from Falchani in the provenance discrimination plot for weathered rocks.	81
Figure 30. Average chondrite-normalized element patterns of lithium-ore units from Falchani, LCT pegmatites and the best studied muscovite-bearing peraluminous granites.	82
Figure 31. Sm/Nd T_{DM} vs. ϵNd_0 plot for analyzed samples from the Macusani Volcanic Field, metamorphic and igneous rocks from the Andean basement of the Arequipa-Antofalla terrain, and Oligocene to Quaternary Andean ignimbrite fields located between 14°S and 27°S.	85
Figure 32. Strontium isotope ratios and elemental abundance in rocks from Macusani Volcanic Field, and metamorphic and igneous rocks from the Andean basement of the Arequipa-Antofalla terrane.	87
Figure 33. Strontium and Nd isotope ratios corrected to 8.9 Ma and simple binary mixing models that reproduce the Nd-Sr isotope signature of volcanogenic rocks from Macusani Volcanic Field.	88
Figure 34. Bivariant plots for volcanogenic units assigned to the Macusani Formation and two samples of Quenamari Suite granite.	92
Figure 35. Geochemical data of analyzed samples from the Macusani Volcanic Field plotted on the Mg/Li vs La/Ta diagram.	96
Figure 36. Simplified genetic model for lithium micas in the Lithium-rich Tuff.	96
Figure 37. Compositional vertical profiles of lithium-ore units from Falchani sorted by depth in drill holes.	97
Figure 38. Bivariant plots including (a) $(La/Sm)_{CN}$ vs. $(Ce/Ce^*)_{CN}$ and (b) Zr/Hf vs. Y/Ho. $(Ce/Ce^*)_{CN} = \log(5Ce^*/(4La^* + Sm^*))$ calculated following Wilde et al. (1995).	98

List of tables

Table 1. Global lithium mine production, reserves, and resources expressed in metric tons (t).	14
Table 2. Values of Pb isotope ratios in studied samples from the Macusani Volcanic Field.	70
Table 3. Values of Rb-Sr isotope ratios in studied rock samples from the Macusani Volcanic Field.	71
Table 4. Values of Sm-Nd isotope ratios and calculated epsilon (ϵNd) in studied rock samples from the Macusani Volcanic Field.	72



1. INTRODUCTION

1.1. Lithium: a critical raw material for the global economy

Global warming and degradation of air quality pose major environmental challenges for society in the 21st century (European Commission 2023; Jowitt et al. 2021). Keeble (1988) defines sustainable development as that which satisfies present needs without prejudicing the resources necessary to satisfy future needs. In the current energy paradigm, about 60 % of the world's electricity supply is generated from non-renewable fossil fuels (Tamayo et al. 2016). Also, exothermic fossil fuel combustion reactions generate chemical sub-products that are emitted into the atmosphere and result in negative impacts on both the environment and public health (e.g., Ciesia 1995; IPCC 1995; Caballero et al. 2007; Báez et al. 2011). A study published by the Economic Commission for Latin America and the Caribbean (CEPAL) has estimated that the average annual external costs of generating electricity based on fossil fuels in Central America are US\$ 307.2 M and 44.3 M due to externalities associated with climate change and health impacts, respectively (Octaviano 2011).

In response to this problem, different countries have established a series of government policies to regulate polluting emissions, increase the supply of energy from renewable sources, and promote the energy independence of each Nation. Globally, institutional investments for the installation of renewable energy sources have increased by 71.49% from 2009 to 2018, with China and Europe being the main promoters (IRENA 2020). As a result, more than 10 % of the primary energy and more than 25 % of the electrical energy generated worldwide in 2018 was produced from green technologies (including hydroelectric power plants). In 2008, the Peruvian Congress issued Legislative Decree No. 1002, Law for the Promotion of Investment in Electricity Generation using Renewable Energies, which establishes a “competition for the market” scheme to decarbonize the energy sector. Consequently, from 2008 to 2014, the mitigated emissions of CO₂ and CH₄ in Peru have gone from 32000 tCO₂ (tons of CO₂ equivalent) to 1443000 tCO₂, representing an accumulated value of US\$ 499 M in the said period due to the sale of Certificates of Reduced Emissions (CER; Tamayo et al. 2016).

This shift toward more eco-efficient energy technologies (e.g., wind turbines, solar panels, electric vehicles; Bauer et al. 2011; European Commission 2023) increases the

demand for raw materials of mineral origin and the associated concern over their supply (Lee et al. 2020; Jowitt et al. 2021). According to the European Commission (2023), a *critical raw material* has high economic importance and risk of supply disruptions (Fig. 1). For the United States Geological Survey (2023), a critical raw material is any non-fuel mineral, element, substance, or material that the Secretary of Energy determines i) has a high risk of supply chain disruption; and ii) serves an essential function in one or more energy technologies, including technologies that produce, transmit, store, and conserve energy. Both organizations consider lithium as a critical raw material.

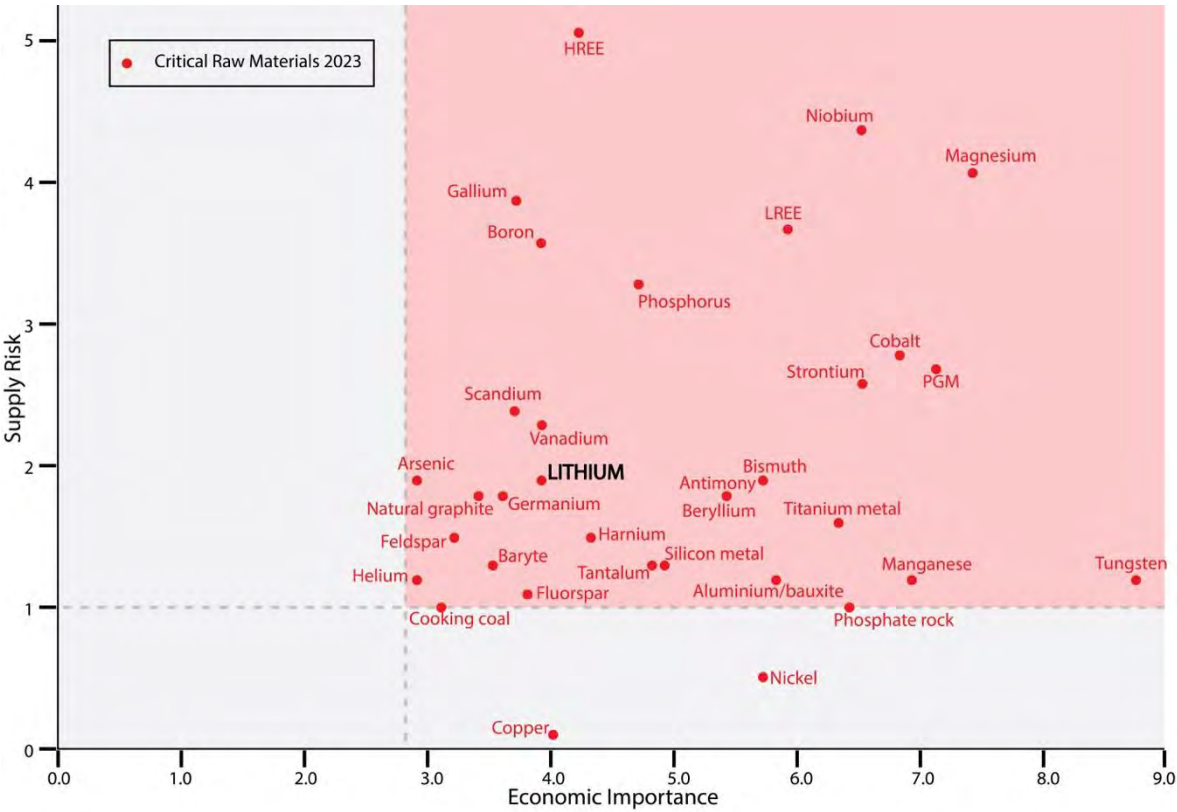


Figure 1. Critical Raw Materials for the European Commission (2023) based on their supply risk and economic importance, including lithium.

Lithium price reached anomalous high values in 2021 triggered by its increasing demand for the manufacture of Li-ion batteries used in plug-in electric-hybrid (PHEV) and pure electric (BEVs) vehicles, and portable technologies such as smartphones, laptops, and tablets (Fig. 2; Evans 2014; Bradley et al. 2017a; Trading Economics 2023). For comparison purposes, Transport & Environment (2021) argues that in 2021 PHEVs lifecycle energy consumption was 42% higher than for BEVs and 41% lower than for gasoline. Also, petrol and diesel cars emit almost 3 times more CO₂ than the average European Union electric cars.

It is expected that by 2028 to 2030, the manufacturing of lithium batteries for electric vehicles will correspond to 95 % of the demand for this metal (Azevedo et al. 2022; Fig. 2). Based on the ambition of the European Green Deal to decarbonize road transport by 2050 (Transport & Environment 2018), the total demand for car batteries in Europe is expected to reach close to 200 GWh in 2025 and more than 910 GWh in 2035, which dictates an increasing future demand. Several factors have been identified to affect lithium risk supply: i) geologic, with the lack of identification of undiscovered lithium resources; ii) technical, with incapacity of most countries for extracting and processing lithium from ore; and iii) environmental, social, and political, considering the influence of governments (National Research Council 2008; European Commission 2023).

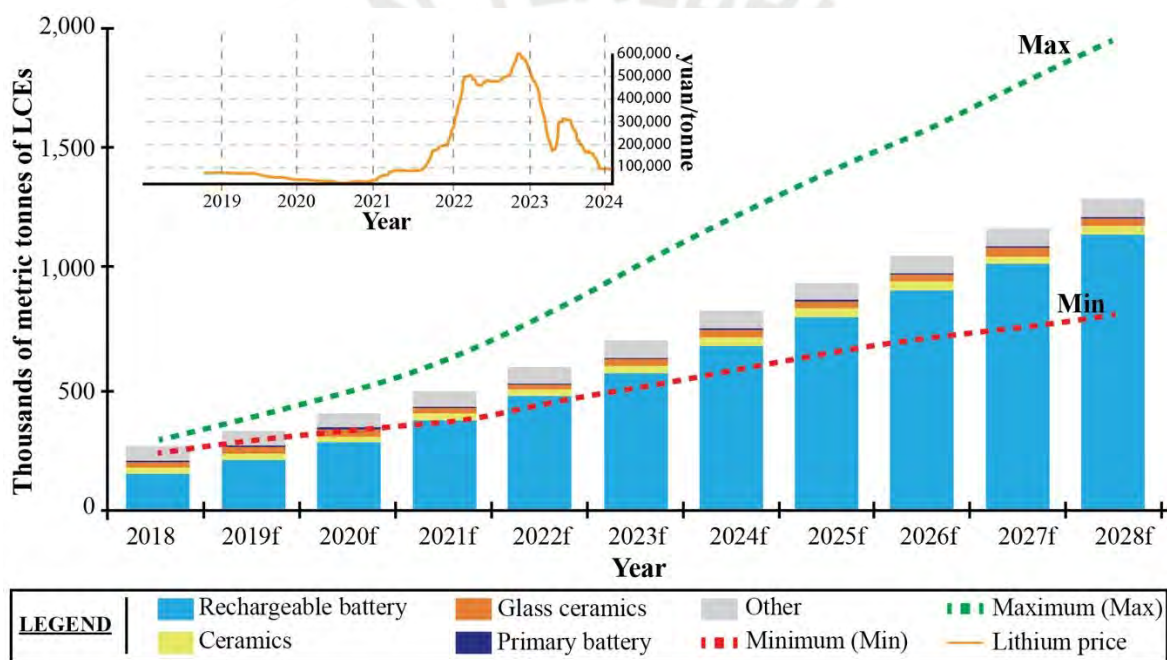


Figure 2. Bar chart of world demand for and major uses of lithium over 2018 and forecast (f) values over 2019-2028 (modified from Bibienne et al. 2020). The dotted green line indicates predicted maximum demand of lithium carbonate equivalents (LCEs), and the red one indicates predicted minimum demand of LCEs. The inset (top left) shows variation of the prices of lithium carbonate in yuan/t during the last 6 years until February 2024 (extracted from Trading Economics 2024).

Lithium resources and production are expressed in tons (t) of LCEs, which is equivalent to 1 t of lithium carbonate with 18.8 wt.% Li (Evans 2014; Bradley et al. 2017a). Lithium is mainly traded as i) lithium *mineral concentrates* (e.g., spodumene, petalite, and lepidolite); ii) *lithium chemicals* or *mineral compounds*, chiefly lithium carbonate (Li_2CO_3) and chloride (LiCl ; equivalent to 0.871 LCEs), and to a lesser extent as lithium bromide

(LiBr; equivalent to 0.425 LCEs) and hydroxide monohydrate (LiOH·H₂O; equivalent to 0.880 LCEs); and iii) *lithium metal* (equivalent to 5.32 LCEs), which is obtained by electrolysis from lithium chloride (Evans 2014; Bradley et al. 2017a; Bibienne et al. 2020). Although the most important lithium resources and with the lowest processing costs are found in continental brines (58%), lithium is mostly extracted from pegmatites with conventional methods due to its relatively higher lithium contents (Fig. 3; Bradley et al. 2017b; Sterba et al. 2019; Karrech et al. 2020). At present, world lithium production is concentrated in Australia (spodumene operations), Latin America (brine operations), China (unknown origin), and smaller producers such as Brazil, Zimbabwe, and Portugal (Table 1; United States Geological Survey 2023). Secondary supply such as recycling of Li-ion batteries is expected to increase in the next years (Azevedo et al. 2022).

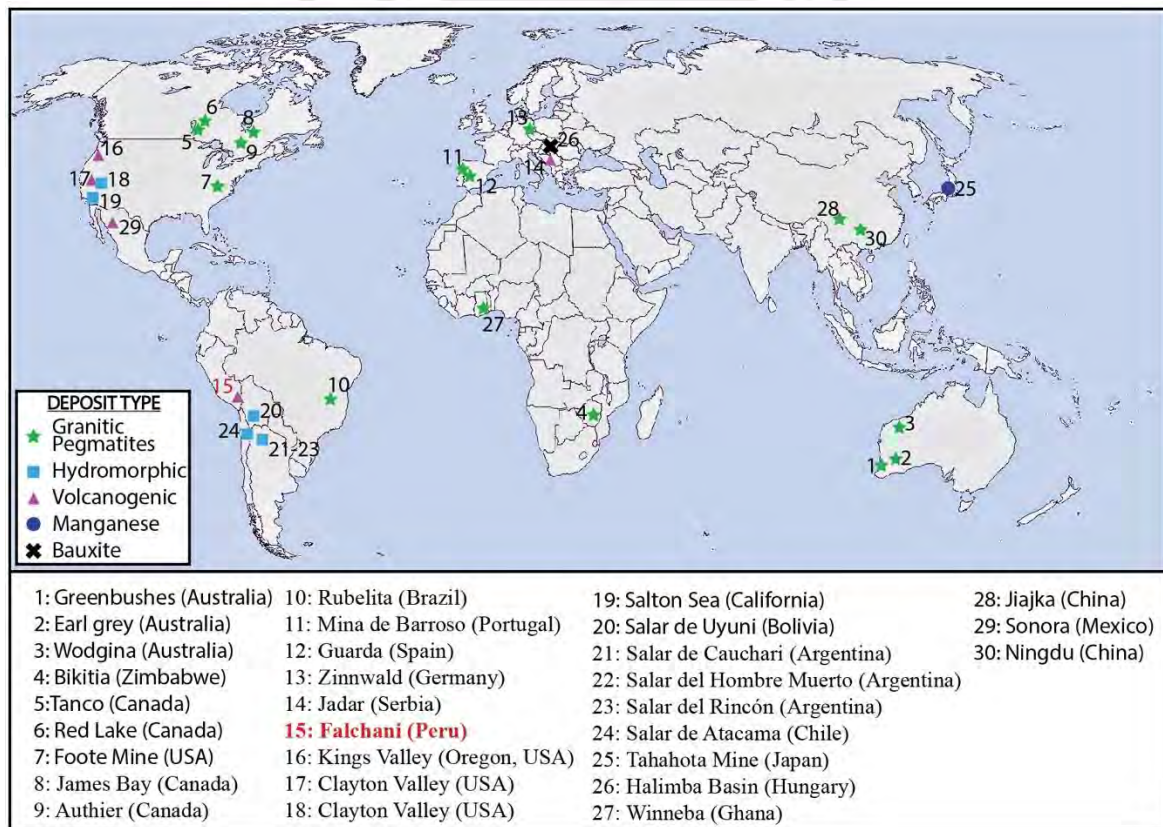


Figure 3. Major lithium deposits classified according to deposit type. Modified from [Bowell et al. \(2020\)](#).

Table 1. Global lithium mine production, reserves, and resources expressed in metric tons (t). Extracted from [United States Geological Survey \(2023\)](#).

	Mine production (2022)	Reserves (2023)	Resources (2023)
Bolivia	-	-	21000000
Argentina	5970	2700000	20000000
United States	-	1000000	12000000
Chile	28300	9300000	11000000
Australia	55300	6200000	7900000
China	14000	2000000	6800000
Germany	-	-	3200000
Congo	-	-	3000000
Canada	-	930000	2900000
Mexico	-	-	1700000
Czechia	-	-	1300000
Serbia	-	-	1200000
Russia	-	-	1000000
Peru	-	-	880000
Mali	-	-	840000
Brazil	1700	250000	730000
Zimbabwe	710	310000	690000
Spain	-	-	320000
Portugal	900	60000	270000
Namibia	-	-	230000
Ghana	-	-	180000
Finland	-	-	68000
Austria	-	-	60000
Kazakhstan	-	-	50000
Other	-	3300000	-
Total	107000	26000000	76318000

1.2. The discovery of a major lithium resource at Falchani

The Falchani Lithium Project is located in the Corani District, Carabaya Province, Puno Department ([Fig. 4](#)). It includes two lithium exploration properties, the Falchani and Oacasa 4 concessions ([Fig. 5](#); [Nupen 2019](#)). The Falchani Lithium Project is owned by Macusani Yellowcake S.A.C., the Peruvian subsidiary of the Canadian company American Lithium ([American Lithium 2021](#)), formerly Plateau Energy Metals ([Saldarriaga 2021a](#)). In a NI-43-101 compliant technical report prepared by The Mineral Corporation in March 2019 ([Nupen 2019](#)), 0.96 Mt LCE (60.92 Mt @ 2954 ppm Li) of indicated resources and 3.75 Mt LCE (260.07 Mt @ 2706 ppm Li) of inferred resources were calculated in the Falchani Lithium Project. In October 2023, American Lithium issued a press release stating a 476 %

increase in measured plus indicated lithium resources at the Falchani Lithium Project and explaining that K, Cs, and Rb had been added to the block model (Clarke 2023). The new measured resources amount to 1.01 Mt LCE (69 Mt @ 2792 ppm Li), the indicated resources, to 4.52 Mt LCE (378 Mt @ 2251 ppm Li), and the inferred resources, to 3.99 Mt LCE (506 Mt @ 1481 ppm Li). A NI-43-101 compliant technical report for the updated resources is in progress (Clarke 2023).

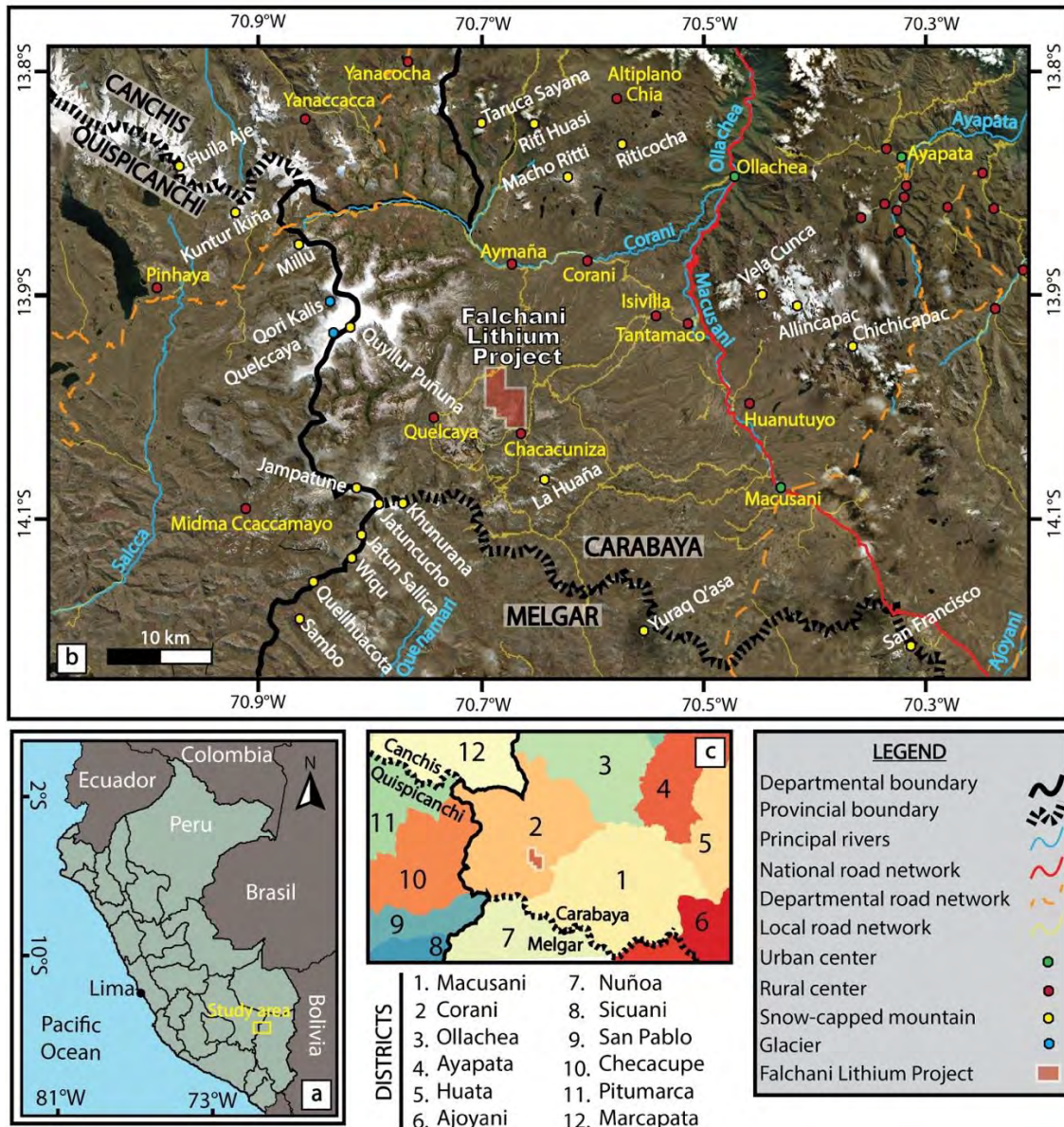


Figure 4. Geographical location of the Falchani Lithium Project. (a) Political map of Peru including departments. The yellow rectangle represents the area covered by maps in (b) and (c). (b) Satellite photograph of the Macusani Volcanic Field and surrounding areas showing departmental and provincial boundaries, access routes, and toponymic elements. (c) Simplified political map of departments, provinces, and districts. Sources: INEI (2017) and MTC (2019).

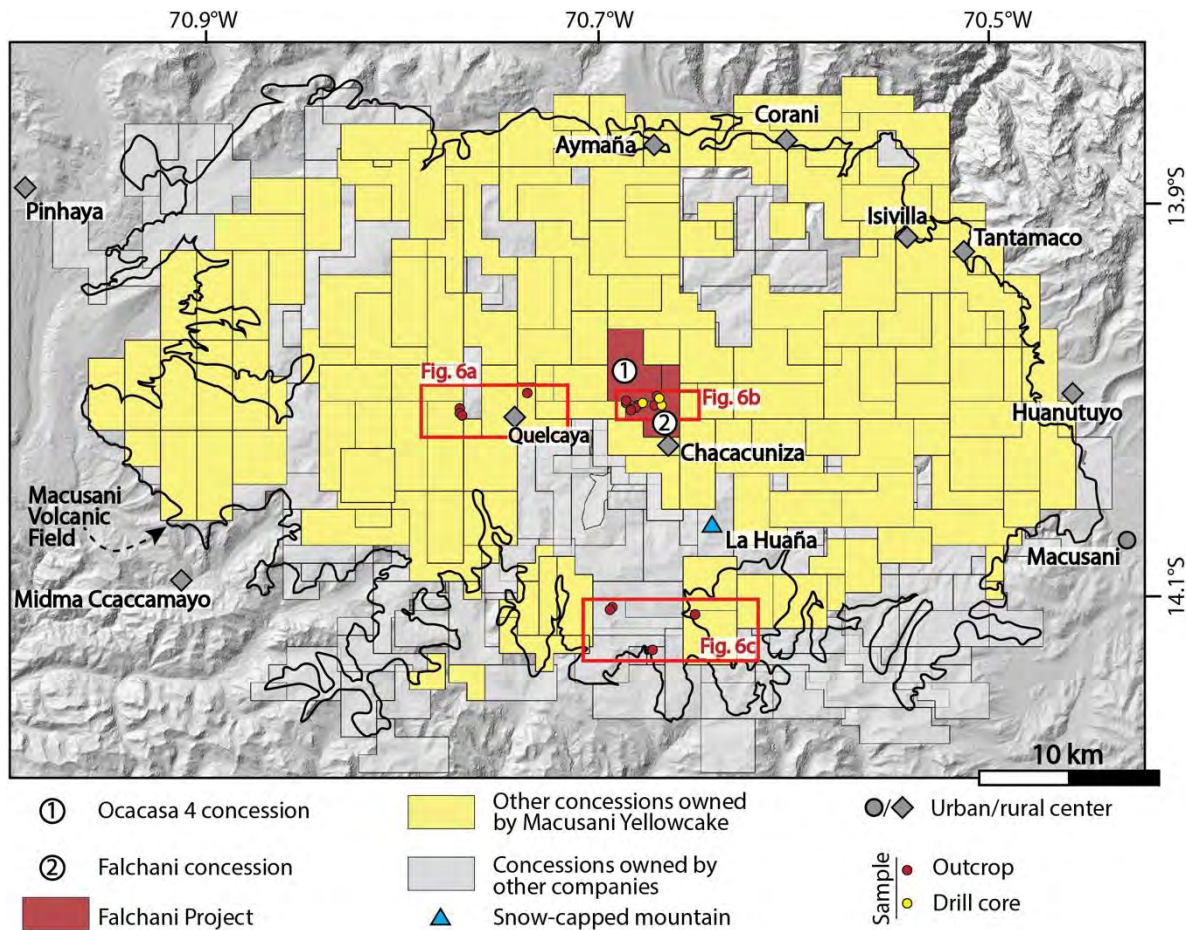


Figure 5. Exploration concessions in the Macusani Volcanic Field. The Falchani Lithium Project covers an area of 17 km² of the 1050 km² covered by all concessions owned by Macusani Yellowcake (SIDEMCAT 2023).

Exploration in the Falchani Lithium Project began in 2007 after the identification of a radiometric anomaly and drilling sampling in the central region of the Macusani Volcanic Field (Fig. 5; Gestión 2018). In November 2017, and after having explored 8000 of the 92000 hectares of the Falchani Lithium Project, the company announced the discovery of a major lithium resource that amounted to ~2.5 Mt of lithium carbonate (Gestión 2018; Redacción RPP 2018). Just three months after this announcement, the company nearly doubled its resources at the Falchani Lithium Project to 4.7 Mt (Cóndor 2019; Nupen 2019). Early metallurgical tests on Falchani lithium ore developed by the Tecnología Minera Metalúrgica Industrial Empleada (Tecmmine) in Peru and the Australian Nuclear Science and Technology Organization (ANSTO) support low-cost lithium recoveries of 88-90% with precipitation of high-purity lithium carbonate (Nupen 2019). The official webpage of American Lithium reports a 4.7-year payback of US\$1.55 billion (Net Present Value of 8% in with the Base

Case scenario), with low Capital Expenditure (US\$ 587 M of initial capital) and a high cash flow (US\$ 430 M average annually; [American Lithium 2021](#)).

In an interview published by [Gestión \(2018\)](#), the CEO of Macusani Yellowcake Ulises Solís pointed out that Li contents in samples of the so-called Lithium-rich Tuff (~ 3,500-4,000 ppm Li; [Nupen 2019](#)) are seven times greater than the average grade in brine deposits (salars) from Bolivia, Chile, and Argentina, which potentially makes the Falchani Lithium Project a high-grade lithium deposit. If we compare grades in hard rock Li deposits, the Falchani Lithium Project has grades (~0.3-0.4 wt.% Li) that are close to cut-off values in many Li-Cs-Ta (LCT) granitic pegmatites (~ 0.5-0.6 wt.% Li; [Bowell et al. 2020](#)) and equivalent to worldwide economically most relevant volcanogenic Li deposits such as Kings Valley in USA (27 Mt @ 0.395 wt.% Li; [Bowell et al. 2020](#)) and Jadar in Serbia (155 Mt @ 0.3 wt.% Li; [Borojević and Branko 2022](#)).

In [Gestión \(2018\)](#), Operations Manager at American Lithium, Laurence Stefan, stated that production could begin by the end of 2020. In a more recent interview, Ulises Solís commented that the production plant will be operational in 2027 ([Salazar 2023a](#)). According to the Canadian company, an annual production of 25000 t of lithium carbonate in the first three years is expected, to gradually increase to 80000 t per year in the sixth year of production ([Gestión 2020](#)). In June 2022, [American Lithium \(2022\)](#) announced the production of potassium sulfate as a by-product of lithium, which stands as an additional potential for the Falchani Lithium Project and an alternative fertilizer supply for Peru.

In [Gestión \(2020\)](#) and [Rumbo Minero \(2023\)](#), Ulises Solís, explained that lithium ore at the Falchani Lithium Project does not contain anomalously high uranium contents and that, as a consequence, the production of Li could begin without the normative framework under development by the Peruvian Institute of Nuclear Energy—advised by the International Atomic Energy Agency—in relation to the management of U in Peru. However, the Ministry of Energy and Mines demands further exploration to demonstrate that uranium and lithium are “*not associated*” ([Vilca 2020](#); [Saldarriaga 2021b](#)). In 2023, the Ministry of Energy and Mines, through the General Directorate of Mining Environmental Affairs, confirmed that the Semi-Detailed Environmental Impact Study (EIASd) of the Falchani lithium exploration project had started its process correctly and within the established deadlines ([Salazar 2023b](#)).

1.3. Previous studies of the Macusani Formation

The Macusani (Sandeman et al. 1997)—also known as Quenamari (López et al. 1996)—Formation is exposed exclusively in the Macusani Volcanic Field (Fig. 5; cf. Section 3.3). It was Francis (1959a, b) who provided the first available description of the pyroclastic flow nature and wide geographical distribution of volcanic rocks in the area, then grouped under the name “*tufos de Carabaya*” (i.e., Carabaya tuff).

Before that, in the 1920s, the Macusani Volcanic Field had caught the interest of the geoscientific community due to the discovery of non-hydrated obsidian glass—known as macusanite—with extreme enrichment in incompatible lithophile and volatile elements (Li, Rb, Cs, Sn, U, B, and F—as later documented by Pichavant et al. 1988a) and an exotic mineralogy including andalusite, sillimanite, wollastonite, and scapolite (Linck 1926; French and Meyer 1970; French et al. 1978). Virgilitite, the solid solution between β -quartz and spodumene [LiAlSi₂O₆] for which the Macusani Volcanic Field is the type locality, was found in macusanite as well (French et al. 1978). Macusanite reports are limited to <10 x 5 cm boulders from specific ravines and valleys of glacio-fluvial origin, riverbeds, and fluvial terraces in the Macusani Volcanic Field (Linck 1926) and Paucartambo (Cuzco; Preuss 1935; Heide 1936), as summarized by Martin and de Sitter-Koomans (1955). In addition, there is one report of in-situ, coarse ash-sized, non-vesicular glass clasts interbedded in the Macusani Formation that was identified as macusanite by Pichavant et al. (1987). Although macusanite was initially interpreted as a tektite (Linck 1926; Martin 1934; Heide 1936), the current consensus is that erupted macusanite-like melts were air-quenched as can be inferred from the ellipsoidal shape and etched surface of the glass pebbles (Martin and de Sitter-Koomans 1955; Elliot and Moss 1965; Barnes et al. 1970; Pichavant et al. 1987). This unique obsidian glass has been studied from geo- and thermo-chronological (Miller and Wagner 1981; McCorkell and Naeser 1988; Miller et al. 1990; Poupeau et al. 1992, 1993), petrological (London et al. 1988, 1989; London and Morgan 2017; Pichavant et al. 2024a), and even archeological (Bigazzi et al. 1997; Craig et al. 2010) perspectives. Most authors convene that the genesis of macusanite-like melts is related to extreme crystal fractionation products of dry, F-, B-, Li-, and P-rich, felsic peraluminous magmas (Noble et al. 1984; Pichavant et al. 1987, 2024a, b). Noteworthy, macusanite is used as a geochemical reference material for the analysis of LCT pegmatites due to the striking trace element equivalence (Fabre et al. 2011;

London 2015). Fission track (Fleischer and Price 1964; Fleischer et al. 1965; Poupeau et al. 1992, 1993), K-Ar (Barnes et al. 1970; Poupeau et al. 1992), Rb-Sr (Pichavant et al. 1987), and Ar-Ar (Cheilletz et al. 1992) dating, constrains the age of studied macusanite specimens in the range between ca. 8 Ma and 3 Ma.

Barnes et al. (1970) were the first to recognize the mineralogical, chemical, and geochronological similitudes between macusanite pebbles and tuff of the Macusani Formation, which further supported a volcanic origin of macusanite. The earliest petrographic study of rocks that were latter grouped under the Macusani Formation described phenocrystic muscovite, feldspar, and quartz, and accessory minerals such as apatite and zircon (Francis 1959a, b). Phenocrystic andalusite (Barnes et al. 1970), sillimanite (Noble et al. 1984), and tourmaline (Arribas and Figueroa 1985a, b) were recognized years later. Rare mullite [$Al_{4.4}Si_{1.2}O_{9.6}$] was also described in tuff from the northwestern part of the field by Francis (1959b). However, more recent and detailed petrographic work in tuff from the Macusani Formation has failed to identify this mineral again (e.g., Pichavant et al. 1988a). Arribas and Figueroa (1985a, b) reported phenocrystic bipyramidal smoky quartz with sparse fluid inclusions in tuff associated with U anomalies.

The earliest whole-rock geochemical data of rocks from the Macusani Formation were published by Francis (1959b) and Barnes et al. (1970), who noted a rhyolitic composition and lower SiO_2 and higher Al_2O_3 contents compared to Pleistocene white tuffs from the neighboring Arequipa region. Barnes et al. (1970) also published the first Sr and O isotope and electron microprobe analyses of rocks from the Macusani Formation. Noble et al. (1984) provided three more whole-rock geochemical analyses of ash-flow tuff as well as fragments of glassy pumice from the same sequence as the one sampled by Francis (1959b) and Barnes et al. (1970). Noble et al. (1984) outlined that the Macusani Volcanic Field is composed of strongly peraluminous, rhyolitic, crystal-rich, ash-flow tuffs that are chemically equivalent to “S-type” or “two-mica” leucogranites. Arribas and Figueroa (1985a, b) and Valencia and Arroyo (1985) published the first petrographic descriptions and whole-rock analyses for an entire stratigraphic section, which stretches along the northeastern margin of the field, in Huiquiza, and was later documented by Pichavant et al. (1988a, b) and Pichavant and Montel (1988). Pichavant et al. (1988b) analyzed the major and trace element and isotope compositions of 16 samples of ash-flow tuff from the northeastern sector of the Macusani

Volcanic Field and proposed what is still the most widely accepted model for its petrogenesis. On the other hand, [Pichavant et al. \(1988a\)](#) and [Pichavant and Montel \(1988\)](#) modelled the ascent and cooling trajectories of magmas and discussed the main processes controlling the trace element signatures of both the tuff from the Macusani Formation and macusanite glass.

Geochronological works on the Macusani Formation developed in the 70s and 80s were limited to K-Ar dating ([Barnes et al. 1970](#); [Noble et al. 1984](#); [Pichavant et al. 1988a](#)) and lacked stratigraphic control at the regional level. Together, they constrained the deposition of the Macusani Formation between ca. 10.5 and 4.1 Ma. Also, that macusanite was broadly coeval with the youngest dated rocks of the Macusani Formation ([Cheilletz et al. 1992](#)). A decisive step forward in the volcanic stratigraphy and geochronology of the Macusani Volcanic Field was made in the early 90s by [Cheilletz et al. \(1990, 1992\)](#). These authors produced five stratigraphic sections in the eastern margin and central part of the field and obtained 42 new $^{40}\text{Ar}/^{39}\text{Ar}$ dates on glass, tuff, and intrusive rocks. From these data, [Cheilletz et al. \(1992\)](#) identified six volcanic cycles or cooling units grouped into two short-lived eruptive episodes at 7 ± 1 Ma and 10 ± 1 Ma and discussed their correlation with Andean tectonic events. [Sandeman et al. \(1997\)](#) correlated the lithostratigraphic, geochemical, and geochronological data of the Neogene volcanic fields in the Eastern Cordillera of southern Peru, contextualizing the Macusani Formation within regional time- and petrochemical-equivalent eruptive episodes which these authors collectively grouped under the Crucero Supergroup.

Very recently, [Pichavant et al. \(2024a\)](#) analyzed major and trace element contents in coexisting minerals and glass in twelve tuff samples from the Macusani Volcanic Field and reanalyzed four macusanite samples previously documented by [Pichavant et al. \(1987\)](#). The results were used to assess mineral/melt partition coefficients for 25 elements in strongly peraluminous rare-metal silicic magmas. The authors also confirmed previous petrogenetic interpretations on macusanite by [Pichavant et al. \(1987, 1988b\)](#) and updated the genetic model proposed for the origin of Macusani magmas. In addition, [Pichavant et al. \(2024a\)](#) have identified, for the first time, unequivocal geochemical evidence of a mafic component—large-ion lithophile element (LILE)- and light rare earths (LREE)-rich shoshonites and high- and moderate-K calc-alkaline basalts—in the magma source region.

The Macusani Volcanic Field has also attracted the attention of many researchers because of the energy mineral resources it hosts, including supergene uranium (Li 2016) and volcanogenic lithium (Nupen 2019). In addition, it also hosts epithermal Ag-Pb-Zn deposits, such as Corani in the southwest sector of the field (Ullrich 2006; Swarthout et al. 2010).

As a result of two exploration programs developed in 1976-1981 and 1982-1986, the Peruvian Institute of Nuclear Energy (IPEN) reported economic concentrations of U in the Macusani Volcanic Field (Rivera et al. 2011). Arribas and Figueroa (1985a, b) pioneered the mineralogical, petrographic, and metallogenetic characterization of the uriferous district located in the eastern sector of the field. The uranium mineralization is dominated by meta-autunite primarily concentrated within the Macusani Formation, and exhibits a pronounced structural control (Arribas and Figueroa 1985a, b; Valencia and Arroyo 1985). Li et al. (2012) published the first U-Pb dating of meta-autunite from the Macusani Volcanic Field and Li (2016) studied the geochemistry and mineralogy of variably altered ash-flow tuff samples from fourteen drill holes at five localities with uranium anomalies in the eastern sector of the field. Oxygen and hydrogen isotope compositions on meta-autunite suggest that the mineralizing fluids were meteoric waters at 15°C of temperature derived from periglacial flooding episodes of the Late Pleistocene (Li 2016). O'Connor et al. (2018) and Arroyo (2021) used Li's (2016) geochemical data to discuss the genetic model of the U mineralization in the district.

Lithium ore is mainly hosted by the so-called Lithium-rich Tuff and, to a lesser extent, an Upper Breccia and a Lower Breccia lithostratigraphic units (Nupen 2019). Torr o et al. (2023) published electron microprobe (EMPA), Raman spectroscopy, and transmission electron microscopy (TEM) analyses of Li-bearing mica (zinnwaldite and lepidolite) crystal clasts from the Lithium-rich Tuff. The high-resolution mineralogy study performed by Segovia-More et al (2023) allowed the identification of dioctahedral smectites and zeolites as the main lithium-bearing phases in the secondary mineral assemblages. Finally, Ramirez-Briones et al. (2023) studied the major and trace element geochemistry of the Lithium-rich Tuff and Upper and Lower Breccia units to discuss its magmatic provenance and post-depositional modifications. Data and discussions in Ramirez-Briones et al. (2023) are reproduced and expanded in this thesis.

1.4. Conundrum

The Macusani Volcanic Field hosts notorious magmatic products derived from strongly peraluminous, rare-metal silicic magmatism in which anomalously high contents of fluxing elements, such as F, B, and P were present (Pichavant et al. 1988a, b; 2024a, b). Unlike Hercynian S-type granites and rare-metal leucogranites, peraluminous magmas at Macusani did not stagnate and cool at depth, but reached the surface as pyroclastic mega-eruptions (Barnes et al. 1970; Noble et al. 1984; Pichavant et al. 1987; Cheilletz et al. 1992; Poupeau et al. 1993). This difference is attributed to the exceptional circumstances of partial melting involving H₂O-undersaturated conditions in the source and the presence of a protolith enriched in volatiles such as F and B (Pichavant et al. 1988a, b). Thus, the Macusani Volcanic Field stands as an exceptional natural laboratory to study magmatic processes. London et al. (1988) selected macusanite to study “melt vapor solubilities and elemental partitioning in peraluminous granite-pegmatite systems”. Pichavant et al. (2024a) used Macusani volcanic rocks to study trace element partitioning in “strongly peraluminous rare-metal silicic magmas”. Pichavant et al. (2024b) concluded that the Macusani volcanics stand as illustrative examples of strongly peraluminous leucogranitic rocks that were generated by mantle contributions into the crustal source region.

Beyond the obvious petrogenetic particularities and interest, the occurrence of volcanogenic Li mineralization in the Falchani Lithium Project, hosted by pyroclastic horizons of the Macusani Formation, offers an excellent opportunity to explore primary controls on this type of Li mineralization in peraluminous volcanic fields with an important ignimbrite component. In particular, a unit referred to as Lithium-rich Tuff, which is the main focus of this thesis, attains Li contents higher than 4,000 ppm (Nupen 2019). This unit is variably altered to clay and zeolite minerals (Segovia-More et al. 2023), and therefore also offers a window into secondary mobility of lithophile elements of interest—including, prominently, Li—during deuteric and/or weathering processes. Despite its high scientific interest, the Lithium-rich Tuff has never been explored from a geochemical—including element and isotope contents—perspective to trace its magmatic provenance and secondary element mobility.

The detailed study of volcanogenic Li deposits itself, as non-conventional sources of this metal, is much needed. The attainment of economical lithium grades in volcanogenic deposits is thought to be a result of surface weathering or hydrothermal alteration of pre-existing lithium-enriched rhyolitic volcanic rocks. This process prompts the deposition of secondary minerals that are lithium-rich, as discussed by [Benson et al. \(2017\)](#) and [Bowell et al. \(2020\)](#). The McDermitt Caldera in Nevada (USA) hosts some of the best studied volcanogenic lithium deposits ([Castor and Henry 2020](#); [Benson et al. 2023](#)). Despite the obvious similitudes between Li deposits in the McDermitt Caldera and Falchani, as their strong affiliation with tuffaceous sediments in large-volume ignimbrite fields related to large-scale anatectic events, systematic mineralogical differences highlighted by [Segovia-More et al. \(2023\)](#) suggest compositional differences of the volcanogenic protolith and/or the physico-chemistry (composition, pH, temperature) of the fluids. The two factors are known to have influence over both the thermodynamic equilibrium and dissolution kinetics ([Aagaard and Helgeson 1983](#); [Knauss et al. 1989](#); [Qinhua and Aizhen 1991](#); [Acker et al. 1992](#); [Kalinowski and Schweda 1996](#); [Buil et al. 2006](#); [Savage et al. 2007](#); [Asta et al. 2017](#); [Wang et al. 2019](#); [Bagheri et al. 2022a, b](#); [Jiménez et al. 2022](#)). Such potential differences are yet to be unveiled and may provide important clues about the impact of the composition of the volcanic protoliths and the physico-chemical characteristics of the secondary fluids during Li upgrading in volcanogenic deposits.

1.5. Objectives

The main objective of this study is the geochemical (elemental and isotopic) characterization of the Lithium-rich Tuff of the Falchani Lithium Project in the Macusani Volcanic Field, with a main focus on magma petrogenesis and post-depositional modifications.

Specific objectives include:

- To document the element and isotope compositions of rocks from the Lithium-rich Tuff;
- To compare the composition of the Lithium-rich Tuff with other lithium-ore units in the Falchani Lithium Project (i.e., Upper and Lower Breccia), and macusanite, ash-flow tuff, and intrusive rocks in the Macusani Volcanic Field;

- To ascertain the source rock and other petrogenetical aspects of magmas related to the genesis of the Lithium-rich Tuff; and
- To assess secondary processes that altered the primary composition of the Lithium-rich Tuff and their impact on Li enrichment.

1.6. Hypothesis

According to previous studies on volcanogenic rocks from the Macusani Volcanic Field (e.g., [Noble et al. 1984](#); [Valencia Herrera et al. 1984](#); [Pichavant et al. 1987, 1988a, b](#)), it is expected that isotope and element compositions of the Lithium-rich Tuff indicate a strong crustal signature and derivation from strongly peraluminous rhyolitic magmas that were highly enriched in incompatible lithophile and volatile elements. Post-depositional metasomatic reactions related to clay and zeolite formation and ensued lithium upgrading are expected to be recorded as systematic compositional trends. Also, by more pronounced variations of Sr isotope ratios, since both radiogenic Sr and parent Rb are more mobile in aqueous media than Pb and Nd, being the latter particularly immobile and hence a best indicator of primary, magmatic features.

1.7. Justification

The goal to supersede internal combustion engines by more eco-efficient technologies, many involving rechargeable Li-ion batteries, has triggered an abrupt increase in the demand for lithium in recent years ([Kesler et al. 2012](#); [Bowell et al. 2020](#)). Accordingly, the development and implementation of *clean energies* will probably push an increasing demand for lithium and other critical raw materials of mineral origin during the next decades ([Bibienne et al. 2020](#)). A shortage of lithium source discoveries and gaps in geological knowledge for a better evaluation of their economic exploitation (reserves) stand as major geological risks, which makes it imperious to better understand the genetic models of both conventional and non-conventional—including volcanogenic—lithium deposits ([National Research Council 2008](#); [European Commission 2020](#)).

The non-conventional volcanogenic Falchani Lithium Project, located in the Neogene Macusani Volcanic Field, hosts 1.01 Mt LCE (69 Mt @ 2792 ppm Li) measured resources, 4.52 Mt LCE (378 Mt @ 2251 ppm Li) indicated resources, and 3.99 Mt LCE (506 Mt @

1481 ppm Li) inferred resources (Clarke 2023). It is situated 750 km to the northeast of the so-called *Lithium Triangle of the Andes* (López Steinmetz and Salvi 2021), which contains more than 50% of the global Li resources. In the Falchani Lithium Project, lithium contents are close to cut-off grades in many LCT granitic pegmatites and comparable to worldwide economically most relevant volcanogenic Li deposits such as Kings Valley in USA and Jadar in Serbia. High-grade lithium ore in the Falchani Lithium Project is mostly related to a Miocene rhyolitic tuff unit, the so-called Lithium-rich Tuff, probably deposited in a lake environment (Nupen 2019), which stands as an exceptional natural laboratory to study primary and secondary processes associated to lithium upgrading from highly evolved, strongly peraluminous, silicic volcanogenic protoliths.

2. METHODOLOGY

2.1. Sampling

Sixty-eight rock samples (seventy-seven if duplicate samples are included) were collected during a fieldwork campaign in the Macusani Volcanic Field in October 2021. Forty-six of these samples were extracted from rock outcrops and the remaining twenty-two samples were extracted from drill holes. From this set of samples, thirty-nine samples (counting duplicates) of tuff and intrusive rocks were selected to investigate their major and trace element compositions in this thesis; in addition, nineteen of these samples were also analyzed for isotope relationships. The selection criteria included petrographic, geographic, and stratigraphic diversity of the rock samples.

Analyzed surface samples were picked up from the Falchani Lithium Project (n = 25, including both the Falchani and Ocacasa 4 concessions), and the Sapanuta 3 (n = 4), Huarituña 4 (n = 2), Antacora Seis (n = 4), San Vicente White (n = 3), and Colibri LXXIII (n = 1; Fig. 6) concessions. Drill core samples were collected from three drill cores that cut the Lithium-rich Tuff in the Falchani Lithium Project. Based on their spatial distribution within the Macusani Volcanic Field, the studied samples were grouped into the i) **Quelcaya** (n = 6; Fig. 6a), ii) **Falchani** (n = 25; Fig. 6b); and iii) **La Huaña** (n = 8; Fig. 6c) areas.

On the other hand, the studied samples were subdivided into six lithotypes taking into account the original ascription provided by Macusani Yellowcake (Nupen 2019), and/or the

nomenclature used in [Sandeman et al. \(1997\)](#), and/or our own lithological and stratigraphic observations, as follows:

- **Upper Breccia:** This unit has been defined by [Nupen \(2019\)](#) in the Falchani Lithium Project. It includes pervasively altered, brecciated, volcanoclastic facies located stratigraphically above the Lithium-rich Tuff unit also defined by this author. Rocks in the Upper Breccia are mostly non-cohesive, clayey, and white and grayish white in color. The limit between clasts and matrix is often diffuse as they both present very similar color and granularity characteristics. The breccia is mostly clast-supported. Most clasts are angular and have sizes in the range between 2 and 5 cm. Scarce medium to coarse ash-sized biotite, K-feldspar, and translucent quartz crystal fragments within clasts are matrix-supported. Studied samples of Upper Breccia were taken from the Falchani (n = 4) concession.
- **Lithium-rich Tuff,** as defined by [Nupen \(2019\)](#) in the Falchani Lithium Project, is the main ore unit and the main focus of this thesis. It consists of finely laminated—with alternating white/gray laminae—or locally massive volcanic mudstone of a characteristic white color. The lamination is mostly strongly folded and contorted and only locally planar. Fairly abundant interlayered biotite crystal clasts up to 3 mm in size stand in the white rock. The Lithium-rich Tuff is mostly cohesive and massive except for the occurrence of cavernous, globular, cm-scale concretions that are aligned parallel to general rock lamination in some samples (e.g., 2021-MAC-08, 2021-MAC-11). The studied Lithium-rich Tuff samples were taken from the Ocacasa 4 (n = 2) and Falchani (n = 15) concessions.
- **Lower Breccia:** This unit has been defined by [Nupen \(2019\)](#) in the Falchani Lithium Project. It consists of brecciated volcanoclastic facies located stratigraphically below the Lithium-rich Tuff. The characteristic pervasive alteration of the samples has obliterated most primary textures and led to distinctive low hardness and clayey and saccharoidal textures. Scarce, medium ash-sized biotite crystal clasts are locally observed. The studied samples of Lower Breccia were taken from the Falchani (n = 1) and Ocacasa 4 (n = 1) concessions.

- **Ash-flow tuff:** Poorly-sorted, crystal-rich lapilli tuff with a white, aphanitic matrix and variable proportions of coarse lapilli-sized juvenile clasts. Crystal clasts are mostly medium ash- to fine lapilli-sized and consist mainly of broken bipyramidal translucent quartz grains up to 5 mm in size, altered, subhedral, tabular feldspar crystals up to 2 mm in length, and euhedral biotite crystals up to 3 mm in length. Scarce, translucent crystals of andalusite are observed in samples 2021-MAC-12, 2021-MAC-018B, 2021-MAC-34, and 2021-MAC-47, and pinitized cordierite crystals with a prismatic habit are locally observed in sample 2021-MAC-20. Scarce prismatic plagioclase molds are observed in most samples. The juvenile clasts have almost equivalent mineralogical and textural characteristics as the surrounding rock except for a lower proportion of crystals. They consist mostly of porphyritic, white pumice fragments that are oriented and show flattened shapes indicating plastic deformation and curvilinear surfaces with delicate, acute, or spinous terminations denoting limited or nil transport. In contrast, lithic fragments are very scarce or absent in most of the samples, smaller (up to 5 mm in diameter) than juvenile clasts, and sub-rounded to sub-angular in shape. These characteristics are very similar to those described in ash-flow tuff of the Macusani Formation by [Sandeman et al. \(1997\)](#). According to their stratigraphic position, the ash-flow tuff samples in this thesis are further divided into pre- and post-lithium-ore units. Pre-lithium-ore ash-flow tuff occurs stratigraphically below the Lower Breccia unit and was sampled in the Falchani concession (n = 2). Post-lithium-ore ash-flow tuff occurs stratigraphically above the Upper Breccia unit and was sampled in the Falchani (n = 2), Ocacasa 4 (n = 2), Sapanuta 3 (n = 1), and Huarituña 4 (n = 1) concessions.
- **White tuff:** By this term I refer to massive or locally finely laminated, white to pale cream tuff that is found outside the Falchani Lithium Project. Matrix-supported biotite, quartz, and feldspar crystal clasts are common in some samples and their sizes are mostly comprised between <0.5 and 3.5 mm. Additionally, the sample 2021-MAC-67 hosts fine to medium lapilli-sized feldspar crystals with simple Carlsbad twinning, coarse ash-sized subhedral-tabular, pinkish muscovite crystals, and medium ash-sized, euhedral, black tourmaline crystals. Other samples do not exhibit

crystal clasts. The studied white tuff samples were picked up from the Sapanuta 3 (n = 4), Antacora seis (n = 4), and San Vicente White (n = 3) concessions.

- **Quenamari Suite granite:** This term refers to sampled intrusive stocks belonging to the middle- to late Miocene Quenamari Suite of the Crucero Intrusive Supersuite as defined by [Sandeman et al. \(1997\)](#). The samples consist of leucocratic, medium- to coarse-grained, tourmaline-bearing, two-mica granites. They show porphyritic and hypidiomorphic textures. The groundmass is white and aphanitic. Coarse- to very coarse-grained feldspar phenocrysts are up to 2 cm long and exhibit simple Carlsbad twinning. Translucent quartz phenocrysts are subhedral to anhedral, and fine- to medium-grain sized. Biotite phenocrysts show three distinct size populations: scarce medium- to coarse-grained crystals up to 6 mm; fine- to medium-grained crystals up to 1.2 mm; and ubiquitous very fine-grained microphenocryst. Euhedral translucent muscovite phenocrysts are fine- to medium-grained, up to 1.7 mm in size, and exhibit brownish-pink color. Euhedral black tourmaline crystals exhibit lengths between <0.5 mm and 2 mm. Quartz, coarse-grained biotite, and feldspar phenocrysts are poikilitic. Studied samples of Quenamari Suite granites include a dyke in the Huarituña 4 concession (n = 1) and a stock in the Falchani (n = 1) concession.
- **Picotani Suite granite:** This term refers to granite samples that belong to the Oligocene-Miocene Picotani Suite of the Crucero Intrusive Supersuite as described by [Sandeman et al. \(1997\)](#). The analyzed sample consists of a leucocratic, medium-grained, cordierite-biotite granite with porphyritic and hypidiomorphic textures and a pinkish-brown aphanitic groundmass. The main textural feature of the sample is the conspicuous occurrence of K-feldspar megacrysts that are up to 15 cm long and exhibit simple Carlsbad twinning. Anhedral, roundish, translucent quartz phenocrysts are medium- to coarse-grained. Biotite phenocrysts have three distinct size populations: sporadic medium-grained crystals up to 3 mm; fine-grained crystals up to 1 mm; and ubiquitous very fine-grained microphenocrysts. Medium- to very coarse-grained, greenish brown, pinitized cordierite phenocrysts and their phantoms exhibit pseudo-rhombic sections, are up to 20 mm in size, and host abundant fine-grained biotite inclusions. The studied sample of the Picotani Suite granite (n = 1)

belongs to the so-called Ninahuisa Stock (Sandeman et al. 1997) and was picked up in the Colibri LKKIII concession.

A list of the analyzed samples and their respective locations and field descriptions is provided in Appendix A. Hand-sample photographs and descriptions are provided in Appendix B.

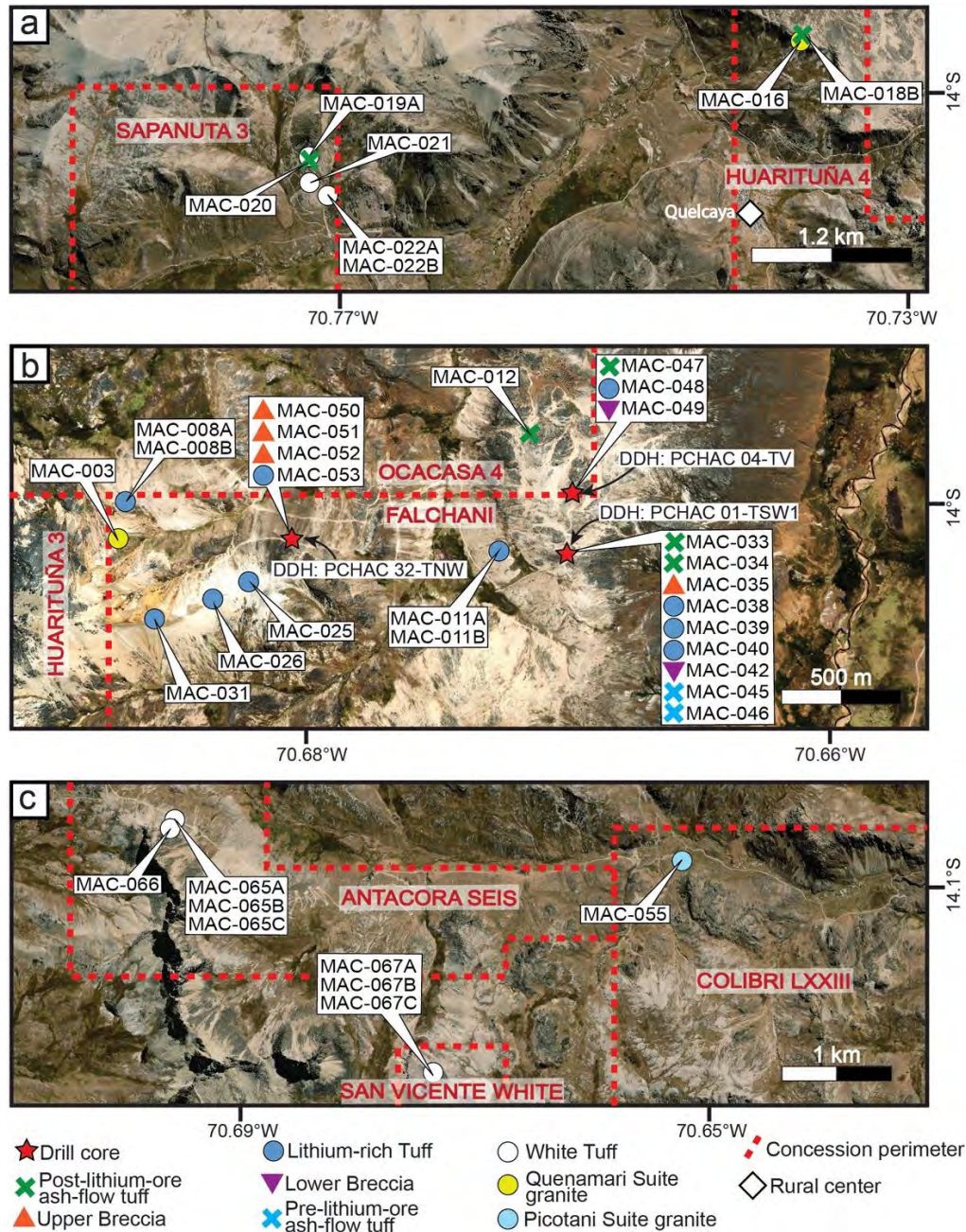


Figure 6. Zoom frames referenced in Figure 5 showing the location of the studied rock samples in the (a) Quelcaya, (b) Falchani, and (c) La Huaña areas. Satellite images are from Bing Maps (<http://www.bing.com/maps>). Concessions according to SIDEMCAT (2023).

2.2. Sample preparation

For bulk geochemical analyses, weathered parts of rock samples were removed by cutting with a diamond saw. The cut samples were then dried at 70 °C overnight (Fig. 7a) and subsequently crushed with a jaw crusher (Fig. 7b) until a fine powder was obtained. A representative fraction of about 10 g of the crushed rock samples was separated through rotary splitters (Fig. 7c-d) and then manually powdered to <50 μm using an agate mortar and pestle.

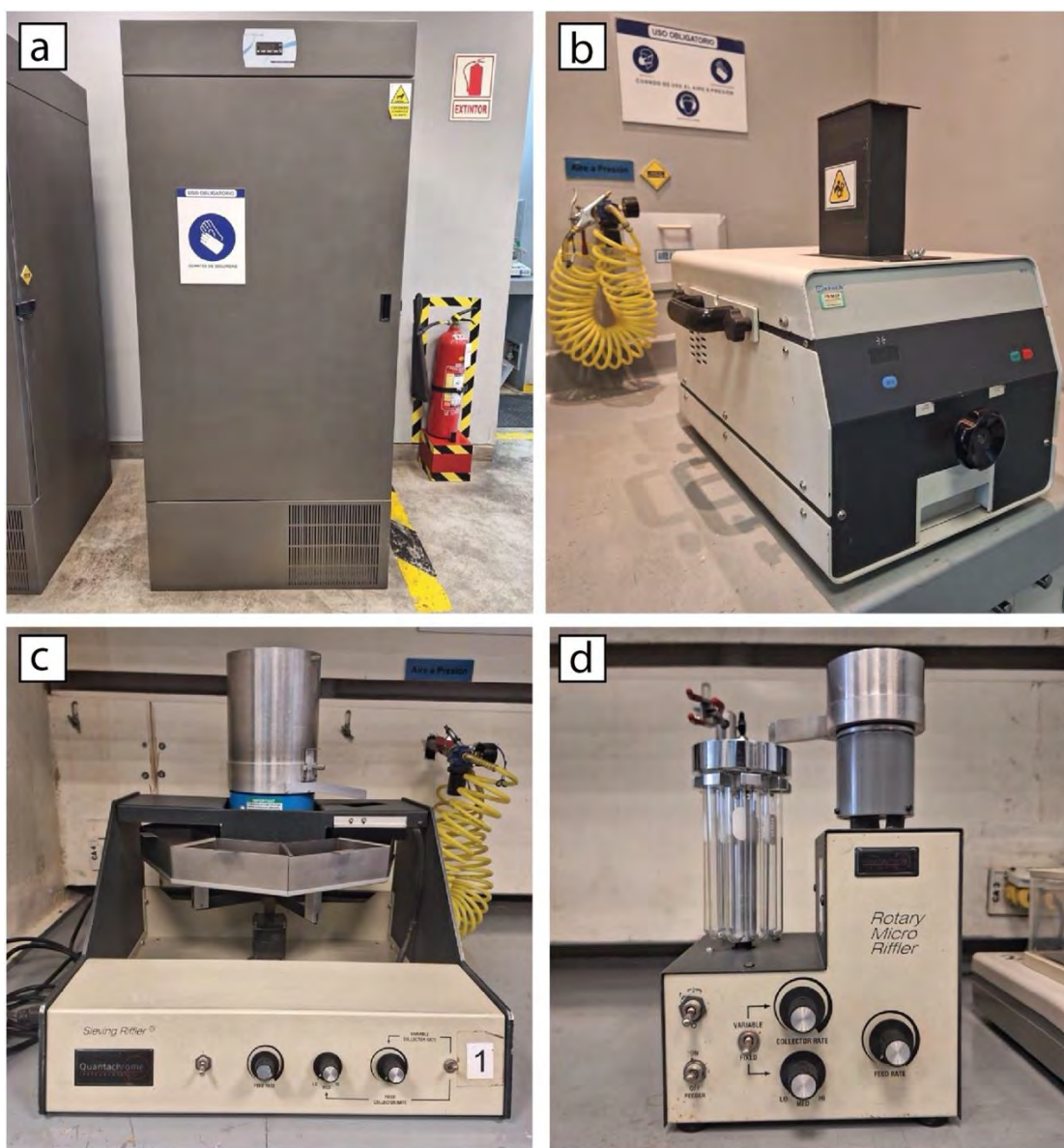


Figure 7. Photographs of equipment used in the QEMSCAN Laboratory at PUCP for the preparation of samples for whole-rock chemical analysis. (a) Furnace. (b) Retsch BB51 tabletop jaw crusher. (c) Sieving Riffler™. (d) Rotary Micro Riffler.

The Loss On Ignition (LOI) values were obtained using a programmable Carbolite muffle with a Eurotherm 301 temperature controller (**Fig. 8a**). About 3.5 g of powdered sample was heated in a ceramic crucible with a heating ramp of 15°C/min and then subjected to two thermal treatments: i) 24 hours at 100°C to volatilize water (H₂O) within rock porosity; and ii) 48 hours at 950°C to release structurally-bounded water (OH⁻, H₂O). Weight changes of each sample were registered before and after both thermal treatments (**Appendix C**). The LOI (wt.%) was calculated as 100*(weight lost on ignition/initial weight of sample).

A 2 g fraction of each thermally treated sample was used to prepare fused beads (homogeneous glass). A homogeneous mix of 1:5 of thermally treated sample and flux (66.67% Li₂B₄O₇, 32.83% LiBO₂, 0.5% LiBr) were introduced into a Katanax K1 Prime Electric Fluxer with a platinum crucible and a cylindrical standard sample holder of 16 mm in diameter and 2.5 mm in height.

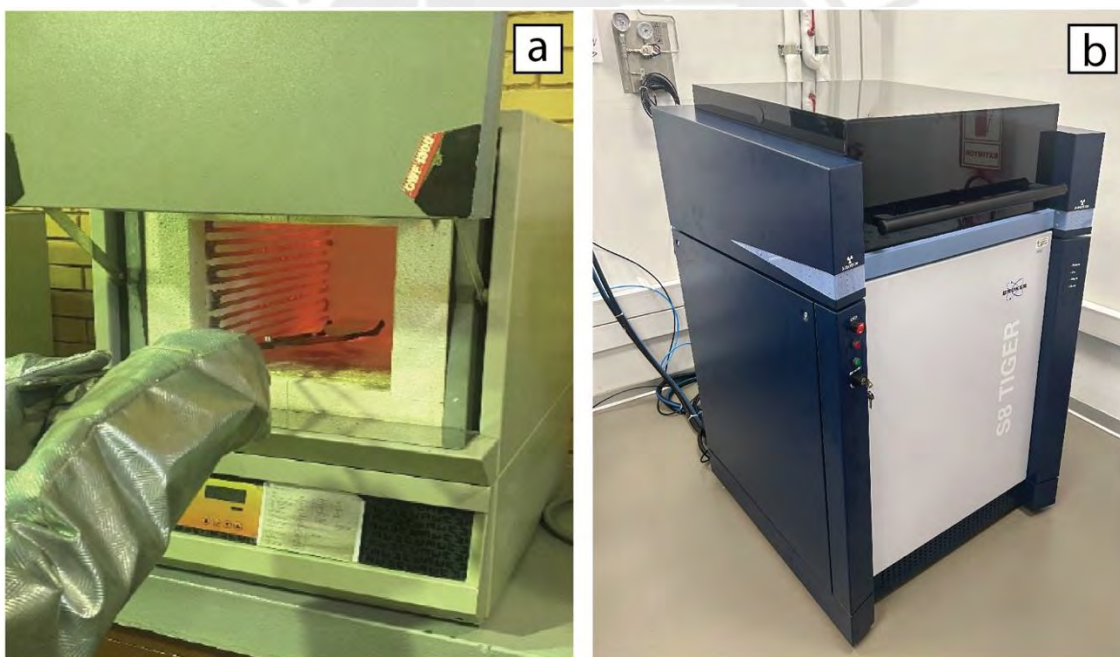


Figure 8. Photographs of equipment used for whole-rock chemical analysis. (a) Insertion of a ceramic crucible with 3.5 g of powdered rock sample into a Carbolite muffle. (b) Bruker-S8 Tiger X-ray fluorescence (XRF) equipment available at CAM-PUCP.

2.3. Whole-rock element geochemistry

Whole-rock major and minor element contents (SiO₂, TiO₂, Al₂O₃, Fe₂O_{3tot}, MnO, MgO, CaO, Na₂O, K₂O, Cr₂O₃, and NiO) were determined by XRF using a Bruker-S8 Tiger

available in the Centro de Caracterización de Materiales of the Pontifical Catholic University of Peru (CAM-PUCP; [Fig. 8b](#)). The analyses were performed on fused beads. Calibration was based on the standards G-1 (USGS), RGM-2 (USGS), JA-3 (Japan GS), and JB-3 (Japan GS). Data are reported on a LOI-free basis. The limits of detection depend on the element concerned but were in the range between 20 and 80 ppm.

Trace element contents were determined in the same fused beads used for XRF analyses by means of laser ablation inductively coupled plasma mass spectrometry (LA-ICP-MS). Measurements were performed with an Excimer 193 nm (ArF) GeoLas (Coherent) laser system coupled to an ELAN 6100 DRC quadrupole mass spectrometer at ETH Zürich. Measurements were conducted using a laser repetition rate of 10 Hz and a laser energy density of $\sim 10 \text{ J/cm}^2$ on the sample surface. The ablation aerosol was mixed in the in-house built ablation cell with carrier gas consisting of helium ($\sim 1 \text{ L/min}$). The ablated aerosol was then mixed with argon make-up gas and homogenized by flushing through an in-house built squid device before introduction into the plasma torch. An analytical scheme of 30 seconds recording gas blank and 40 seconds of target ablation was implemented following standard-sample bracketing procedure. Synthetic glass NIST SRM610 ([Jochum et al. 2011](#)) was analyzed every 15 unknowns with a spot size of $40 \mu\text{m}$ and used as primary reference material for normalization and instrumental drift correction. Fluxer blank was ablated using a spot size of $110 \mu\text{m}$ to correct for matrix effects on the glass beads. Secondary standard USGS BCR-2 ([Raczek et al. 2001](#)) was also analyzed with a spot size of $110 \mu\text{m}$ to test the accuracy and reproducibility of the analysis (ca. in the range of 2%–10% depending on the element). Three individual measurements per sample were made following the same parameters as for blanks and secondary standards. Data reduction was carried out in the MATLAB-based SILLS program ([Guillong et al. 2008](#)). XRF results (SiO_2 content) were used as an internal standard to convert raw counts to concentrations.

Whole-rock B and Li contents were determined at ALS Laboratories (Vancouver, Canada) by sodium peroxide fusion followed by ICP-MS analysis using the ME-ICP82b analytical package. Whole-rock Cl and F contents were analyzed in the same laboratory by KOH fusion and ion chromatography using the Cl-IC881 and F-IC881 analytical packages, respectively.

Whole-rock major and trace element contents are provided in [Appendix C](#).

2.4. Whole-rock isotope geochemistry

Whole-rock isotopic compositions were measured in nineteen samples. Isotopic ratios were corrected for an age of 8.9 Ma based on new $^{40}\text{Ar}/^{39}\text{Ar}$ dates on mica crystals from the Lithium-rich Tuff (unpublished data – L. Torró personal communication).

Lead isotopic compositions were measured on powdered samples using a Thermo Neptune Plus Multi-Collector ICPMS in static mode at the University of Geneva following the method described in [Chiaradia et al. \(2020\)](#). External reproducibility (1σ) of the Pb isotope analyses assessed using the NIST SRM 981 is 0.11% for $^{206}\text{Pb}/^{204}\text{Pb}$, 0.12% for $^{207}\text{Pb}/^{204}\text{Pb}$, and 0.20% for $^{208}\text{Pb}/^{204}\text{Pb}$.

Whole rock Sr and Nd isotopic compositions were obtained in GET-OMP, Toulouse University (France), using the Thermo Scientific TRITON+ solid source mass spectrometer, following [Li et al. \(2011, 2012\)](#) and [Labou et al. \(2020\)](#) procedures. Before measurement, about 100 mg of whole rock powder was weighed in a Teflon beaker and dissolved in a mixture HF/HNO₃ 1:1. After dissolution, samples were diluted in 1 mL, 2% HNO₃ and Nd/Sr were extracted from the matrix (0.126M HNO₃) using a combination of Sr-Spec and Thru-spec Eichrom resins. Mixed Sr and REE were loaded on a Re filament and run sequentially (first Sr then Nd) using a double Re filament protocol. Monitoring of the interferences of ^{87}Rb and ^{144}Sm were proceeded according to the protocol of [Li et al. \(2012\)](#) and the quality and reproducibility of the measurements were controlled using a sequential measurement of isotopic standards (SRM 987 and JNdi), doped isotopic standards (NBS 987+ Rb and JNdi + Sm), and laboratory-dedicated Sr+REE artificial solutions. Standard reproducibilities are 0.710270 ± 20 (n=47) for SRM-987 and 0.512099 ± 7 (n=22) for JNdi and fall within the recommended values. Measured blanks are 300 pg for Nd and 7 pg for Sr. $^{87}\text{Sr}/^{86}\text{Sr}$ and $^{143}\text{Nd}/^{144}\text{Nd}$ ratios were normalized against $^{86}\text{Sr}/^{88}\text{Sr} = 0.1194$ and $^{146}\text{Nd}/^{144}\text{Nd} = 0.7219$ respectively, after corrections from isobaric interferences using $^{87}\text{Rb}/^{85}\text{Sr} = 0.387041$ on ^{87}Sr and combination of $^{147}\text{Sm}/^{149}\text{Sm} = 1.08583$ and $^{147}\text{Sm}/^{144}\text{Sm} = 4.87090$ on ^{144}Nd .

3. GEOLOGICAL SETTING

3.1. Neogene ignimbrite fields in the Central Andes

With ~4000 km of extension from ~15 to 33°S, the Central Andes stands as the highest (up to ~6800 m.a.s.l.), widest (up to ~750 km), and thickest (up to ~78 km) segment of the Andes, the longest active subduction-related continental orogen on the world extending for ~8500 km from Venezuela to Patagonia (Fig. 9a; Wörner et al. 2018; Kay and Mpodozis 2020). Geomorphotectonic provinces in the Central Andes include the topographically-high Western and Eastern cordilleras and intervening low-relief Altiplano-Puna plateau, and the topographically-low Sub Andean Zone orogenic front (Fig. 9b; Kay and Mpodozis 2020). The Andes bend in the Central Andean (also known as Bolivian) orocline, with the northern branch trending northwest and the southern branch trending north (Capitanio et al. 2011).

The building history of the Central Andes is complex and encompasses non-accreting convergence between the Nazca oceanic plate and the South America continent with periods of shallowing and steepening of the Nazca slab, forearc subduction erosion, and delamination of thick dense continental crust and lithospheric mantle (Kay and Mpodozis 2020). Quasi-continuous subduction-related calc-alkaline magmatism along specific segments of the western margin of South America has been recorded since at least 200 Ma, following the breakup of Pangea (Kay and Mpodozis 2020). On the other hand, the so-called Inner Arc (Clark et al. 1983) or rear arc (Kay et al. 2010; Salisbury et al. 2022) displays episodic mantle- and crust-derived magmatic products exposed discontinuously along the Eastern Cordillera and Altiplano (Kontak 1985).

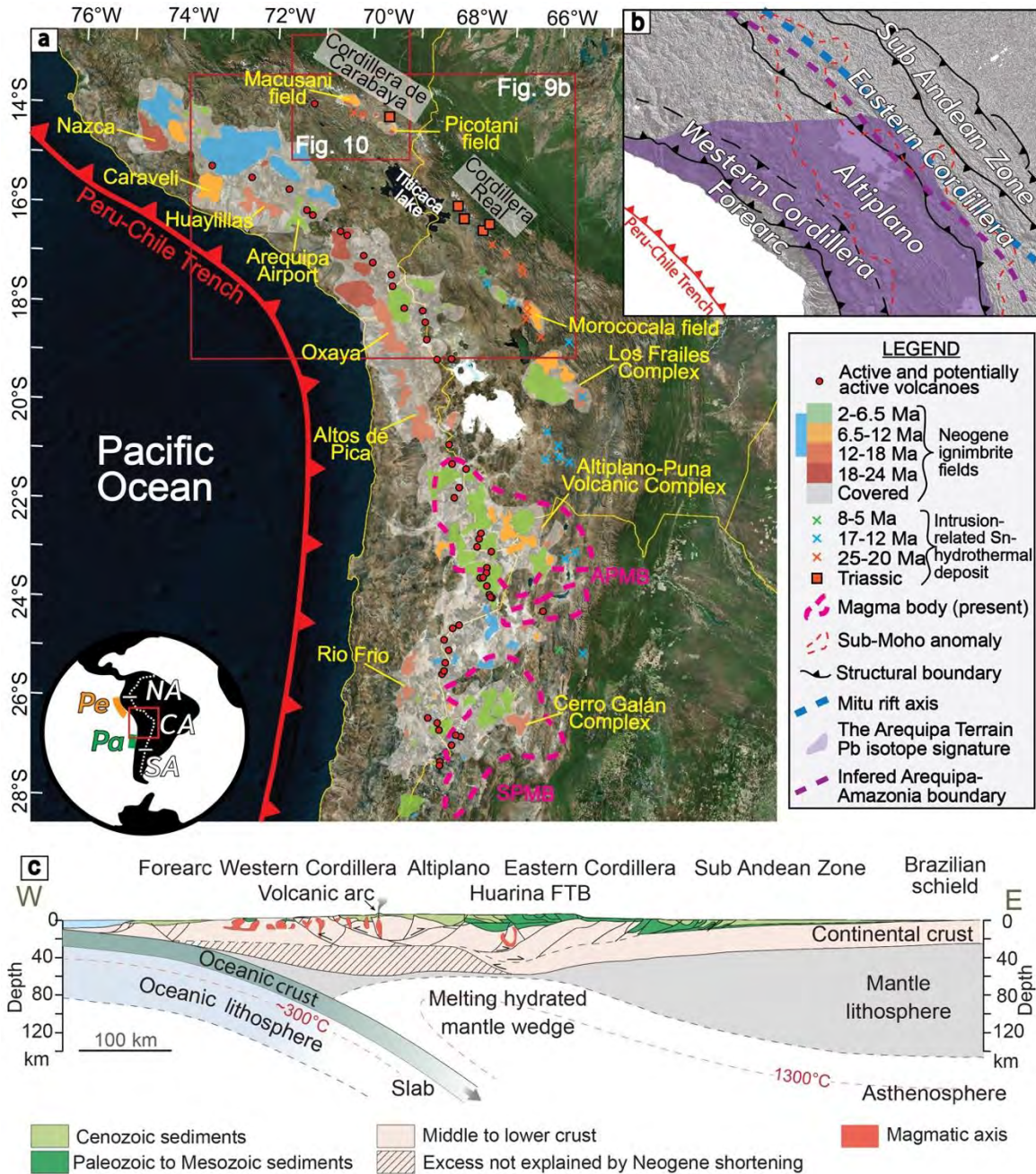


Figure 9. Location of the Macusani Volcanic Field and other Neogene ignimbrite fields in the Central Andes. (a) Satellite image of the Central Andes between 13° and 28° S (<https://www.bing.com>) showing the temporal distribution of Neogene Ignimbrite Province of the Central Andes (Wörner et al. 2018; Sandeman et al. 1997) and Triassic and Neogene (Gemrich et al. 2021; Sillitoe and Lehmann 2022) intrusion-related Sn hydrothermal deposits. Active and potentially active volcanoes are after Garzione et al. (2017) and Wörner et al. (2018). Geophysical anomalies APMB (Altiplano-Puna Magma Body) and SPMB (Southern Puna Magma Body) are after Ibarra and Prezzi (2019). Other abbreviations: NA (Northern Andes); CA (Central Andes); SA (Southern Andes); Pe (Peruvian flat-slab subduction zone); and Pa (Pampean flat-slab subduction zone). (b) Map of the structural boundaries of morpho-tectonic domains in the Central Andes in Peru-Bolivia-Chile (Armijo et al. 2015), sub-Moho Altiplano anomaly (Göğüş et al. 2022), Arequipa Domain region (Wörner et al. 2018), interpreted Arequipa-Amazonia boundary (Ramos 2018), and Mitu rift system axis (Sempere et al. 2002; Spikings et al. 2016). (c) Schematic cross-section of Pacific subduction and crustal structure of the Andes at 20°S (Moretti et al. 2023, modified from Baby et al. 1997 and Rochat et al. 1998).

The Neogene magmatic history of the Central Andes is characterized by large-scale caldera- and ignimbrite-forming eruptive events, referred to as ignimbrite flare-ups (de Silva 1989a, b; de Silva and Gosnold 2007; Ward et al. 2017; de Silva and Kay 2018). These events are considered unequivocal proof of large volumes of mantle-derived magma injections into a thermally prepared crust (de Silva et al. 2006; De Silva and Kay 2018) broadly contemporaneous with lithospheric removal, tectonic shortening, ductile crust flow, and crustal thickening (Baby et al. 1997; Husson and Sempere 2003; Kay et al. 2010; Garzione et al. 2017; Göğüş et al. 2022; Salisbury et al. 2022). Neogene ignimbrite fields are grouped under the so-called Neogene Ignimbrite Province of the Central Andes (de Silva et al. 2006), which extends from southern Peru to northern Argentina and covers a total area of approximately 300000 km² (Baker 1981). The Neogene ignimbrite cover is relatively continuous along-strike of the Western Cordillera main arc and more discontinuous along the rear arc in the Eastern Cordillera and Altiplano (Fig. 9a).

In general, there is a strong structural control on the distribution of volcanic centers along the Neogene Ignimbrite Province of the Central Andes (Viramonte and Petrinovic 1990; de Silva et al. 2006). For example, ignimbrite fields in southwestern Peru are focalized along E-W, NE-SW, and N-S strike-slip structural corridors controlled by NW-SE arc-parallel regional fault systems (Cerpa et al. 2012). Volcanic centers in western Argentina are spatially linked to a NW-SE to WNW-ESE transcurrent ‘megafracture’ system, especially at intersections with N-S arc-parallel structures (e.g., the eastern part of Altiplano-Puna Volcanic Complex; Viramonte et al. 1984) and, less commonly, faults of the NNE-SSW conjugate system (e.g., the Vilma, Coruto, and Guacha calderas; Soler 2005). In contrast, the structural controls are less clear in other segments of the Neogene Ignimbrite Province of the Central Andes such as in the western and central parts of the Altiplano-Puna Volcanic Complex (de Silva et al. 2006). There, main regional structural controls are covered by younger volcanic rocks (Baker 1981) and/or overprinted by the stress field associated with volcano-tectonic depressions (de Silva 1989b; de Silva et al. 2006).

The Neogene Ignimbrite Province of the Central Andes comprises regionally extensive dacitic to rhyolitic monotonous ignimbrite sheets, cake-shaped domes, and large, complex, multicyclic calderas and ignimbrite-dome complexes (Baker 1981; Gardeweg and

Ramirez 1987; Ort et al. 1987; Lindsay et al 2001; de Silva et al. 2006). Voluminous ignimbrite eruptions have occurred episodically over periods of several million years (e.g., Noble et al. 1974; Cheilletz et al. 1992; Wörner et al. 2000; Salisbury et al. 2011) and individual plateau-forming ignimbrite flows can reach volumes in excess of several 100s km³ (e.g., de Silva 1989b; Wörner et al. 2000; Salisbury et al. 2011; Kay et al. 2010) in this province.

The best documented ignimbrites related to the main arc in the Central Andes include, from south to north, the Río Frío (26-19 Ma; Siebel et al. 2001), Altos de Pica (24-16 Ma; Victor et al. 2004), and Oxaya (22-19 Ma; van Zalinge et al. 2022) ignimbrites in Chile, and the Arequipa Airport (ca. 1.6 Ma; Paquereau et al. 2006), Huaylillas (14-12 Ma), Caraveli (9.5-8.9 Ma), Alpbamba (19-18 Ma; Thouret et al. 2007), and Nazca (25-22 Ma; Noble et al. 1979; Roperch et al. 2011) ignimbrites in Peru (Fig. 9a; Brandmeier 2014; Wörner et al. 2018).

In the rear arc, thick piles of ignimbrite form discrete clusters around eruptive centers arrayed along-strike of the Eastern Cordillera north of 16°S (Fig. 9a). The most significant examples are the Macusani and Picotani volcanic fields in Peru (ca. 26-6.5 Ma; Sandeman et al. 1997). There is little or no record of Neogene volcanic activity in large areas of the Eastern Cordillera between ~16 and 18 °S, southeast of the Titicaca Lake (Fig. 9a). South of 18°S, rear arc-related ignimbrites form clusters along structural bounding zones between the Altiplano and the Western and Eastern cordilleras (Fig. 9a; Baker 1981; de Silva 1989a). They stand as some of the most voluminous and best preserved silicic volcanic complexes worldwide, such as the Los Frailes Complex at ~19.5°S, with ~2000 km³ of ejecta volume (25 Ma to present; Schneider 1985); the Altiplano Puna Volcanic Complex at ~23°S, with ~15000 km³ of ejecta volume (10 to 1 Ma; de Silva et al. 2006; Salisbury et al. 2011; de Silva and Kay 2018); and the Cerro Galán Complex at ~25°S, with ~1240 km³ of ejecta volume (6.4 to 2.1 Ma; Kay et al. 2010; 2011) (Fig. 9a). Some of them are genetically related to Sn, W, Ag, and base metal deposits (Clark et al. 1990; Sillitoe and Lehmann 2022) and hydromorphic Li deposits of the *Lithium Triangle of the Andes* (López Steinmetz and Salvi 2021).

The most widely accepted model for the petrogenesis of the Neogene Ignimbrite Province of the Central Andes involves crustal assimilation with simultaneous fractional crystallization (AFC) and hybridization during several residence periods in different stacked and interconnected crustal magmatic reservoirs (Wörner et al. 2018). In this model, lower-crust reservoirs of primitive (mantle-derived) and crustal melts are connected to middle to upper-crust reservoirs with andesitic and basaltic-andesitic magmas, and upper-crust reservoirs with dacitic to rhyolitic magmas (de Silva and Kay 2018; Wörner et al. 2018). Mid-crustal (~20 km depth) low-velocity regions such as the so-called Altiplano–Puna Magma Body (Schilling et al. 2006) and Cerro Galán Magma Body (Ward et al. 2017) (Fig. 9a) are present-day examples of large magmatic chambers composed of crystal mushes with up to 20% melt. Elevated geotherms enhanced by the injection of large volumes of hot, mantle-derived magmas and crustal stacking would promote rheological conditions favorable for protracted melt storage in the upper crust (3–8 km) and the formation of highly evolved, crystal-rich magmatic chambers (McQuarrie et al. 2005; de Silva et al. 2006; de Silva and Kay 2018). During episodes of high recharge rates of mantle-derived magmas, acidic magmas would mobilize from previously accumulated crystal mushes in the upper crust in relatively short periods of time triggering the eruption of great volumes (>1000 km³) of phenocryst-rich ignimbrites (Wörner et al. 2000, 2018; de Silva and Gosnold 2007; Salisbury et al. 2011; de Silva and Kay 2018). This mechanism explains why ignimbrite flare-ups are often coeval with mafic magmatism embracing shoshonite, medium- to high-K basalt, and/or calc-alkaline basalt in the Neogene Ignimbrite Province of the Central Andes (Kay et al. 1994; Carlier et al. 1997, 2005; Sandeman et al. 1996, 1997; de Silva and Kay 2018; Wörner et al. 2018; Pichavant et al. 2024a).

The intensified injection of mantle-derived magma into the crust under the Neogene Ignimbrite Province of the Central Andes has been correlated with asynchronous events of lithospheric mantle—and, probably eclogitic crustal roots—removal (Kay et al. 2010; Garzione et al. 2017). These events are interpreted either as widespread lithospheric delamination (Kay and Kay 1993; Kay et al. 1994) with lateral melt migration (Hoke and Lamb 2007) or localized lithospheric drip and ensued lower crustal flow and thickening/thinning (Göğüş et al. 2022). Seismic analyses point to a decrease in the crust thickness of ~15 km in the vicinity of the Altiplano-Puna Volcanic Complex relative to

adjoining areas (Beck and Zandt 2002; Yuan et al. 2002). Seismic tomographic models through the Los Frailes Complex (Myers et al. 1998; Baumont et al. 2002; Beck and Zandt 2002), Altiplano-Puna Volcanic Complex (Yuan et al. 2002; Asch et al. 2006; Schurr et al. 2006; Wölbern et al. 2009), and Cerro Galán Complex (Bianchi et al. 2013; Heit et al. 2014; Liang et al. 2014; Beck et al. 2015) suggest that delamination is an ongoing process in the Central Andes (Ryan et al. 2016; Ward et al. 2016, 2017). The most widely accepted triggers for lithospheric delamination are the steepening of the oceanic slab (Kay and Coira 2009) and focalized crustal thickening by lower-crust lateral flow from overthickened adjacent domains (Salisbury et al. 2022).

Pre-Neogene thermal weakening of the mantle lithosphere leading to its eventual removal can be explained by hydration during shallowing of the subduction angle (James and Sacks 1999; Wagner et al. 2005, 2006; Kay and Coira 2009). A period of low-angle subduction during the Eocene and early Oligocene is recorded in Peru (e.g., Perelló et al. 2003) and Chile (e.g., Trumbull et al. 2006). Latest Oligocene and Neogene diachronous southward episodes of slab steepening in the Central Andes post-date this episode (Kay and Coira 2009; Mamani et al. 2010). Geochronologic studies of Neogene volcanic rocks in the Central Andes are consistent with a latest Oligocene switch from steady-state subduction-related magmatism—dominantly, andesite–dacite composite cones—in the Western Cordillera, to an ignimbrite flare-up mode—dominated by large-scale ignimbrite-dome complexes—in the Western Cordillera, Altiplano, and Eastern Cordillera (Roperch et al. 2006; de Silva and Kay 2018). The steepening of the subduction angle and consequent decompression melting of asthenospheric mantle in the mantle wedge above the steepening slab is invoked as a key factor to explain ignimbrite flare ups by Kay and Coira (2009) and Freymuth et al. (2015). Southward younging of ignimbrite flare-up events has been correlated with the passage of the southwardly-subducting Juan Fernández Ridge over the last 25 M.yr. to its actual position at ~32°S in central Chile (Yañez et al. 2001; Kay and Coira 2009; Bello-González et al. 2018). This is consistent with the observations of James and Sacks (1999), Wörner et al. (2000), Paquereau et al. (2006), Thouret et al. (2007), and Picard et al. (2008) who highlight the existence of a magmatic lull, uplift, and erosion followed directly by large-scale ignimbrite eruptions as a typical succession of events in the Central Andes during the Neogene.

Several authors have used Sr/Y, Dy/Yb, Sm/Yb, and La/Yb ratios in rocks of known age to track regional variations in crustal thickness in the Central Andes. Results in volcanic rocks from southern Peru, Chile, and northern Bolivia reveal a relatively thin crust (<40 km) at the end of the Mesozoic, followed by a long period of incipient crustal thickening from the Upper Cretaceous to Eocene and two short periods of significant crustal thickening during the Oligocene-early Miocene (45 to 20 Ma) and Pliocene-Quaternary (Garziona et al. 2017). Radiogenic Sr, Nd, and Pb and stable O isotope analyses in the youngest Neogene ignimbrites are consistent with increasing degrees of cortical assimilation and longer residence times in a thicker crust (Kay et al. 2010; Freymuth et al. 2015; Garziona et al. 2017). Mass balance calculations by Freymuth et al. (2015) point to a shift from 15-37% to 22-68% crustal contribution in the Neogene Ignimbrite Province of the Central Andes at around 10 Ma. Further, calculations by Kay et al. (2010) point to 50:50 volume mixtures of mantle-derived basalts and low to middle crust-derived melts in Neogene ignimbrite fields between 22° S and 27° S that are younger than 7 Ma.

Although mantle-derived endmembers in hybrid magmas can be traced through isotope ratios, these are often obliterated by assimilation of regionally variable lower to middle crust (Garziona et al. 2017; Wörner et al. 2018). High Nb, Ta, and Ti contents in Neogene volcanics located between 19°S and 20°S led Salisbury et al. (2022) to propose a metasomatized mantle-derived component. On the other hand, Pb isotopes are particularly sensitive to the age and metamorphic history of the assimilated crust. In the particular case of the southern Central Andes, the Paleoproterozoic Arequipa Domain has been circumscribed based on its unusually non-radiogenic $^{206}\text{Pb}/^{204}\text{Pb}$ (Fig. 9b; Casquet et al. 2010; Mamani et al. 2010; Goss et al. 2013; Wörner et al. 2018).

3.2. Tectonic framework of the Eastern Cordillera in southern Peru

The southern segment of the Eastern Cordillera in Peru, located between the Altiplano plateau and the Sub-Andean Zone orogenic front, is characterized by its general NW-trending orientation and high elevations reaching 6000 m (Perez et al. 2016a, b; Baby et al. 2018; Fig. 9b). Several authors have modeled the deep structure of the crust based on geophysics, structural, and stratigraphic datasets reaching different models of crustal shortening. Baby et al. (1997) interpreted that the Eastern Cordillera overlies an east-verging crustal duplex (Fig.

9c) with lower detachment at the Moho discontinuity and the upper detachment at the base of Paleozoic strata. Alternatively, Müller et al. (2002) and Elger et al. (2005) proposed a bivergent system of stacked thrust slices of upper- and middle-crust transported over an east-verging frontal ramp that roots within the ductile lower crust beneath the Eastern Cordillera. On the other hand, McQuarrie et al. (2005, 2008) considers the Eastern Cordillera and the Altiplano as overlying an east-verging system of two stacked, ~10 km-thick basement megathrust sheets that accommodate the motion of a major mid-crustal decollement zone. In this model, the formation of the Eastern Cordillera is linked to the Eocene-Oligocene movement of the upper basement megathrust sheet, whereas the Miocene activation of the lower basement megathrust fed the shortening in the Sub Andean Zone (McQuarrie et al. 2008). An oriented balanced cross-section covering the Eastern Cordillera and Sub-Andean Zone in southern Peru (~13–15 °S) published by Perez et al. (2016b) constrains 130 km of orogen-normal deformation during the Cenozoic (Fig. 10). Also, Baby et al. (2018) calculated 47 km of total structural shortening in the Sub-Andean Zone in southern Peru.

The Eastern Cordillera in southern Peru developed during the Andean orogeny from selective tectonic inversion of pre-Cenozoic normal faults (Sempere et al. 2002). Inherited structures from the middle to upper Triassic Mitu rift accommodated the highest degree of Cenozoic transpression (Fig. 10; Sempere et al. 1990, 2002; Perez et al. 2016a). The Mitu rift encompassed a system of half grabens and pull-apart basins formed during the breakup of Pangea and controlled by the inherited pre-Mesozoic lithospheric architecture in the western margin of Gondwana (Tankard et al. 1995; Carlotto 2013; Ramos 2019). Syn-rift igneous and sedimentary deposits have been reported from Venezuela (240-225 Ma) to Patagonia (222 Ma; Reitsma 2012; Spikings et al. 2016). The main axis of the Triassic rift system in Peru and Bolivia coincides with the axis of the Eastern Cordillera, along which deeper structural levels are exposed relative to the Western Cordillera and Altiplano (Sempere et al. 2002; Perez et al. 2016a; Fig. 10). Rocks of the Mitu Group exposed across Peru are made up of molasse facies and alkaline to subalkaline basalts and andesites (Laubacher 1978; Marocco 1978; Mégard 1978; Dalmayrac et al. 1980; Carlotto 1998; Cenkic et al. 2000; Panca 2010; Valencia et al. 2010; Spikings et al. 2016). Coeval alkali-calcic, calc-alkalic, and calcic peraluminous granites to quartz diorites are most voluminous at

~14°S and decrease in volume northward before disappearing at latitudes northern than ~10°S (Mišković et al. 2009; Reitsma 2012).

In southern Peru, arc activity during the upper Triassic to lower Cretaceous period is recorded in the Western Cordillera by calc-alkaline basalts and andesites of the ~216-135 Ma-age Chocolate Arc (Boekhout et al. 2013; Spikings et al. 2016). Arc-related plutonism include the early Jurassic gabbros to monzonalites of the Punta Coles Superunit in the Western Cordillera (Mukasa 1986, 1990; Demouy et al. 2012; Santos et al. 2019) and the late Jurassic diorites to tonalites of the Ilo batholith in the present-day forearc (Mukasa 1986; Boekhout et al. 2012). Extension and lithospheric thinning in southern Peru continued from the early Jurassic until at least the early Cretaceous (Boekhout et al. 2012, 2013, 2015) as recorded by juvenile, poorly evolved magmatic arc products (Petford and Atherton 1995; Romero et al. 2013). In the Eastern Cordillera, the lower Jurassic Allinapac volcano-plutonic complex (Fig. 10), which include the so-called Macusani syenite, is mostly characterized by highly high-field-strength element (HFSE)-enriched and SiO₂-undersaturated alkaline to peralkaline gabbro, diorite, and nepheline-bearing syenite (Francis 1956; Kontak et al. 1990). This complex likely resulted from low degrees of partial melting of shallowest asthenospheric mantle beneath a thinned lithosphere in an extensional back-arc setting (Kontak et al. 1990; Mišković et al. 2009; Reitsma 2012).

The development of the Andean relief initiated at the end of the late Albian due to a shift in subduction dynamics prompted by the separation of Africa and South America in the framework of the breakup of Gondwana (Benavides and Cáceres 1999; Jaillard et al. 2005; Callot et al. 2008). The westward drift of South America towards the Nazca/Farallón plate increased the mechanical coupling between both plates (Ramos 2018). Crustal thickening due to structural shortening and magmatic additions began in present-day Western Cordillera, as inferred from upper Cretaceous-Eocene calc-alkaline batholiths (Mukasa 1986) and the Paleocene–Eocene foreland basin system in present-day Altiplano (Carlotto 2013; Perez and Horton 2014; Perez et al. 2016a; Sundell et al. 2019).

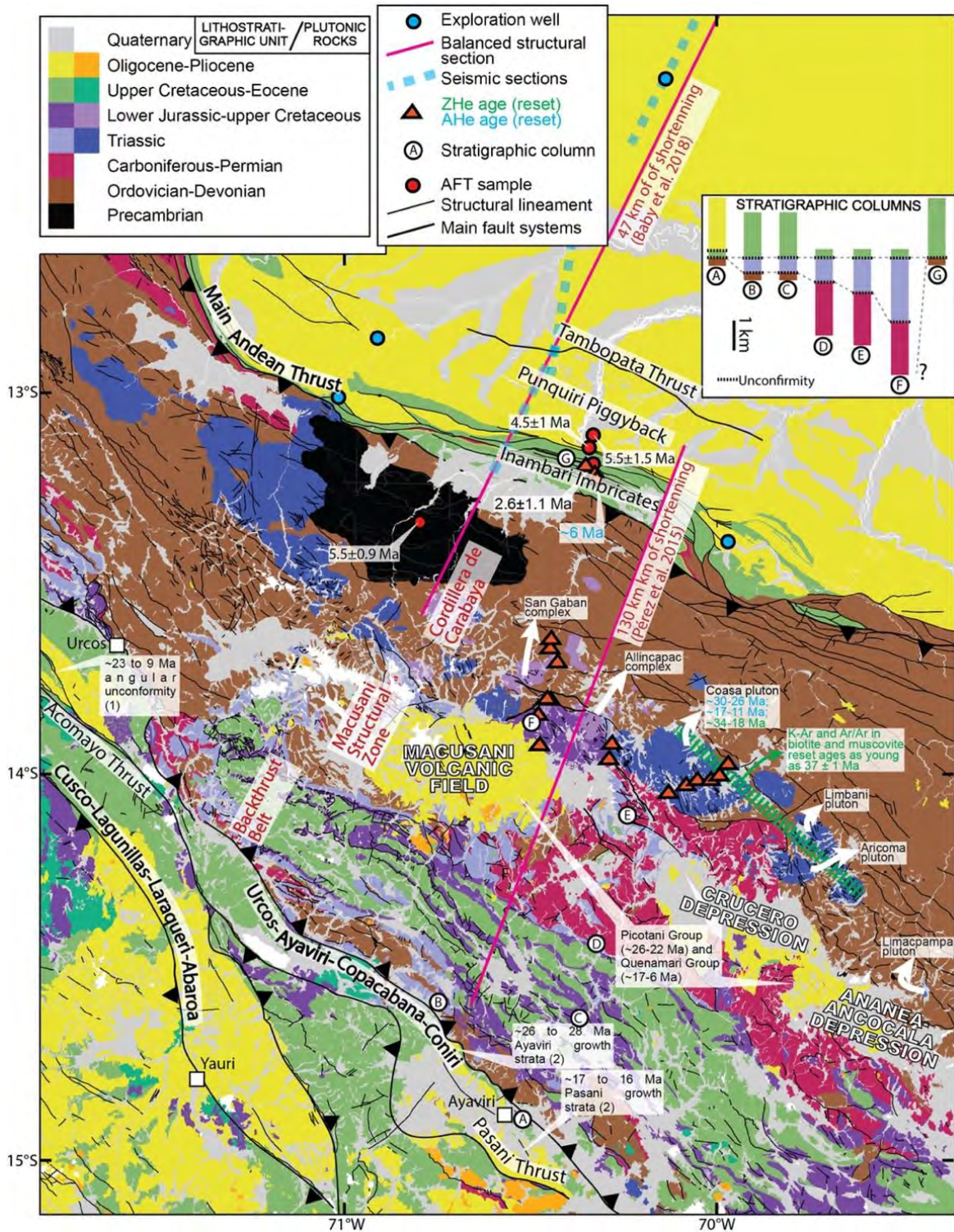


Figure 10. Geological map of the Altiplano, Eastern Cordillera, and Sub Andean Zone in southern Peru. Modified from Sempere et al. (2004), Perez and Horton (2014), Perez et al. (2016a), Baby et al. (2018), Sundell et al. (2019), and INGEMMET (2023). Balanced structural cross sections, exploration wells, seismic sections, and AFT (apatite fission track), apatite (AHe), and zircon (ZHe) (U–Th)/He thermochronology data are after Lease and Ehlers (2013), Perez et al. (2016b), and Baby et al. (2018). Stratigraphic columns are after Perez and Horton (2014). (1) and (2) in white boxes correspond to the references Sundell et al. (2019) and Perez et al. (2016b), respectively.

During a period of low-angle subduction at ca. 45-30 Ma (Sandeman et al. 1995), the magmatic arc occupied an eastward (i.e., inland) anomalous position, more than 400 km eastward from the present subduction-margin location (Carlier et al. 1996; Perelló et al. 2003; Mamani et al. 2010) and more than 510 km taking into account removed forearc by tectonic erosion during the last 11 M.yr. (Clift 2003). This is supported by the calc-alkaline Andahuaylas-Anta Arc (45-30 Ma) along the Cusco-Lagunillas-Laraqueri-Abaroa fault system (Fig. 10; Carlotto 2013), and the Acomayo (48-34 Ma) and Pomacanchi (44-37 Ma) plutons in the northernmost Altiplano at 14°S (Carlier et al. 1996). The Eocene/early Oligocene period of slab horizontalization coincided with extensive shortening-related exhumation in the Eastern Cordillera (Farrar et al. 1988; James and Sacks 1999; Gillis et al. 2006; Perez and Horton 2014). Available K–Ar, $^{40}\text{Ar}/^{39}\text{Ar}$, and fission track dates in the Eastern Cordillera of southern Peru and northern Bolivia support an eastward jump in locus of deformation from the Western Cordillera to the Eastern Cordillera at 45-38 Ma (Kontak et al. 1985; Benjamin et al. 1987; Farrar et al. 1988; Gillis et al. 2006).

Voluminous shoshonitic to absarokitic basalt and subordinate high-K calc-alkaline andesite of the Tacaza Arc exposed along the Cusco-Lagunillas-Laraqueri-Abaroa fault system (Fig. 10; Clark et al. 1990; Wasteneys 1990; Sandeman et al. 1995; Carlier et al. 1996) pinpoint the beginning of the westward retreat of the magmatic arc toward the trench and associated slab steepening from ca. 30 Ma (Mamani et al. 2004, 2010; Wörner et al. 2018). Widespread magmatism between 30 Ma and 27 Ma in southern Peru encompassed both alkaline and calc-alkaline magmas (Sandeman et al. 1995; Carlier et al. 1996). Between the Pasani thrust and the Urcos-Ayaviri-Copacabana-Coniri fault system, exposed leucite-bearing basanite levels were deposited at ca. 29-27 Ma and leucite-bearing basanite-phonotephrite-trachyte suites and high-K monzogabbroic subvolcanic intrusions were emplaced at ca. 30-28 Ma (Fig. 10; Carlier et al. 1996). Broadly contemporaneous alkaline volcanoclastic breccias are exposed west of the Pasani Thrust with thicknesses of several hundreds of meters (Ibarra et al. 2004). Reports of intraplate alkaline intrusive rocks along the Pasani Thrust include ~29 Ma-age diorite, monzodiorite, and monzonite of the Cupi massif, and the ~28 Ma-age nepheline-bearing syenite of the Livichaco stock (Mamani et al. 2004). Alkaline syenite dykes of similar age are reported in the northern edge of the Altiplano (Carlier et al. 1996).

(U-Th)/(He) dates on apatite and zircon from the Triassic Coasa Pluton (**Fig. 10**) record two rapid exhumation-cooling events in the Oligocene and middle Miocene (**Perez et al. 2016a**). The first deformation event was broadly coincident with the deposition of growth strata in Puno Group along the synsedimentary Ayaviri thrust and a gradual change of the detrital source in Altiplano basins from the Western Cordillera to the Eastern Cordillera at 30-26 Ma (**Perez and Horton 2014**). This was broadly concomitant with the breakup of the oceanic Farallon plate and ensued abrupt increase in the convergence rate along the subduction margin in southern Peru (12°S) at 28-26 Ma (**Somoza and Guidella 2005**). The onset of the second exhumation-cooling event identified in the Eastern Cordillera coincided partially with the compressional reactivation of the out-of-sequence Pasani thrust recorded by the 17-Ma growth strata in the Upper Tinojani Formation in the Altiplano (**Fig. 10**; **Perez and Horton 2014**).

Paleo-altimetry data support 1.5–2 km of surface-uplift in the Eastern Cordillera of southern Peru between 25 and 10 Ma (**Sundell et al. 2019**), and 2-3 km of rapid uplift in the northern Altiplano either between 15 and 10 Ma (**Sundell et al. 2019**) or between 10 and 5 Ma (**Kard et al. 2016**). The (U-Th)/He apatite dates from the San Gaban canyon in the Eastern Cordillera are consistent with slow (≤ 0.5 mm/y) shortening rates from ca. 10 Ma to present (**Buford Parks et al. 2023**). Partial to complete resetting of (U-Th)/He systems in apatite from the Sub Andean Zone in southern Peru suggests that deformation and associated exhumation cooling peaked at 6 Ma (**Fig. 10**; **Perez et al. 2016a**).

Three morpho-structural domains are established in the modern Eastern Cordillera in southern Peru (**Fig. 10**). From east to west, these are:

- The **Cordillera de Carabaya** is the NW continuation of the Cordillera de Apolobamba in Peru-Bolivia and the Cordillera Real in Bolivia (**Brad et al. 1974**; **Clark et al. 1983**; **Gillis et al. 2006**). To the northeast, the Cordillera de Carabaya is limited by the Main Andean Thrust and acts as a major deformable backstop of the Sub Andean Zone (**Hermoza et al. 2005**; **Eude et al. 2015**; **Calderón et al. 2017**). To the southwest, it is limited by the Cordillera de Carabaya backthrust, a SW-verging post-Triassic thrust that crosscuts Triassic normal faults in the eastern margin of the

Mitu rift fault system (Perez et al. 2016a). The Carabaya mountain belt encompasses the deepest exposed structural levels in the Eastern Cordillera. It is interpreted as a large passive roof duplex over the higher basement thrust sheet that feeds slip to the Sub Andean Zone (Perez et al. 2016a). The Cordillera de Carabaya embraces a series of middle to upper Triassic batholiths and less abundant lower Jurassic plutons with strongly variable geochemical affinities (Lancelot 1978; Kontak et al. 1990; Mišković et al. 2014; Spikings et al. 2016). The exposed intrusive rocks are hosted by an Ordovician to Silurian metasedimentary sequence and, to a lesser extent, pre-Ordovician metamorphic rocks (Sánchez and Zapata 2003; Bahlburg et al. 2006; Calle et al. 2023), Carboniferous to Permian silico-calcareous marine deposits, Triassic syn-rift deposits (Spikings et al. 2016), and Jurassic peralkaline volcanics (Fig. 10; Laubacher 1978; Clark et al. 1990; Kontak et al. 1990).

- The **Macusani Structural Zone** (Perez et al. 2016a) was previously known as ‘Late Hercynian’ fold domain (Laubacher 1978) or Pre-Cordillera de Carabaya (Kontak et al. 1990; Sandeman et al. 1997). To the southwest, it is structurally limited by the San Anton boundary (Fig. 10), a non-outcropping pre-Andean fault that controlled the spatial distribution of Permian to Triassic sediment accumulation in southern Peru (Perez et al. 2016a). However, at surface, the limit between the Central Andean Backthrust Belt and the Macusani Structural Zone is delineated by the stratigraphic contact between Jurassic-Cretaceous and underlying Paleozoic and Triassic rocks (Perez et al. 2016b). The Macusani Structural Zone coincides with the northernmost segment of a late Permian Gondwanide orogenic belt that recorded multiphase, non-coaxial deformation of Permo-Carboniferous strata (Mégard et al. 1978; Laubacher 1978; Marocco 1978; Perez et al. 2016a, b) sealed by Triassic syn-rift deposits (Spikings et al. 2016). Selective reactivation of pre-Andean normal faults as thrust faults during Andean shortening explains the lack of the typical NW-SE trending regional Andean faults in the Macusani Structural Zone. The broad folds, wide thrust fault spacing, and thick deformed sedimentary cover that characterize the Macusani Structural Zone is interpreted by Perez et al. (2016b) as basement-involved, thick-skinned shortening. Thicknesses in excess of 1 km of rocks of the Triassic Mitu Group (Fig. 10) with the most voluminous exposures of syn-rift alkaline basalts are found

in the Macusani Structural Zone (Laubacher 1978; Mégard 1978). Three major Neogene volcanic fields, represented geomorphologically by the Macusani (also known as Quenamari; Audebaud 1973; Rodríguez et al. 2021), Cayconi, and Picotani mesetas, are spatially related to NW-oriented, intermontane topographic depressions, namely Macusani, Crucero, and Ananea-Ancocala (Kontak et al. 1990; Sandeman et al. 1997). Neogene extrusive rocks in the Macusani Structural Zone were grouped by Sandeman et al. (1997) into the Crucero Supergroup.

- The **Central Andean Backthrust Belt** comprises the Putina Fold-Thrust Belt (Canaza 2018), which is the NW continuation of the Huarina Fold-Thrust Belt in Bolivia (Sempere et al. 1990; McQuarrie and DeCelles 2001; Jiménez and López-Velásquez 2008). To the southwest, the Central Andean Backthrust Belt is limited by the Ayaviri fault (Perez and Horton 2014; Perez et al. 2016a, b). The Ayaviri fault is part of the 400-km-long Urcos-Ayaviri-Copacabana-Coniri Fault System stretching from southern Peru to central Bolivia and defining the structural boundary between the Eastern Cordillera and the Altiplano (Sempere et al. 1990, 2004; Dorbath et al. 1993; Ibarra et al. 2004; Carlier et al. 2005; Sempere and Jacay 2008; Carlotto 2013; Perez et al. 2016b). In this domain, SW-verging fold-thrust structures expose Cretaceous-Jurassic strata and, to a lesser extent, Permian to Ordovician basement sequences (Canaza 2018).

3.3. The Macusani Volcanic Field

The Macusani Volcanic Field hosts the youngest and most septentrional Neogene eruptive system in the Macusani Structural Zone (Cheilletz et al. 1992). Preserved Neogene ignimbrite sheets delineate a perimeter with a broadly quadrilateral shape covering an approximate area of ~1300 km² (Fig. 11; Cheilletz et al. 1992; De la Cruz et al. 1996; López 1996; Chávez et al. 1997). The volcano-sedimentary sequence rests on Silurian-Devonian pelite and psammite, Carboniferous limestone, sandstone and shale, Triassic syn-rift red siliciclastic rocks and intra-plate alkaline basalt, Jurassic extrusive peralkaline rocks, and Cretaceous to Paleogene clastic sedimentary series (Fig. 11).

Tertiary volcanic and volcano-sedimentary strata in the Macusani Volcanic Field belong to the Crucero Supergroup of Sandeman et al. (1997). They include restricted

exposures of Oligocene-Miocene Picotani Group rhyodacitic tuff and basaltic andesite of the Lago Perhuacarca, Pucalacaya, and the Cerro Sumpiruni formations and volumetrically dominant rhyolitic rocks of the Macusani Formation, the youngest formation of the middle- to late-Miocene Quenamari Group (Sandeman et al. 1997). The Macusani Formation hosts the lithium-bearing units that have been studied in this thesis and therefore a more detailed description for this unit is provided below. Likewise, the Li-rich macusanite obsidian (1500-4076 ppm Li; Pichavant et al. 1987, 2024a) is referenced here to discuss primary controls on lithium enrichment in tuff. Finally, information about silicic hypabyssal bodies of the Crucero Intrusive Supersuite defined by Sandeman et al. (1997) is disclosed.

3.3.1. Crucero Supergroup

Rocks of the Picotani Group were mapped by Sandeman et al. (1997) in the southern portion of the Macusani Volcanic Field. In contrast, INGEMMET (1999, 2023) and Nupen (2019) have neglected to discriminate rocks of the Picotani Group in their respective geological maps and consider that all exposed volcanic and volcano-sedimentary rocks in the Macusani Volcanic Field belong to the younger Quenamari Group.

Sandeman et al. (1997) distinguished three formations of the Picotani Group in the Macusani Volcanic Field. The ~250 m thick *Cerro Sumpiruni Formation* (Fig. 12) is composed of peraluminous, greyish-green, cordierite and biotite-bearing, rhyodacitic-to-rhyolitic ash-flow tuff unconformably overlying the Paleozoic-Mesozoic basement. Biotite crystals from the lowest and highest exposed levels at Cerro Sumpiruni (Fig. 11) yielded $^{40}\text{Ar}/^{39}\text{Ar}$ dates of 24.13 ± 0.11 Ma and 24.00 ± 0.25 Ma, respectively. The *Pucalacaya Formation* consists of intercalated series of olivine and plagioclase-phyric, high-K calc-alkaline, basaltic andesite flows and peraluminous, cordierite-biotite-bearing, rhyodacitic ash-flow tuff. It unconformably overlies pre-Cenozoic units and is locally mantled by rhyolitic ash-flows of the Macusani Formation. A whole-rock $^{40}\text{Ar}/^{39}\text{Ar}$ analysis of a shoshonite from the southern slope of the Ninahuisa river yielded an integrated date of 21.90 ± 1.68 Ma and a five-step plateau date of 22.29 ± 1.43 Ma. Finally, the *Lago Perhuacarca Formation* is composed of interbedded metaluminous to peraluminous andesite and rhyodacitic-rhyolitic ash-flow tuff (Sandeman and Clark 2004). An $^{40}\text{Ar}/^{39}\text{Ar}$ whole-rock plateau date on andesite yielded 23.28 ± 0.50 Ma, while biotite yielded $^{40}\text{Ar}/^{39}\text{Ar}$ plateau and

integrated dates of 23.86 ± 0.40 Ma. The thicknesses of the Pucalacaya and Lago Perhuacarca formations have not been described.

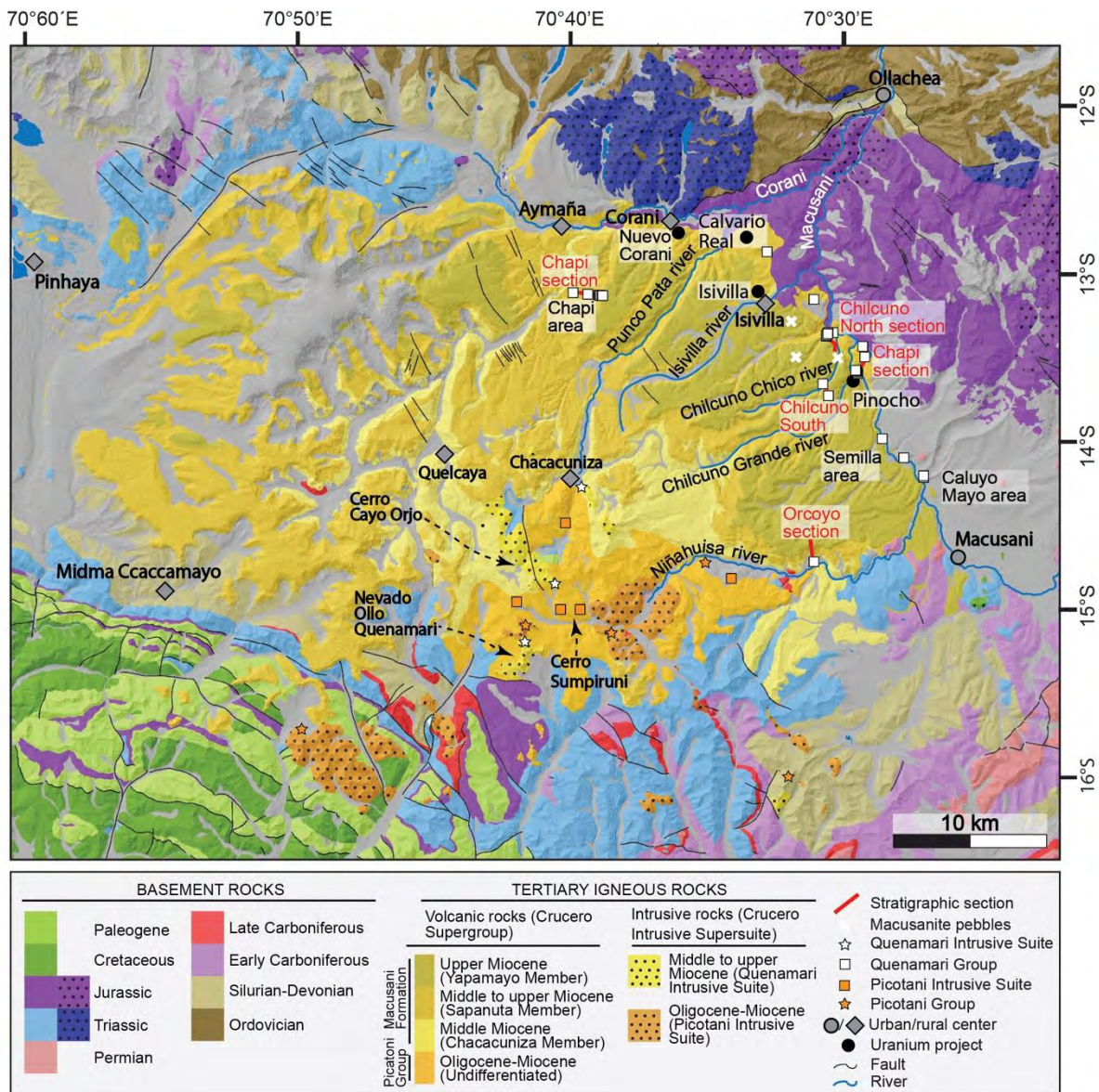


Figure 11. Simplified geological map of the Macusani Volcanic Field and adjacent areas in the Eastern Cordillera modified from Sandeman et al. (1987) and INGEMMET (2023). Dotted patterns refer to intrusive rocks. The location of samples dated by previous authors (Barnes et al. 1970; Kontak 1984; Noble et al. 1984; Bonhomme et al. 1985; Kontak et al. 1987; Pichavant et al. 1987, 1988a; Cheilletz et al. 1992; Poupeau et al. 1992, 1993; Sandeman et al. 1997) has been plotted.

Rocks of the Quenamari Group in the Macusani Volcanic Field belong to the Macusani Formation, a thick sequence of whitish-gray, poorly-stratified, unwelded, crystal-rich, rhyolitic ash- and lapilli-flow tuff (Sandeman et al. 1997). Juvenile pumice and shard fragments are common while lithic fragments of pelite, andesite, granite, and quartzite are

scarce (Cheilletz et al. 1992). Erosional unconformities separate the Macusani Formation from underlying Oligocene-Miocene Picotani Group and Paleozoic-Mesozoic basement rocks (Figs. 12-13; Li 2016). The formation comprises multiple, alternate eruptive events of tuff and ignimbrite (Valencia and Arroyo 1983). Tuff levels exhibit a smooth topography, whereas the ignimbrite levels give rise to escarpments and in places feature columnar jointing. Valencia and Arroyo (1983) described tens of meters of whitish lacustrine facies composed by argillites and redeposited tuff, but no clear statements about its stratigraphic position and location are given. The original thickness of the Macusani Formation is unknown since the top of the sequence is eroded. In the eastern margin of the volcanic field, where the youngest units are exposed, the thickness ranges from 340 to 440 m (Cheilletz et al. 1992).

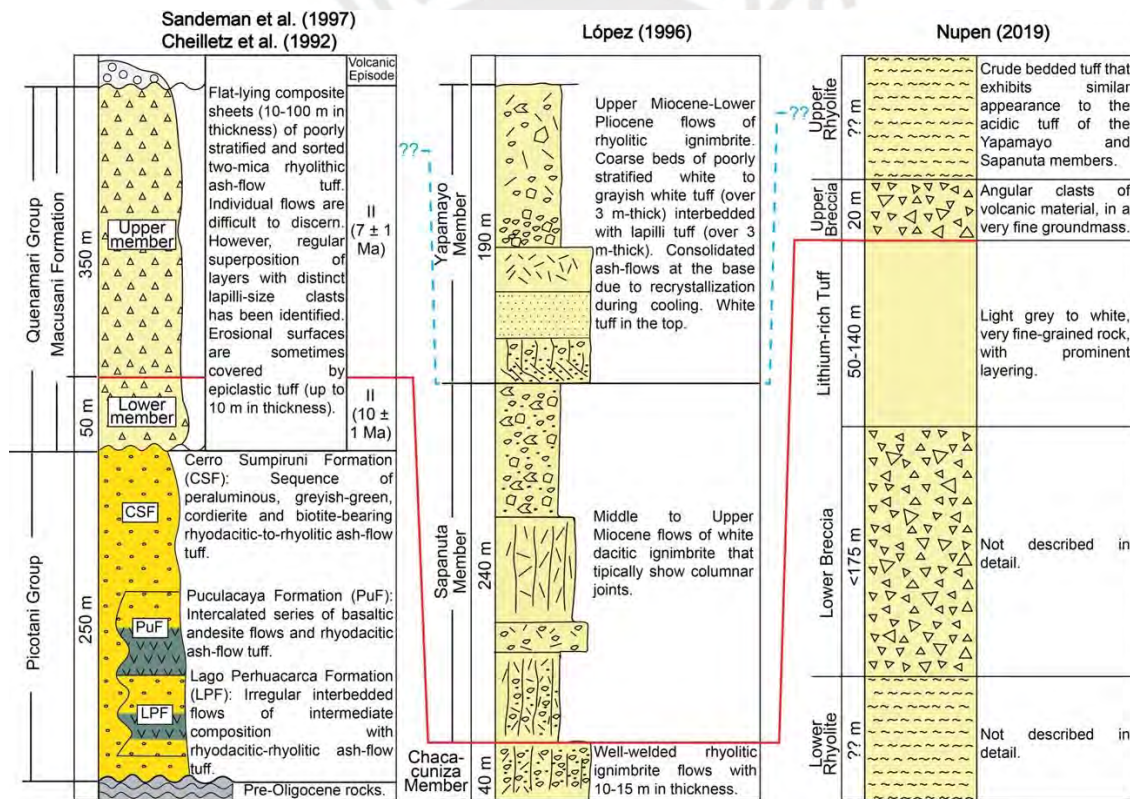


Figure 12. Summary of stratigraphic units in the Macusani Volcanic Field as proposed by Cheilletz et al. (1992), López (1996), Sandeman et al. (1997), and Nupen (2019).

The Macusani Formation is comprised of strongly peraluminous felsic volcanic series related to S-type reduced magmas. Ash-flow tuff exhibit a narrow range in silica (71.1-72.8 wt% SiO₂), very high alumina (14.3-16.2 wt% Al₂O₃; A/CNK > 1.2), high alkali (4.54-5.47 wt% K₂O and 1.19-1.35 wt% Na₂O), and minor FeO_t, MgO, CaO, and TiO₂ (Pichavant et al.

1988b). Tuff from the Macusani Formation is highly enriched in lithophile incompatible elements like Li, Rb, Cs, Be, B, Sn, F, P and U compared to average values in highly silicic igneous rocks (Noble et al. 1984; Pichavant et al. 1988b). In terms of major elements, tuff of the Macusani Formation is similar to Hercynian S-type granites (Noble et al. 1984; Pichavant et al. 1988b).

Li (2016) described that the main mineral components of the Macusani Formation were quartz (7-15 vol.%), sanidine (15-20 vol.%), plagioclase (10-15 vol.%), biotite (2-4 vol.%), and muscovite (0-1 vol.%). Pichavant et al. (1988a) discriminated two stages of crystallization. The early magmatic stage included the crystallization of plagioclase, biotite, tourmaline, spinel, cordierite-type phases, sillimanite, and accessory ilmenite, apatite, monazite, and zircon. A subsequent, volumetrically dominant, magmatic stage included the crystallization of quartz, sanidine, plagioclase, muscovite, andalusite, niobian rutile, and a minor proportion of biotite, tourmaline, and accessory ilmenite, apatite, monazite, and zircon (Pichavant et al. 1988a). “Restite” content remained below 5% by volume and comprised biotite, part of the sillimanite, apatite, monazite, and potentially some tourmaline and cordierite-type phases according to Pichavant et al. (1988a). Based on the anorthite contents of plagioclase (% An) and the strong enrichment in Sr, Ba, and La, Pichavant et al. (2024a) have interpreted that the plagioclase of the first magmatic stage crystallized during mixing and hybridization of crustal melts and LILE- and LREE-rich potassic to ultrapotassic mafic intrusions at or near the anatectic zone.

According to Pichavant et al. (1988a), the lack of systematic variation in mineral chemistry throughout the stratigraphy of the Macusani Formation is compatible with a derivation from spatially and/or temporally separate magma bodies with similar magmatic evolutions. Systematic variations in trace element contents and ratios from base to top of the sequence are consistent with a lower degree of fractionation in the last erupted magmas relative to the first erupted ones due to different degrees of shallow-level fractionation and/or differences in conditions of partial melting (Pichavant et al. 1988b). Available geochemical data are consistent with batch melting of isotopically heterogeneous crustal rocks dominated by pelitic metasediments (Pichavant et al. 1988b). Partial melting of continental crust was triggered by heat and volatiles sourced by potassic to ultrapotassic mafic magmas and was followed by mixing and homogenization of anatectic melts with mantle-derived basalts

(Pichavant et al. 2024a). Temperatures of $\sim 800\text{ }^{\circ}\text{C}$ and pressures $< 5\text{-}7.5\text{ kbar}$ near the magma source region have been constrained, and partial melting occurred under H_2O -undersaturated conditions (Pichavant et al. 1988b).

$^{40}\text{Ar}/^{39}\text{Ar}$ biotite dates for the Chapi, Huiquiza, Chilcuno Norte, Chilcuno Sur, and Orcoyo stratigraphic sections (Fig. 13) revealed two brief eruption episodes recorded by two intraformational members at 10 ± 1 and 7 ± 1 Ma (Cheilletz et al. 1992). Furthermore, these authors managed to identify six fundamental cooling units or volcanic cycles dated at 10.0 ± 0.5 , $7.8\text{-}8.0 \pm 0.1$, 7.5 ± 0.1 , 7.3 ± 0.1 , $6.8\text{-}7.0 \pm 0.1$, and 6.7 ± 0.1 Ma. These cycles may correspond to a single flow or several decreasing-grain flow units indistinguishable by $^{40}\text{Ar}/^{39}\text{Ar}$ dating. In the Huiquiza section, there are two levels of layered tuff within units of 7.5 and 6.8 Ma, respectively. Likewise, Cheilletz et al. (1992) have correlated levels of epiclastic tuff at the top of the 7.3 Ma cooling units in Huiquiza and Chilcuno Norte sections (Fig. 13). An unpublished report submitted to Bear Creek Mining by Ullrich (2006) reveals an $^{40}\text{Ar}/^{39}\text{Ar}$ biotite plateau date of 10.357 ± 0.080 Ma in a sample from the Corani Ag-Pb-Zn district in the southwest part of the field.

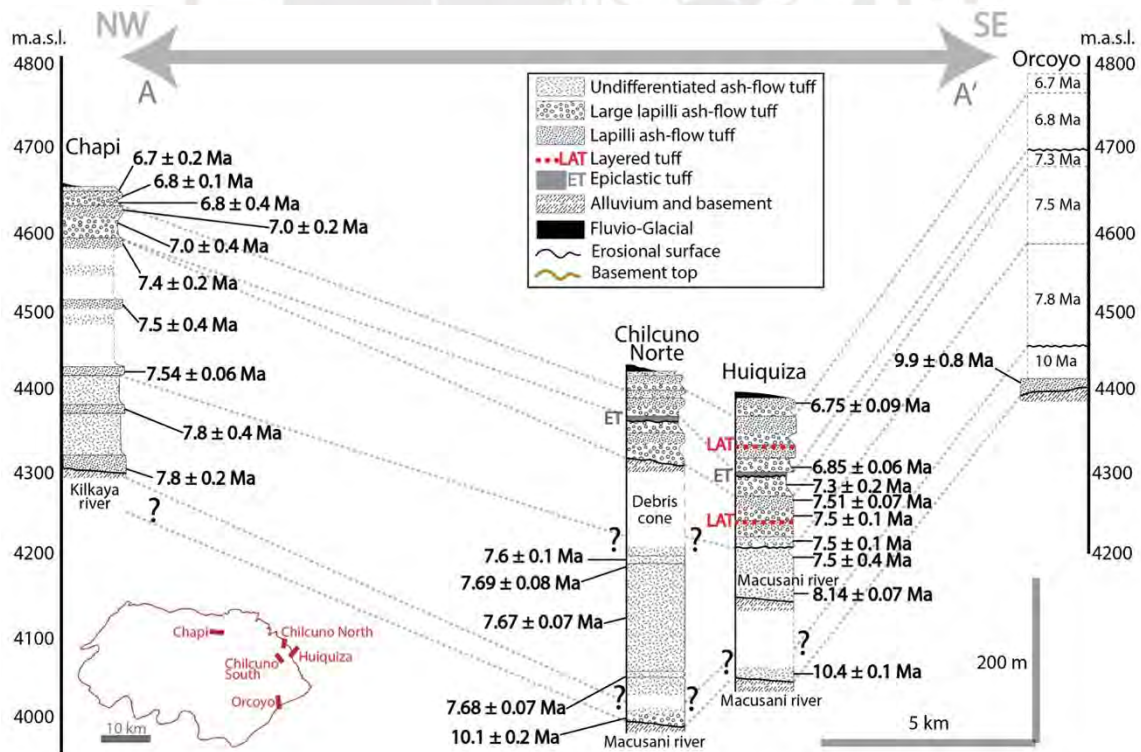


Figure 13. Volcano-stratigraphic correlation chart of the Macusani volcanic rocks in the Chapi, Chilcuno North, Huiquiza, and Orcoyo sections including fundamental cooling units or volcanic cycles as defined by Cheilletz et al. (1992). The inset shows the location of the stratigraphic sections in the Macusani Volcanic Field.

López (1996) identified three intra-formational members within the Macusani Formation separated by erosive unconformities that are continuously mappable at a regional scale (Fig. 12):

- The >35 m-thick Chacacuniza Member is described as white-to-grey, poorly-consolidated, rhyolitic tuff with 20-30 vol.% of crystals. It is considered to be stratigraphically equivalent to the first eruptive member of Cheilletz et al. (1992) (Li 2016; Soberón et al. 2022). This member rests on metapelites and volcanic rocks of the Paleozoic-Mesozoic basement and Picotani Group volcanics (Swarthout et al. 2010) and related intrusive rocks. Li (2016) reported strong argillic (illite-smectite) alteration in rocks of the Chacacuniza Member in the eastern margin of the field. Phenocrystic plagioclase, quartz, biotite, and strongly altered lapilli glass are embedded in a matrix of quartz, sanidine, and plagioclase crystals in volcanic glass.
- The ~175-240 m-thick Sapanuta Member comprises whitish gray to yellowish white, well-consolidated, crystal-rich (30-45 vol.%), rhyolitic tuff with variable amounts of lapilli. It rests in an erosional unconformity over the Chacacuniza Member and rocks of the pre-Oligocene basement. Geomorphologically, the Sapanuta Member is characterized by columnar disjunction. It comprises quartz, sanidine, biotite, muscovite, and andalusite crystals and lapilli-size juvenile fragments. The juvenile fragments are sub-equant to elongated, up to 2 cm in diameter, and show common coarse-grained quartz and biotite crystal clasts embedded in a white, porous, altered matrix. In its lower part, the size and proportion of lapilli increases to reach 10 cm and 30 vol.%, respectively. Strong alteration to kaolinite along the contact between the Chacacuniza and Sapanuta members has been described in the eastern margin of the field (Li 2016).
- The ~40-190 m-thick Yapamayo Member comprises brown-to-grey, crystal-rich (40-50 vol.%), rhyolitic tuff. It is stratigraphically correlated with the younger cooling units from the second eruptive event identified by Cheilletz et al. (1992) (Soberón et al. 2022). This member rests in erosional unconformity over the Sapanuta Member (Li 2016). Crystal clasts mainly include sanidine, quartz, biotite, and muscovite. Similar to the Sapanuta Member, the base of the Yapamayo Member is rich in lapilli

and lithoclasts. The rocks of the Yapamayo Member have been affected by weak-to-moderate alteration to illite-smectite (Li 2016).

More recently, Nupen (2019) has reported white, very fine-grained, tuffaceous rocks with lithium contents up to 4200 ppm, namely Lithium-rich Tuff, and transitional Li-rich breccias in the central area of Macusani Volcanic Field (Fig. 12). The Lithium-rich Tuff unit is 50 to 140 m thick and is sandwiched between the 10-20 m-thick Upper Breccia and the <175 m-thick Lower Breccia units. Its stratigraphic location within the Sapanuta Member is unclear. The Lithium-rich Tuff comprises finely laminated and massive facies with different degrees of pervasive alteration that obliterated deposition figures (Nupen 2019; Segovia-More et al. 2023). According to Nupen (2019), the Lithium-rich Tuff was subaerially deposited in a crater lake volcano-sedimentary environment.

3.3.2. Macusanite pebbles

Macusanite has been chiefly found as pebbles in stream gravels from the Caluyo Mayo area (Barnes et al. 1970; Pichavant et al. 1987, 1988b; Poupeau et al. 1992), Chilcuno Chico river (Arribas and Figueroa 1985; Valencia and Arroyo 1985; Pichavant et al. 1987; Poupeau et al. 1992), Samilla area (Poupeau et al. 1992), Chilcuno Grande river (Poupeau et al. 1993), and Isivilla river (Craig et al. 2010) (Fig. 11). Other reports include a glass boulder interbedded in a tuff located near the Chilcuno Chico river (Pichavant et al. 1987), glass interbedded in a 6.7 Ma-age (Cheilletz et al. 1992) ash-flow tuff of the Macusani Formation in the Chapi area (Pichavant et al. 1987), and glass artifacts in the Isivilla river (Craig et al. 2010). Macusanite pebbles of unspecified provenance within the Macusani Volcanic Field have been studied by Martin and de Sitter-Koomans (1955), Elliot and Moss (1965), and MacDonald et al. (1992).

Macusanite pebbles and glass inclusions show etched surfaces and slightly flattened ovular shapes. Pebble sizes are up to 5x10 cm, while glass inclusions are up to 2 cm in diameter (Pichavant et al. 1987). Studied macusanite specimens display several colors, including translucent green, opaque milky green, opaque red brown, and clear yellow (Pichavant et al. 1987; Craig et al. 2010). Certain samples of macusanite exhibit flow textures and red or milky-green bands (Barnes et al. 1970). Variation in the degree of milkiness has

been correlated with the abundance of irregularly shaped fluid inclusions (Barnes et al. 1970). The red brown color has been attributed to unevenly scattered, opaque, red-brown spots (Pichavant et al. 1987; Bigazzi et al. 1997).

Obsidian pebbles are depleted in K₂O, CaO, MgO, FeO, and TiO₂, and enriched in Na₂O and normative corundum relative to tuff from the Macusaní Formation (Pichavant et al. 1987). In particular, they are extremely enriched in P₂O₅ (0.5 wt%), F (1.3 wt%), Li₂O (0.7 wt%), and B₂O₃ (0.6 wt%; Barnes et al. 1970; Pichavant et al. 1987) and exhibit major element compositions that are similar to rare metal-rich leucogranites as the Beauvoir topaz-lepidolite-albite granite in France (Noble et al. 1984; Pichavant et al. 1988b). The mineralogy of both the ash-flow tuff and macusanite glass is broadly equivalent (Barnes et al. 1970). Uncommon aluminosilicate phases like virgilite have been reported within the macusanite glass (French et al. 1978). The glass inclusions within the tuff lack of andalusite and typically contain fewer microphenocrysts compared to the pebbles (Pichavant et al. 1987).

Macusanite resulted from highly evolved melts produced by 50-70% fractional crystallization of non-cogenetic, strongly peraluminous, silicic magmas that were chemically equivalent to glass matrix and glass inclusions in phenocrysts from Macusaní Formation tuff (Pichavant et al. 2024a). Pichavant et al. (1987) concluded that although glass clasts in tuff and macusanite pebbles shared a common magmatic evolution, only glass clasts and their respective host tuffs are cogenetic.

Fission-track dates on macusanite pebbles from the Chilcuno Chico and Chilcuno Grande rivers and the Caluyo Mayo area cluster around 7 ± 1 , 5.7-5.3, and 4.8-4.3 Ma (Poupeau et al. 1992, 1993). Glass K-Ar and ⁴⁰Ar/³⁹Ar dates between 5.67 ± 0.1 and 3.5 ± 0.6 Ma are considered minimum eruption dates because of radiogenic Ar loss accompanying magma degassing prior to and during the eruption (Barnes et al. 1970; Cheilletz et al. 1992; Poupeau et al. 1992). Finally, Rb–Sr dating of macusanite pebbles from Chilcuno Chico and Caluyo Mayo yielded dates between 4.9 and 4.4 Ma (Pichavant et al. 1987).

3.3.3. Crucero Intrusive Supersuite

Small Tertiary silicic stocks and dykes of the Crucero Intrusive Supersuite are petrographically similar to, and broadly coeval with, rocks of the Crucero Supergroup (Sandeman et al. 1997). They include two-mica syenogranite of the Quenamari Intrusive

Suite and biotite-cordierite monzogranite of the Picotani Intrusive Suite. In the Macusani Volcanic Field, intrusive bodies of the Quenamari Suite include the *Chacacuniza Stock*, the *Nevado Ollo Quenamari Plug*, and the *Cayo Orjo Plug*. Intrusive bodies of the Picotani Suite in the Macusani Volcanic Field include the *Quebrada Centilla Stock*, the *Ninahuisa Stock*, and the *Revancha Dyke*. All information below is based on [Sandeman et al. \(1997\)](#) unless stated otherwise.

The *Quebrada Centilla Stock* is a cordierite-biotite monzogranite stock exposed along the northern and northeastern flanks of the Ollo Quenamari snow-capped mountain (**Fig. 11**). $^{40}\text{Ar}/^{39}\text{Ar}$ analyses on biotite and sanidine yielded dates of 24.09 ± 0.18 Ma and 23.65 ± 0.14 Ma, respectively, which indicate a cogenetic relationship with the Lago Perhuacarca Formation. The *Ninahuisa Stock* is a peraluminous, cordierite-biotite monzogranite stock exposed along the floor of the Ninahuisa river (**Fig. 11**). It shows enclaves of minette with scalloped margins. $^{40}\text{Ar}/^{39}\text{Ar}$ dating of biotite and sanidine yielded 23.52 ± 0.58 Ma and 23.15 ± 0.20 Ma, respectively. The *Revancha Dyke* is a peraluminous, glass-rich, cordierite-biotite, rhyodacite dike with chilled, flow-banded margins and a coarsely porphyritic interior that crops out in the southern slope of the Ninahuisa river (**Fig. 11**). It cuts rhyodacitic ash-flow tuff and monzogranitic intrusive rocks (see also [Sandeman and Clark 2003](#)). $^{40}\text{Ar}/^{39}\text{Ar}$ biotite dating yielded 24.07 ± 0.09 Ma and 24.18 ± 0.72 Ma ([Clark et al. 1990](#)).

The *Cayo Orjo Plug*, which is a weakly-altered, sanidine-quartz-phyric, flow-banded, rhyolitic intrusion exposed nearby Cerro Cayo Orjo (**Fig. 11**), was dated at 12.26 ± 0.14 Ma (total-fusion $^{40}\text{Ar}/^{39}\text{Ar}$ sanidine; [Clark et al. 1990](#)). The *Nevado Ollo Quenamari Plug* is a sanidine-quartz-biotite intrusion exposed to the north of the Nevado Ollo Quenamari snow-capped mountain. $^{40}\text{Ar}/^{39}\text{Ar}$ dating of sanidine from this plug yielded a plateau date of 12.14 ± 0.11 Ma, which clearly pre-dates the oldest dated levels of the Macusani Formation ([Cheilletz et al. 1992](#); [López 1996](#)). Finally, the tourmaline-bearing, muscovite-biotite-phyric *Chacacuniza Stock*, mapped as *La Huaña* by [INGEMMET \(2023\)](#), is exposed in the central part of the Macusani Volcanic Field (**Fig. 11**). $^{40}\text{Ar}/^{39}\text{Ar}$ analysis on muscovite from the *Chacacuniza Stock* yielded a date of 7.51 ± 0.14 Ma, which is coeval with the second volcanic event recorded in the Macusani Formation according to [Cheilletz et al. \(1992\)](#).

4. RESULTS

4.1. Major and minor element composition

This section is devoted to the description of the chemical compositions of the analyzed lithium-ore rock units, namely the Lithium-rich Tuff and the Upper and Lower Breccia. The compositions of other samples analyzed in this thesis are also briefly reported here and will be used in conjunction with geochemical data reported by previous authors for the purpose of comparison in the Discussion (cf. Section 5.1).

Overall, the analyzed samples of Lithium-rich Tuff, Upper Breccia, and Lower Breccia exhibit variable LOI values (1.7-13.5 wt.%; **Fig. 14**) and a wide range of SiO₂ (60.4-80.8 wt.%), alkali (K₂O+Na₂O = 3.1-8.4 wt.%), and Al₂O₃ (11.7-20 wt.%) contents (**Fig. 15a**). Other elements present in minor amounts (TiO₂, Fe₂O_{3tot}, MnO, MgO, and CaO) add to 1.13 wt.%, on average. Of these, MgO contents are conspicuously low, typically below the detection threshold at 0.02 wt.% (**Fig. 14**). In contrast, the studied samples exhibit very high F (1.05-1.98 wt.%) and P₂O₅ (0.2-0.8 wt.%) contents, which are up to thirty-five and five times higher, respectively, than the average values reported for the upper continental crust (**Fig. 14**).

In the TAS diagram ([Le Maitre et al. 1989](#)), all samples of Lithium-rich Tuff, Upper Breccia, and Lower Breccia plot in the sub-alkaline field ([Irvine and Baragar 1971](#)) and most of them plot in the rhyolite field, except for the sample of Upper Breccia with the highest LOI value (13.5 wt.%), which plots in the dacite field (**Fig. 15b**). All of them exhibit a linear positive correlation ($R^2 = 0.9$) between the A/CNK (Al₂O₃/(CaO+Na₂O+K₂O)) and A/NK (Al₂O₃/(Na₂O+K₂O)) parameters (**Fig. 16a**) and are strongly peraluminous (A/CNK = 1.1-2.8). In the B-A diagram of [Debon and Lefort \(1983\)](#), all samples have B parameter (i.e., Fe+Mg+Ti) values between 7.2 and 11.3, which are typical of felsic rocks, and plot mostly above the felsic peraluminous field due to their extremely high A parameter (i.e., Al-(K+Na+2Ca)) values, similar to highly-evolved rare metal-rich granites and highly evolved volcanic rocks (**Fig. 16b**).

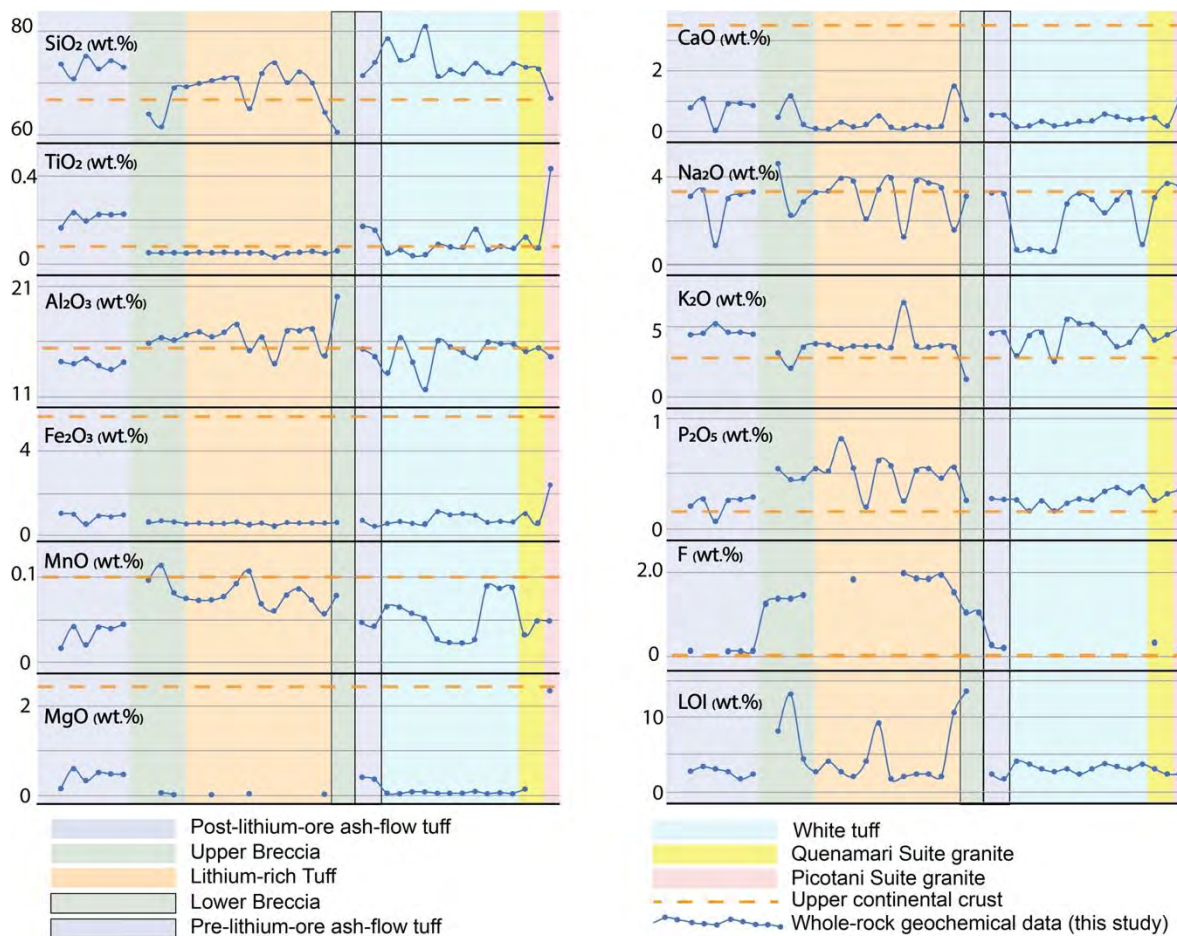


Figure 14. Major and minor element contents in analyzed samples (dots) from the Macusani Volcanic Field according to lithotype (cf. Section 2.1). Upper continental crust values after Rudnick and Gao (2003).

The samples of Lithium-rich Tuff yielded LOI values typically in the range between 1.7 and 4.0 wt.%, except for much higher values in samples 2021-MAC-026 (9.2 wt.%) and 2021-MAC-053 (10.6 wt.%). They have high SiO₂ (64.3-73.9 wt.%; average [av.] = 69.8 wt.%) and Al₂O₃ (14.0-17.6 wt.%; av. = 16.3 wt.%) and moderate K₂O (3.5-6.8 wt.%; av. = 3.9 wt.%) and Na₂O (1.3-3.9 wt.%; av. = 3.1 wt.%) contents (Fig. 15a). Their F (1.54-1.98 wt.%; av. = 1.83 wt.%) and P₂O₅ (0.2-0.8 wt.%; av. = 0.5 wt.%) contents are high compared to upper continental crust values (Fig. 14). Minor amounts of CaO (0.07-1.5 wt.%; av. = 0.3 wt.%), Fe₂O₃_{tot} (0.5-0.7 wt.%; av. = 0.6 wt.%), MnO (0.06-0.1 wt.%; av. = 0.08 wt.%), TiO₂ (0.03-0.06 wt.%; av. = 0.05 wt.%), and MgO (< 0.06 wt.%) were measured (Fig. 14). The Na/K molar ratios in the analyzed rocks are very variable, ranging between 0.3 and 1.7, with most of the analyses clustering between 1.3 and 1.7. The samples with the highest LOI show the lowest Na/K.

The samples of Lower Breccia and Upper breccia have characteristically high LOI values (4.4-13.5 wt.%; av. = 9.8 wt.%), as well as variable, though in general lower, SiO₂ (60.4-69.0 wt.%; av. = 72.1 wt.%) and higher Al₂O₃ (15.9-20.0 wt.%; av. = 17.1 wt.%) contents than the Lithium-rich Tuff (Fig. 14). They yielded moderate to low K₂O (1.3-3.6 wt.%; av. = 2.5 wt.%) and Na₂O (2.2-4.5 wt.%; av. = 3.2 wt.%) contents, which add to total alkali contents (K₂O+Na₂O) between 3.1 and 8.4 wt.% (Fig. 15a). These rocks have also remarkably high F (1.05-1.47 wt.%; av. = 1.27 wt.%) and P₂O₅ (0.3-0.5 wt.%; av. = 0.4 wt.%) contents (Fig. 14). Minor amounts of TiO₂ (0.05-0.06 wt.%; av. = 0.06 wt.%), Fe₂O_{3tot} (0.6-0.7 wt.%; av. = 0.7 wt.%), MnO (0.07-0.11 wt.%; av. = 0.09 wt.%), CaO (0.2-1.2 wt.%; av. = 0.6 wt.%), and MgO (< 0.06 wt.%) were measured (Fig. 14). The Na/K ratios range from 1.2 to 3.7, with the highest ratios found in the samples with lower SiO₂.

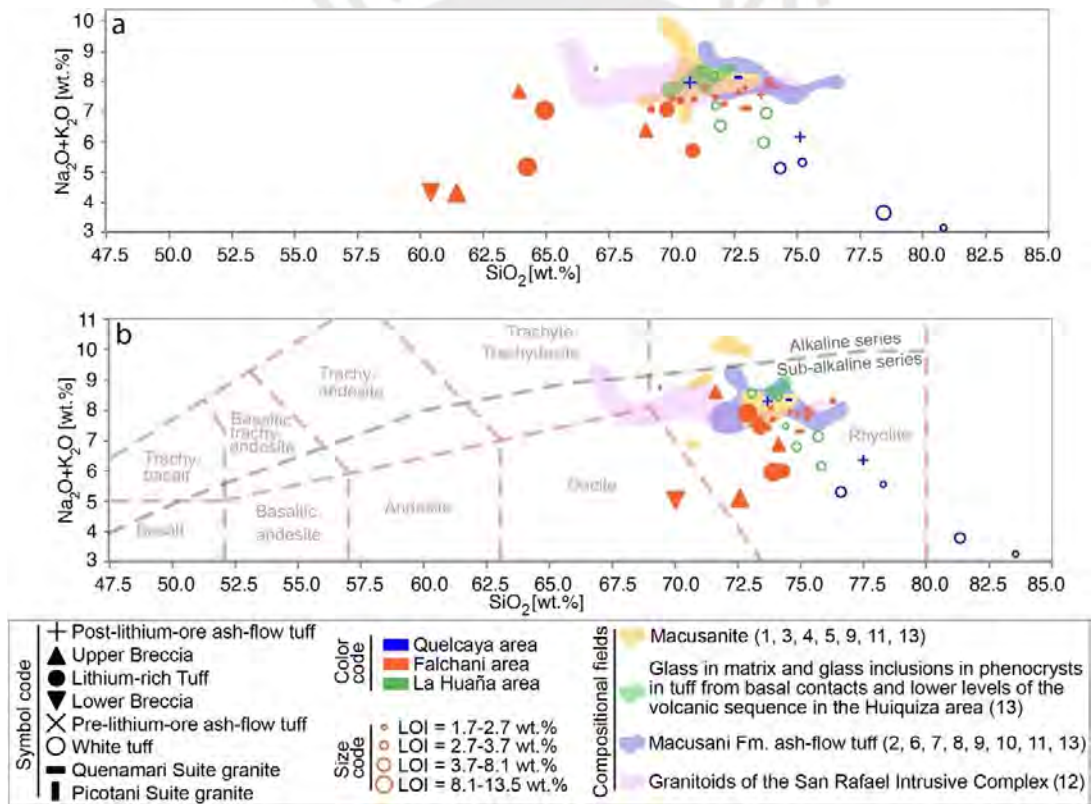


Figure 15. Total alkalis-silica plots with analyzed samples from the Macusaní Volcanic Field. (a) Na₂O+K₂O vs. SiO₂ diagram and (b) TAS diagram of Le Maitre et al. (1989). Note that in (b), data have been recalculated to 100% on an anhydrous (volatile-free) basis. Compositional fields of other volcanic and intrusive rocks in the study area are plotted for comparison. References: (1) Linck (1926); (2) Francis (1953b); (3) Martin and de Sitter-Koomans (1955); (4) Elliott and Moss (1965); (5) Barnes et al. (1970); (6) Noble et al. (1984); (7) Arribas and Figueroa (1985); (8) Valencia and Arroyo (1985); (9) Pichavant et al. (1987); (10) Pichavant et al. (1988b); (11) Poupeau et al. (1992); (12) Harlaux et al. (2021); (13) Pichavant et al. (2024a). Only unaltered samples from the San Rafael Intrusive Complex (Harlaux et al. 2021) have been plotted. Macusanite include pebbles and clasts found within ash-flow tuff levels in Chapi area and within a boulder of tuff near Chilcuno Chico (see Pichavant et al. 1987).

The normative mineralogy was calculated according to the CIPW norm (Johannsen 1931; Appendix D). For Lithium-rich Tuff, it includes quartz (35.1-46.6 wt.%; av. = 39.1 wt.%), albite (11.0-34.3 wt.%; av. = 27.7 wt.%), orthoclase (21.5-41.5 wt.%; av. = 24.5 wt.%), corundum (5.2-10.8 wt.%; av. = 8.1 wt.%), anorthite (up to 4.4 wt.%), apatite (0.5-1.9 wt.%; av. = 1.2 wt.%), hypersthene (0.9-1.3 wt.%; av. = 1.1 wt.%), and ilmenite (0.1 wt.%). Upper Breccia and Lower Breccia yield normative quartz (28.5-45.6 wt.%; av. = 39.7 wt.%), albite (22.3-43.1 wt.%; av. = 30.3 wt.%), orthoclase (8.7-22.9 wt.%; av. = 16.8 wt.%), corundum (6.1-15.7 wt.%; av. = 10.4 wt.%), anorthite (up to 3.4 wt.%), apatite (0.7-1.4 wt.%; av. = 1.1 wt.%), hypersthene (1.2-1.7 wt.%; av. = 1.4 wt.%), and ilmenite (0.1 wt.%).

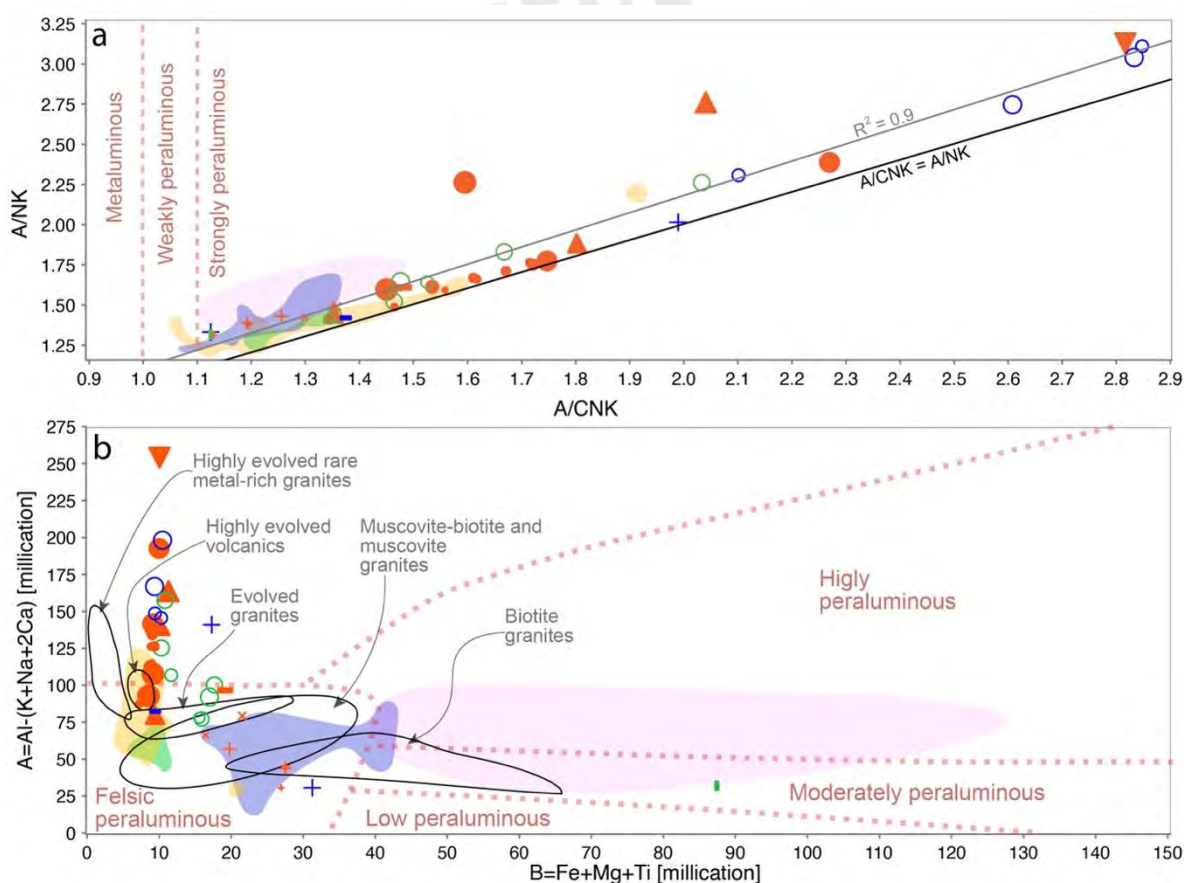


Figure 16. Major elements bivariate plots with analyzed samples from the Macusani Volcanic Field. (a) $\text{Al}_2\text{O}_3/(\text{CaO}+\text{Na}_2\text{O}+\text{K}_2\text{O})$ vs. $\text{Al}_2\text{O}_3/(\text{Na}_2\text{O}+\text{K}_2\text{O})$ (Shand 1943) and (b) B vs. A (Debon and Lefort 1983) diagrams. Compositional fields of highly evolved rare metal-rich granites, highly evolved volcanics, evolved granites, muscovite-biotite and muscovite granites, and biotite granites are after Michaud et al. (2021). Symbology as in Figure 15.

The analyzed samples of ash-flow tuff have low LOI (1.7-3.3 wt.%; av. = 2.5 wt.%). They are silicic ($\text{SiO}_2 = 70.7\text{-}75.1$ wt.%; av. = 73.1 wt.%; Fig. 15a) and exhibit narrow compositional ranges for Al_2O_3 (13.5-15.3 wt.%; av. = 14.3 wt.%), K_2O (4.5-5.3 wt.%; av. =

4.7 wt.%), and Na₂O (0.9-3.4 wt.%; av. = 2.9 wt.%; **Fig. 14**). Minor amounts of Fe₂O_{3tot} (0.4-1.1 wt.%; av. = 0.9 wt.%), CaO (0.05-1.1 wt.%; av. = 0.7 wt.%), MgO (0.15-0.59 wt.%; av. = 0.41 wt.%), TiO₂ (0.16-0.23 wt.%; av. = 0.20 wt.%), and MnO (0.02-0.05 wt.%; av. = 0.04 wt.%) were detected (**Fig. 14**). They contain moderate P₂O₅ (0.07-0.3 wt.%; av. = 0.2 wt.%) and F (0.15-0.29 wt.%; av. = 0.19 wt.%; **Fig. 14**). The data cluster in the rhyolite classification field (**Fig. 15b**) and their Na/K values are in the range between 0.25 and 1.1. Noteworthy, the post-lithium-ore ash-flow tuff is richer in TiO₂ and CaO relative to the pre-lithium-ore ash-flow tuff (**Fig. 14**).

The samples of white tuff yielded LOI values in the range between 2.3 and 4.0 wt.% and high and variable contents of SiO₂ (71.2-81.8 wt.%; av. = 74.1 wt.%), Al₂O₃ (11.7-16.4 wt.%; av. = 14.9 wt.%), and alkali (K₂O + Na₂O = 3.2-8.5 wt.%; av. = 6.3 wt.%; **Fig. 15a**). They contain minor amounts of Fe₂O_{3tot} (0.6-1.2 wt.%; av. = 0.8 wt.%), CaO (0.2-0.6 wt.%; av. = 0.3 wt.%), TiO₂ (0.04-0.16 wt.%; av. = 0.08 wt.%), MgO (0.04-0.09 wt.%; av. = 0.06 wt.%), and MnO (0.02-0.09 wt.%; av. = 0.05 wt.%; **Fig. 14**). Moderate P₂O₅ (0.2-0.4 wt.%; av. = 0.3 wt.%) contents were detected (**Fig. 14**). All analyzed white tuff samples plot in the rhyolite field (**Fig. 15b**) except for the sample 2021-MAC-022B, which has >80 wt.% SiO₂ and hosts secondary As-Sb-Hg-S minerals. The datapoints display a downward linear relationship ($r^2 = 0.9$) between alkali and silica, progressing from samples from La Huaña to lower alkali and higher silica (and LOI) values in samples from Quelcaya (**Fig. 15**).

The analyzed granite of the Picotani Suite has a LOI value of 3.3 wt.%, is silicic (SiO₂ = 67.0 wt.%), sub-alkaline (K₂O + Na₂O = 8.4; **Fig. 15a**), and strongly peraluminous (A/CNK = 1.12; **Fig. 16a**). It contains moderate K₂O (4.9 wt.%), Fe₂O_{3tot} (2.6 wt.%), MgO (2.0 wt.%), CaO (1.0 wt.%), and P₂O₅ (0.4 wt.%), and low F (0.2 wt.%; **Fig. 14**). The two granite samples from the Quenamari Suite yielded LOI values of 2.4 and 3.0 wt.%, are highly silicic (SiO₂ = 72.7-73.0 wt.%), sub-alkaline (K₂O + Na₂O = 7.1-8.1 wt.%), and strongly peraluminous (A/CNK = 1.4-1.5; **Fig. 16a**). They contain moderate K₂O (4.1-4.5 wt.%) and Na₂O (3.0-3.6 wt.%) and low CaO (0.2-0.4 wt.%), Fe₂O_{3tot} (0.6-1.1 wt.%), MgO (< 0.13 wt.%), and TiO₂ (0.07-0.12 wt.%) contents (**Fig. 14**). The measured P₂O₅ contents were 0.26-0.32 wt.%. Fluorine was analyzed only in the sample 2021-MAC-003, which returned a content of 0.34 wt.% (**Fig. 14**).

4.2. Trace element composition

Compared to the average upper continental crust, the Lithium-rich Tuff is enriched in Li (2920-4160 ppm; av. = 3496 ppm), Rb (1139-2177 ppm; av. = 1508 ppm), and Cs (210-8993 ppm; av. = 1600), mostly at the thousands of ppm level; B (200-1800 ppm; av. = 675 ppm), Sn (175-271 ppm; av. = 220 ppm), and Be (54-271 ppm; av. = 125 ppm), mostly at the hundreds of ppm level; and Nb (35-60 ppm; av. = 49 ppm), Ta (23-34 ppm; av. = 31 ppm), and U (9.2-24.2 ppm; av. = 15 ppm), mostly at the tens of ppm level (Figs. 17-18). In contrast, it is depleted relative to the upper continental crust in Ba (21-239 ppm; av. = 72 ppm), Zr (35-181 ppm; av. = 59 ppm), Sr (10-197 ppm; av. = 47 ppm), and Cl (80-130 ppm; av. = 100 ppm). The contents of Ni, Zn, Cu, Ge, and W are highly variable though mostly at the ppm or tens of ppm levels (Fig. 17). In terms of Nb, Ta, Nb/Ta, Rb, and Li, the Lithium-rich Tuff has an equivalent composition to rare metal-rich granites and highly evolved volcanics (Fig. 19). They exhibit total REE (Σ REE) contents between 12 and 25 ppm (av. = 19 ppm) and Y contents between 4.5 and 12 ppm (av. = 6.4 ppm; Fig. 17). Individual REE and Y values are ~1 to 20 times enriched relative to chondritic values (Fig. 20). Chondrite C1-normalized (CN) REY (lanthanides + Y) patterns display negative slopes ($(\text{La}/\text{Sm})_{\text{CN}} = 2.3\text{-}3.6$), $(\text{Sm}/\text{Yb})_{\text{CN}} = 1.2\text{-}2.9$) and strong negative Eu anomalies $((\text{Eu}/\text{Eu}^*)_{\text{CN}} = 0.11\text{-}0.34$; Fig. 20).

The Upper Breccia and Lower Breccia are enriched in Li (780-2890 ppm; av. = 1647 ppm), B (600-2100 ppm; av. = 1550 ppm), Cs (656-1822 ppm; av. = 1297 ppm), and Rb (1139-2177 ppm; av. = 1044 ppm), mostly at the thousands of ppm level; Cl (130-790 ppm; av. = 483 ppm), Sn (210-274 ppm; av. = 231 ppm), and Be (84-166 ppm; av. = 120 ppm), mostly at the hundreds of ppm level; and Nb (49-59 ppm; av. = 55 ppm), Ta (31-39 ppm; av. = 34 ppm), and U (17-28 ppm; av. = 22 ppm), mostly at the tens of ppm level, compared to the upper continental crust (Figs. 17-18). In contrast, they are depleted in Zr (37-715 ppm; av. = 210 ppm), Ba (15-295 ppm; av. = 88 ppm), Sr (13-31 ppm; av. = 22 ppm), and Th (3.0-3.4 ppm; av. = 3.1 ppm) relative to upper continental crust values. The analyzed sample of Lower Breccia is enriched in Ba, U, Sn, Ta, and Ga, and depleted in F and P relative to the samples of Upper Breccia (Figs. 14, 17). All analyzed Upper Breccia samples exhibit Rb, Nb, Ta, Nb/Ta, and Li that match those of rare metal-rich granites and highly evolved volcanics. In contrast, the sample of Lower Breccia does not align with any of the projected compositional fields due to its markedly lower Rb content (Fig. 19). Σ REE contents are

between 18 and 22 ppm (av. = 20 ppm) and Y contents span from 4.3 to 48 ppm (av. = 16 ppm; **Fig. 20**). CN REY patterns display negative slopes ($(La/Sm)_{CN} = 2.6-3.0$; $(Sm/Yb)_{CN} = 1.8-2.2$) and strong negative Eu anomalies (0.13-0.17).

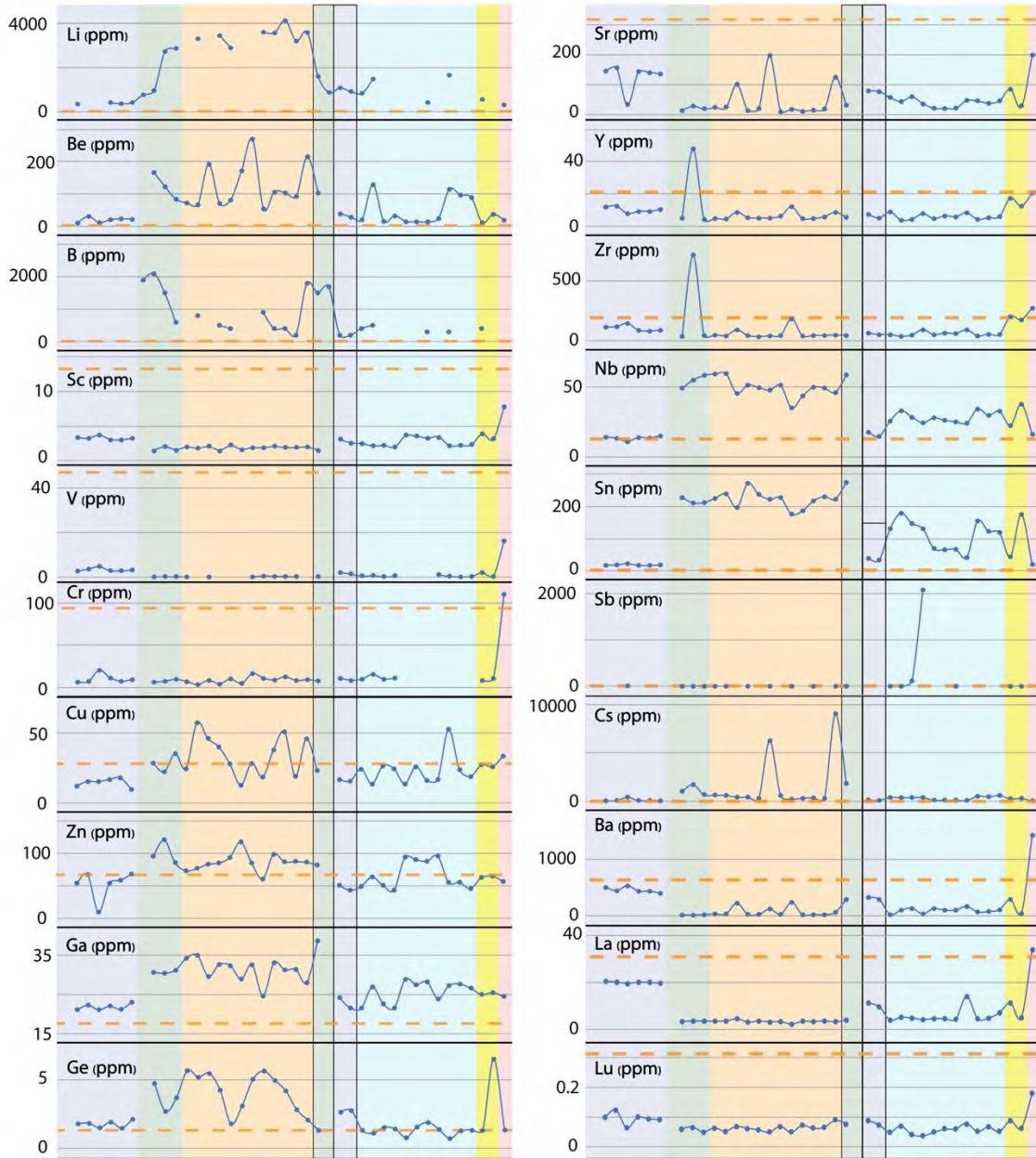


Figure 17. Trace element composition of analyzed samples from the Macusani Volcanic Field. Symbology as in **Figure 14**. Upper continental crust values after [Rudnick and Gao \(2003\)](#).

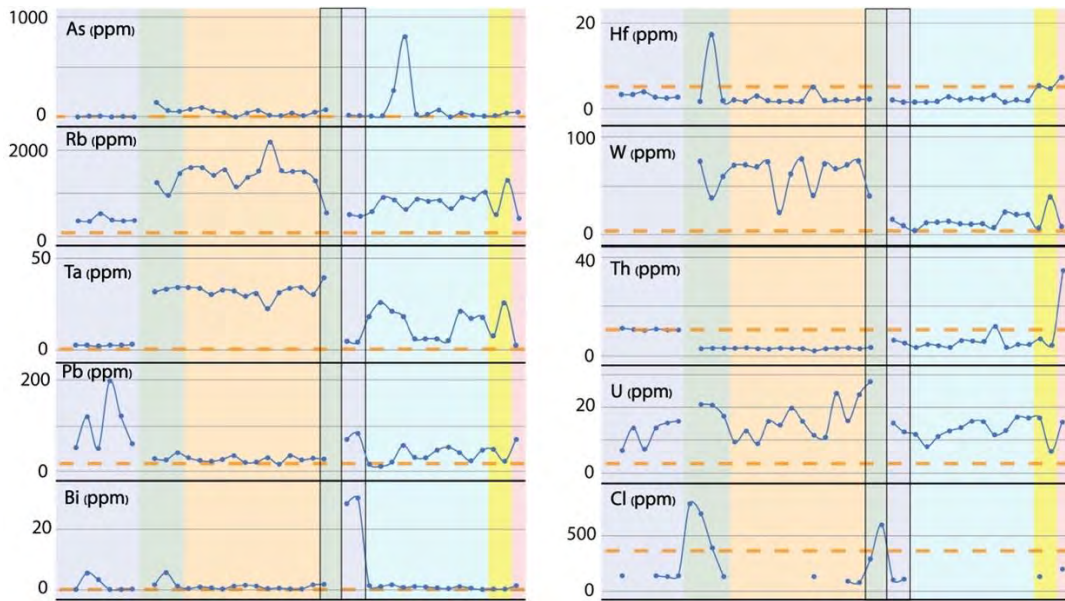


Figure 17. (Continued)

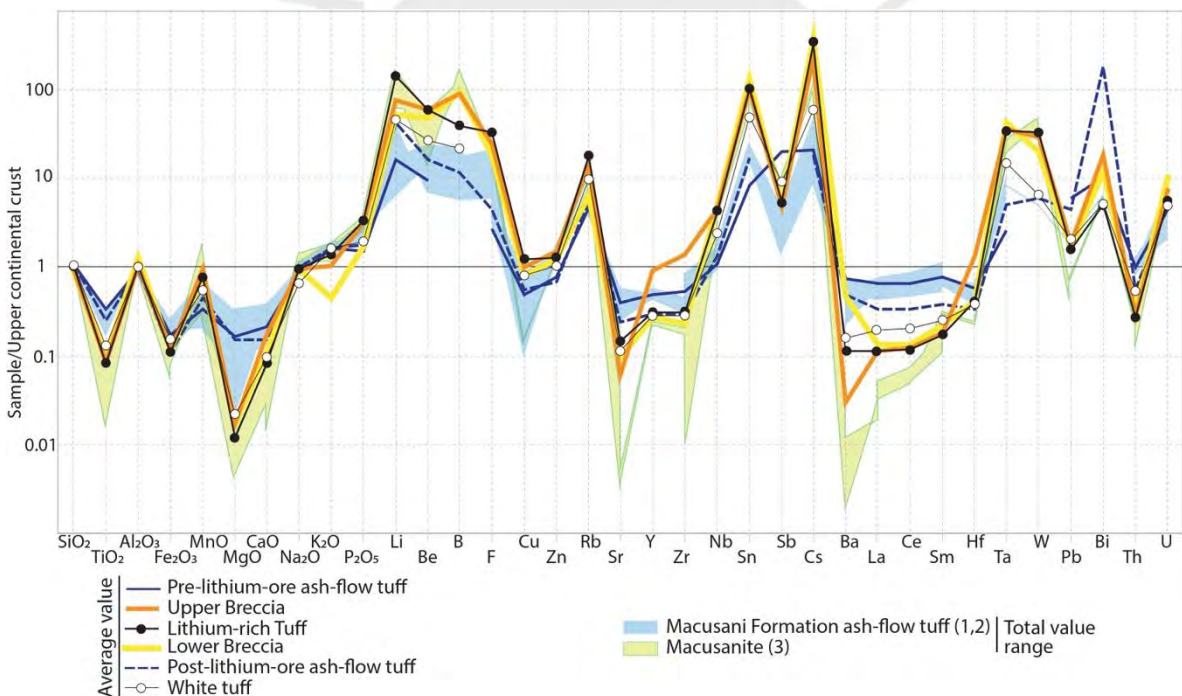


Figure 18. Upper continental crust-normalized element patterns of all analyzed volcanogenic rocks from the Macusani Volcanic Field. References: (1) Noble et al. (1984); (2) Pichavant et al. (1988b); (3) Pichavant et al. (2024a). Samples 2021-MAC-022A and 2021-MAC-022B were not included due to evidence of epithermal sulfide mineralization. Upper continental crust values after Rudnick and Gao (2003).

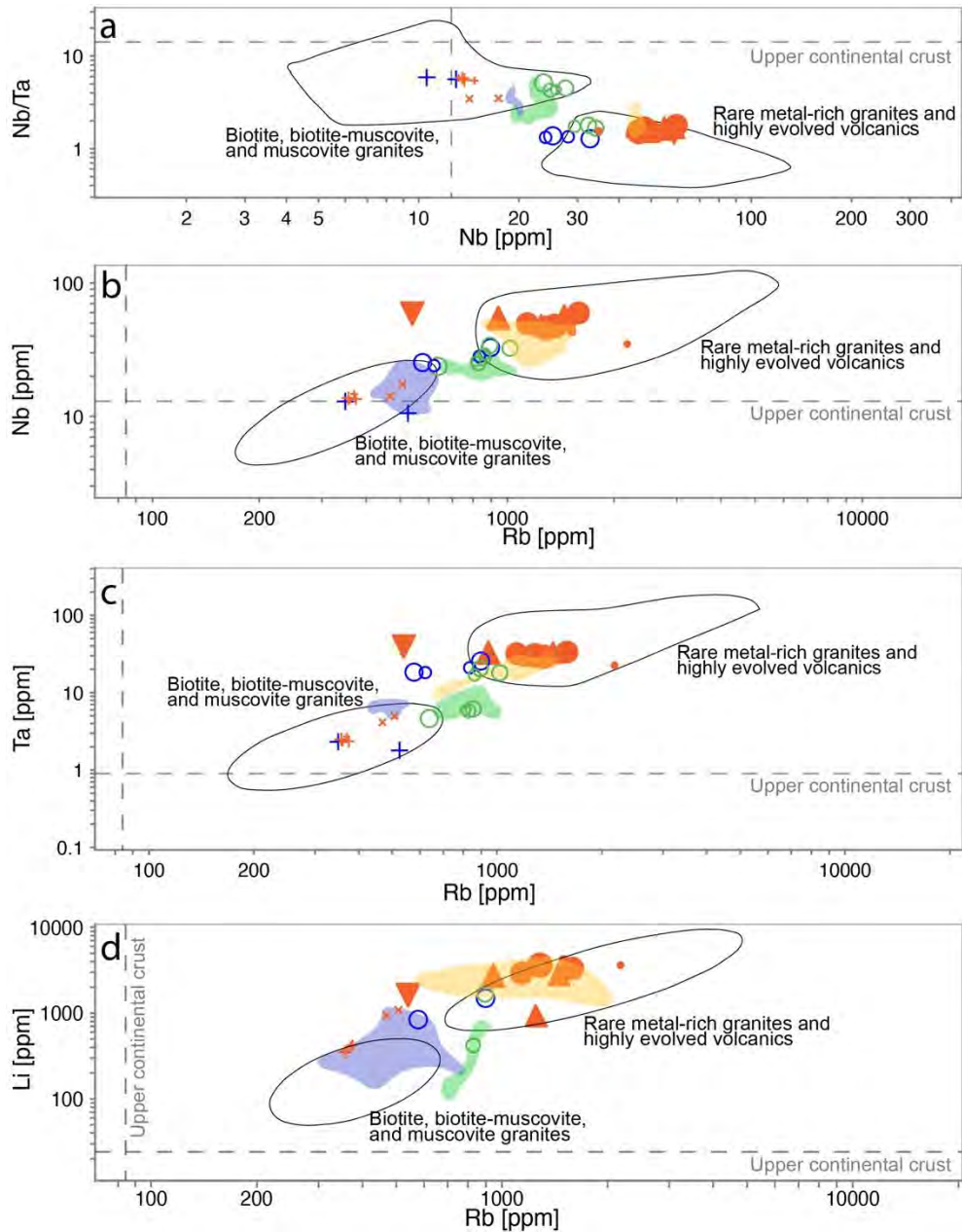


Figure 19. Geochemical composition of samples from the Macusani Volcanic Field in terms of (a) Nb vs. Nb/Ta, (b) Rb vs. Nb, (c) Rb vs. Ta, and (d) Rb vs. Li. Compositional fields of biotite, biotite-muscovite, muscovite, and muscovite granites and rare metal-rich granites and highly evolved volcanics are after [Michaud et al. \(2021\)](#). Upper continental crust values are after [Rudnick and Gao \(2003\)](#). Symbology as in [Figure 15](#).

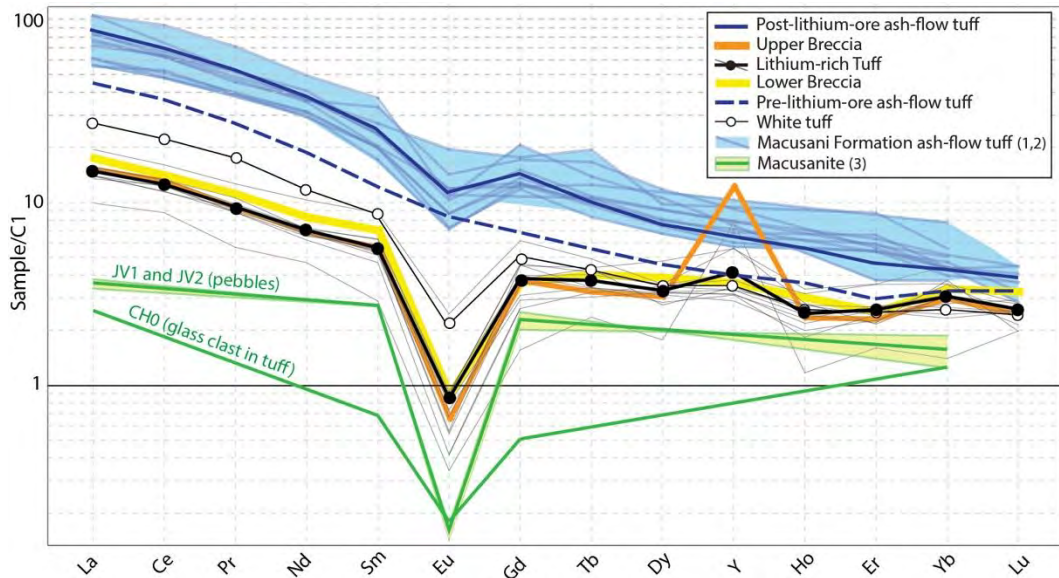


Figure 20. Chondrite-normalized REY patterns of all analyzed volcanogenic rocks from the Macusani Volcanic Field. Samples 2021-MAC-022A and 2021-MAC-022B were not included due to evidence of strong hydrothermal alteration involving sulfide mineralization. Average values of pre- and post-lithium-ore ash-flow tuff, Upper Breccia, Lower Breccia, and white tuff are represented as thick lines. For the Lithium-rich Tuff, individual analyses are represented as thin lines and their average value, as a thick line. The average values of macusanite are represented as thick lines whereas the total range of values are represented as polygons. The compositional range of Macusani Formation ash-flow tuff is represented as polygons whereas individual samples are represented as translucent lines. References: (1) Noble et al. (1984); (2) Pichavant et al. (1988b); (3) Pichavant et al. (2024a). C1 chondrite values after McDonough and Sun (1995).

The analyzed samples of ash-flow tuff are enriched in Li (350-1090 ppm; av. = 597 ppm), Rb (350-525 ppm; av. = 414 ppm), B (200 ppm), Cs (22-388 ppm; av. = 101 ppm), Be (11-40 ppm; av. = 24 ppm), Sn (16-38 ppm; av. = 22 ppm), Nb (11-17 ppm; av. = 14 ppm), Ta (1.8-5.0 ppm; av. = 2.9 ppm), and U (7-16 ppm; av. = 13 ppm), and depleted in Ba (292-534 ppm; av. = 423 ppm), Sr (31-156 ppm; av. = 114 ppm), Zr (51-144 ppm; av. = 93 ppm), and Th (5-11 ppm; av. = 9.3 ppm) relative to the upper continental crust (Figs. 17-18). They have Σ REE contents between 45 and 97 ppm (av. = 83 ppm) and Y contents between 5.1 and 13 ppm (av. = 9.3 ppm; Fig. 17). REY contents are higher in post-lithium-ore (88-97 ppm, av. = 94 ppm) than in pre-lithium-ore (45-54 ppm, av. = 50 ppm) ash-flow tuff. CN REY patterns display negative slopes ($(La/Sm)_{CN} = 3.4-4.0$; $(Sm/Yb)_{CN} = 3.7-7.2$; Fig. 20). The post-lithium-ore ash-flow tuff shows weak negative Eu anomalies (0.43-0.70), which are almost absent in the pre-lithium-ore ash-flow tuff (0.81-1.04; Fig. 20). Pre-lithium-ore ash-flow tuff samples are depleted in Ti, Sr, Ba, REE, and Th and enriched in Li, Ge, Rb, Sn, and Ta compared to post-lithium-ore ash-flow tuff (Fig. 17). Bismuth is extremely enriched in pre-lithium-ore ash-flow tuff samples compared to all other analyzed rock types (Fig. 17).

White tuff samples are enriched in Li (420-1670 ppm; av. = 1105 ppm), Rb (577-1017 ppm; av. = 803), B (300-500 ppm; av. = 375 ppm), Cs (52-590 ppm; av. = 305 ppm), Sn (41-178 ppm; av. = 111 ppm), Be (14-129 ppm; av. = 52 ppm), Nb (24-34 ppm; av. = 28 ppm), and Ta (4.6-26 ppm; av. = 14.7 ppm) and depleted in Ba (23-168 ppm; av. = 96 ppm), Zr (37-91 ppm; av. = 58 ppm), Sr (20-59 ppm; av. = 39 ppm), and Th (3.4-12 ppm; av. = 5.2 ppm) compared to the upper continental crust (**Figs. 17-18**). Measured Σ REE contents range between 21 and 71 ppm (av. = 28 ppm) and Y contents are between 3.9 and 9.0 ppm (av. = 6.1 ppm; **Fig. 17**). CN REY patterns display negative slopes ($(\text{La}/\text{Sm})_{\text{CN}} = 2.8\text{-}5.2$; $(\text{Sm}/\text{Yb})_{\text{CN}} = 1.6\text{-}8.0$) and negative Eu anomalies (0.20-0.87; **Fig. 20**).

The two analyzed granite samples of the Quenamari Suite are enriched in Rb (503-1,291 ppm), Li (570 ppm), B (400 ppm), Cs (237-268 ppm), Sn (43-174 ppm), Nb (22-38 ppm), Be (12-38 ppm), and Ta (7.4-26 ppm) and depleted in Ba (47-293 ppm), Zr (176-203 ppm), Sr (24-85 ppm), and Th (4.2-6.7 ppm) relative to the upper continental crust (**Figs. 17-18**). Their Σ REE is of 26-56 ppm and their Y is of 13-17 ppm (**Fig. 17**). CN REY patterns display negative slopes ($(\text{La}/\text{Sm})_{\text{CN}} = 2.9\text{-}3.4$; $(\text{Sm}/\text{Yb})_{\text{CN}} = 3.0\text{-}4.6$) and negative Eu anomalies (0.36-0.59; **Fig. 20**). In terms of Li, Rb, Nb, Ta, and Nb/Ta, the sample 2021-MAC-003 is comparable to biotite, biotite-muscovite, and muscovite granites, while the sample 2021-MAC-003 is comparable to rare metal-rich granites and highly evolved volcanics (**Fig. 19**).

The analyzed granite sample of the Picotani Suite yielded higher Ba (1429 ppm), Rb (417 ppm), Li (310 ppm), Zr (272 ppm), Th (34 ppm), Cs (29 ppm), Be (20 ppm), Sn (18 ppm), Nb (16 ppm), and Ta (2.2 ppm), and lower Sr (198 ppm) contents than the upper continental crust (**Figs. 17-18**). This granite sample has Σ REE = 190 ppm and Y = 21 ppm (**Fig. 17**) and its CN REY pattern displays a negative slope ($(\text{La}/\text{Sm})_{\text{CN}} = 2.4$; $(\text{Sm}/\text{Yb})_{\text{CN}} = 7.9$) and a weak negative Eu anomaly (0.68; **Fig. 20**). It plots in the biotite, biotite-muscovite, and muscovite granite compositional domain in the Nb vs. Nb/Ta, Rb vs. Nb, Rb vs. Ta, and Rb vs. Li diagrams (**Fig. 19**).

Selected bivariate plots show decoupled geochemical trends for the Upper and Lower Breccia vs. the Lithium-rich Tuff samples (**Fig. 21**). The Upper and Lower Breccia datapoints show good ($R^2 > 0.75$) positive linear correlations for the $\text{SiO}_2\text{-K}_2\text{O}$, $\text{SiO}_2\text{-Cu}$, Mn-Zn , CaO-

Mg, K₂O-Ge, K₂O-Rb, Cl-Be, and As-Cl pairs and negative linear correlation for the LOI-SiO₂, SiO₂-Cs, and K₂O-Sr pairs. The analyses of Lithium-rich Tuff yield positive linear covariance ($R^2=0.8$) in the SiO₂-F diagram.

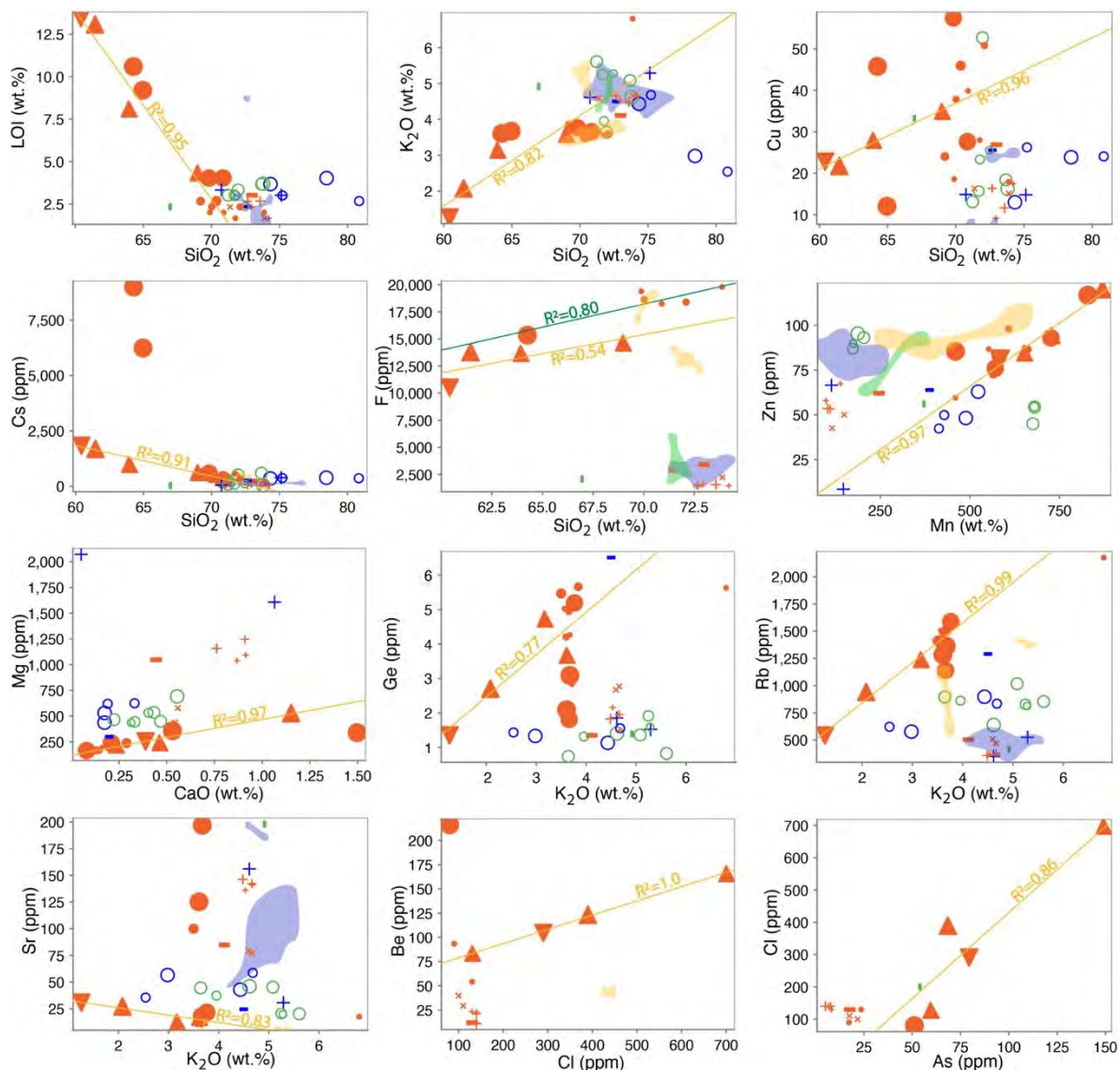


Figure 21. Bivariate plots of selected elements in Lithium-rich Tuff, Upper Breccia, and Lower Breccia. The composition of non-ore units (new and previous data) is also shown. Yellow lines represent linear correlations of Lower Breccia and Upper Breccia datapoints, and the green line represents a linear correlations of Lithium-rich Tuff datapoints. Symbology as in [Figure 15](#).

4.3. Lead, Sr, and Nd isotope ratios

Initial isotope ratios have been recalculated at 8.9 Ma except for the granite sample from the Picotani Suite, which was recalculated at 24 Ma ([Tables 2-4](#)). Lead isotope compositions of the analyzed samples exhibit a high degree of homogeneity, with $^{206}\text{Pb}/^{204}\text{Pb}_{(t)}$, $^{207}\text{Pb}/^{204}\text{Pb}_{(t)}$,

and $^{208}\text{Pb}/^{204}\text{Pb}_{(t)}$ ratios in the range of 18.9757–18.8043 (av. = 18.889), 15.7040–15.6864 (av. = 15.692), and 38.8560–38.9755 (av. = 38.9398), respectively (Fig. 22). $^{87}\text{Sr}/^{86}\text{Sr}_{(t)}$ ratios have a remarkable dispersion, between 0.717983 and 0.771468 (av. = 0.733733), relative to $^{143}\text{Nd}/^{144}\text{Nd}_{(t)}$ ratios, which are in the narrow range of 0.51209 to 0.51300 (av. = 0.512214; Fig. 23). The generally very low contents of radiogenic ^{143}Nd are reflected in negative $\varepsilon_{\text{Nd}}^t$ values in the range from -10.3 to -8.0 (av. = -8.2). The Lithium-rich Tuff sample 2021-MAC-031 is a clear outlier with significantly lower $^{87}\text{Sr}/^{86}\text{Sr}_{(t)}$ (0.756666) and higher $^{143}\text{Nd}/^{144}\text{Nd}_{(t)}$ (0.51300) ratios and $\varepsilon_{\text{Nd}}^t$ (7.4) values. The granite sample from the Picotani Suite yielded the lowest $^{143}\text{Nd}/^{144}\text{Nd}_{(t)}$ ratio of all analyzed rocks (Fig. 23, Table 4).



Table 2. Values of Pb isotope ratios in studied samples from the Macusani Volcanic Field.

Sample	Lithotype	U/Pb	Th/U	$^{206}\text{Pb}/^{204}\text{Pb}$	1σ	$^{207}\text{Pb}/^{204}\text{Pb}$	1σ	$^{208}\text{Pb}/^{204}\text{Pb}$	1σ	$^{206}\text{Pb}/^{204}\text{Pb}_{(t)}$	$^{207}\text{Pb}/^{204}\text{Pb}_{(t)}$	$^{208}\text{Pb}/^{204}\text{Pb}_{(t)}$
2021-MAC-003	Quenamari Suite granite	0.3425	0.3983	18.8691	0.0009	15.6943	0.0007	38.9525	0.0019	18.8691	15.6943	38.9525
2021-MAC-012	Lithium-rich Tuff	0.1324	1.5775	18.8289	0.0033	15.6874	0.0027	38.9628	0.0067	18.8289	15.6874	38.9628
2021-MAC-019A	White tuff	0.6962	0.2900	18.8729	0.0024	15.6868	0.0019	38.9594	0.0047	18.873	15.6870	38.9590
2021-MAC-021	White tuff	0.6610	0.5619	18.9498	0.0021	15.6889	0.0017	38.9666	0.0042	18.95	15.6890	38.9670
2021-MAC-025	Lithium-rich Tuff	0.4183	0.2122	18.9329	0.0008	15.6926	0.0007	38.8560	0.0017	18.9329	15.6926	38.8560
2021-MAC-031	Lithium-rich Tuff	0.7504	0.1884	18.9753	0.0008	15.7041	0.0007	38.9346	0.0017	18.9752	15.7041	38.9346
2021-MAC-033	Post-lithium-ore units ash-flow tuff	0.0691	0.7793	18.8448	0.0011	15.6903	0.0009	38.9725	0.0023	18.8448	15.6903	38.9725
2021-MAC-034	Post-lithium-ore units ash-flow tuff	0.1251	0.6810	18.8395	0.0008	15.6920	0.0007	38.9756	0.0017	18.8395	15.6920	38.9756
2021-MAC-038	Lithium-rich Tuff	0.3768	0.1709	18.9160	0.0003	15.6921	0.0003	38.9256	0.0007	18.9160	15.6921	38.9256
2021-MAC-039	Lithium-rich Tuff	0.6467	0.2634	18.9155	0.0002	15.6923	0.0002	38.9298	0.0006	18.9155	15.6923	38.9298
2021-MAC-040	Lithium-rich Tuff	0.6854	0.1253	18.9767	0.0013	15.6864	0.0011	38.9029	0.0026	18.9766	15.6864	38.9029
2021-MAC-045	Pre-lithium-ore units ash-flow tuff	0.2156	0.4150	18.8622	0.0005	15.6927	0.0004	38.9467	0.0010	18.8622	15.6927	38.9467
2021-MAC-046	Pre-lithium-ore units ash-flow tuff	0.1504	0.4032	18.8365	0.0005	15.6909	0.0004	38.9423	0.0011	18.8365	15.6909	38.9423
2021-MAC-047	Post-lithium-ore units ash-flow tuff	0.2586	0.6592	18.8571	0.0005	15.6914	0.0005	38.9691	0.0011	18.8571	15.6914	38.9691
2021-MAC-048	Lithium-rich Tuff	0.6026	0.2046	18.9666	0.0003	15.6931	0.0003	38.9280	0.0007	18.9666	15.6931	38.9280
2021-MAC-055	Picotani Suite granite	0.2204	2.1871	18.8046	0.0004	15.6901	0.0003	38.9720	0.0009	18.8046	15.6901	38.9720
2021-MAC-065B	White tuff	0.5094	0.3743	18.8688	0.0005	15.6884	0.0004	38.9047	0.0011	18.869	15.6880	38.9050
2021-MAC-066	White tuff	0.2176	0.9944	18.8438	0.0004	15.6898	0.0003	38.9182	0.0008	18.844	15.6900	38.9180
2021-MAC-067B	White tuff	0.7088	0.2647	18.8672	0.0003	15.6905	0.0003	38.9527	0.0007	18.867	15.6910	38.9530

Lead isotope ratios at a time t are calculated considering the ^{238}U , ^{235}U , and ^{232}Th decay constants ($\lambda_{238\text{U}} = 0.0155125 \times 10^{-9} \text{ years}^{-1}$; $\lambda_{235\text{U}} = 0.98485 \times 10^{-9} \text{ years}^{-1}$; $\lambda_{232\text{Th}} = 0.049475 \times 10^{-9} \text{ years}^{-1}$) published in [Steiger and Jager \(1977\)](#). All calculations are done following the procedure described in [Faure and Mensing \(2005\)](#).

Table 3. Values of Rb-Sr isotope ratios in studied rock samples from the Macusani Volcanic Field.

Sample	Rb/Sr	$^{87}\text{Rb}/^{86}\text{Sr}$	$^{87}\text{Sr}/^{86}\text{Sr}$	2σ	$^{87}\text{Sr}/^{86}\text{Sr}(t)$
2021-MAC-003	5.939871	17.2227662	0.724218	0.000005	0.722041249
2021-MAC-012	2.437626	7.06608982	0.721533	0.000004	0.720639931
2021-MAC-019A	10.200101	29.5720397	0.723061	0.000004	0.719323449
2021-MAC-021	20.899944	60.6215277	0.727893	0.000004	0.720231167
2021-MAC-025	62.662358	181.942717	0.738421	0.000005	0.715425626
2021-MAC-031	144.106453	419.170906	0.756846	0.000007	0.703867833
2021-MAC-033	2.636161	7.64223279	0.722388	0.000006	0.721422114
2021-MAC-034	2.554153	7.40457796	0.722510	0.000005	0.72157415
2021-MAC-038	123.684365	360.285536	0.771622	0.000006	0.726086237
2021-MAC-039	140.065148	407.854388	0.767905	0.000006	0.716357105
2021-MAC-040	109.655500	318.949068	0.756449	0.000005	0.71613767
2021-MAC-045	6.4053493	18.5778625	0.727213	0.000004	0.724864981
2021-MAC-046	6.056142	17.5647212	0.727031	0.000004	0.72481103
2021-MAC-047	2.719262	7.88314471	0.722391	0.000005	0.721394665
2021-MAC-048	87.639075	254.762456	0.750461	0.000006	0.718262086
2021-MAC-055	2.106762	6.10773657	0.722775	0.000005	0.722003055
2021-MAC-065B	41.118346	119.443596	0.743127	0.000004	0.728030764
2021-MAC-066	13.866698	40.2355326	0.731548	0.000005	0.726462712
2021-MAC-067B	23.103976	67.0047327	0.726407	0.000005	0.717938407

Strontium isotope ratios at a time t are calculated considering the ^{87}Rb decay constant ($\lambda_{^{87}\text{Rb}} = 1.42 \times 10^{-11}$ years $^{-1}$) published in [Steiger and Jager \(1977\)](#). All calculations are done following the procedure described in [Faure and Mensing \(2005\)](#).

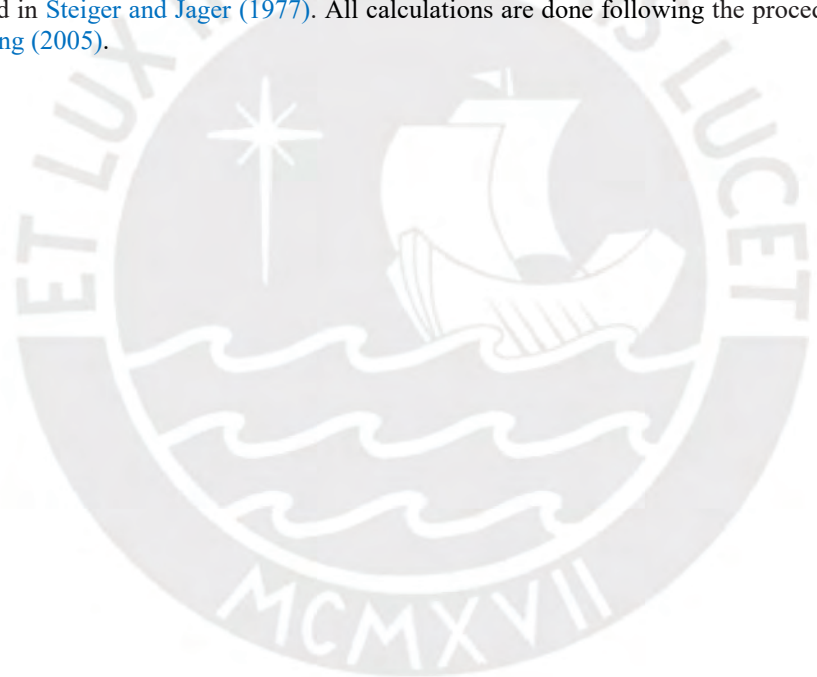


Table 4. Values of Sm-Nd isotope ratios and calculated epsilon (ϵ_{Nd}) in studied rock samples from the Macusani Volcanic Field.

Sample	Sm/Nd	$^{147}\text{Sm}/^{144}\text{Nd}$	$^{145}\text{Nd}/^{144}\text{Nd}$	2σ	$^{143}\text{Nd}/^{144}\text{Nd}$	2σ	$^{143}\text{Nd}/^{144}\text{Nd}_{(t)}$	ϵ_{Nd}^t
2021-MAC-003	0.256471	0.154414	0.348412	0.000004	0.512181	0.000007	0.512172	-8.5
2021-MAC-012	0.219041	0.131878	0.348399	0.000005	0.512190	0.000007	0.512182	-8.3
2021-MAC-019A	0.221365	0.133277	0.348413	0.000004	0.512182	0.000006	0.512174	-8.5
2021-MAC-021	0.181518	0.109287	0.348410	0.000003	0.512186	0.000006	0.512179	-8.4
2021-MAC-025	0.257369	0.154954	0.348406	0.000003	0.512176	0.000005	0.512167	-8.6
2021-MAC-031	0.289327	0.174195	0.348405	0.000004	0.513000	0.000006	0.512990	7.4
2021-MAC-033	0.228766	0.137733	0.348404	0.000004	0.512168	0.000006	0.512160	-8.8
2021-MAC-034	0.218259	0.131407	0.348415	0.000003	0.512190	0.000005	0.512182	-8.3
2021-MAC-038	0.199712	0.120241	0.348403	0.000004	0.512174	0.000007	0.512167	-8.6
2021-MAC-039	0.245339	0.147711	0.348411	0.000005	0.512189	0.000008	0.512180	-8.4
2021-MAC-040	0.248148	0.149402	0.348410	0.000004	0.512178	0.000007	0.512169	-8.6
2021-MAC-045	0.204957	0.123399	0.348409	0.000005	0.512172	0.000007	0.512165	-8.7
2021-MAC-046	0.211923	0.127593	0.348398	0.000004	0.512160	0.000006	0.512152	-8.9
2021-MAC-047	0.213494	0.128538	0.348407	0.000002	0.512185	0.000003	0.512177	-8.4
2021-MAC-048	0.287275	0.172960	0.348408	0.000003	0.512196	0.000006	0.512186	-8.2
2021-MAC-055	0.266563	0.160490	0.348423	0.000004	0.512090	0.000008	0.512080	-10.3
2021-MAC-065B	0.285490	0.171885	0.348410	0.000005	0.512132	0.000007	0.512122	-9.5
2021-MAC-066	0.230889	0.139011	0.348406	0.000008	0.512169	0.000013	0.512161	-8.7
2021-MAC-067B	0.213217	0.128371	0.348408	0.000004	0.512151	0.000007	0.512143	-9.1

The decay constant of ^{147}Sm ($\lambda_{^{147}\text{Sm}} = 6.54 \times 10^{-12} \text{ years}^{-1}$) is extracted from [Lugmair and Marti \(1978\)](#). All calculations are done following the procedures described in [Faure and Mensing \(2005\)](#). Chondrite Uniform Reservoir (CHUR) values are used to calculate the ϵ_{Nd} values [$\epsilon_{Nd}^t = ((^{143}\text{Nd}/^{144}\text{Nd}_{(\text{rock},t)}/^{143}\text{Nd}/^{144}\text{Nd}_{(\text{CHUR},t)}) - 1) \times 10^4$] ([Rollinson and Pease 2021](#)). The present-day $^{143}\text{Nd}/^{144}\text{Nd}_{\text{CHUR}}$ ratio normalized against $^{146}\text{Nd}/^{144}\text{Nd} = 0.7219$ is extracted from [Goldstein et al. \(1984\)](#). The $^{143}\text{Nd}/^{144}\text{Nd}_{\text{CHUR}}$ ratio at a time t is calculated considering a Sm/Nd_{CHUR} ratio of 0.325 ([Wasserburg et al. 1981](#)).

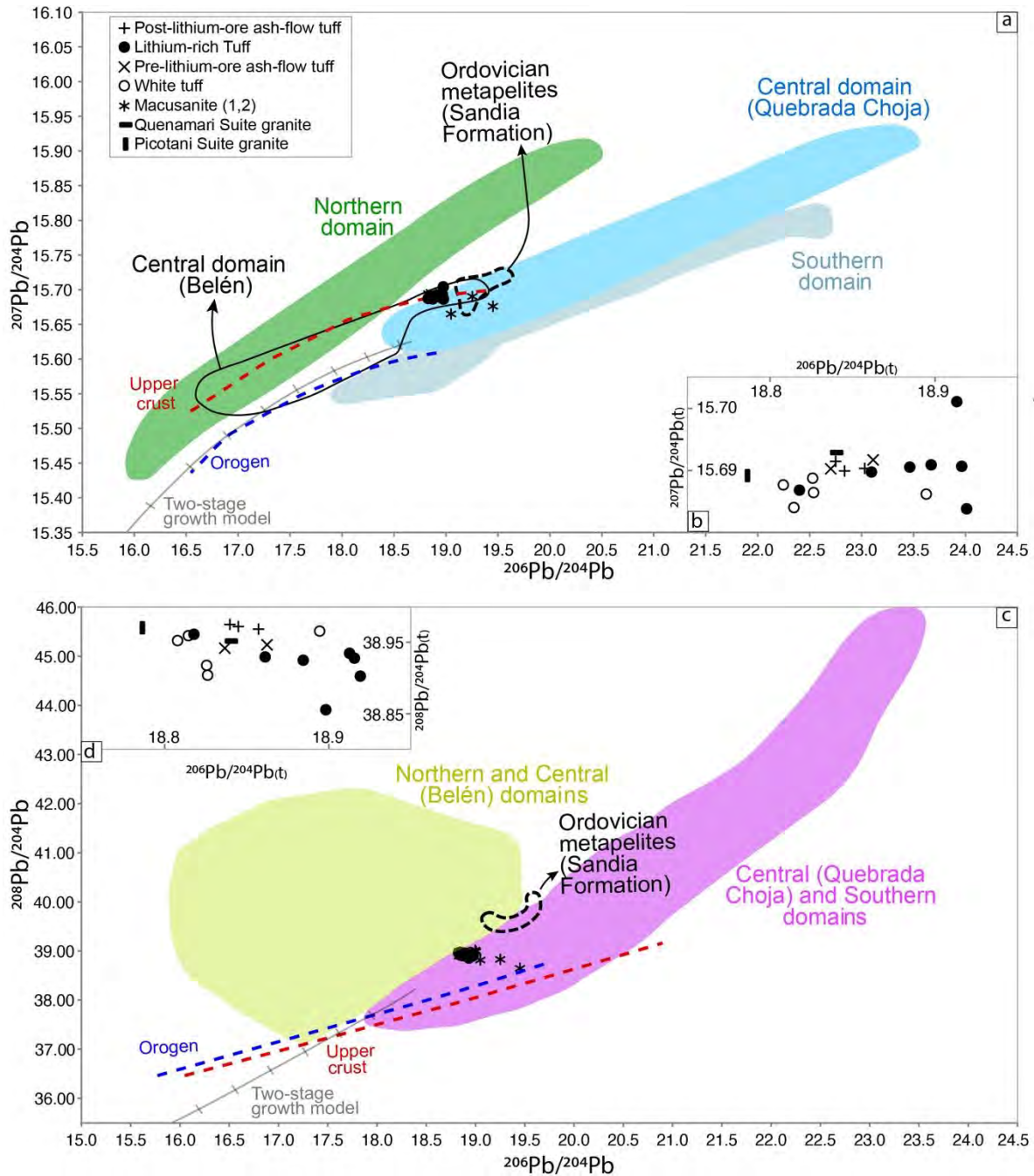


Figure 22. Lead isotope compositions of volcanogenic and intrusive rocks (this and previous studies) from the Macusani Volcanic Field plotted in (a-b) $^{206}\text{Pb}/^{204}\text{Pb}$ vs. $^{207}\text{Pb}/^{204}\text{Pb}$ and (c-d) $^{206}\text{Pb}/^{204}\text{Pb}$ vs. $^{208}\text{Pb}/^{204}\text{Pb}$ diagrams. (b) and (d) show initial Pb isotope composition of the analyzed samples from the Macusani Volcanic Field recalculated at 8.9 Ma. Compositional fields of metamorphic rock domains in the Arequipa-Antofalla terrane were adapted from Loewy et al. (2004). The compositional field of Ordovician metapelites of the Sandia Formation in the Eastern Cordillera of southern Peru were extracted from Harlaux et al. (2021). Upper crust and orogen evolution curves are from Zartman and Doe (1981). The two-stage growth Pb evolution model is after Stacey and Kramers (1975). References: (1) Pichavant et al. (1987); (2) Pichavant et al. (1988b).

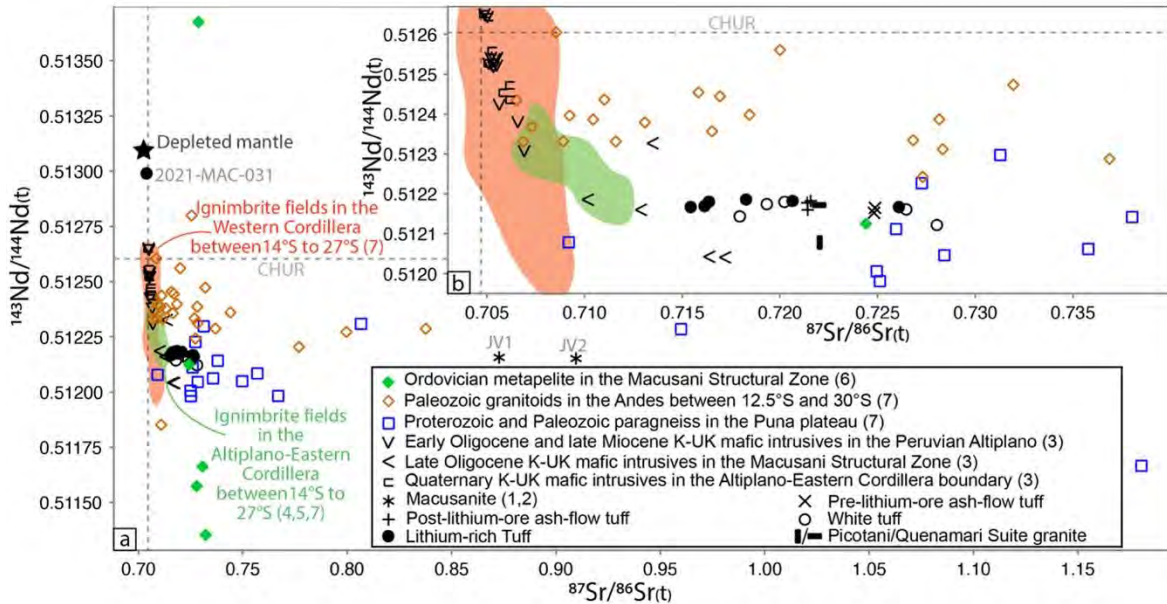


Figure 23. Strontium and Nd isotope ratios of volcanogenic and intrusive rocks (this and previous studies) from the Macusani Volcanic Field. Datapoints of Cenozoic potassic-ultrapotassic mafic rocks and Andean basement are also plotted. All data is recalculated at to 8.9 Ma. Ignimbrite fields in the Western Cordillera include Huaylillas, La Joya, Caraveli, Sencca, Oxaya, Toquepala, and Capillune (DIGIS Team 2023) whereas ignimbrite fields in the Altiplano-Eastern Cordillera include Los Frailes, Altiplano-Puna Volcanic Complex, Cerro Galán Complex, and other ignimbrites in southern Puna (Kay et al. 2010; Kato 2013; DIGIS Team 2023). References: (1) Pichavant et al. (1987); (2) Pichavant et al. (1988b); (3) Carlier et al. (2005); (4) Kay et al. (2010); (5) Kato (2013); (6) Harlaux et al. (2021); (7) DIGIS Team (2023). CHUR = chondritic uniform reservoir (Wasserburg et al. 1981; Goldstein et al. 1984). DM = depleted mantle (McCulloch et al. 1983; Michard et al. 1985; Salters and Stracke 2004).

5. DISCUSSION

5.1. Chemical composition of the lithium ore units within the geochemical diversity of the Macusani Formation

In this section I will compare the chemical composition of lithium ore units, namely the Lithium-rich Tuff, Upper Breccia, and Lower Breccia, with other rocks from the Macusani Formation and related products (i.e., macusanite pebbles) using new and previous geochemical data. Regarding major and minor elements, the Lithium-rich Tuff, macusanite, and ash-flow tuff have relatively homogeneous total alkalis ($\text{Na}_2\text{O}+\text{K}_2\text{O}$) and SiO_2 contents (Fig. 15a) and plot in the rhyolite field in the TAS diagram (Fig. 15b). The exceptions are the samples of lithium-ore with higher LOI values, particularly those of the Upper and Lower Breccia, which are scattered outside the general cluster and show coupled depletion in SiO_2 and alkalis (Fig. 15a), specifically in K_2O (Fig. 24h), and variable degrees of enrichment in CaO (Fig. 24f). Compared to Macusani Formation ash-flow tuff, the lithium-ore rocks are

enriched in Al_2O_3 , P_2O_5 , and MnO and depleted in TiO_2 , K_2O , CaO , MgO , and $\text{Fe}_2\text{O}_{3\text{tot}}$ (Fig. 24a-f, i). In contrast, the lithium-ore units, and particularly the samples of Lithium-rich Tuff with $\text{LOI} < 2.7$ wt.%, show similar compositions to macusanite in terms of most major elements except for their generalized depletion in Na_2O (Fig. 24). Furthermore, when compared to matrix glass and phenocryst-hosted glass inclusions in Macusani Formation ash-flow tuff, the Lithium-rich Tuff is enriched in Al_2O_3 , P_2O_5 , and TiO_2 and slightly depleted in $\text{Fe}_2\text{O}_{3\text{tot}}$, MgO , K_2O , and CaO . Finally, the lithium-bearing units are enriched in Al_2O_3 , Na_2O , and P_2O_5 , and depleted in TiO_2 , $\text{Fe}_2\text{O}_{3\text{tot}}$, MgO , CaO , and K_2O compared to the white tuff.

Regarding trace elements, the Lithium-rich Tuff is strongly enriched in volatiles such as halogens (F, Cl) and B and other incompatible lithophile elements such as Li, Be, and some LILE (Cs, Rb) and HFSE (Nb, Ta, Sn, W) compared to Macusani Formation ash-flow tuff (Fig. 25). In contrast, it is depleted in other HFSE (Zr, Hf, Th) and LILE (Ba, Sr) and show equivalent Pb in relation to the ash-flow tuff (Fig. 26). As with major elements, the trace element contents in the Lithium-rich Tuff are similar to those of macusanite, particularly in terms of F, Li, Be, Rb, Sr, Nb, Zr, Hf, Cs, and Ba, with lower contents of B and U and higher contents of Ta and Pb. Finally, most of the lithium-ore bearing rocks, particularly the Lithium-rich Tuff, are enriched in Li, Be, F, Rb, Zr, Nb, and Ta and depleted in B compared to matrix glass and phenocryst-hosted glass inclusions in Macusani Formation ash-flow tuff.

In terms of REY, most Lithium-rich Tuff, Upper Breccia, and Lower Breccia analyses show equivalent ΣREE and Y contents, which are intermediate between those of Macusani Formation ash-flow tuff and macusanite (Figs. 20, 27). The CN REY patterns of lithium-ore units closely resemble those of macusanite except for slightly higher La/Sm and less pronounced Eu negative anomalies (Fig. 20). Ash-flow tuff analyses yield higher $(\text{La/Sm})_{\text{CN}}$ and $(\text{Sm/Yb})_{\text{CN}}$ and lower to non-existent Eu negative anomalies relative to the lithium-ore units. Finally, the lithium-ore units exhibit similar to lower Eu and higher La, Sm, and Yb compared to matrix glass and phenocryst-hosted glass inclusions in ash-flow tuff (Fig. 27).

The lithium-ore units are enriched in the transition metal Cu but show similar contents of Zn compared to Macusani Formation ash-flow tuff, matrix glass and phenocryst-hosted glass inclusions, and macusanite (Fig. 28).

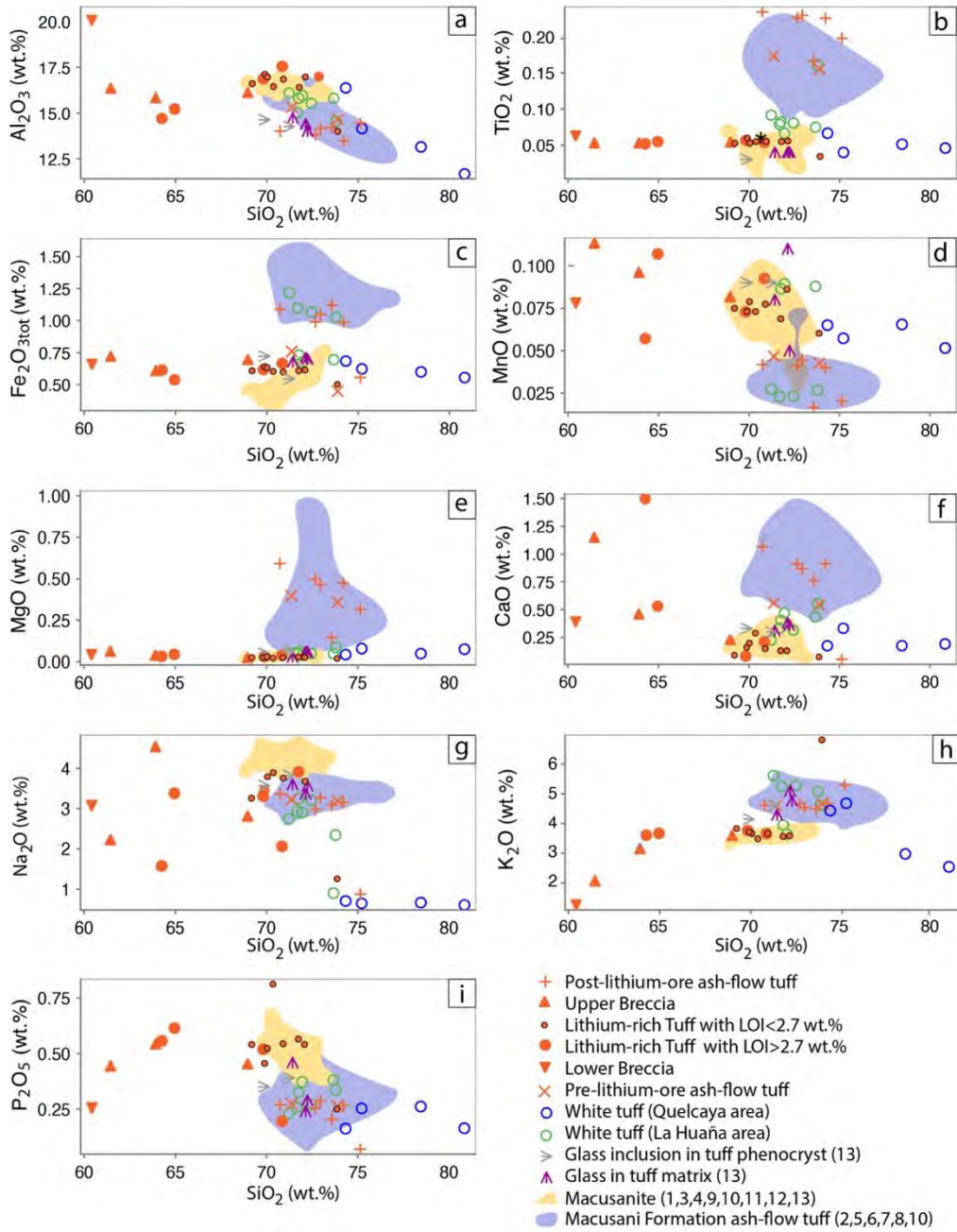


Figure 24. Major element Harker diagrams for volcanogenic units assigned to the Macusani Formation. References: (1) Linck (1926); (2) Francis (1953b); (3) Martin and de Sitter-Koomans (1955); (4) Elliott and Moss (1965); (5) Barnes et al. (1970); (6) Noble et al. (1984); (7) Arribas and Figueroa (1985); (8) Valencia and Arroyo (1985); (9) Pichavant et al. (1987); (10) Pichavant et al. (1988b); (11) Poupeau et al. (1992); (12) Craig et al. (2010); (13) Pichavant et al. (2024a). The phenocryst-hosted glass inclusions in ash-flow tuff are from basal contacts and lower levels of the volcanic sequence in the Huiquiza section. The compositional field shown for macusanite represents 95 % of data available in literature in order to exclude far outliers.

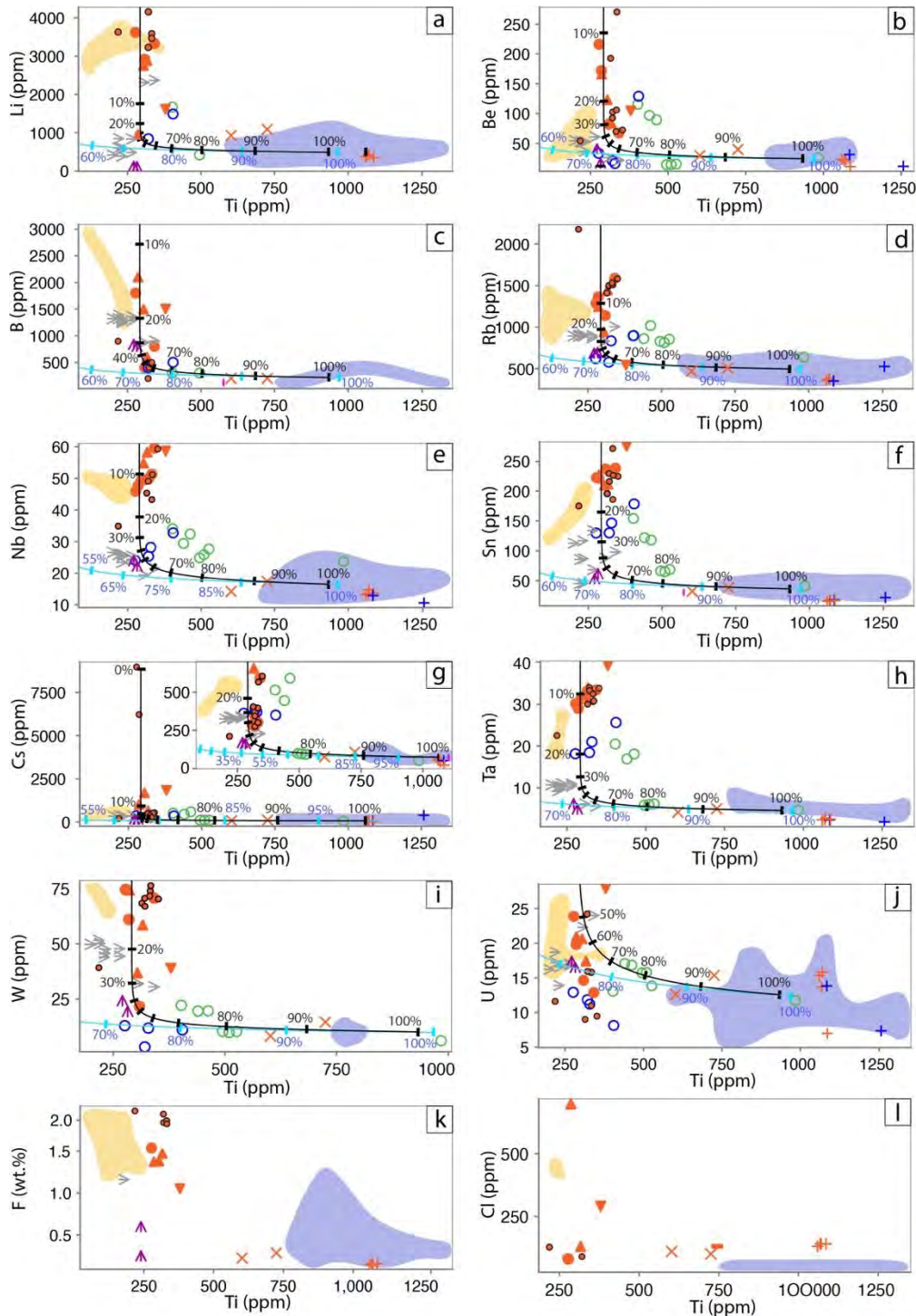


Figure 25. Bivariate plots of Ti vs. elements that behaved as incompatible in parental magmas to Macusaní Formation rocks including (a) Li, (b) Be, (c) B, (d) Rb, (e) Nb, (f) Sn, (g) Cs, (h) Ta, (i) W, (j) U, (k) F, and (l) Cl. Blue lines represent a geochemical evolution model of a melt during fractional crystallization using mineral/melt partition coefficients in [Pichavant et al. \(2024a\)](#); percentages represent the proportion of remanent melt. Black lines represent assimilation + fractional crystallization (AFC) models for a melt following the procedure in [DePaolo \(1981a\)](#), considering a r factor (fractional crystallization/assimilation rate) of 0.2 and assimilation of a host rock chemically equivalent to the average composition of Ordovician metapelites of the Sandia Formation reported by [Harlaux et al. \(2021\)](#). The starting member of all models corresponds to the average composition of ash-flow tuff samples. Symbology and references as in [Figure 24](#).

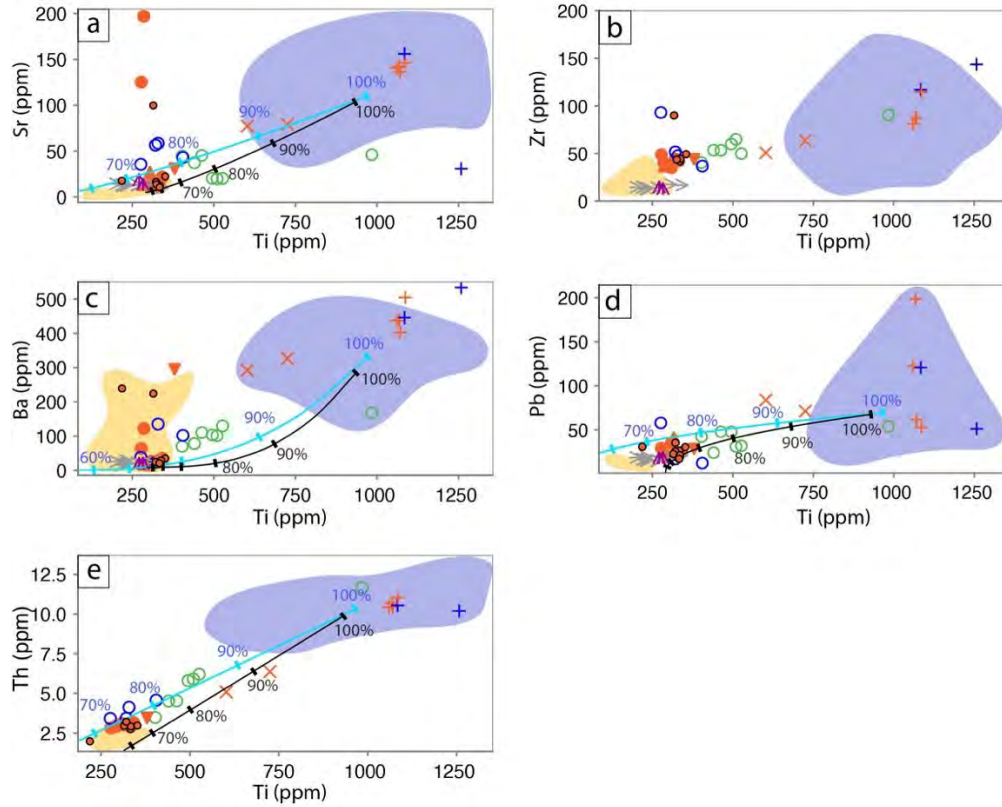


Figure 26. Bivariate plots of Ti vs. elements that behaved as compatible in parental magmas to Macusani Formation rocks including (a) Sr, (b) Zr, (c) Ba, (d) Pb, and (e) Th. Symbology and references as in [Figures 24](#) and [25](#).

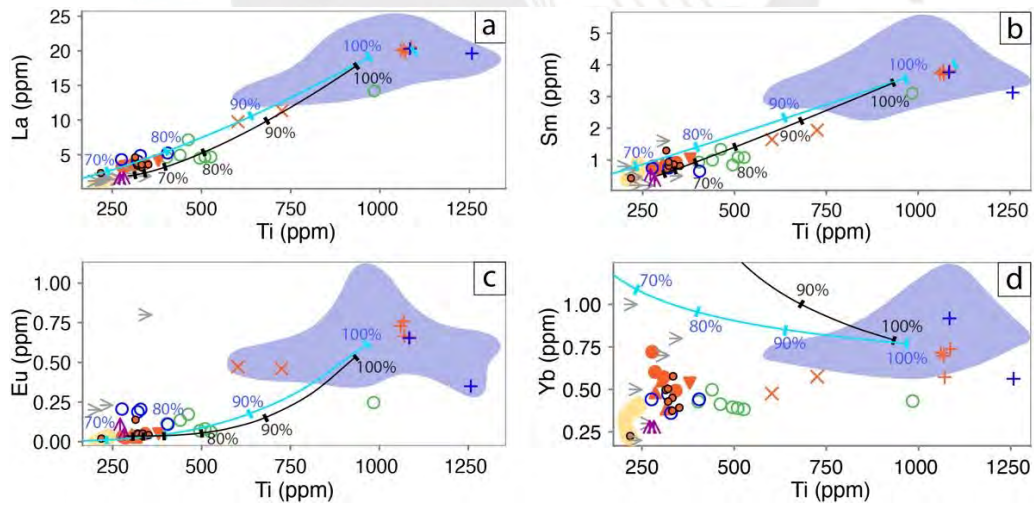


Figure 27. Bivariate plots of Ti vs. REE in Macusani Formation rocks including (a) La, (b) Sm, (c) Eu, and (d) Yb. Symbology and references as in [Figures 24](#) and [25](#).

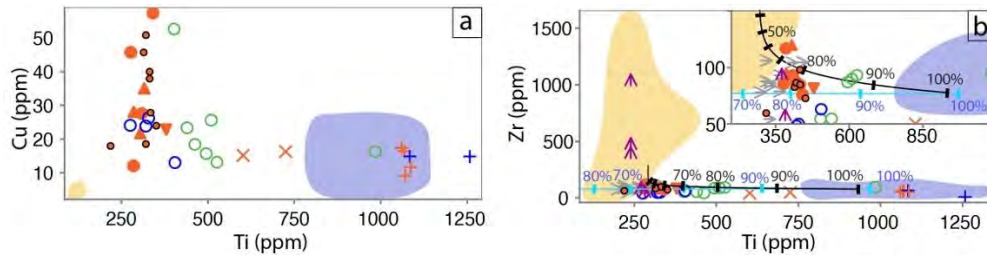


Figure 28. Bivariant plots of Ti vs. transition metals in Macusani Formation rocks including (a) Cu and (b) Zn. Symbology and references as in [Figures 24](#) and [25](#).

Finally, the white tuff and Lithium-rich Tuff show remarkable compositional differences in terms of most trace elements ([Figs. 17](#)). Compared to the Lithium-rich Tuff, the white tuff is slightly to moderately depleted in Li, Rb, Sn, and W ([Fig. 25](#)), enriched in Sr, Zr, Ba, and Th, and shows equivalent Pb contents ([Fig. 26](#)). The white tuff exhibits lower $(La/Sm)_{CN}$ values and negative Eu anomalies than the lithium-ore units ([Fig. 20](#)). In terms of transition metals, the white tuff yielded equivalent contents of Cu and Zn compared to the lithium-ore units ([Fig. 28](#)).

To sum up, the ore-bearing units (Lithium-rich Tuff and Upper and Lower Breccia) are distinctly enriched in Li, Be, F, Nb, Ta, Sn, Cs, Cl, Rb, Cu, Al, and P and depleted in Sr, Ti, Ba, Pb, Zr, Y, Th, Hf, LREE, and MREE relative to other tuffaceous rocks of the Macusani Formation including those analyzed in this thesis. Their composition is, in contrast, very similar to that of macusanite with the notable exceptions of the enrichment in Ta and depletion in B and U in the lithium-ore units.

5.2. Nature of the magmatic component in the Lithium-rich Tuff

The lack of specific studies on the depositional history of the Lithium-rich Tuff unit obscures a direct linkage between its chemical composition and the parental magma composition. [Nupen \(2019\)](#) initially interpreted this unit as a subaerial volcanic sequence deposited into a lake volcano-sedimentary environment. This interpretation is based on the observed finely regular layering in the Lithium-rich Tuff, the high angularity of clasts in the transitional Upper Breccia and Lower Breccia, and the lenticular geometry of the depositional unit. This interpretation is compatible with the lithological description of Lithium-rich Tuff samples in this thesis ([Appendix B](#)). Pyroclasts undergo physical segregation during the formation of either subaerial fallout or syn-eruptive water-settled fallout deposits ([Cas and](#)

Wright 1988; McPhie et al. 1993). In addition, the sediment input in lakes in volcanic terranes is transported by rivers, lahars, and subaerial mass flows, implying physical sorting of clasts according to their size or density (Nichols 2009). Finally, metasomatic reactions, either during pre-eruptive stages or post-depositional processes can further modify the geochemical signature inherited from the magma (Gifkins et al. 2004). Thus, a careful analysis is required before making petrogenetic interpretations of parental magmas to the Lithium-rich Tuff.

The trace element composition of volcanoclastic rocks, whether in primary or secondary deposits, can be employed as provenance indicators, enabling us to “see” through sorting processes and the determination of the nature of the source(s) (Rollinson and Pease 2021). Given the conspicuous alteration of the Lithium-rich Tuff in the Falchani Lithium Project (Segovia-More et al. 2023), it is necessary to turn to immobile elements in order to discriminate the nature of the protolith. Elements such as Ti, Zr, Y, Nb, V, and P are relatively immobile in aqueous fluids and are effective discriminators in tectono-magmatic studies since their behavior in silicate melts is significantly influenced by petrogenetic factors (Winter 2014; Rollinson and Pease 2021). However, extra caution should be taken as their mobility in aqueous fluids can be enhanced by high fluoride ion activity (Bau 1996; Ballouard et al. 2016).

In the Zr-Al₂O₃-TiO₂ provenance discrimination plot for weathered rocks of García et al. (1994), most of the Lithium-rich Tuff, Upper Breccia, and Lower Breccia datapoints plot in the field of strongly peraluminous silicic igneous rocks (Fig. 29). This is in good agreement with the general strong peraluminous composition of rocks in the Macusani Formation (Noble et al. 1984; Pichavant et al. 1988b).

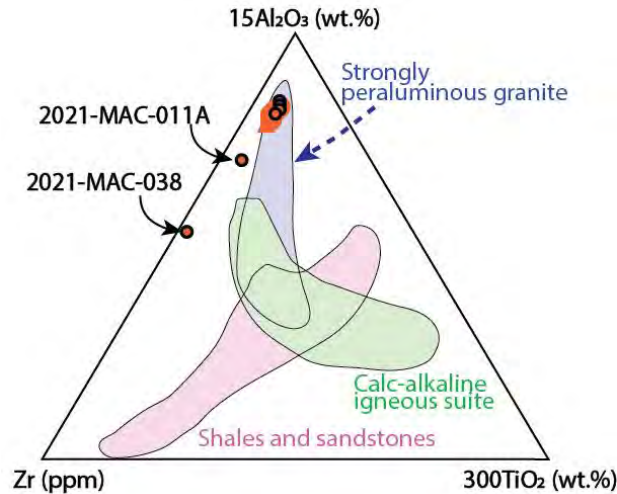


Figure 29. Composition of lithium-ore units from Falchani in the provenance discrimination plot for weathered rocks after [García et al. \(1994\)](#). Symbology as in [Figure 24](#).

Compared to archetypal global examples of muscovite-bearing peraluminous granites (MPG in the classification of [Barbarin 1996](#)), the Falchani Lithium-rich Tuff exhibits significant enrichment in F, Sn, W, and other rare metals such as Li, Nb, Ta, and Cs, while simultaneously displaying strong depletion in Zr, Th, Y, REE, and Sr ([Fig. 30](#)) and very low Nb/Ta ratios ([Fig. 19a](#)). This is a distinctive geochemical fingerprint of peraluminous rare metal-rich granites ([Ballouard et al. 2020](#)), such as Beauvoir ([Raimbault et al. 1995](#)), Jalama ([Ramírez and Grundvig 2000](#)), Eibenstock ([Förster et al. 1999b](#)), Jiepailing ([Xie et al. 2016](#)), and Songshugang ([Zhu et al. 2015](#)), as well as LCT pegmatites ([Stilling et al. 2006](#); [Canosa et al. 2012](#); [Fuchsloch et al. 2018](#)). The Lithium-rich Tuff is even more enriched in Li, Cs, and F, than all of these evolved granites and pegmatites ([Fig. 30](#)). However, when comparing a magmatic differentiation index for peraluminous granitic melts such as the Zr/Hf ratio ([Dostal and Chatterjee 2000](#); [Zaraisky et al. 2009](#)), the Lithium-rich Tuff (21-36) show less evolved values than rare metal-rich granites (<18; [Fig. 30](#); [Ballouard et al. 2016](#)).

Lithophile rare metals are incompatible in the structure of most common rock-forming minerals and concentrate in the melt during partial melting and magmatic differentiation ([Michaud 2019](#)) and/or may partition into volatile-rich aqueous fluids exsolved from residual melts ([London et al. 1988](#)). The compositional similarity between the Lithium-rich Tuff and macusanite, rather than to previously reported ash-flow tuff from the Macusani Formation (cf. Section 5.1), may reflect a significant component of highly evolved rhyolitic volcanic material, including glass equivalent or similar to macusanite, in this unit

prior to its alteration. Concordantly, [Torró et al. \(2023\)](#) have described contrasting compositions for micas hosted in the Lithium-rich Tuff (zinnwaldite and lepidolite) relative to micas in other volcanic and intrusive rocks of the Macusani Formation suggesting a crystallization from more evolved rhyolitic melts.

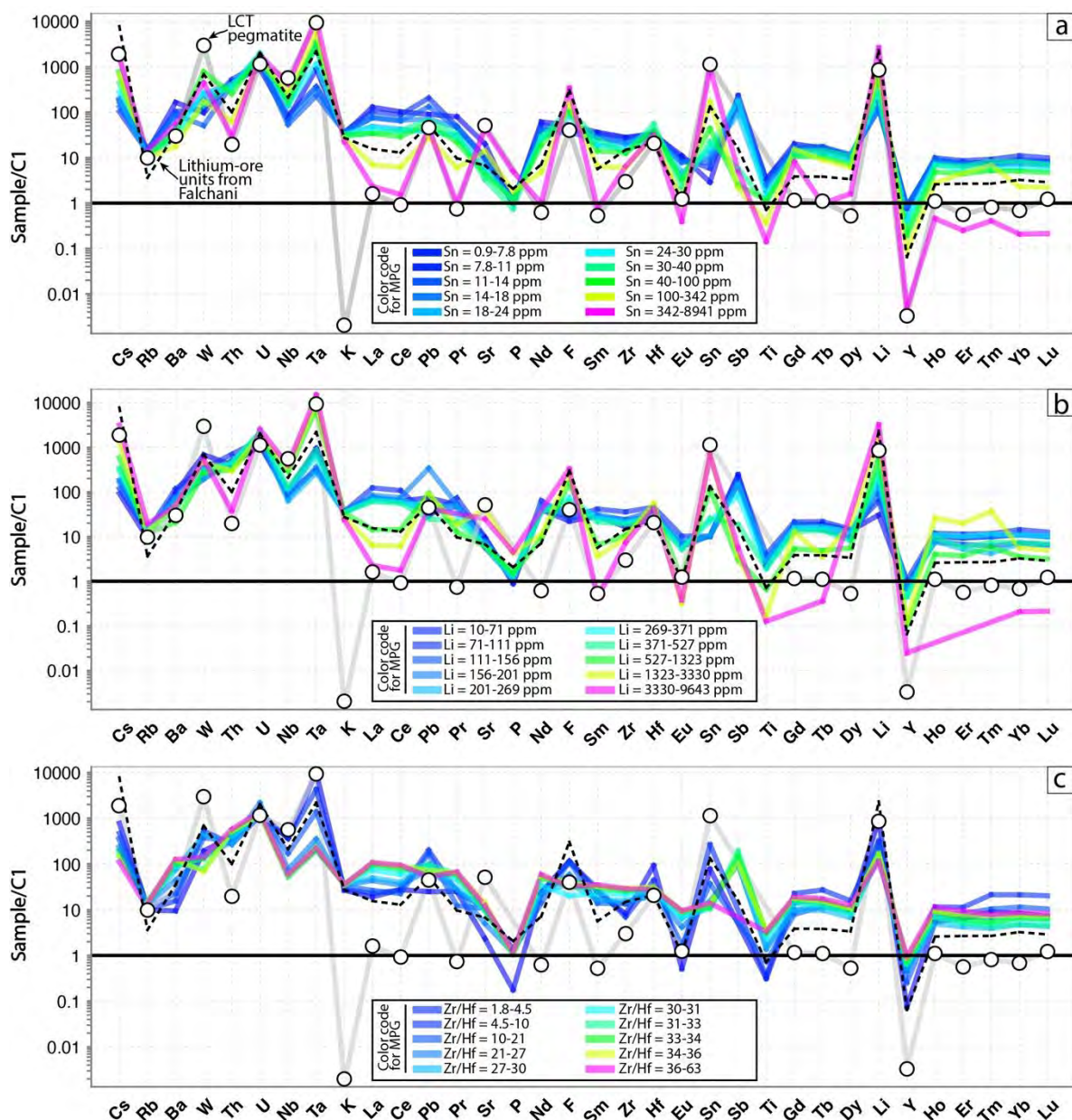


Figure 30. Average chondrite-normalized element patterns of lithium-ore units from Falchani, LCT pegmatites ([Stilling et al. 2006](#); [Canosa et al. 2012](#); [Fuchsloch et al. 2018](#)), and the best studied muscovite-bearing peraluminous granites (MPG; [Ballouard et al. 2020](#) and references therein) grouped by deciles of (a) Sn and (b) Li contents and (c) Zr/Hf ratios. C1 chondrite values after [McDonough and Sun \(1995\)](#).

5.3. Source regions of parental magmas to the Lithium-rich Tuff

The petrogenesis of ash-flow tuff and macusanite—including pebbles and clasts in tuff—assigned to the Macusani Formation has been constrained by [Pichavant et al. \(1987; 1988a, b; 2024a\)](#) in terms of batch melting of isotopically heterogeneous crustal rocks probably dominated by pelitic metasedimentary rocks. The low $f_{\text{H}_2\text{O}}/f_{\text{F}}$ in biotite, tourmaline, and apatite and the absence of muscovite in the early magmatic stage support partial melting under H_2O -undersaturated conditions, with $a_{\text{H}_2\text{O}}$ internally controlled by dehydration melting of F-rich muscovite and incipient melting of biotite ([Pichavant et al. 1988a, b](#)). The relatively high anorthite content (>30 % An; [Pichavant et al. 1988a](#)) and the strong enrichment in Sr, Ba, and La in relicts of plagioclase from this early magmatic stage is interpreted by [Pichavant et al. \(2024a\)](#) as evidence of high degrees of hybridization between crustal melts and LILE- and LREE-rich potassic to ultrapotassic mantle-derived magmas at or near the anatexis zone.

At the latitude of the Macusani Volcanic Field, the Andean basement is composed principally of the northern domain of the Arequipa-Antofalla terrane ([Loewy et al. 2004](#) and references therein). This domain is mapped based on two criteria: i) the existence of Paleoproterozoic basement rocks exposed along the Western Cordillera and fore arc of southern Peru and ii) the ^{206}Pb -poor whole-rock Pb isotopic signatures of igneous rocks that assimilated or derived from Paleoproterozoic crust ([Fig. 22a, c; Wörner et al. 2018](#)). The Macusani Volcanic Field is located to the east of the eastern limit of the northern domain, also known as the Arequipa domain, according to the spatial constraint based on the distribution of Pb isotopes in magmatic rocks along the Central Andes compiled by [Wörner et al. \(2018\)](#). The boundary between the Arequipa domain to the west and the Amazonian craton to the east is obscured by the intrusion of younger igneous rocks, the deposition of overlying sequences, and the deformation associated with orogenic events during the last 2 Ga ([Loewy et al. 2004; Ramos 2018](#)).

Despite its location, the Lithium-rich Tuff exhibits isotope ratios and Sm/Nd T_{DM} ages (i.e., theoretical time in the past when $\epsilon_{\text{Nd}}^{\text{rock}} = \epsilon_{\text{Nd}}^{\text{Depleted Mantle}}$) that are broadly similar to those of the central domain of the Arequipa-Antofalla terrane ([Figs. 22-23, 31](#)). It is noteworthy that [Loewy et al. \(2004\)](#) reported the presence of Ordovician plutons in the Paleoproterozoic northern domain that exhibited central domain-like Pb and Nd isotope

signatures and equivalent Sm/Nd T_{DM} ages and U/Pb zircons dates at 1.5 Ga. [Loewy et al. \(2004\)](#) proposed that the Mesoproterozoic Pb isotopic reservoir that defines the central domain may be underplated beneath the Paleoproterozoic northern domain, at least in the Coastal Cordillera of southern Peru. The results of this thesis suggest a similar scenario in which the crustal component of the magmas related to the Lithium-rich Tuff in the Eastern Cordillera were derived from the assimilation of Paleoproterozoic crust and underplated Mesoproterozoic crust from the northern domain of the Arequipa-Antofalla terrane. The marked dispersion of Sm/Nd T_{DM} ages among Macusani Formation rocks, extending to values as high as 3.8 Ga, does not suggest the involvement of Archean crust. Instead, this variation is attributed to an artifact resulting from lower $(La/Sm)_{CN}$ values and higher Sm/Nd ratios observed in the more fractionated rocks ([Fig. 31](#)). The depletion in LREE during magmatic differentiation in Macusani magmas has been explained by [Pichavant et al. \(1988b\)](#) and is further discussed in Section 5.4 of this thesis. The least differentiated (i.e., lowest Sm/Nd) Lithium-rich Tuff sample yields a Sm/Nd T_{DM} age of ca. 1.5 Ga, which is consistent with the derivation or assimilation of a Mesoproterozoic crust. In contrast, the isotopically heterogeneous and ^{144}Nd -depleted Ordovician metapelite rocks of the Sandia Formation in the Macusani Structural Zone ([Harlaux et al. 2021](#)) are not compatible with the narrow range of ϵ_{Nd}^0 values in Macusani Formation rocks ([Figs. 23, 31](#)). Furthermore, the lithium-ore units and ash-flow tuff from the Macusani Formation are consistently depleted in radiogenic Pb compared to the Sandia Formation ([Fig. 22](#)). Sedimentary provenance studies using U-Pb dating of detrital zircons extracted from the Sandia Formation indicate that the main sources of sediments were 0.7–0.5 Ga metamorphic and igneous rocks related to the Brazilian orogenic event in the western part of the Amazonian Craton ([Reimann et al. 2010](#)).

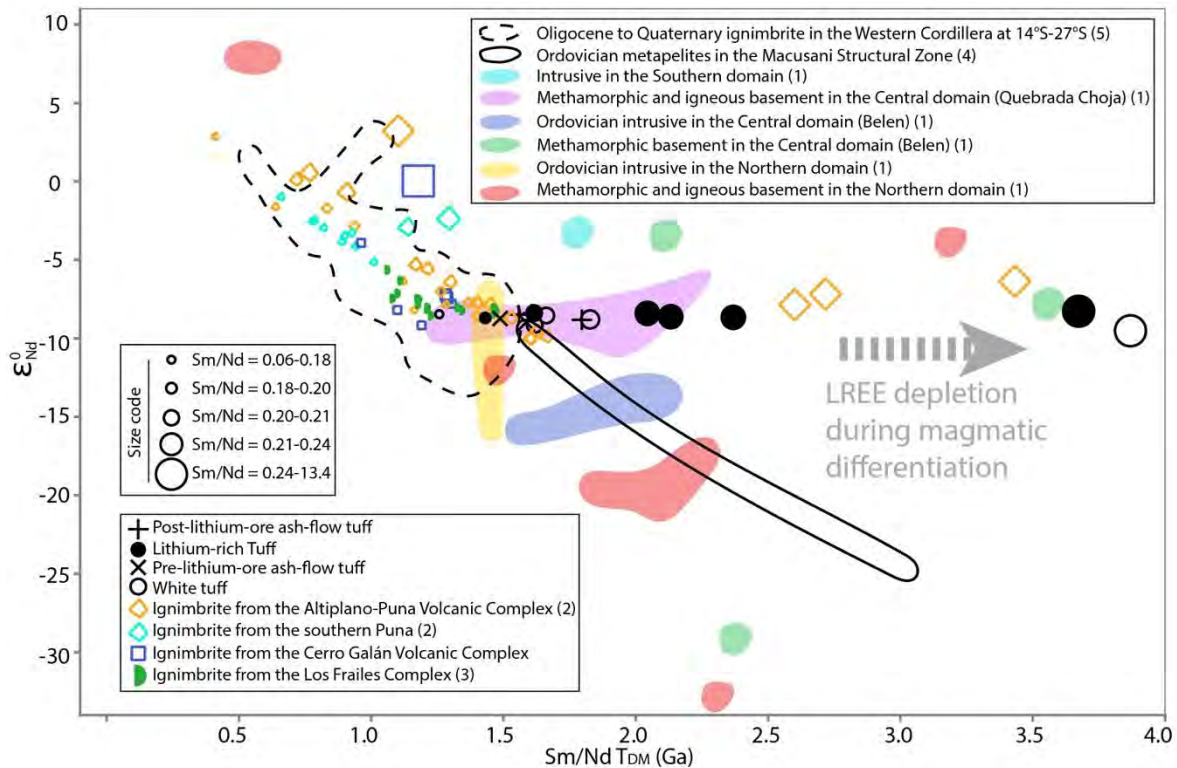


Figure 31. Sm/Nd T_{DM} vs. ε_{Nd}⁰ plot for analyzed samples from the Macusani Volcanic Field, metamorphic and igneous rocks from the Andean basement of the Arequipa-Antofalla terrane, and Oligocene to Quaternary Andean ignimbrite fields located between 14°S and 27°S. Sm/Nd T_{DM} ages are calculated using the theoretical isotopic decay constant ($\lambda_{147Sm} = 6.54 \times 10^{-12} \text{ years}^{-1}$) of [Lugmair and Marti \(1978\)](#) and the depleted mantle model of [DePaolo \(1981b\)](#). References: (1) [Loewy et al. \(2004\)](#); (2) [Kay et al. \(2010\)](#); (3) [Kato \(2013\)](#); (4) [Harlaux et al. \(2021\)](#); (5) [DIGIS Team \(2023\)](#).

In order to assess the relative contribution of older continental crust- and mantle-derived melts in magmas parental to the Lithium-rich Tuff and other volcanogenic materials assigned to the Macusani Formation, I have produced simple binary mixing models ([Heinonen et al. 2021](#) and references therein). Sm-Nd and Rb-Sr are very useful in distinguishing possible magma sources and are often used to study the origins and processes of magma hybridization ([DePaolo 1981a, b](#)). The $^{143}\text{Nd}/^{144}\text{Nd}$ and $^{87}\text{Sr}/^{86}\text{Sr}$ values in crustal rocks depend upon their age and the relative degree of Sm/Nd and Rb/Sr fractionation, respectively ([Faure and Mensing 2005](#)). Even for crustal reservoirs with equivalent $^{143}\text{Nd}/^{144}\text{Nd}$ ratios, upper crustal rocks yield drastically higher $^{87}\text{Sr}/^{86}\text{Sr}$ ratios than lower crustal rocks of the same age because higher Rb/Sr ratios are typically restricted to paragneiss, granite, and/or metapelite ([DePaolo 1981b](#)). On the other hand, enriched-mantle Nd-Sr isotope signatures are distinguished by lower $^{143}\text{Nd}/^{144}\text{Nd}$ ratios and higher $^{86}\text{Sr}/^{86}\text{Sr}$ ratios than those of the depleted mantle ([Garapić et al. 2015](#); [Jackson et al. 2016](#)), indicating

an ancient ^{143}Nd depletion event of melt removal and later Rb metasomatic enrichment (Peccerillo 1999; Donnelly et al. 2004; Peccerillo and Frezzotti 2015; Rodrigues et al. 2022). In this sense, the Nd and Sr isotope ratios of Neogene and Quaternary ignimbrite fields in the Western Cordillera (Huaylillas, Caraveli, Nazca, Oxaya, and Rio Frio; Fig. 9) and Eastern Cordillera-Altiplano (Los Frailes Complex, Altiplano-Puna Volcanic Complex, Cerro Galán Complex, and southern Puna; Fig. 9) between 15°S and 27°S are typically interpreted as delineating variable proportions of mixing between basalts with a depleted mantle signature and crustal rocks of variable composition (Fig. 23; de Silva 1989a; Kay et al. 2010; Freymuth et al. 2015). Late Miocene volcanic rocks from the Macusani Volcanic Field have generally higher $^{87}\text{Sr}/^{86}\text{Sr}_{(t)}$ ratios compared to other Neogene to Quaternary ignimbrite rocks in the Central Andes, suggesting a higher proportion of old crustal component with high Rb/Sr ratios. It is crucial to note that the match between the Rb-Sr isochrone age of 8.9 Ma for the Lithium-rich Tuff calculated in this thesis (Fig. 32) and the $^{40}\text{Ar}/^{39}\text{Ar}$ mica dates for the same rocks (unpublished data – L. Torró personal communication) indicates that the measured Sr isotope ratios reflect a magmatic isotope signature. The relatively high dispersion of $^{88}\text{Sr}/^{87}\text{Sr}$ ratios in the Lithium-rich Tuff can be explained either as isotopically heterogeneous crustal protoliths (Pichavant et al. 1988b; Guillot and Le Fort 1995; Romer et al. 2014), a lack of complete $^{87}\text{Sr}/^{86}\text{Sr}$ homogenization during metamorphism and/or anatexis (Wolf et al. 2019; Pichavant et al. 2024b), and/or different melting mechanisms and kinetics (Hammouda et al. 1996; Farina et al. 2014). In any case, such $^{88}\text{Sr}/^{87}\text{Sr}$ dispersion reduces the accuracy of Nd-Sr mixing modeling.

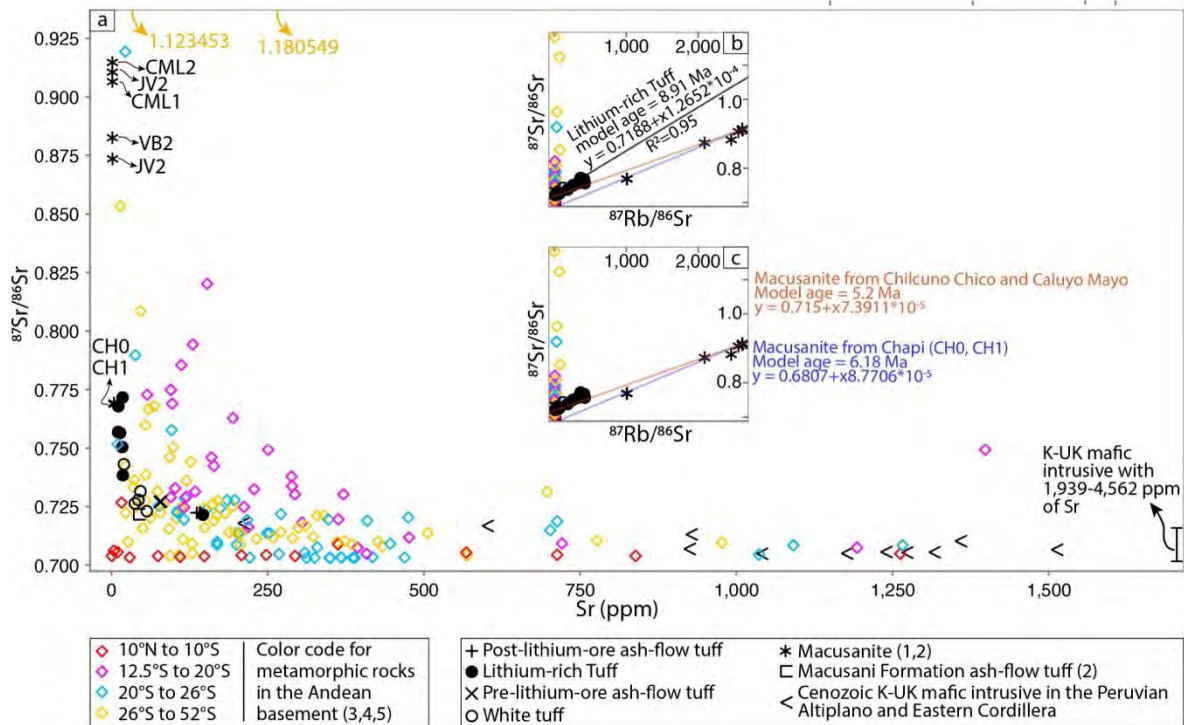


Figure 32. Strontium isotope ratios and elemental abundance in rocks from Macusani Volcanic Field, and metamorphic and igneous rocks from the Andean basement of the Arequipa-Antofalla terrane. (a) Present-day $^{88}\text{Sr}/^{87}\text{Sr}$ vs Sr plot with analyzed samples from the Macusani Volcanic Field, metamorphic rocks in the Andean basement, and potassic and ultrapotassic (U-UK) mafic rocks in the Eastern Cordillera and Altiplano. Small boxes represent $^{88}\text{Rb}/^{87}\text{Sr}$ vs. $^{88}\text{Sr}/^{87}\text{Sr}$ plots with isochrones for (b) the Lithium-rich Tuff (black line) and (c) macusanite pebbles from Caluyo Mayo such as VB2, CML1, and CML2 (pale brown line) and Chilcuno Chico such as JV1 and JV2 (purple line). References: (1) Pichavant et al. (1987); (2) Pichavant et al. (1988b); (3) Loewy et al. (2004); (4) Harlaux et al. (2021); (5) DIGIS Team (2023).

Based on the exposed evidence, felsic, Al_2O_3 -rich, ^{87}Sr -rich, ^{144}Nd -poor rocks from the Andean basement have been assessed as potential representative proxies for the compositions of potential crustal endmembers. Options include Paleozoic and Precambrian paragneiss from the Puna plateau (DIGIS Team 2023) and Ordovician metapelite rocks of the Sandia Formation from the Macusani Structural Zone (Harlaux et al. 2021). As discussed above, the best possible candidates are Paleozoic and Precambrian paragneiss, which show the highest $^{87}\text{Sr}/^{86}\text{Sr}$ and lowest $^{143}\text{Nd}/^{144}\text{Nd}$ ratios among all mentioned groups (Fig. 23), with a possible contribution of Paleozoic metapelite rocks of the Sandia Formation.

With regard to the mantle-derived endmember, and based of the findings of Pichavant et al. (2024a), Oligocene and late Miocene LILE-, LREE-, Ba-, Pb-rich potassic to ultrapotassic (K-UK) mafic intrusions exposed in the Altiplano and Eastern Cordillera between 14°S and 16°S may represent suitable candidates. These rocks have been interpreted by Carlier et al. (2005) as derived from hybridized magmas containing mainly enriched

mantle-derived melts and a volumetrically minor depleted asthenospheric mantle component (Fig. 23b).

When setting the mafic endmember with the average isotope signature of the late Miocene K-UK mafic melts (i.e., those that are closer in age to the Lithium-rich Tuff), the parental magma of the Lithium-rich Tuff is modeled as containing ~15-30% of mantle contribution, and ~70-85% of paragneiss + metapelite contribution (Fig. 33). The assimilation of local Ordovician metapelites during shallow level fractionation of the magma would explain the scattering of the data toward less radiogenic compositions. The obtained fractions of mantle-derived component in Lithium-rich Tuff are within the range of those calculated for late Miocene rhyodacitic-rhyolitic ignimbrites (22-68%) at >22°S and lower than those computed for Oligocene-Miocene dacitic ignimbrites (63-85 %) at <22°S (Freymuth et al. 2015). Also, our results are not compatible with estimations of ~50 % of mantle-derived component in late Miocene to Quaternary ignimbrite fields from the Altiplano-Puna Volcanic Complex and southern Puna, between 22°S and 27°S (Kay et al. 2010). Our model suggests that the felsic nature of the igneous rocks in the Macusani Formation (Noble et al. 19884; Pichavant et al. 1988a, b) are the result of a notably elevated crustal contribution in parental magmas, compared to the aforementioned ignimbrite fields.

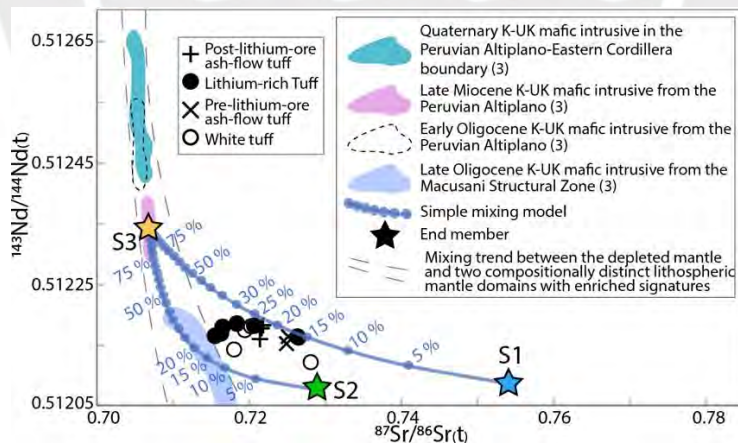


Figure 33. Strontium and Nd isotope ratios corrected to 8.9 Ma and simple binary mixing models that reproduce the Nd-Sr isotope signature of volcanogenic rocks from Macusani Volcanic Field. The selected endmembers represent average values of Proterozoic and Paleozoic paragneiss in the Puna plateau (S1), Ordovician metapelite of the Sandia Formation in the Macusani Structural Zone (S2), and late Miocene K-UK mafic intrusive in the Peruvian Altiplano and Eastern Cordillera (S3). Here, both magmatic stages of Pichavant et al. 1988a, b; 2024a) consisting of i) mantle-derived magmas assimilating mid-crustal rocks without important crystallization and becoming a chemically homogenized magma body; and ii) AFC processes in shallower crustal levels are simplified as a simple chemical mixing (cf. Heinonen et al. 2021). The employed models assume complete chemical mixing of two endmembers resulting in a homogeneous mixture, also called hybridization (cf. Heinonen et al. 2021). Percentages represent the fraction of the mantle-derived endmember.

Mantle-derived, LILE-rich, K-UK basalts sourced heat and volatiles to the magma source region in Macusani (Pichavant et al. 2024a). Heterogeneous initial conditions for different magma batches in the Macusani magma source region could be reproduced by focalized metasomatism with addition of F and other alkaline and fluxing elements such as Na, Li, K, Rb, and Cs from fluids exsolved from cooling K-UK basaltic dykes in the middle crust (cf. Troch et al. 2022). This could explain the geochemical specialization of the magma source rocks in Macusani, which is defined as F-rich by Pichavant et al. (1988b).

In the particular case of Li in volcanogenic environments, previous works remark the role of a pre-enriched protolith to generate Li-rich granitic melts (Benson et al. 2017; Pichavant et al. 2024b). This has been extensively investigated using Sr-Nd simple mixing models applied to volcanic rocks associated to the Yellowstone hotspot. Specifically, it has been observed that rhyolitic rocks with higher proportions of crustal contribution or originated from a more felsic crustal source tend to contain glass inclusions with higher Li and lower Zr contents (Benson et al. 2017). Although this might be also the case in the protolithic material of the Lithium-rich Tuff, the analyzed rocks from this unit exhibit $^{143}\text{Nd}/^{144}\text{Nd}$ ratios that are nearly identical to those in all of the other volcanogenic units in the Macusani Volcanic Field area (Fig. 23b). This would rule out a greater proportion of more felsic crustal components in the magmas as the ultimate reason for the higher lithium contents in the Lithium-rich Tuff. Therefore, further mechanisms to explain the distinctly high Li content in the Falchani lithium-ore units are needed.

5.4. Magma differentiation and fluid-mediated controls on the composition of the Lithium-rich Tuff

This chapter assesses the magmatic and hydrothermal processes that explain the primary and secondary evolution of the Lithium-rich Tuff, with a particular focus on its high Li contents. According to Pichavant et al. (1988b), an early crystallization event, which is recorded as restitic mineral phases and occurred at $\sim 800\text{ }^{\circ}\text{C}$ and $< 5\text{-}7.5\text{ kbar}$ at or near the magma source region, was followed by the main crystallization stage triggered by a rapid ascent of the magmas and consequent temperature and pressure drop to $\sim 650\text{ }^{\circ}\text{C}$ and 1.5 kbar . According to Pichavant and Montel (1988), the homogeneity in the major element

composition and mineral chemistry along the stratigraphy of the Macusani Formation is inconsistent with a cogenetic nature of ignimbrite sheets. Rather, the authors propose that it reflects spatially and/or temporally separate magma bodies that followed similar petrogenetic histories with only slightly different partial melting conditions and/or P-T- $a_{\text{H}_2\text{O}}$ paths. In this scenario, macusanite-like melts would have been formed by 50-60 % of crystal fractionation of interstitial liquids in the driest and F-, B-, Li-, and P-richest magma batches (Noble et al. 1984; Pichavant et al. 1987, 2014a).

Models of fractional crystallization (Rollinson and Pease 2021) and simultaneous assimilation and fractional crystallization (DePaolo 1981a) were developed using constant partition coefficients experimentally obtained for felsic peraluminous magmas by Pichavant et al. (2024a), except for monazite in rhyolitic melts, which was taken from Stepanov et al. (2014). The fractionated assemblage corresponds to the average modal proportions of phenocrysts in ash-flow tuff estimated by Pichavant et al. (2024a) consisting of quartz (0.39), alkali feldspar (0.31), plagioclase (0.23), biotite (0.05), andalusite (0.008), and muscovite (0.007). Also, we set the initial melt as the average composition of the Macusani Formation ash-flow tuff (data from Barnes et al. 1979, Noble et al. 1984, Pichavant et al. 1988, and this thesis). Of course, the obtained results are semi-quantitative since the average composition of the ash-flow tuff is not necessarily representative of the parental magmas to the lithium-ore units. This is considered a reasonable approach for our first-order modeling, and further refinements considering the mineral geochemistry and melt inclusion data are required. Other authors have used the same approach to better understand the processes responsible for geochemical fractionation in rare-metal-enriched felsic igneous rocks (e.g., Ballouard et al. 2020). Finally, since I am modelling only the main stage of crystallization defined by Pichavant et al. (1988b), we consider the assimilation of shallow crustal levels with the average composition of local Ordovician metapelites of the Sandia Formation (Harlaux et al. 2021).

Volcanogenic rocks from the Macusani Volcanic Field exhibit a progressive depletion in Ba, Sr, Pb, Ti, Zr, Th, and REE from the least to the most evolved products (Pichavant et al. 1988b), indicating that these elements behaved as compatible during magmatic differentiation (Figs. 26-27). The coupled decrease in Ba/Sr and $(\text{Eu}/\text{Eu}^*)_{\text{CN}}$ values

supports feldspar fractionation (Fig. 34a; Müller et al. 2006; Xu et al. 2015). The coupled decrease in Ti and Nb/Ta is consonant with biotite fractionation (Fig 34b; Stepanov et al. 2014; Ballouard et al. 2016), which would have contributed to the extreme depletion in Mg, Ti, Sc, and Fe in volcanic glasses and lithium-ore units compared to ash-flow tuff in the Macusani Formation. Furthermore, the covariant enrichment in Li and Ta discard Li-mica fractionation, since Ta solubility in granitic melts increase with increasing Li contents (Fig 34c; Linnen 1998; Breiter et al. 2007; Zhu et al. 2015). It is known that highly fractionated melts enriched in rare metals equilibrate a greater variety and abundance of accessory minerals (Watson and Harrison 1983). Mathematical models of LREE partition calculated by Pichavant and Montel (1988) concluded that LREE variations in macusanite are best reproduced through crystal fractionation of monazite. This is consistent with the observed decreasing La/Sm and Th/U ratios in the Lithium-rich Tuff (Fig. 34d). Considering the partition coefficients for monazite/melt of Stepanov et al. (2012), the AFC model reproduces evolving contents of La, Sm, and Eu in volcanic units from Macusani for 2 % modal abundance of monazite at 55-65 % fractionation degrees. The equivalent Zr contents (Fig. 26) and positive correlations between Zr/Hf and HREE (Fig. 34e) are consistent with a subordinate role of zircon fractionation (Zaraisky et al. 2009) probably due to the fact that Zr contents were already low as it is typically observed in anatectic melts derived from felsic continental material (Watson and Harrison 1983). Finally, the proposed models do not replicate the behavior of Yb, probably due to the fractionation of an accessory phase not taken into account in the calculation, such as xenotime (Förster et al. 1999; Engi 2017). Xenotime has been identified throughout the entire differentiation history in biotite, two-mica, and Li-mica granites from the Aue-Schwarzenberg granite zone, in Germany, being most abundant in the F-, P₂O₅-richest Li-mica granitic melts (e.g., Eibenstock granite; Förster et al. 1999).

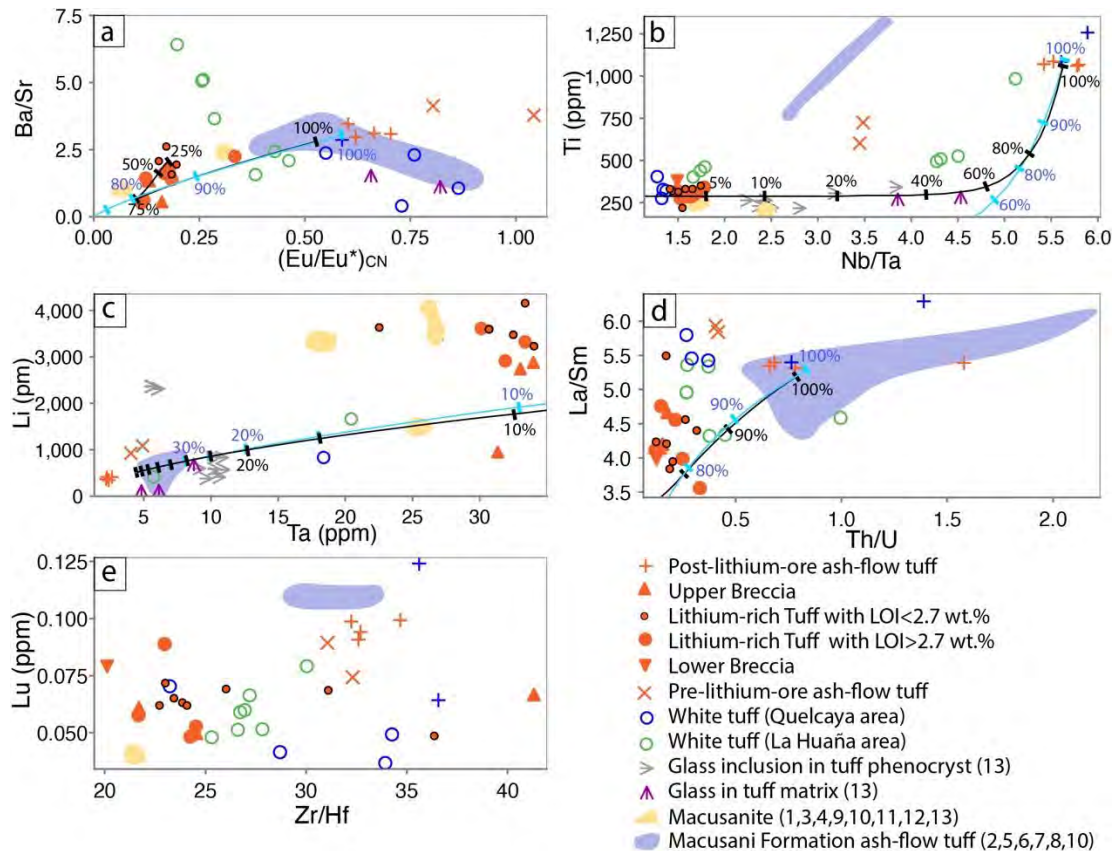


Figure 34. Bivariate plots including (a) $(Eu/Eu^*)_{CN}$ vs. Ba/Sr, (b) Nb/Ta vs. Ti, (c) Ta vs. Li, (d) Th/U vs. La/Sm, and (e) Zr/Hf vs. Lu for volcanogenic units assigned to the Macusaní Formation and two samples of Quenamari Suite granite. References: (1) Linck (1926); (2) Francis (1953b); (3) Martin and de Sitter-Koomans (1955); (4) Elliott and Moss (1965); (5) Barnes et al. (1970); (6) Noble et al. (1984); (7) Arribas and Figueroa (1985); (8) Valencia and Arroyo (1985); (9) Pichavant et al. (1987); (10) Pichavant et al. (1988b); (11) Poupeau et al. (1992); (12) Craig et al. (2010); (13) Pichavant et al. (2024a). The phenocryst-hosted glass inclusions in ash-flow tuff are from basal contacts and lower levels of the volcanic sequence in the Huiquiza section. The compositional field shown for macusanite represents 95 % of data available in literature in order to exclude far outliers.

Both theoretical models—fractional crystallization and simultaneous assimilation and fractional crystallization (AFC)—yield nearly identical geochemical evolution trends for the most compatible elements (Figs. 26-27). However, the crystal fractionation model is unable to account for the early enrichment in incompatible elements observed in the Lithium-rich Tuff parental magmas, which is in part explained by the AFC model (Fig. 25). Nevertheless, the AFC model underestimates the measured incompatible element contents at plausible fractional crystallization degrees, indicating the necessity of an additional mechanism to elucidate the extreme enrichment in Li, Be, Rb, Nb, and Ta in the Lithium-rich Tuff.

Fluid-mobile metals are highly enriched in the magmatic-hydrothermal transition due to their high incompatibility during magmatic differentiation involving ligand-rich H₂O-dominated fluids, either in the liquid, gas/vapor, or supercritical state (London et al. 1988; Thomas and Davidson 2012; Iveson et al. 2019). Fluids enhance the capacity to transport heavy metals, including some HFSE (Nb, Ta), LILE (Rb), and other incompatible lithophile elements such as Li and Be through molecular complexation with ligands such as B, F, and Cl (Brenan et al. 1998). These ligands are volatile and behave as incompatible elements during magmatic differentiation. However, they also act as fluxing elements and melt network modifiers (London and Morgan 2017), reducing the magma solidus and viscosity and promoting its concentration in the apical region of the magma reservoir (Webster and Duffield 1994).

All Lithium-rich Tuff samples with LOI < 2.7 wt.% have similar MnO, Na₂O, P₂O₅, Li, B, Rb, Ta, and F (Figs. 24-25) suggesting that the enrichment in these elements was not related to the alteration process associated with the formation of secondary clays and zeolites (see below). The fact that the whole-rock Rb-Sr isochron age on Lithium-rich Tuff (Fig. 31b) yields virtually the same age as the one obtained by ⁴⁰Ar/³⁹Ar dating of mica from the same rocks is compatible with either a metasomatic enrichment in a pre-eruptive stage of the magma (Ballouard et al. 2016) or a post-depositional deuteric alteration occurring in close temporal proximity to the eruptive event (Gifkins et al. 2005). Through quantitative X-ray images and Raman spectra on micas in the Lithium-rich Tuff, Torr o et al. (2023) revealed subhedral mica crystal clasts characterized by zinnwaldite cores and lepidolite rims. The lepidolite rims exhibited higher F and Rb and lower Ti contents than the cores. Such overgrowth textures have also been reported in rare metal-rich leucogranites (e.g., Monier et al. 1987; F orster et al. 1999) and LCT pegmatites (e.g., Anderson et al. 2013; Kaeter et al. 2018). In these systems, lepidolite is most commonly interpreted to be metasomatically superimposed over early magmatic phases (Charoy et al. 1995; Charoy and Noronha 1996). Examples include the late strong enrichment in Cs and Rb at the margins of primary (i.e., magmatic) muscovite in the Moose II LCT pegmatite, in Canada (Anderson et al. 2013). Additionally, lepidolite rims over resorbed primary phengite in the Argemela microgranite have been described by Charoy and Noronha (1996) as forming during a late stage in the crystallization sequence. Furthermore, metasomatic zinnwaldite in autometasomatized zones

from the rare metal-rich Erzgebirge granites exhibits elevated contents of P, F, Li, Rb, Cs, Ba, and Sr in comparison to the late magmatic protolithionite-zinnwaldite (Förster et al. 1999). In such instance, rocks that have undergone significant metasomatism can yield contents of Cs and Li twice as high as the magmatic protolith (Förster et al. 1999). The fact that all lithium-ore units from Falchani also deviate from the magmatic trends toward higher Rb, F, and Li contents (Fig. 25a-f) is consistent with the hypothesis of secondary, metasomatic element mobility. The orthomagmatic hydrothermal fluids that are involved in these reactions are typically described as reduced, acidic, and F-rich (Charoy and Noronha 1996; Förster et al. 1999; Anderson et al. 2013).

The post-magmatic hydrothermal alteration of rare metal-rich granites has been extensively reviewed in the literature (Ballouard et al. 2020). However, the metasomatism that occurs in the presence of crystals, melt, and aqueous fluids during the late magmatic stages remains poorly understood (Thomas and Davidson 2016; Kaeter et al. 2018; Linnen et al. 2019; McNeil et al. 2020; Rusak et al. 2021; Ellis et al. 2022; Dupont de Dinechin 2023). Melt inclusion studies have revealed instances where Li can yield exceedingly high concentrations in evolved melts prior to eruption, yet without showing linear correlation with other incompatible elements such as Rb (Ellis et al. 2022). Experimental studies with rare metal-rich granitic melts have demonstrated that HFSE minerals (e.g., columbite-tantalite, pyrochlore group minerals, zircon, eudialyte) can crystallize from fluid-melt interaction as euhedral crystals, texturally indistinguishable from other phenocrysts crystallized previously during purely magmatic stages (Linnen et al. 2019; McNeil et al. 2020). A combined petrographic and high-resolution geochemical analysis of the magmatic–hydrothermal transition in rare-element pegmatites from southeast Ireland has evidenced that immiscible polymerized silicic and depolymerized alkaline aqueous melts can coexist (Kaeter et al. 2018). As defined by Thomas et al. (2000) and Thomas and Davidson (2012a, 2016), both represent conjugate melt pairs resulting from melt–melt immiscibility along a pseudo-binary solvus boundary in the silicate melt–H₂O system. The presence of two immiscible endmembers has been reported in melt inclusion studies, not only in pegmatites but also in both normal and highly evolved granites (Thomas and Davidson 2012, 2013) and in experiments with Li-, F-, H₂O-rich, felsic, silicic melts (Rusak et al. 2021). This implies that this phenomenon is likely to operate in most magmatic chambers provided there is sufficient

abundance of volatiles and fluxing elements (Thomas and Davidson 2016). The volatile-rich member, referred to as fluid/melt by these authors, shows viscosities that are sufficiently low to facilitate its escape from a crystal mush, while scavenging incompatible rare metals on its way up.

The analyses of Lithium-rich Tuff plot in the LCT pegmatite field in the Mg/Li vs. La/Ta diagram (Fig. 35). The strong association of Li with LCT pegmatites is explained by the crystallization of late-stage, volatile-rich liquids sourced from granitic igneous bodies, regardless of the timing and mechanism of extraction of pegmatitic liquids from their source (Troch et al. 2021 and references therein). Theoretical models by Troch et al. (2022) indicate that the additional input of magmatic volatile phases into the top of a magmatic chamber can result in concentrations of fluid-mobile trace elements in the melt that are up to 10 times greater than what would be expected for either closed-system equilibrium or crystal fractionation in magmas. Recent models of mush-dominated magma reservoirs (Parmigiani et al. 2016, 2017; Degruyter et al. 2019) commonly anticipate the presence of an exsolved magmatic volatile phase, which is pivotal in governing differentiation processes and, in certain instances, the explosivity of magmatic systems (Cassidy et al. 2018; Townsend et al. 2019). As proposed by Troch et al. (2022), a 40-70 % of crystallization in the crystal-mush allows for the following processes: i) degasification from deeper more fractionated and compacted horizons of a crystal mush body; ii) rapid upward migration of volatile-rich fluids without experiencing significant fluid/melt equilibrium before reaching the top; and iii) fluid/melt equilibrium in the accumulation zone at the top of the magma chamber/granite cupola, which explain the anomalous enrichment in elements with low crystal/melt and fluid/melt partition coefficients (e.g., Li, F, B, Cl; Troch et al. 2022; Fig. 36). This hypothesis posits a link between the origin of the lepidolite in the Lithium-rich Tuff and an abrupt enrichment in volatile and incompatible elements during the crystal-melt-fluid interaction at the end of the pre-eruptive magma storage, when the magmatic vapor phase reached their maximum abundance relative to the residual melt before the explosive eruption (Kaeter et al. 2018; Linnen et al. 2019; McNeil et al. 2020).

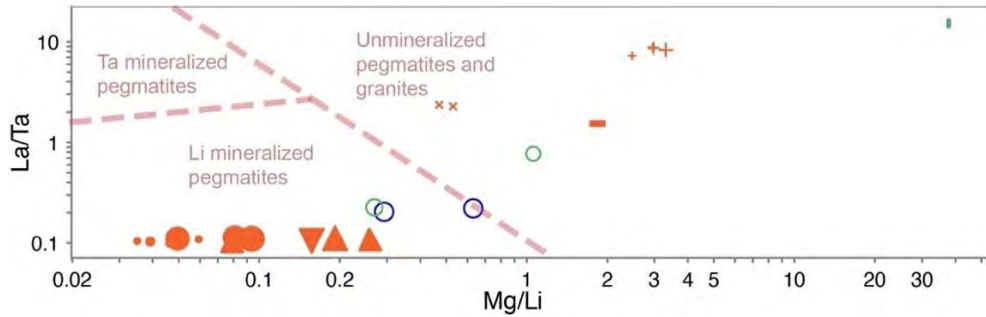


Figure 35. Geochemical data of analyzed samples from the Macusani Volcanic Field plotted on the Mg/Li vs La/Ta diagram. Pegmatite compositional fields are after [Shaw et al. \(2022\)](#). Symbology as in [Figure 15](#).

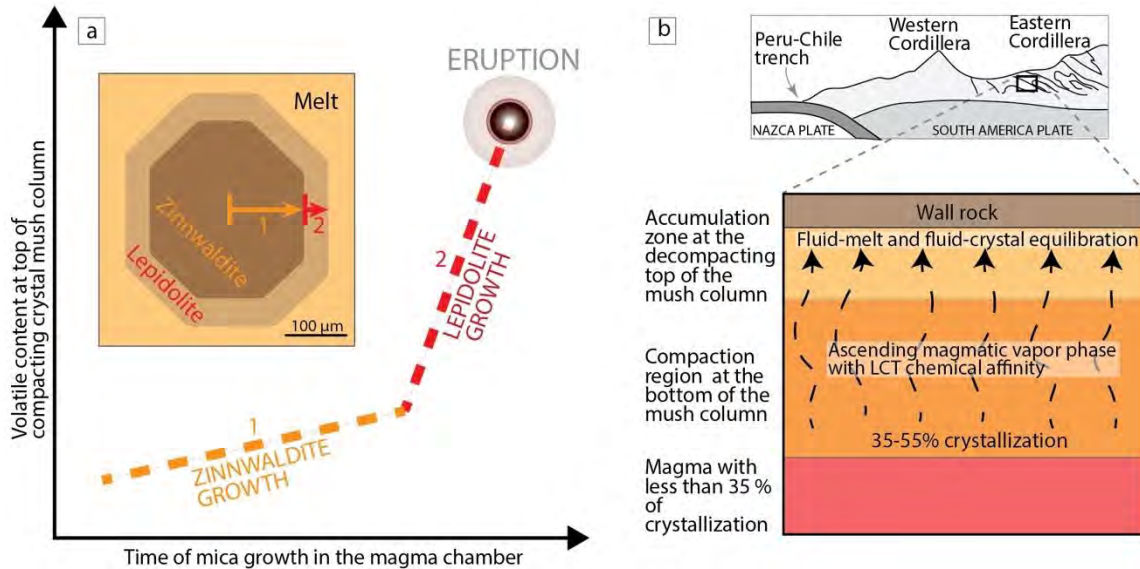


Figure 36. Simplified genetic model for lithium micas in the Lithium-rich Tuff. (a) Schematic diagram that explains the magmatic growth of zinnwaldite and lepidolite crystal clasts found in the Lithium-rich Tuff based on a change in the volatile contents at the top of a compacting crystal mush prior to pyroclastic eruption. (b) Geotectonic context and integrated view of a compacting crystal mush column in the upper crust. The generation of a magmatic vapor phase in the crystal mush column is simulated by [Troch et al. \(2022\)](#) with TheDUDE (Theoretical Determination of Upward Disequilibrium Enrichment) model.

Further secondary element mobility probably occurred in the lithium-ore units subsequent to their deposition. The observed coupled depletion in alkalis (K_2O+Na_2O) and SiO_2 ([Fig. 15a-i](#)) and enrichment in Al_2O_3 and CaO ([Figs. 24a, f](#)) in Lithium-rich Tuff and Upper and Lower Breccia connect the compositions of kaolinite-rich and smectite-rich samples ([Figs. 37, 38a-b](#); [Segovia-More et al. 2023](#)) and are consistent with alkali and silica leaching during feldspar hydrolysis and smectite/zeolite formation under alkaline pH conditions. A higher LOI and CaO content accords well with a predominance of Ca-smectite in the most pervasively altered samples ([Fig. 37](#)). Finally, the strong positive correlation between Sr and Cs ($r = 0.99$) and the distinctively high contents of these two elements in the

sample 2021-MAC-053 (Fig. 37) are consistent with Cs^+ and Sr^{2+} being selectively sorbed onto zeolites such as mordenite as reported by Segovia-More et al. (2023).

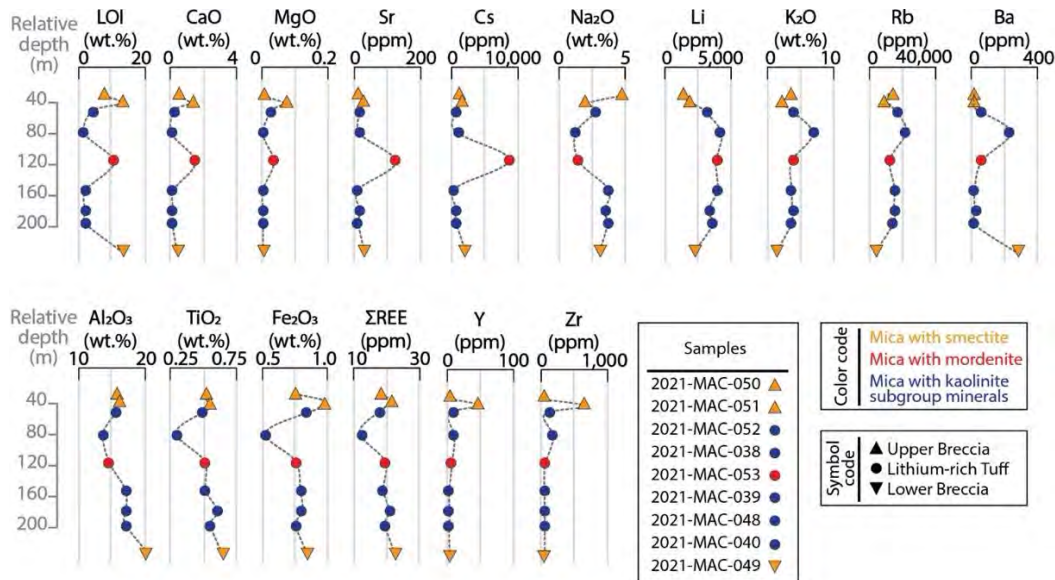


Figure 37. Compositional vertical profiles of lithium-ore units from Falchani sorted by depth in drill holes. The mineralogy is according to Segovia-More et al. (2023).

Li (2016) also documented the occurrence of widespread argillic alteration in ash-flow tuff from the eastern sector of the Macusani Volcanic Field characterized by the crystallization of Ca-smectite and illite, the latter of which exhibits exceptionally high F contents (7.8-8.7 wt.%). The authors report the local occurrence of advanced argillic alteration to kaolinite and quartz restricted to the stratigraphic contact between the Chacacuniza and Yapamayo members (Li 2016). The leaching of REE coupled with an increase in $(\text{Ce}/\text{Ce}^*)_{\text{CN}}$ in the argillized tuff compared to fresh tuff (Fig. 38a) has been interpreted by Li (2006) as the result of an interaction of the rocks with oxidating fluids during post-magmatic, low-temperature alteration. This would not have been the case for the lithium-ore units in Falchani, as REE were apparently relatively immobile during alteration (cf. Section 5.2) and kaolinite is the main alteration product in smectite-poor samples (Fig. 37a).

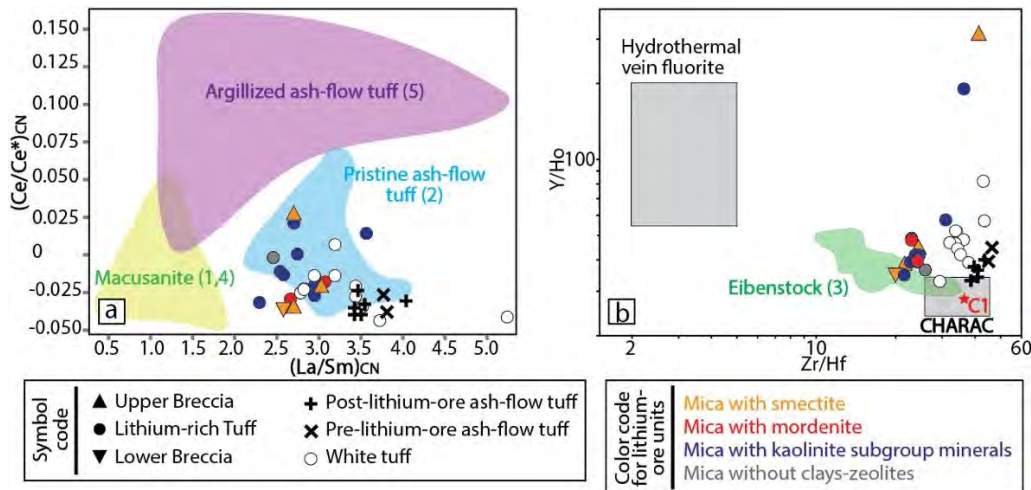


Figure 38. Bivariate plots including (a) $(La/Sm)_{CN}$ vs. $(Ce/Ce^*)_{CN}$ and (b) Zr/Hf vs. Y/Ho . $(Ce/Ce^*)_{CN} = \log(5Ce^*/(4La^* + Sm^*))$ calculated following [Wilde et al. \(1995\)](#). Chondrite C1 values are after [Sun and McDonough \(1989\)](#). The CHARAC and hydrothermal vein fluorite compositional fields are adapted from [Bau \(1996\)](#). References: (1) [Pichavant et al. \(1987\)](#); (2) [Pichavant et al. \(1988b\)](#); (3) [Bau \(1996\)](#); (4) [MacDonald et al. \(1992\)](#); (5) [Li \(2006\)](#).

In the Y/Ho vs Zr/Hf diagram, the majority of the datapoints plot in a narrow area outside the CHARAC (i.e., CHArge-and-RADius-Controlled; [Bau 1996](#)) field and display similar compositions as the autometasomatized topaz-zinnwaldite, alkali-feldspar Eibenstock granite in Germany ([Fig. 38b](#)). The non-CHARAC geochemical fractionation observed in the lithium-ore units suggests sub-solidus metasomatic reactions with fluids enriched in a variety of ligands (e.g., F, B), which leads to fractionation between geochemical twin pairs—i.e., isoivalent with similar radii—due to selective molecular complexation ([Bau 1996](#)). For example, Zr/Hf ratios below ~ 25 in peraluminous granites are interpreted to reflect sub-solidus hydrothermal alteration by F-rich, acidic, reduced fluids of magmatic origin ([Ballouard et al. 2016](#)). Furthermore, alkaline fluids yield high Zr/Hf and very high Y/Ho ratios due to selective adsorption onto the surface of authigenic Fe-, Al-oxyhydroxides. This indicates that the first alteration stage by F-rich, acidic, and reduced fluids that affected all lithium-ore units was followed by a second alteration stage that produced smectite and zeolite alteration under neutral or alkaline pH conditions. Alkaline hydrothermal fluids, with pH values up to 9, and temperatures around $250^\circ C$, have been extensively documented in active geothermal areas, including the Yellowstone National Park in the U.S.A ([White 1957](#); [Buil et al. 2006](#); [Wang et al. 2019](#); [Jiménez et al. 2022](#); [Morgan et al. 2023](#)). The pervasive alteration to smectite and zeolite in Falchani is largely confined to the Upper and Lower Breccia, indicating that fluid-rock metasomatic processes with higher water/rock ratios were

enhanced along the most permeable levels. In contrast, the Lithium-rich Tuff, which is very fine-grained and cohesive, is likely to have precluded the efficient circulation of fluids.

6. CONCLUSIONS

The composition of Lithium-rich Tuff samples from the Macusani Volcanic Field indicates derivation from a strongly peraluminous rhyolitic magma, which is equivalent to some rare metal-rich, muscovite-bearing, peraluminous granites and LCT pegmatites. The incompatible trace element compositions and CN REY patterns of Lithium-rich Tuff samples are more similar to those of macusanite than to previously reported ash-flow tuff from the Macusani Volcanic Field. This suggests a higher proportion of highly evolved volcanogenic material, probably involving macusanite-like glass prior to its alteration.

Simple mixing models based on Nd-Sr isotope ratios indicate that the parental magma of the Lithium-rich Tuff contained a ~15-30% of mantle contribution with the isotope signature of late Miocene K-UK mafic melts in the Peruvian Altiplano-Eastern Cordillera, and ~70-85% of Proterozoic and Paleozoic paragneiss and metapelite contribution. The felsic nature of the Macusani Formation rocks can be explained because of a higher crustal component compared to other late Miocene ignimbrite fields in the Neogene Ignimbrite Province of the Central Andes.

Crystal fractionation alone is insufficient to explain the initial enrichment of incompatible elements in the Lithium-rich Tuff parental magmas, a gap partly addressed by AFC processes. Furthermore, the extreme enrichment in incompatible lithophile elements in the Lithium-rich Tuff, including lithium, appears to be linked to pre-eruptive metasomatic processes involving fluids exsolved from a volatile-rich, highly fractionated, crystal-rich magmatic reservoir rather than during post-eruptive alteration processes forming secondary mineral assemblages of clays and zeolites.

7. REFERENCES

Aagaard P, Helgeson HC (1983) Activity/composition relations among silicates and aqueous solutions: II. Chemical and thermodynamic consequences of ideal mixing of atoms on homological sites in montmorillonites, illites, and mixed-layer clays. *Clays Clay Miner* 31(3):207-217. <https://doi.org/10.1346/CCMN.1983.0310306>

- Acker JG, Bricker OP (1992) The influence of pH on biotite dissolution and alteration kinetics at low temperature. *Geochim Cosmochim Acta* 56(8):3073–3092. [https://doi.org/10.1016/0016-7037\(92\)90290-Y](https://doi.org/10.1016/0016-7037(92)90290-Y)
- American Lithium (2021) Falchani Lithium Project, Peru. <https://americanlithiumcorp.com/falchani-lithium-project>). Accessed 11 Dec. 2023
- American Lithium (2022) American Lithium validates Sulfate of Potash as a strategic by-product of future lithium production at Falchani. <https://americanlithiumcorp.com/american-lithium-validates-sulfate-of-potash-as-a-strategic-by-product-of-future-lithium-production-at-falchani/>. Accessed 10 July 2022
- Anderson MO, Lentz DR, McFarlane CRM, Falck H (2013) A geological, geochemical and textural study of an LCT pegmatite: Implications for the magmatic versus metasomatic origin of Nb-Ta mineralization in the Moose II pegmatite, Northwest Territories, Canada. *J Geosci* 58:299–320. <https://doi.org/10.3190/jgeosci.149>
- Arroyo GP (2021) Distrito uranífero de Macusani: modelo de mineralización usando isótopos estables. ProEXPLO2021
- Armijo R, Lacassin R, Coudurier-Curveur A, Carrizo D (2015) Coupled tectonic evolution of Andean orogeny and global climate. *Earth Sci Rev* 143:1-35. <https://doi.org/10.1016/j.earscirev.2015.01.005>
- Arribas A, Figueroa E (1985a) Las mineralizaciones de uranio en las rocas volcánicas de Macusani, Puno (Perú). *Estudios geológicos* 41:323–342. <https://doi.org/10.3989/egeol.85415-6714>
- Arribas A, Figueroa E (1985b) Geología y metalogenia de las mineralizaciones uraníferas de Macusani, Puno (Perú). IAEA-TC-490/14:237-254
- Asch G, Schurr B, Bohm M, Yuan X, Haberland C, Heit B, Kind R, Woelbern I, Bataille K, Comte D, Pardo M, Viramonte J, Rietbrock A, Giese P (2006) Seismological studies of the Central and Southern Andes. In: Oncken O, Chong G, Franz G, Giese P, Götze H-J, Ramos VA, Strecker MR, Wigger P (eds) *The Andes – active subduction orogeny,*

1st edn. Springer Berlin, Heidelberg, pp 443–458. <https://doi.org/10.1007/978-3-540-48684-8>

Asta MP, Gimeno MJ, Auqué LF, Galve JP, Gómez J, Acero P, Lapuente P (2017) Temporal variability of secondary processes in alkaline geothermal waters associated to granitic rocks: The Caldes de Boí geothermal system (Spain). *Geol Acta* 15(2):67-87. <https://doi.org/10.1344/GeologicaActa2017.15.2.1>

Audebaud E (1973) Geología de los cuadrángulos de Ocongate y Sicuani. Instituto Geológico Minero y Metalúrgico, Boletín 25, 72 pp

Azevedo M, Baczyńska M, Hoffman K, Krauze A (2022) Lithium mining: How new production technologies could fuel the global EV revolution. McKinsey & Company, 10 pp

Baby P, Rochat P, Mascle G, Hérail G (1997) Neogene shortening contribution to crustal thickening in the back arc of the Central Andes. *Geology* 25(10):883–886. [https://doi.org/10.1130/0091-7613\(1997\)025<0883:NSCTCT>2.3.CO;2](https://doi.org/10.1130/0091-7613(1997)025<0883:NSCTCT>2.3.CO;2)

Baby P, Calderón Y, Hurtado C, Louterbach M, Espurt N, Brusset S, Roddaz M, Brichau S, Eude A, Calvès G (2018) The Peruvian sub-andean foreland basin system: structural overview, geochronologic constraints, and unexplored plays. In: Zamora G, McClay KR, Ramos VA (eds) *Petroleum Basins and Hydrocarbon Potential of the Andes of Peru and Bolivia*. AAPG Special Volumes 117:87–116. <https://doi.org/10.1306/13622118M1173767>

Báez S, Cuesta F, Cáceres Y, Arnillas CA, Vásquez R (2011) Síntesis del conocimiento de los efectos del Cambio Climático en la biodiversidad de los Andes Tropicales. Consorcio para el Desarrollo Sostenible de la Ecorregión Andina, Lima-Quito, 49 pp

Bagheri M, Lothenbach B, Shakoorioskooie M, Scrivener K (2022a) Effect of different ions on dissolution rates of silica and feldspars at high pH. *Cem Concr Res* 152:106644. <https://doi.org/10.1016/j.cemconres.2021.106644>.

- Bagheri M, Lothenbach B, Shakoorioskooie M, Scrivener K (2022b) Corrigendum to “Effect of different ions on dissolution rates of silica and feldspars at high pH”. *Cem Concr Res* 160:106928. <https://doi.org/10.1016/j.cemconres.2022.106928>
- Bahlburg H, Carlotto V, Cárdenas J (2006) Evidence of Early to Middle Ordovician arc volcanism in the Cordillera Oriental and Altiplano of southern Peru, Ollantaytambo Formation and Umachiri beds. *J South Am Earth Sci* 22(1-2):52–65. <https://doi.org/10.1016/j.jsames.2006.09.001>
- Baker MCW (1981) The nature and distribution of upper Cenozoic ignimbrite centres in the Central Andes. *J Volcanol Geotherm Res* 11(2-4):29–315. [https://doi.org/10.1016/0377-0273\(81\)90028-7](https://doi.org/10.1016/0377-0273(81)90028-7)
- Ballouard C, Poujol M, Boulvais P, Branquet Y, Tartèse R, Vignerresse JL (2016) Nb-Ta fractionation in peraluminous granites: A marker of the magmatic-hydrothermal transition. *Geology* 44(3):231–234. <https://doi.org/10.1130/G37475.1>
- Ballouard C, Massuyeau M, Elburg M, Tappe S, Viljoen F, Brandenburg J-T (2020) The magmatic and magmatic-hydrothermal evolution of felsic igneous rocks as seen through Nb-Ta geochemical fractionation, with implications for the origins of rare-metal mineralizations 203:103115. <https://doi.org/10.1016/j.earscirev.2020.103115>
- Barbarin B (1996) Genesis of the two main types of peraluminous granitoids. *Geology* 24(4):295–298. [https://doi.org/10.1130/0091-7613\(1996\)024<0295:GOTTMT>2.3.CO;2](https://doi.org/10.1130/0091-7613(1996)024<0295:GOTTMT>2.3.CO;2)
- Barnes VE, Edwards G, Mclaughlin WA, Friedman I, Joensuu O (1970) Macusanite occurrence, age, and composition, Macusani, Peru. *Bull Geol Soc Am* 81(5):1539–1546. [https://doi.org/10.1130/0016-7606\(1970\)81\[1539:MOAACM\]2.0.CO;2](https://doi.org/10.1130/0016-7606(1970)81[1539:MOAACM]2.0.CO;2)
- Bau M (1996) Controls on the fractionation of isovalent trace elements in magmatic and aqueous systems: evidence from Y/Ho, Zr/Hf and lanthanide tetrad effect. *Contrib Mineral Petrol* 123:323–333

- Bauer D, Diamond D, Li J, McKittrick M, Sandalow D, Telleen P (2011) Critical Materials Strategy. US Department of Energy, 196 p
- Baumont D, Paul A, Zandt G, Beck SL, Pedersen B (2002) Lithospheric structure of the central Andes based on surface wave dispersion. *J Geophys Res* 107(B12):ESE 18-1-ESE 18-13
- Beck SL, Zandt G (2002) The nature of orogenic crust in the central Andes. *J Geophys Res Solid Earth* 107(B10):ESE 7-1-ESE 7-16
- Beck SL, Zandt G, Ward KM, Scire A (2015) Multiple styles and scales of lithospheric foundering beneath the Puna Plateau, central Andes. *Memoir Geol Soc Am* 212:43–60. <https://doi.org/10.1130/MEM212>
- Bello-González JP, Contreras-Reyes E, Arriagada C (2018) Predicted path for hotspot tracks off South America since Paleocene times: Tectonic implications of ridge-trench collision along the Andean margin. *Gondwana Res* 64:216–234. <https://doi.org/10.1016/j.j.gr.2018.07.008>
- Benavides Cáceres V (1999) Orogenic evolution of the Peruvian Andes: The Andean cycle. In: Skinner B (ed) *Geology and mineral deposits of Central Andes*, 1st edn. SEG Special Publication 7:61–107. <https://doi.org/10.5382/SP.07.03>
- Benjamin MT, Johnson NM, Naeser CW (1987) Recent rapid uplift in the Bolivian Andes: evidence from fission-track dating. *Geology* 15(7):680–83. [https://doi.org/10.1130/0091-7613\(1987\)15<680:RRUITB>2.0.CO;2](https://doi.org/10.1130/0091-7613(1987)15<680:RRUITB>2.0.CO;2)
- Benson TR, Coble MA, Dilles JH (2023) Hydrothermal enrichment of lithium in intracaldera illite-bearing claystones. *Sci Adv* 9(35):8183. <https://doi.org/10.1126/sciadv.adh8183>
- Benson TR, Coble MA, Rytuba JJ, Mahood GA (2017) Lithium enrichment in intracontinental rhyolite magmas leads to Li deposits in caldera basins. *Nat Commun* 8(1):270. <https://doi.org/10.1038/s41467-017-00234-y>

- Bianchi M, Heit B, Jakovlev A, Yuan X, Kay SM, Sandvol E, Alonso RN, Coira BL, Brown LD, Kind R, Compte D (2013) Teleseismic tomography of the southern Puna plateau in Argentina and adjacent regions. *Tectonophysics* 586:65-83. <https://doi.org/10.1016/j.tecto.2012.11.016>
- Bibienne T, Magnan J-F, Rupp A, Laroche N (2020) From mine to mind and mobiles: Society's increasing dependence on lithium. *Elements* 16(4):265–270. <https://doi.org/10.2138/gselements.16.4.265>
- Bigazzi G, Coltelli M, Hadler JC, Osorio AM (1997) Provenance studies of obsidian artefacts using the fission-track analysis in South America: An overview. 49th Congreso Internacional del Americanistas, Quito, Ecuador
- Boekhout F, Spikings R, Sempere T, Chiaradia M, Ulianov A, Schaltegger U (2012) Mesozoic arc magmatism along the southern Peruvian margin during Gondwana breakup and dispersal. *Lithos* 146–147:48–64. <https://doi.org/10.1016/j.lithos.2012.04.015>
- Boekhout F, Sempere T, Spikings R, Schaltegger U (2013) Late Paleozoic to Jurassic chronostratigraphy of coastal southern Peru: Temporal evolution of sedimentation along an active margin. *J South Am Earth Sci* 47:179-200. <https://doi.org/10.1016/j.jsames.2013.07.003>
- Boekhout F, Roberts N, Gerdes A, Schaltegger U (2015) A Hf-isotope perspective on continent formation in the south Peruvian Andes. *Geol Soc Spec Publ* 238:305-321. <https://doi.org/10.1144/SP389.6>
- Bonhomme MG, Audebaud E, Vivier G (1985b) Edades K-Ar de rocas hercínicas y neógenas de un perfil E-W en el Perú meridional. *Universidad de Chile Comunicaciones* 35:27-30
- Borojević S, Brenko T (2022) The Miocene Western Balkan lithium-boron metallogenic zone. *Miner Depos* 58:639–658. <https://doi.org/10.1007/s00126-022-01151-x>

- Bowell RJ, Lagos L, de los Hoyos CR, Declercq J (2020) Classification and characteristics of natural lithium resources. *Elements* 16(4):259–264. <https://doi.org/10.2138/gselements.16.4.259>
- Brad JP, Botello R, Martinez C, Subieta T (1974) Relations entre tectonique, métamorphisme et mise en place d'un granite éohercynien a deux micas dans la Cordillère Real de Bolivie (Massif de Zongo-Yani). *Cahier ORSTOM Série Géologie* 6:3-18. https://horizon.documentation.ird.fr/exl-doc/pleins_textes/cahiers/geologie/20082.pdf
- Bradley DC, Stillings LL, Jaskula BW, Munk L, McCauley AD (2017a) Critical mineral resources of the United States—Economic and environmental geology and prospects for future supply. US Geological Survey Professional Paper 1802-K:K1–K21, Reston, Virginia. <https://doi.org/10.3133/pp1802K>
- Bradley DC, McCauley AD, Stillings LML (2017b) Mineral-deposit model for lithium-cesium-tantalum pegmatites: US Geological Survey Scientific Investigations Report 2010–5070–O, 48 pp. <https://doi.org/10.3133/sir20105070O>
- Brandmeier (2014) A remote sensing and geospatial statistical approach to understanding distribution and evolution of ignimbrites in the Central Andes with a focus on Southern Peru. Doctoral dissertation, Göttingen University
- Brenan JM, Ryerson FJ, Shaw HF (1998) The role of aqueous fluids in the slab-to-mantle transfer of boron, beryllium, and lithium during subduction: Experiments and models. *Geochim Cosmochim Acta* 62(19):3337–3347. [https://doi.org/10.1016/S0016-7037\(98\)00224-5](https://doi.org/10.1016/S0016-7037(98)00224-5)
- Breiter K, Škoda R, Uher P (2007) Nb–Ta–Ti–W–Sn-oxide minerals as indicators of a peraluminous P- and F-rich granitic system evolution: Podlesí, Czech Republic. *Mineral Petrol* 91:225–248. <https://doi.org/10.1007/s00710-007-0197-1>
- Buford Parks V, McQuarrie N, Falkowski S, Perez N, Ehlers T (2023) Timing and drivers of exhumation and sedimentation in the eastern Peruvian Andes: Insights from

thermokinematic modelling. *Earth Planet Sci Lett* 620:118355.
<https://doi.org/10.1016/j.epsl.2023.118355>

Buil B, Gómez P, Turrero MJ, Garralón A, Lago M, Arranz E, de la Cruz B (2006) Factors that control the geochemical evolution of hydrothermal systems of alkaline water in granites in Central Pyrenees (Spain). *J Iber Geol* 32(2):283-302

Caballero M, Lozano S, Ortega B (2007) Efecto invernadero, calentamiento global y cambio climático: una perspectiva desde las ciencias de la tierra. *Universidad Nacional Autónoma de México* 8(10):12 pp

Calderón Y, Baby P, Hurtado C, Brusset S (2017) Thrust tectonics in the Andean retroforeland basin of northern Peru: Permian inheritances and petroleum implications. *Mar Pet Geol* 82:238–250. <https://doi.org/10.1016/j.marpetgeo.2017.02.009>

Calle A, Horton B, García R, Anderson R, Stockli D, Flaig P, Long S (2023) Sediment dispersal and basin evolution during contrasting tectonic regimes along the western Gondwanan margin in the central Andes. *J South Am Earth Sci* 125:104286. <https://doi.org/10.1016/j.jsames.2023.104286>

Callot P (2008) La Formation Ayabacas (limite Turonien-Coniacien, Sud-Pérou): collapse sous-marin en réponse à l'amorce de l'orogénèse andine. Doctorat thesis, Université de Toulouse, Toulouse, France

Canaza MS (2018) Estilo estructural y evolución tectónica sedimentaria de la faja plegada y corrida, del norte de la cuenca Titicaca, ubicado entre Azángaro y Putina. Undergraduated thesis, Universidad Nacional del Altiplano, Facultad de Ingeniería Geológica y Metalurgia, Escuela Profesional de Ingeniería Geológica, Puno, Peru

Canosa F, Martin-Izard A, Fuertes-Fuente M (2012) Evolved granitic systems as a source of rare-element deposits: The Ponte Segade case (Galicia, NW Spain). *Lithos* 153:165-176. <https://doi.org/10.1016/j.lithos.2012.06.029>.

- Capitanio FA, Faccenna C, Zlotnik S, Stegman DR (2011) Subduction dynamics and the origin of Andean orogeny and the Bolivian orocline. *Nature* 480:83–86. <https://doi.org/10.1038/nature10596>
- Carlier G, Lorand J, Bonhomme M, Carlotto V (1996) A reappraisal of the Cenozoic Inner Arc magmatism in southern Peru: consequences for the evolution of the central Andes for the past 50 Ma. ORSTOM, Third International Symposium on Andean Geodynamics pp 551-554
- Carlier G, Lorand JP, Audebaud E, Kienast JR (1997) Petrology of an unusual orthopyroxene-bearing minette suite from southeastern Peru, Eastern Andean Cordillera: Al-rich lamproites contaminated by peraluminous granites. *J Volcanol Geotherm Res* 75(1-2):59–87. [https://doi.org/10.1016/S0377-0273\(96\)00035-2](https://doi.org/10.1016/S0377-0273(96)00035-2)
- Carlier G, Lorand J-P, Liégeois J-P, Fornari M, Soler P, Carlotto V, Cardenas J (2005) Potassic-ultrapotassic mafic rocks delineate two lithospheric mantle blocks beneath the southern Peruvian Altiplano. *Geology* 33(7):601–604. <https://doi.org/10.1130/G21643.1>
- Carlotto V (1998) Evolution and raccourcissement au niveau de Cusco (13-16°S), Pérou: enregistrement sédimentaire, chronologie, contre les paléogéographiques, évolution cinématique. Doctoral dissertation, University Grenoble I
- Carlotto V (2013) Paleogeographic and tectonic controls on the evolution of Cenozoic basins in the Altiplano and Western Cordillera of southern Peru. *Tectonophysics* 589:195–219. <https://doi.org/10.1016/j.tecto.2013.01.002>
- Cas RF, Wright JV (1988) *Volcanic Successions Modern and Ancient*. Springer Dordrecht, 528 pp. <https://doi.org/10.1007/978-94-009-3167-1>
- Casquet C, Fanning C, Galind C, Pankhurst R, Rapela C, Torres P (2010) The Arequipa massif of Peru: new SHRIMP and isotope constraints on a Paleoproterozoic inlier in the Grenvillian orogen. *J South Am Earth Sci* 29(1):128-142. <https://doi.org/10.1016/j.jsames.2009.08.009>

- Cassidy M, Manga M, Cashman K, Bachmann O (2018) Controls on explosive-effusive volcanic eruption styles. *Nat Commun* 9:2839
- Castor SB, Henry CD (2000) Geology, geochemistry, and origin of volcanic rock-hosted uranium deposits in northwestern Nevada and southeastern Oregon. *Ore Geol Rev* 16(1-2):1–40. [https://doi.org/10.1016/S0169-1368\(99\)00021-9](https://doi.org/10.1016/S0169-1368(99)00021-9)
- Cenki B, Jaillard E, Carlotto V (2000) Estudio petrográfico-geoquímico del volcanismo pre-Huancané de la región de Cusco-Sicuani (Sur del Perú): Interpretación geodinámica. *Sociedad Geológica del Perú, Boletín de la Sociedad Geológica del Perú* 89:45–56. <https://10.7892/boris.86968>
- Cerpa L, Cereceda C, Torres D, Muñoz L, Aguilar R, Martínez J, Siesquen D, Chacón A (2012) Controles tectono-magmáticos en el sur del Perú (72°-70°30' y 14°-16°S): implicancias metalogénicas. XVI Congreso Peruano de Geología, Lima, 23-26 pp
- Charoy B, Chaussidon M, Noronha F (1995) Lithium zonation in white micas from the Argemela body (Central Portugal): An ion-, electron-microprobe and vibrational spectroscopy investigation. *Eur J Mineral* 7:335-352
- Charoy B, Noronha F (1996) Multistage Growth of a rare-element, volatile-rich microgranite at Argemela (Portugal). *J Petrol* 37(1):73-94. <https://doi.org/10.1093/petrology/37.1.73>
- Chávez A, Salas G, Gutiérrez E, Cuadros J (1997) Geología de los cuadrángulos de Corani y Ayapata. Hojas 28-u y 28-v. Instituto Geológico, Minero y Metalúrgico, Boletín 90, 128 pp
- Cheilletz A, Clark AH, Farrar E, Arroyo Pauca G, Pichavant M, Sandeman HA (1992) Volcano-stratigraphy and $^{40}\text{Ar}/^{39}\text{Ar}$ geochronology of the Macusani ignimbrite field: Monitor of the Miocene geodynamic evolution of the Andes of southeast Peru. *Tectonophysics* 205(1-3):307–327. [https://doi.org/10.1016/0040-1951\(92\)90433-7](https://doi.org/10.1016/0040-1951(92)90433-7)
- Chiaradia M, Müntener O, Beate B (2020) Effects of aseismic ridge subduction on the geochemistry of frontal arc magmas. *Earth Planet Sci Lett* 531:115984. <https://doi.org/10.1016/j.epsl.2019.115984>

- Ciesia WM (1995) Cambio climático, bosques y ordenación forestal: Una visión de conjunto. Food & Agriculture Org., 146 pp
- Clark AH, Palma VV, Archibald DA, Farrar E, Mario J, Arenas F, Robertson RC (1983) Occurrence and age of tin mineralization in the Cordillera Oriental, Southern Peru. *Econ Geol* 78(3):514–520. <https://doi.org/10.2113/gsecongeo.78.3.514>
- Clark A, Farrar E, Kontak D, Langridge R, Arenas M, France L, McBride S, Woodman H, Wasteneys H, Sandeman H, Archibald D (1990) Geologic and Geochronologic Constraints on the Metallogenic Evolution of the Andes of Southeastern Peru. *Econ Geol* 85(7):1520-1583
- Clarke S (2023) American Lithium Announces 476% Increase in Measured + Indicated Lithium Resources at Falchani – Adds K, Cs and Rb to Block Model. <https://americanlithiumcorp.com/american-lithium-announces-476-increase-in-measured-indicated-lithium-resources-at-falchani-adds-k-cs-and-rb-to-block-model/>. Accessed 10 December 2023
- Clift PD (2003) Tectonic erosion of the Peruvian forearc, Lima Basin, by subduction and Nazca Ridge collision: *Tectonics* 22(3):1023 pp. <https://doi.org/10.1029/2002TC001386>
- Cóndor J (2019) Litio: Descubren nuevas reservas en yacimiento en Puno. *Gestión*. <https://gestion.pe/economia/empresas/peru-plateau-energy-anuncia-descubrimiento-nueva-area-rica-litio-269047-noticia/> Accessed 2 July 2023
- Craig N, Speakman RJ, Popelka-Filcoff RS, Aldenderfer M, Flores Blanco L, Vega MB, Stanish C (2010) Macusani obsidian from southern Peru: A characterization of its elemental composition with a demonstration of its ancient use. *J Archaeol Sci* 37(3):569–576. <https://doi.org/10.1016/j.jas.2009.10.021>
- Dalmayrac B, Laubacher G, Marocco R (1980) Caractéristiques géologiques et évolution géologique des Andes péruviennes. ORSTOM, Travaux et documents:501 pp

- Debon F, Le Fort P (1983) A chemical-mineralogical classification of common plutonic rocks and associations. *Trans R Soc Edinb Earth Sci* 73(3):135-149. <https://doi.org/10.1017/S0263593300010117>
- Degruyter W, Parmigiani A, Huber C, Bachmann O (2019) How do volatiles escape their shallow magmatic hearth? *Philosophical Transactions. Phil Trans R Soc A* 377:20180017. <https://doi.org/10.1098/rsta.2018.0017>
- De la Cruz J, López JC, León W, Lara M (1996) Geología del cuadrángulo de Macusani. Hoja 29-v. Instituto Geológico, Minero y Metalúrgico, Boletín, Serie A: Carta Geológica Nacional 79, 197 pp
- de Silva SL (1989a) The Altiplano–Puna Volcanic Complex of the Central Andes. *Geology* 17(12):1102–1106. [https://doi.org/10.1130/0091-7613\(1989\)017<1102:APVCOT>2.3.CO;2](https://doi.org/10.1130/0091-7613(1989)017<1102:APVCOT>2.3.CO;2)
- de Silva SL (1989b) Geochronology and stratigraphy of the ignimbrites from the 21°30'S to 23°30'S portion of the Central Andes of northern Chile. *J Volcanol Geotherm Res* 37(2):93–131. [https://doi.org/10.1016/0377-0273\(89\)90065-6](https://doi.org/10.1016/0377-0273(89)90065-6)
- de Silva SL, Gosnold WD (2007) Episodic construction of batholiths: Insights from the spatiotemporal development of an ignimbrite flare-up. *J Volcanol Geotherm Res* 167(1-4):320–335. <https://doi.org/10.1016/j.jvolgeores.2007.07.015>
- de Silva SL, Kay SM (2018) Turning up the heat: high-flux magmatism in the Central Andes. *Elements* 14(4):245-250. <https://doi.org/10.2138/gselements.14.4.245>
- de Silva SL, Zandt G, Trumbull R, Viramonte J, Salas G, Jiménez N (2006) Large ignimbrite eruptions and volcanotectonic depressions in the Central Andes: A thermomechanical perspective. In: de Natale G, Troise C, Kilburn C (eds) *Mechanisms of Activity and Unrests at Large Calderas*. *Geol Soc Spec Publ* 269: 47–63
- Demouy S, Paquette J-L, de Saint Blanquet M, Benoit M, Belousova EA, O'Reilly SY, García F, Tejada LC, Gallegos R, Sempere T (2012) Spatial and temporal evolution of Liassic

to Paleocene arc activity in southern Peru unraveled by zircon U-Pb and Hf in-situ data on plutonic rocks. *Lithos* 155:183-200. <https://doi.org/10.1016/j.lithos.2012.09.001>

DePaolo D (1981a) Trace element and isotopic effects of combined wallrock assimilation and fractional crystallization. *Earth Planet Sci Lett* 53(2):189-202

DePaolo D (1981b) A Neodymium and Strontium Isotopic Study of the Mesozoic Calc-Alkaline Granitic Batholiths of the Sierra Nevada and Peninsular Ranges, California. *J Geophys Res* 86(B11):10470-10488. <https://doi.org/10.1029/JB086iB11p10470>

DIGIS Team (2023) GEOROC Compilation Convergent Margins. <https://doi.org/10.25625/PVFZCE>

Donnelly K, Goldstein S, Langmuir C, Spiegelman M (2004) Origin of enriched ocean ridge basalts and implications for mantle dynamics. *Earth Planet Sci Lett* 226(3-4):347-366. <https://doi.org/10.1016/j.epsl.2004.07.019>

Dorbath C, Granet M, Poupinet G, Martinez C (1993) A teleseismic study of the Altiplano and the Eastern Cordillera in northern Bolivia: New constraints on a lithospheric model. *J Geophys Res* 98(B6):9825–9844

Dostal J, Chatterjee AK (2000) Contrasting behaviour of Nb/Ta and Zr/Hf ratios in a peraluminous granitic pluton (Nova Scotia, Canada). *Chem Geol* 163:207–218. [https://doi.org/10.1016/S0009-2541\(99\)00113-8](https://doi.org/10.1016/S0009-2541(99)00113-8)

Dupont de Dinechin M, Balcone-Boissard H, Martel C, Rusiecka M (2023) Lithium in felsic magmas: A volcanological perspective. *Front Earth Sci* 11:1149020. <https://doi.org/10.3389/feart.2023.1149020>.

Elger K, Oncken O, Glodny J (2005) Plateau-style accumulation of deformation: Southern Altiplano. *Tectonics* 24(4):TC4020. <https://doi.org/10.1029/2004TC001675>

Ellis BS, Neukampf J, Bachmann O, Harris C, Forni F, Magna T, Laurent O, Ulmer P (2022) Biotite as a recorder of an exsolved Li-rich volatile phase in upper-crustal silicic magma reservoirs. *Geology* 50(4):481–485. <https://doi.org/10.1130/G49484.1>

- Elliott J, Moss A (1965) Natural glass from Macusani, Peru. *Mineral Mag* 35(270):423–424. <https://doi.org/10.1180/minmag.1965.035.270.18>
- Engi M (2017) Petrochronology based on REE-minerals: Monazite, allanite, xenotime, apatite. *Rev Mineral Geochem* 83(1):365–418. <https://doi.org/10.2138/rmg.2017.83.12>
- European Commission (2020) Study on the EU's list of Critical Raw Materials. European Commission, Brussels, Belgium, 158 p
- Eude A, Roddaz M, Brichau S, Brusset S, Calderon Y, Baby P, Soula JC (2015) Controls on timing of exhumation and deformation in the northern Peruvian eastern Andean wedge as inferred from low-temperature thermochronology and balanced cross section. *Tectonics* 34(4):715–730. <https://doi.org/10.1002/2014TC003641>
- Evans K (2014) Lithium. In: Gunn G (ed) *Critical Metals Handbook*, John Wiley and Sons, Nottingham. <https://doi.org/10.1002/9781118755341.ch10>
- Fabre C, Maurice S, Cousin A, Wiens RC, Forni O, Sautter V, Guillaume D (2011) Onboard calibration igneous targets for the Mars Science Laboratory Curiosity rover and the Chemistry Camera laser induced breakdown. *Spectrochim Acta Part B At Spectrosc* 66(3-4):280-289. <https://doi.org/10.1016/j.sab.2011.03.012>
- Farina F, Dini A, Rocchi S, Stevens G (2014) Extreme mineralscale Sr isotope heterogeneity in granites by disequilibrium melting of the crust. *Earth Planet Sc Lett* 399:103–115. <https://doi.org/10.1016/j.epsl.2014.05.018>
- Farrar E, Clark AH, Kontak DJ, Archibald DA (1988) Zongo-San Gaban zone: Eocene foreland boundary of the Central Andean orogen, northwest Bolivia and southeast Peru. *Geology* 16(1):55-58. [https://doi.org/10.1130/0091-7613\(1988\)016<0055:ZSGNZE>2.3.CO;2](https://doi.org/10.1130/0091-7613(1988)016<0055:ZSGNZE>2.3.CO;2)
- Faure G, Mensing TM (2005) *Isotopes: principles and applications*, 3rd edn. Wiley & Sons, Hoboken, pp 873

- Förster H-J, Tischendorf G, Trumbull RB, Gottesmann B (1999) Late-Collisional Granites in the Variscan Erzgebirge, Germany. *J Petrol* 40(11):1613–1645. <https://doi.org/10.1093/petroj/40.11.1613>
- Francis GA (1956) La Geología de la zona entre Macusani y Ollachea, Departamento de Puno. Instituto Nacional de Investigaciones y Fomento Minero, Boletín 15:5-10
- Francis GH (1959a) El Nevado de Quenamari en la Cordillera Oriental del sur del Perú: Instituto Nacional de Investigaciones y Fomento Minero, Boletín 21:5-10
- Francis GH (1959b) Ignimbritas (sillar) de la Cordillera Oriental del sur del Perú: Instituto Nacional de Investigaciones y Fomento Minero, Boletín 21:13-32
- French BM, Meyer HOA (1970) Andalusite and " β -quartz" in Macusani glass, Peru. *Carnegie Inst. Wash. Year Book* 68:339-342
- French BM, Jezek PA, Appleman DE (1978) Virgilite: A new lithium aluminum silicate mineral from the Macusani glass, Peru. *Am Min* 63(5-6):461–465
- Freytmuth H, Brandmeier M, Wörner G (2015) The origin and crust/mantle mass balance of Central Andean ignimbrite magmatism constrained by oxygen and strontium isotopes and erupted volumes. *Contrib Mineral Petrol* 169, 58 pp. <https://doi.org/10.1007/s00410-015-1152-5>
- Fleischer RL, Price PB (1964). Fission track evidence for the simultaneous origin of tektites and other natural glasses. *Geochim Cosmochim Acta* 28(6):755-756. [https://doi.org/10.1016/0016-7037\(64\)90029-8](https://doi.org/10.1016/0016-7037(64)90029-8)
- Fleischer RL, Price PB, Walker RM (1965) Tracks of charged particles in solids. *Science* 149(3682):383–393. <https://doi.org/10.1126/science.149.3682.3>
- Fuchsloch WC (2018) Pegmatites of the Cape Cross-Uis pegmatite belt, Namibia: Structural, mineralogical, geochemical and mineral chemical characterisation with implications for petrogenesis and mineralisation. Thesis, University of the Witwatersrand, 287 pp

- Garapić G, Jackson MG, Hauri EH, Hart SR, Farley KA, Blusztajn JS, Woodhead JD (2015) A radiogenic isotopic (He-Sr-Nd-Pb-Os) study of lavas from the Pitcairn hotspot: Implications for the origin of EM-1 (enriched mantle 1). *Lithos* 228:1–11. <https://doi.org/10.1016/j.lithos.2015.04.010>
- Garcia D, Fonteilles M, Moutte J (1994) Sedimentary fractionations between Al, Ti, and Zr and the genesis of strongly peraluminous granites. *J Geol* 102(4):411–422
- Gardeweg PM, Ramirez CF (1987) The La Pacana Caldera and the Atana ignimbrite: A major ash-flow and resurgent caldera complex in the Andes of northern Chile. *Bull Volcanol* 49:547-566
- Garzzone CN, McQuarrie N, Perez N, Ehlers T, Beck S, Kar N, Eichelberger N, Chapman A, Ward K, Ducea M, Lease R, Poulsen C, Wagner L, Saylor J, Zandt G, Horton B (2017) Tectonic evolution of the central Andean plateau and implications for the growth of plateaus. *Annu Rev Earth Planet Sci* 45:529–559. <https://doi.org/10.1146/annurev-earth-063016-020612>
- Gemrich L, Torró L, Melgarejo JC, Laurent O, Vallance J, Chelle-Michou C, Sempere TPA (2021) Trace element composition and U-Pb ages of cassiterite from the Bolivian tin belt. *Miner Deposita* 56:1491-1520. <https://doi.org/10.1007/s00126-020-01030-3>
- Gestión (2018) ¿Cómo se descubrió en Perú el yacimiento de litio que podría convertirse en el más grande del mundo? *Gestión*. <https://gestion.pe/peru/descubrio-peru-yacimiento-litio-convertirse-grande-mundo-238710-noticia/?ref=gesr>. Accessed 2 July 2023
- Gestión (2020) Plateau Energy Metals recauda US\$ 600 millones para producir litio en Perú, con retraso por pandemia. *Gestión*. <https://gestion.pe/economia/plateau-energy-metals-recauda-us-600-millones-para-producir-litio-en-peru-con-retraso-por-pandemia-nndc-noticia/>. Accessed 2 July 2023
- Gifkins CC, Herrmann W, Large RR (2005) *Altered volcanic rocks: a guide to description and interpretation*. University of Tasmania

- Gillis R, Horton B, Grove M (2006) Thermochronology, geochronology, and upper crustal structure of the Cordillera Real: Implications for Cenozoic exhumation of the central Andean plateau. *Tectonics* 25(6):TC6007
- Göğüş OH, Sundell K, Uluocak ES, Saylor J, Çetiner U (2022) Rapid Surface Uplift and Crustal Flow in the Central Andes (Southern Peru) Controlled by Lithospheric Drip Dynamics. *Sci Rep* 12:5500. <https://doi.org/10.1038/s41598-022-08629-8>
- Goldstein SL, O'Nions RK, Hamilton PJ (1984) A Sm-Nd study of atmospheric dusts and particulates from major river systems. *Earth Planet Sci Lett* 70(2):221-236. [https://doi.org/10.1016/0012-821X\(84\)90007-4](https://doi.org/10.1016/0012-821X(84)90007-4)
- Goss AR, Kay SM, Mpodozis C (2013) Andean adakites-like highMg andesites on the northern margin of the Chilean-Pampean flat-slab (27-28.5°S) associated with frontal arc migration and forearc subduction erosion. *J Petrol* 54(11):2193-2234. <https://doi.org/10.1093/petrology/egt044>
- Guillong M, Meier DL, Allan MM, Heinrich CA, Yardley BW (2008) Appendix A6: SILLS: a MATLAB-based program for the reduction of laser ablation ICP-MS data of homogeneous materials and inclusions. *Mineralogical Association of Canada Short Course* 40:328–333.
- Guillot S, Le Fort P (1995) Geochemical constraints on the bimodal origin of High Himalayan leucogranites. *Lithos* 35:221–234
- Hammouda T, Pichavant M, Chaussidon M (1996) Isotopic equilibration during partial melting: an experimental test of the behaviour of Sr. *Earth Planet Sci Lett* 144(1-2):109–121. [https://doi.org/10.1016/0012-821X\(96\)00144-6](https://doi.org/10.1016/0012-821X(96)00144-6)
- Harlaux M, Kouzmanov K, Gialli S, Clark AH, Laurent O, Corthay G, Prado Flores E, Dini A, Chauvet A, Ulianov A, Chiaradia M, Menzies A, Villón Durand G, Kalinaj M, Fontboté L (2021) The Upper Oligocene San Rafael intrusive complex (Eastern Cordillera, southeast Peru), host of the largest-known high-grade tin deposit. *Lithos* 400-401:106409. <https://doi.org/10.1016/j.lithos.2021.106409>

- Heide F (1936) Neue kristallführende Gläser von Macusani in Peru. *Sci Nat* 24:281–282
- Heit B, Bianchi M, Yuan X, Kay SM, Sandvol E, Kumar P, Kind R, Alonso RN, Brown LD, Comte D (2014) Structure of the crust and the lithosphere beneath the southern Puna plateau from teleseismic receiver functions. *Earth Planet Sci Lett* 385:1–11. <https://doi.org/10.1016/j.epsl.2013.10.017>
- Hermoza W, Brusset S, Baby P, Gil W, Roddaz M, Guerrero N, Bolaños M (2005) The Huallaga foreland basin evolution: Thrust propagation in a deltaic environment, northern Peruvian Andes. *J South Am Earth Sci* 19(1):21–34. <https://doi.org/10.1016/j.jsames.2004.06.005>
- Hoke L, Lamb S (2007) Cenozoic behind-arc volcanism in the Bolivian Andes, South America: Implications for mantle melt generation and lithospheric structure. *J Geol Soc Lond* 164:795–814. <https://doi.org/10.1144/0016-76492006-092>
- Husson L, Sempere T (2003) Thickening the Altiplano crust by gravity-driven crustal channel flow. *Geophys Res Lett* 30(5):1243. <https://doi.org/10.1029/2002GL016877>
- Ibarra F, Prezzi C (2019) The thermo-mechanical state of the Andes in the Altiplano-Puna region: insights from Curie isotherm and effective elastic thickness determination. *Rev Asoc Geol Argent* 76(4):352–362
- Ibarra I, Mamani M, Rodríguez R, Sempere T, Carlotto V, Carlier G (2004) Estratigrafía y tectónica de la parte sur de la cuenca de Ayaviri. *Sociedad Geológica del Peru, Publicación Especial* 5:143–155
- Inguaggiato C, Censi P, Zuddas P, Londono JM, Chacon Z, Alzate D, Brusca L, D'Alessandro W (2015) Geochemistry of REE, Zr and Hf in a wide range of pH and water composition: The Nevado del Ruiz volcano-hydrothermal system (Colombia). *Chem Geol* 417:125–133. <https://doi.org/10.1016/j.chemgeo.2015.09.025>
- Instituto Geológico, Minero y Metalúrgico (1999) Carta Geológica Nacional - Escala 1:100,000. Ministerio de Energía y Minas. <https://portal.ingemmet.gob.pe/web/guest/carta-geologica-nacional-escala-1-100-000>

- INEI (2017) Directorio nacional de centros poblados. Censos Nacionales 2007: XI de Población y VI de Vivienda. Sistemas Nacionales de Estadística e Informática en el Perú, Instituto Nacional de Estadística e Informática. https://www.inei.gov.pe/media/MenuRecursivo/publicaciones_digitales/Est/Lib1541/index.htm
- Instituto Geológico, Minero y Metalúrgico (2023) Carta Geológica Nacional - Escala 1:50,000. Ministerio de Energía y Minas, Repositorio Institucional INGEMMET. <https://repositorio.ingemmet.gob.pe/handle/20.500.12544/4761>
- IPCC (1996) Climate Change 1995: The Science of Climate Change. Press Syndicate of the University of Cambridge
- IRENA (2019) Global Energy Transformation: A Roadmap to 2050. Abu Dhabi, 52 pp
- Irvine TN, Baragar WRA (1971) A guide to the chemical classification of the common volcanic rocks: *Can J Earth Sci* 8(5):523–548. <https://doi.org/10.1139/e71-055>
- Iveson AA, Webster JD, Rowe MC, Neill OK (2019) Fluid-melt trace-element partitioning behaviour between evolved melts and aqueous fluids: Experimental constraints on the magmatic-hydrothermal transport of metals. *Chem Geol* 516:18–41. <https://doi.org/10.1016/j.chemgeo.2019.03.029>
- Jackson MG, Shirey SB, Hauri EH, Kurz MD, Rizo H (2016) Peridotite xenoliths from the Polynesian Austral and Samoa hotspots: Implications for the destruction of ancient ^{187}Os and ^{142}Nd isotopic domains and the preservation of Hadean ^{129}Xe in the modern convecting mantle. *Geochim Cosmochim Acta* 185:21–43. <https://doi.org/10.1016/j.gca.2016.02.011>
- Jaillard E, Bengtson P, Dhondt A (2005) Late Cretaceous marine transgressions in Ecuador and northern Peru: a refined stratigraphic framework. *J South Am Earth Sci* 19(3):307–323. <https://doi.org/10.1016/j.jsames.2005.01.006>

- James DE, Sacks S (1999) Cenozoic formation of the central Andes: a geophysical perspective. In: Skinner B (ed) *Geology and Ore Deposits of the Central Andes*, Vol. 7. Society of Economic Geologists. <https://doi.org/10.5382/SP.07.01>
- Jiménez N, López-Velásquez S (2008) Magmatism in the Huarina belt, Bolivia, and its geotectonic implications. *Tectonophysics* 459(1–4):85-106. <https://doi.org/10.1016/j.tecto.2007.10.012>
- Jiménez J, Gimeno M, Auqué F (2022) Geochemical characterisation and modelling of the Luchon hydrothermal system (Central Pyrenees, France) and lessons learnt for the use of geochemical modelling techniques in granite-hosted alkaline thermal waters. *Geothermics* 106:102573. <https://doi.org/10.1016/j.geothermics.2022.102573>
- Jochum KP, Weis U, Stoll B, Kuzmin D, Yang Q, Raczek I, Jacob DE, Stracke A, Birbaum K, Frick DA, Günther D, Enzweiler J (2011) Determination of reference values for NIST SRM 610-617 glasses following ISO guidelines. *Geostand Geoanalytical Res* 35(4):397–429. <https://doi.org/10.1111/j.1751-908X.2011.00120.x>
- Johannsen A (1931) *A Descriptive Petrography of the Igneous Rocks*, Vol. 1. Introduction, Textures, Classification, and Glossary. *J Geol* 40:182-185
- Jowitt SM, McNulty BA (2021) Battery and Energy Metals: Future Drivers of the Minerals Industry? *Discovery, Society of Economic Geologists* 127:11–18. <https://doi.org/10.5382/2021-127.fea-01>
- Heinonen J, Iles K, Heinonen A, Fred R, Virtanen V, Bohrsen W, Spera F (2020) From Binary Mixing to Magma Chamber Simulator - Geochemical Modeling of Assimilation in Magmatic Systems. <https://doi.org/10.1002/essoar.10504606.2>
- Kaeter D, Barros R, Menuge J, Chew DM (2018) The magmatic hydrothermal transition in rare element pegmatites from southeast Ireland: LA ICP MS chemical mapping of muscovite and columbite tantalite. *Geochim Cosmochim Acta* 240:98-130. <https://doi.org/10.1016/j.gca.2018.08.024>

- Kalinowski BE, Schweda P (1996) Kinetics of muscovite, phlogopite, and biotite dissolution and alteration at pH 1–4, room temperature. *Geochim Cosmochim Acta* 60(3):367–385. [https://doi.org/10.1016/0016-7037\(95\)00411-4](https://doi.org/10.1016/0016-7037(95)00411-4)
- Kar N, Garzzone C, Jaramillo C, Shanahan T, Carlotto V, Pullen A, Moreno F, Anderson V, Moreno E, Eiler J (2016) Rapid regional surface uplift of the northern Altiplano plateau revealed by multiproxy paleoclimate reconstruction. *Earth Planet Sci Lett* 447:33–47. <https://doi.org/10.1016/j.epsl.2016.04.025>
- Karrech A, Azadi MR, Elchalakani M, Shahin MA, Seibi AC (2020) A review on methods for liberating lithium from pegmatites. *Miner Eng* 145:106085. <https://doi.org/10.1016/j.mineng.2019.106085>
- Kato JJ (2013) Geochemistry of the Neogene Los Frailes Ignimbrite Complex on the Central Andean Altiplano plateau. Master dissertation, Cornell University
- Kay RW, Kay S (1993) Delamination and delamination magmatism. *Tectonophysics* 219(1–3):177–189. [https://doi.org/10.1016/0040-1951\(93\)90295-U](https://doi.org/10.1016/0040-1951(93)90295-U)
- Kay SM, Coira B, Viramonte J (1994) Young mafic back-arc volcanic rocks as a guide to lithospheric delamination beneath the Argentine Puna Plateau. *J Geophys Res* 99(B12):24323–24339. <https://doi.org/10.1029/94JB00896>
- Kay SM, Coira BL (2009) Shallowing and steepening subduction zones, continental lithospheric loss, magmatism, and crustal flow under the Central Andean Altiplano-Puna Plateau. In: Kay SM, Ramos VA, Dickinson WR (eds) *Backbone of the Americas: Shallow Subduction, Plateau Uplift, and Ridge and Terrane Collision*. *Mem Geol Soc Am* 204:229–259. [https://doi.org/10.1130/2009.1204\(11\)](https://doi.org/10.1130/2009.1204(11))
- Kay SM, Coira BL, Caffè PJ, Chen C-H (2010) Regional chemical diversity, crustal and mantle sources and evolution of central Andean Puna plateau ignimbrites. *J Volcanol Geotherm Res* 198(1–2):81–111. <https://doi.org/10.1016/j.jvolgeores.2010.08.013>

- Kay SM, Coira B, Wörner G, Kay RW, Singer S (2011) Geochemical, isotopic and single crystal $^{40}\text{Ar}/^{39}\text{Ar}$ age constraints on the evolution of the Cerro Galán ignimbrites. *Bull Volcanol* 73:1487–1511. <https://doi.org/10.1007/s00445-010-0410-7>
- Keeble BR (1988) *The Brundtland Report: "Our Common Future."* United Nations, the Oxford University Press. <https://doi.org/10.1080/07488008808408783v>
- Kesler SE, Gruber PW, Medina PA, Keoleian GA, Everson MP, Wallington, TJ (2012) Global lithium resources: Relative importance of pegmatite, brine, and other deposits. *Ore Geol Rev* 48:55–69. <https://doi.org/10.1016/j.oregeorev.2012.05.006>
- Knauss KG, Wolery TJ (1989) Muscovite dissolution kinetics as a function of pH and time at 70°C. *Geochim Cosmochim Acta* 53(7):1493–1501. [https://doi.org/10.1016/0016-7037\(89\)90232-9](https://doi.org/10.1016/0016-7037(89)90232-9)
- Kontak DJ (1984) *The magmatic and metallogenic evolution of a craton-orogen interface: the Cordillera de Carabaya, Central Andes, SE Peru.* Doctoral dissertation, Queen's University
- Kontak DJ, Clark AH, Farrar E, Archibald DA, Baadsgaard H (1990) Late Paleozoic-early Mesozoic magmatism in the Cordillera de Carabaya, Puno, southeastern Peru: Geochronology and petrochemistry. *J South Am Earth Sci* 3(4):213–230. [https://doi.org/10.1016/0895-9811\(90\)90004-K](https://doi.org/10.1016/0895-9811(90)90004-K)
- Kontak DJ, Clark AH, Farrar E, Pearce TE, Strong DF, Baadsgaard H (1986) Petrogenesis of a Neogene shoshonite suite, Cerro Moromoroni, Puno, Southeastern Peru. *Can Mineral* 24(1):117–135
- Labou I, Benoit M, Baratoux L, Grégoire M, Ndiaye PM, Thebaud N, Béziat D, Debat P (2020) Petrological and geochemical study of Birimian ultramafic rocks within the West African Craton: Insights from Mako (Senegal) and Loraboué (Burkina Faso) lherzolite/harzburgite/wehrlite associations. *J Afr Earth Sci* 162:103677. <https://doi.org/10.1016/j.jafrearsci.2019.103677>

- Lancelot JR, Laubacher G, Marocco R, Renaud U (1978) U/Pb radiochronology of two granitic plutons from the eastern Cordillera (Peru) - Extent of Permian magmatic activity and consequences. *Geol Rundschau* 67:236–243. <https://doi.org/10.1007/BF01803263>
- Laubacher G (1978) Estudio geológico de la región norte del lago Titicaca. Instituto Geológico, Minero y Metalúrgico, 120 pp
- Le Maitre RW, Bateman P, Dudek A, Keller J, Lameyre J, Le Bas MJ, Sabine PA, Schmid R, Sorensen H, Streckeisen A, Woolley AR, Zanettin B (1989) A classification of igneous rocks and glossary of terms: Recommendations of the International Union of Geological Sciences Subcommittee on the Systematics of Igneous Rocks. Blackwell Scientific Publications, Oxford, U.K.
- Lease R, Ehlers T (2013) Incision into the Eastern Andean Plateau During Pliocene Cooling. *Science* 341(6147):774-776. <https://doi.org/10.1126/science.1239132>
- Lee J, Bazilian M, Sovacool B, Hund K, Jowitt SM, Nguyen TP, Månberger A, Kah M, Greene S, Galeazzi C, Awuah-Offei K, Moats M, Tilton J, Kukoda S (2020) Reviewing the material and metal security of low-carbon energy transitions. *Renew Sust Energ Rev* 124:24. <https://doi.org/10.1016/j.rser.2020.109789>
- Le Maitre RW, Bateman P, Dudek A, Keller J, Lameyre J, Le Bas MJ, Sabine PA, Schmid R, Sorensen H, Streckeisen A, Woolley AR, Zanettin B (1989) A classification of igneous rocks and glossary of terms: Recommendations of the International Union of Geological Sciences Subcommittee on the Systematics of Igneous Rocks. Blackwell Scientific Publications, Oxford, U.K.
- Li V (2016). The Uranium Mineralization of the Macusani District, Southeast Peru: Mineralogy, Geochemistry, Geochronology and Ore-Genetic Model. Doctoral dissertation, Queen's University. Canada

- Li CF, Li X, Li Q, Guo J, Li X (2011) Directly determining $^{143}\text{Nd}/^{144}\text{Nd}$ isotope ratios using thermal ionization mass spectrometry for geological samples without separation of Sm-Nd: *J Anal At Spectrom* 26(10):2012-2022
- Li V, Clark AH, Kyser TK, Cuba W, Brisbin D, O'Connor T, Stefan L (2012) The uranium deposits of the Macusani District, Puno, southeastern Peru: A new ore-genetic model. Society of Economic Geology 2012 Conference, Lima, Peru
- Li CF, Li XH, Li QL, Guo JH, Li XH, Yang YH (2012) Rapid and precise determination of Sr and Nd isotopic ratios in geological samples from the same filament loading by thermal ionization mass spectrometry employing a single-step separation scheme. *Anal Chim Acta* 727:54-60. <https://doi.org/10.1016/j.aca.2012.03.040>
- Liang X, Sandvol E, Kay S, Heit B, Yuan X, Mulcahy P, Chen C, Brown L, Comte D, Alvarado P (2014) Delamination of southern Puna lithosphere revealed by body wave attenuation tomography. *J Geophys Res Solid* 119(1):549-566. <https://doi.org/10.1002/2013JB010309>
- Linck G (1926) Ein neuer knstallfiihrender Tektit von Paucartambo in Peru. *Chem Erde* 2:57-174
- Lindsay JM, Schmitt AK, Trumbull RB, de Silva SL, Siebel W, Emmermann R (2001) Magmatic evolution of the La Pacana Caldera System, Central Andes, Chile: compositional variation of two cogenetic, large-volume felsic ignimbrites. *J Petrol* 42(3):459-486. <https://doi.org/10.1093/petrology/42.3.459>
- Linnen R, McNeil A, Flemming R (2019) Some thoughts on metasomatism in pegmatites. *Can Mineral* 57(5):765-766. <https://doi.org/10.3749/canmin.AB00016>
- Linnen RL (1998) The solubility of Nb-Ta-Zr-Hf-W in granitic melts with Li and Li + F: constraints for mineralization in rare metal granites and pegmatites. *Econ Geol* 93(7):1013-1025. <https://doi.org/10.2113/gsecongeo.93.7.1013>
- London D (2015) Reading pegmatites: What beryl says. *Rocks Miner* 90:138-149. <https://doi.org/10.1080/00357529.2014.949173>

- London D, Morgan GB (2017) Experimental crystallization of the Macusani Obsidian, with applications to lithium-rich granitic pegmatites. *J Petrol* 58(5):1005–1030. <https://doi.org/10.1093/PETROLOGY/EGX044>
- London D, Hervig RL, Morgan GB (1988) Melt-vapor solubilities and elemental partitioning in peraluminous granite-pegmatite systems: Experimental results with Macusani glass at 200 MPa. *Contrib Mineral Petrol* 99:360–373. <https://doi.org/10.1007/BF00375368>
- London D, Morgan GB, Hervig RL (1989) Vapor-undersaturated experiments with Macusani glass+H₂O at 200 MPa, and the internal differentiation of granitic pegmatites. *Contrib Mineral Petrol* 102(1):1–17. <https://doi.org/10.1007/BF01160186>
- Loewy S, Connelly J, Dalziel I (2004) An orphaned basement block: The Arequipa-Antofalla Basement of the central Andean margin of South America. *Geol Soc Am Bull* 116(1-2):171-187. <https://doi.org/10.1130/B25226.1>
- López JC (1996) Geología del cuadrángulo de Nuñoa. Hoja 29-u. Instituto Geológico, Minero y Metalúrgico, 171pp
- López Steinmetz RL, Salvi S (2021) Brine grades in Andean salars: When basin size matters. A review of the Lithium Triangle. *Earth Sci Rev* 217:103615. <https://doi.org/10.1016/j.earscirev.2021.103615>
- Lugmair GW, Marti K (1978) Lunar initial ¹⁴³Nd/¹⁴⁴Nd: differential evolution of the lunar crust and mantle. *Earth Planet Sci Lett* 39(3):349-357. [https://doi.org/10.1016/0012-821X\(78\)90021-3](https://doi.org/10.1016/0012-821X(78)90021-3)
- Mamani M, Ibarra I, Carlier G, Fornari M (2004) Petrología y geoquímica del magmatismo alcalino de la zona noroeste del Altiplano peruano (departamento de Puno). *Sociedad Geológica del Peru, Publicación Especial* 5:157-174
- Mamani M, Wörner G, Sempere T (2010) Geochemical variations in igneous rocks of the Central Andean orocline (13°S to 18°S): Tracing crustal thickening and magma generation through time and space. *Geol Soc Am Bull* 122(1-2):162–182. <https://doi.org/10.1130/B26538.1>

- Marocco R (1978) *Géologie des Andes Péruviennes*. ORSTOM, Paris, 195 pp
- Martin WR (1934) Are the “Americanites” Tektites? *Leidsche Geologische Mededeelingen* 6(1):123–132
- Martin R, de Sitter-Koomans C (1955) Pseudotectites from Colombia and Peru. *Leidse Geologische Mededeelingen* 20(1):151–164
- MacDonald R, Smith RL, Thomas JE (1992) *Chemistry of the Subalkalic Silicic Obsidians*. U.S. Geological Survey Professional Paper 1523, 214 pp
- McCorkell R, Naeser CW (1988) Natural Glass Inter-laboratory Reference Materials for fission-track dating. 6th Int. Workshop on Fission-Track Dating, Besançon, 5-9 September, (Abstract). *Nucl Tracks Radiat Meas* 17:422
- McCulloch MT, Jaques AL, Nelson DR, Lewis JD (1983) Nd and Sr isotopes in kimberlites and lamproites from western Australia: An enriched mantle origin. *Nature* 302:400–403. <https://doi.org/10.1038/302400a0>
- McDonough WF, Sun SS (1995) Composition of the Earth. *Chem Geol* 120(3-4):223-253. [https://doi.org/10.1016/0009-2541\(94\)00140-4](https://doi.org/10.1016/0009-2541(94)00140-4)
- McNeil A, Linnen R, Flemming R, Fayek M (2020) An experimental approach to examine fluid-melt interaction and mineralization in rare-metal pegmatites. *Am Min* 105(7):1078–1087. <https://doi.org/10.2138/am-2020-7216>
- McPhie J, Doyle M, Allen R (1993) *Volcanic textures: a guide to the interpretation of textures in volcanic rocks*. Centre for Ore Deposit and Exploration Studies, University of Tasmania
- McQuarrie N, Decelles P (2001) Geometry and structural evolution of the central Andean backthrust belt, Bolivia. *Tectonics* 20(2):669–92. <https://doi.org/10.1029/2000TC001232>

- McQuarrie N, Horton BK, Zandt G, Beck S, DeCelles PG (2005) Lithospheric evolution of the Andean fold-thrust belt, Bolivia, and the origin of the Central Andean plateau. *Tectonophysics* 399(1-4):15–37. <https://doi.org/10.1016/j.tecto.2004.12.013>
- McQuarrie N, Barnes J, Ehlers TA (2008) Geometric, kinematic and erosional history of the central Andean Plateau (15-17°S), northern Bolivia. *Tectonics* 27(3):TC3007. <https://doi.org/10.1029/2006TC002054>
- Mégard F (1978) Etude géologique des Andes du Pérou central. ORSTOM, Paris, 310 pp
- Michard G (1990) Behaviour of major elements and some trace elements (Li, Rb, Cs, Sr, Fe, Mn, W, F) in deep hot waters from granitic areas. *Chem Geol* 89(1-2):117-134. [https://doi.org/10.1016/0009-2541\(90\)90062-C](https://doi.org/10.1016/0009-2541(90)90062-C)
- Michard A, Gurriet P, Soudant M, Albarede F (1985) Nd isotopes in French phanerozoic shales: External vs internal aspects of crustal evolution. *Geochim Cosmochim Acta* 49(2):601–610. [https://doi.org/10.1016/0016-7037\(85\)90051-1](https://doi.org/10.1016/0016-7037(85)90051-1)
- Michaud J, Pichavant M, Villaros A (2021) Rare elements enrichment in crustal peraluminous magmas: Insights from partial melting experiments. *Contrib Mineral Petrol* 176(11):33. <https://doi.org/10.1007/s00410-021-01855-9>. insu-03431952
- Michaud J (2019) Les granites à métaux rares: origine, mise en place et mécanismes de la transition magmatique-hydrothermale. *Sciences de la Terre. Université d'Orléans. Français*
- Miller DS, Wagner GA (1981) Fission-track ages applied to obsidian artefacts from South America using the plateau-annealing and track-size age-correction techniques. *Nucl Tracks Radiat Meas* 5(1-2):147-155. [https://doi.org/10.1016/0191-278X\(81\)90037-8](https://doi.org/10.1016/0191-278X(81)90037-8)
- Miller DS, Eby N, McCorkell R, Rosenberg PE, Suzuki M (1990) Results of interlaboratory comparison of fission track ages for the 1988 fission track Workshop. *Nucl Tracks Radiat Meas* 17(3):237-245. [https://doi.org/10.1016/1359-0189\(90\)90041-U](https://doi.org/10.1016/1359-0189(90)90041-U)

- MTC (2019). Descarga de datos espaciales. Ministerio de Transportes y Comunicaciones. <https://portal.mtc.gob.pe/estadisticas/descarga.html>. Accessed 2 July 2023
- Mišković A, Spikings RA, Chew DM, Košler J, Ulianov A, Schaltegger U (2009) Tectonomagmatic evolution of Western Amazonia: Geochemical characterization and zircon U-Pb geochronologic constraints from the Peruvian Eastern Cordilleran granitoids. *Bull Geol Soc Am* 121(9-10):1298–1324. <https://doi.org/10.1130/B26488.1>
- Monier G, Charoy B, Cuncy M, Ohnenstetter D, and Robert JL (1987) Evolution spatiale et temporelle de la composition des micas du granite albitique a topaze—lepidolite de Beauvoir. *Geologie de la France* 2(3):179-188
- Moretti I, Baby P, Alvarez Zapata P, Mendoza RV (2023), Subduction and hydrogen release: The case of Bolivian Altiplano. *Geosciences* 13(4):109. <https://doi.org/10.3390/geosciences13040109>.
- Morgan LA, Shanks WCP, Pierce KL, Iverson N, Schiller CM, Brown SR, Zahajska P, Cartier R, Cash RW, Best JL, Whitlock C, Fritz S, Benzel W, Lowers H, Lovalvo DA, Licciardi JM (2023) The dynamic floor of Yellowstone Lake, Wyoming, USA: The last 14 k.y. of hydrothermal explosions, venting, doming, and faulting: *Geol Soc Am Bull* 135(3-4):547-574. <https://doi.org/10.1130/B36190.1>
- Mukasa SB (1986) Zircon U-Pb ages of super-units in the Coastal batholith, Peru: Implications for magmatic and tectonic processes. *Geol Soc Am Bull* 97(2):241–254. [https://doi.org/10.1130/0016-7606\(1986\)97<241:ZUAOSI>2.0.CO;2](https://doi.org/10.1130/0016-7606(1986)97<241:ZUAOSI>2.0.CO;2)
- Mukasa SB, Henry DJ (1990) The San Nicolas Batholith of coastal Peru: early Paleozoic continental arc or continental rift magmatism. *J Geol Soc London* 147(1):27–39. <https://doi.org/10.1144/gsjgs.147.1.0027>
- Müller J, Kley J, Jacobshagen V (2002) Structure and Cenozoic kinematics of the Eastern Cordillera, southern Bolivia (21 S). *Tectonics* 21(5):1037 <https://doi.org/10.1029/2001TC001340>

- Müller A, Seltmann R, Halls C, Siebel W, Dulski P, Jeffries T, Spratt J, Kronz A (2006) The magmatic evolution of the Land's End pluton, Cornwall, and associated pre-enrichment of metals. *Ore Geol Rev* 28(3):329–367. <https://doi.org/10.1016/j.oregeorev.2005.05.002>
- Myers S, Beck S, Zandt G, Wallace T (1998) Lithospheric-scale structure across the Bolivian Andes from tomographic images of velocity and attenuation for P and S waves. *J Geophys Res* 103(B9):21233-21252. <https://doi.org/10.1029/98JB00956>
- National Research Council (2008) Minerals, critical minerals, and the U.S. Economy. National Academies Press, Washington, 245 pp. <https://doi.org/10.17226/12034>
- Nichols G (2009) Sedimentology and Stratigraphy. 2nd ed. Wiley-Blackwell
- Noble DC, McKee EH, Farrar E, Petersen U (1974) Episodic Cenozoic volcanism and tectonism in the Andes of Peru. *Earth Planet Sci Lett* 21(2):213-220. [https://doi.org/10.1016/0012-821X\(74\)90057-0](https://doi.org/10.1016/0012-821X(74)90057-0)
- Noble DC, Farrar E, Cobbing EJ (1979) The Nazca Group of south-central Peru: Age, source, and regional volcanic and tectonic significance. *Earth Planet Sci Lett* 45(1):80-86. [https://doi.org/10.1016/0012-821X\(79\)90109-2](https://doi.org/10.1016/0012-821X(79)90109-2)
- Noble DC, Vogel TA, Peterson PS, Landis GP, Grant NK, Jezek P, McKee EH (1984) Rare-element-enriched, S-type ash-flow tufts containing phenocrysts of muscovite, andalusite, and sillimanite, southeastern Peru. *Geology* 12(1):35-39. [https://doi.org/10.1130/0091-7613\(1984\)12<35:RSATCP>2.0.CO;2](https://doi.org/10.1130/0091-7613(1984)12<35:RSATCP>2.0.CO;2)
- Nupen S (2019) Mineral Resource Estimates for the Falchani Lithium Project in the Puno District of Peru. Bryanston, 72 pp
- O'Connor T, Stefan L, Clark A, Kyser K, Li V (2018) Macusani Uranium Deposits, Puno, Peru: Products of Episodic Late Pleistocene Periglacial Flooding
- Octaviano C (2011) Análisis General de la Externalidades Ambientales Derivadas de la Utilización de Combustibles Fósiles en la Industria Eléctrica Centroamericana.

Comisión Económica para América Latina y el Caribe (CEPAL), Sede Subregional en México

Ort MH, Mattison JM, Fisher RV (1988) Trace element and Sr, Nd, and Pb isotopic variations with stratigraphy in Miocene ignimbrites and lava flows of Cerro Panizos, Argentina and Bolivia. *Geological Society of America Abstracts with Programs* 20: A9 pp

Pandarínath K, Dulski P, Torres-Alvarado I, Verma S (2008) Element mobility during the hydrothermal alteration of rhyolitic rocks of the Los Azufres geothermal field, Mexico. *Geothermics* 37(1):53-72. <https://doi.org/10.1016/j.geothermics.2007.10.002>

Paquereau P, Thouret J-C, Wörner G, Fornari M (2006) Neogene and Quaternary ignimbrites in the area of Arequipa, Southern Peru: Stratigraphical and petrological correlations. *J Volcanol Geotherm Res* 154(3-4):251–275. <https://doi.org/10.1016/j.jvolgeores.2006.02.014>

Panca F (2010) The late Permian–Lower Triassic Mitu Group, SE of Cusco (Peru). Field Relations, Volcanosedimentary Facies and Geochemistry. Technische Universität Bergakademie, Freiberg MSc thesis

Parmigiani A, Faroughi S, Huber C, Bachmann O, Su Y (2016) Bubble accumulation and its role in the evolution of magma reservoirs in the upper crust. *Nature* 532:492–495. <https://doi.org/10.1038/nature17401>

Parmigiani A, Degruyter W, Leclaire S, Huber C, Bachmann O (2017) The mechanics of shallow magma reservoir outgassing. *Geochem Geophys* 18:2887–2905

Perez ND, Horton BK (2014) Oligocene-miocene deformational and depositional history of the andean hinterland basin in the northern altiplano Plateau, Southern Peru. *Tectonics* 33(9):1819–1847. <https://doi.org/10.1002/2014TC003647>

Peccerillo A (1999) Multiple mantle metasomatism in central-southern Italy: Geochemical effects, timing and geodynamic implications. *Geology* 27(4):315–318. [https://doi.org/10.1130/0091-7613\(1999\)027<0315:MMMICS>2.3.CO;2](https://doi.org/10.1130/0091-7613(1999)027<0315:MMMICS>2.3.CO;2)

- Peccerillo A, Frezzotti M (2015) Magmatism, mantle evolution and geodynamics at the converging plate margins of Italy. *J Geol Soc* 172:407–427. <https://doi.org/10.1144/jgs2014-085>
- Perez ND, Horton BK (2014) Oligocene-Miocene deformational and depositional history of the Andean hinterland basin in the northern Altiplano plateau, southern Peru. *Tectonics* 33(9):1819-1847. <https://doi.org/10.1002/2014TC003647>
- Perez ND, Horton BK, Carlotto V (2016a). Structural inheritance and selective reactivation in the Central Andes: Cenozoic deformation guided by pre-Andean structures in Southern Peru. *Tectonophysics* 671:264-280. <https://doi.org/10.1016/j.tecto.2015.12.031>
- Perez ND, Horton BK, McQuarrie N, Stübner K, Ehlers TA (2016b) Andean shortening, inversion and exhumation associated with thin- and thick-skinned deformation in southern Peru. *Geol Mag* 153(5-6):1013–1041. <https://doi.org/10.1017/S0016756816000121>
- Perelló J, Carlotto V, Zarate A, Ramos P, Posso H, Caballero A (2003) Porphyry-style alteration and mineralization of the middle Eocene to early Oligocene Andahuaylas-Yauri Belt, Cusco region, Peru. *Econ Geol* 98(8):1575–1605. <https://doi.org/10.2113/gsecongeo.98.8.1575>
- Petford N, Atherton MP (1995) Cretaceous-Tertiary volcanism and syn-subduction crustal extension in northern central Peru. In: Smellie JL (ed) *Volcanism associated with extension at consuming plate margins*. *J Geol Soc London* 81:233–248. <https://doi.org/10.1144/GSL.SP.1994.081.01.13>
- Poupeau G, Labrin E, Sabil N, Bigazzi G, Arroyo G, Vatin-Pérignon N (1993) Fission-track dating of 15 macusanite glass pebbles from the Macusani Volcanic Field (SE Peru). *Nucl Tracks Radiat Meas* 21(4):449–506. [https://doi.org/10.1016/1359-0189\(93\)90189-G](https://doi.org/10.1016/1359-0189(93)90189-G)

- Poupeau G, Sabil N, Villa IM, Bigazzi G, Vatin-Perignon N, Flores P, Pereyra P, Salas G, Arroyo G (1992) Fission-track and K-Ar ages of “macusanite” obsidian glasses, (SE Peru): Geodynamic implications. *Tectonophysics* 205(1-3):295-305. [https://doi.org/10.1016/0040-1951\(92\)90432-6](https://doi.org/10.1016/0040-1951(92)90432-6)
- Pichavant M, Montel JM (1988) Petrogenesis of a two-mica ignimbrite suite: The Macusani Volcanics, SE Peru. *Earth Environ Sci Trans* 79(2-3):197–207. <https://doi.org/10.1017/S0263593300014218>
- Pichavant M, Valencia Herrera J, Boulmier S, Briquieu L, Joron JL, Juteau M, Marin L, Michard A, Sheppard AMF, Treuil M, Vernet M (1987) The Macusani glasses, SE Peru: evidence of chemical fractionation in peraluminous magmas. In: Mysen BO (ed) *Magmatic processes, physicochemical principles*. *Geochem Soc Special Publ* 1:359-373
- Pichavant M, Kontak DJ, Valencia Herrera J, Clark AH (1988a) The Miocene-Pliocene Macusani Volcanics, SE Peru - I. Mineralogy and magmatic evolution of a two-mica aluminosilicate-bearing ignimbrite suite. *Contrib Mineral Petrol* 100:300–324. <https://doi.org/10.1007/BF00379742>
- Pichavant M, Kontak DJ, Briquieu L, Valencia Herrera J, Clark AH (1988b) The Miocene-Pliocene Macusani Volcanics, SE Peru - II. Geochemistry and origin of a felsic peraluminous magma. *Contrib Mineral Petrol* 100:325–338. <https://doi.org/10.1007/BF00379742>
- Pichavant M, Villaros A, Michaud J, Scaillet B (2024) Granite magmatism and mantle filiation. *Eur J Mineral* 36(1):225–246. <https://doi.org/10.5194/ejm-36-225-2024>
- Pichavant M, Erdmann S, Kontak DJ, Michaud J, Villaros A (2024) Trace element partitioning in strongly peraluminous rare-metal silicic magmas – Implications for fractionation processes and for the origin of the Macusani Volcanics (SE Peru). *Geochim Cosmochim Acta* 365:229–252. <https://doi.org/10.1016/j.gca.2023.11.021>

- Picard D, Sempere T, Plantard O (2008) Direction and timing of uplift propagation in the Peruvian Andes deduced from molecular phylogenetics of highland biotaxa. *Earth Planet Sci Lett* 271(1-4):326–336. <https://doi.org/10.1016/j.epsl.2008.04.024>
- Qinhua X, Aizhen Y (1991) Hydrothermal synthesis and crystallization of zeolites. *Prog Cryst Growth Charact Mater* 21(1-4):29-70. [https://doi.org/10.1016/0960-8974\(91\)90007-Y](https://doi.org/10.1016/0960-8974(91)90007-Y)
- Raczek I, Stoll B, Hofmann AW, Peter Jochum K (2001) High-precision trace element data for the USGS reference materials BCR-1, BCR-2, BHVO-1, BHVO-2, AGV-1, AGV-2, DTS-1, DTS-2, GSP-1 and GSP-2 by ID-TIMS and MIC-SSMS. *Geostand Geoanalytical Res* 25(1):77–86. <https://doi.org/10.1111/j.1751-908X.2001.tb00789.x>
- Raimbault L, Burnol L (1998) The Richemont rhyolite dyke, Massif Central, France: A subvolcanic equivalent of rare-metal granites. *Can Mineral* 36(2):265–282
- Ramos VA (2018) Tectonic evolution of the central Andes: From terrane accretion to crustal delamination. In: Zamora G, McClay KM, Ramos V (eds) *Petroleum basins and hydrocarbon potential of the Andes of Peru and Bolivia*. The American Association of Petroleum Geologists Memoir 117:1–34. <https://doi.org/10.1306/13622115M1172855>
- Ramírez JA, Grundvig S (2000) Causes of geochemical diversity in peraluminous granitic plutons: the Jálama pluton, Central-Iberian Zone (Spain and Portugal): *Lithos* 50(1-3):171–190. [https://doi.org/10.1016/S0024-4937\(99\)00047-X](https://doi.org/10.1016/S0024-4937(99)00047-X)
- Ramírez-Briones J, Torró L, Tavazzani L, Monnier L, Laurent O, Segovia-More M, Sannandres-Flores M, Vallance J, Chelle-Michou C, Salvi S, Baby P (2023) Major and trace element composition of the Lithium-rich Tuff from the Macusani Volcanic Field, Puno, Peru. *Proceedings of the 17th SGA Biennial Meeting*:295-298
- Redacción RPP (2018) El Perú podría llegar a ser el país con más reservas de litio en el mundo. *RPP Noticias*. <https://rpp.pe/economia/economia/peru-tendria-la-primera-mina-de-litio-del-mundo-si-explota-yacimiento-puno-noticia-1137200?ref=rpp>. Accessed 2 June 2023

- Reitsma MJ (2012) Reconstructing the Late Paleozoic–Early Mesozoic Plutonic and Sedimentary Record of South-East Peru: Orphaned Back-arcs Along the Western Margin of Gondwana. Doctoral dissertation, Terre & Environment, University of Geneva, Switzerland
- Rochata P, Hérail G, Baby P, Mascle G, Aranibar O (1998) Geometric analysis and tectonosedimenta y model of the northern Bolivian Altiplano. *Earth Planet Sci Lett, Series IIA* 327(11):769-775
- Rudnick RL, Gao S (2014) Composition of the Continental Crust. In: Holland HD, Turekian KK (eds) *Treatise on geochemistry*, 2nd edn, Amsterdam, Elsevier, p 1–51. <https://doi.org/10.1016/B978-0-08-095975-7.00301-6>
- Rodríguez R, Choquehuanca S, Sánchez E, Fabián C, Del Castillo B (2021) Geología de los cuadrángulos de Macusani (hojas 29v1, 29v2, 29v3, 29v4) y Limbani (hojas 29x1, 29x2, 29x3, 29x4). Instituto Geológico, Minero y Metalúrgico, Boletín Serie L4, 82 pp
- Rollinson H, Pease V (2021) *Using Geochemical Data To Understand Geological Processes*, 2nd edition. Cambridge University Press
- Romer R, Meixner A, Förster H-J (2014) Lithium and boron in late-orogenic granites – Isotopic fingerprints for the source of crustal melts? *Geochim Cosmochim Acta* 131:98-114. <https://doi.org/10.1016/j.gca.2014.01.018>.
- Romero D, Valencia K, Alarcón P, Peña D, Ramos VA (2013) The offshore basement of Perú: Evidence for different igneous and metamorphic domains in the forearc: *J South Am Earth Sci* 42:47–60
- Rodrigues R, Gervasoni F, Jallowitzki T, Bussweiler Y, Berndt J, Botelho N, Queiroga G, Castro M, da Silva S, Ciriaco B, de Oliveira I, Klemme S (2022) Multiple metasomatic events recorded by a stratified lithosphere beneath the SW margin of the São Francisco Craton, SE Brazil. *Social Science Research Network*, 45 pp. <http://dx.doi.org/10.2139/ssrn.4249639>

- Roperch P, Sempere T, Macedo O, Arriagada C, Fornari F, Tapia C, García M, Laj C (2006) Counterclockwise rotation of late Eocene–Oligocene fore-arc deposits in southern Peru and its significance for oroclinal bending in the Central Andes. *Tectonics* 25(3):TC3010. <https://doi.org/10.1029/2005TC001882>
- Roperch P, Carlotto V, Ruffet G, Fornari M (2011) Tectonic rotations and transcurrent deformation south of the Abancay deflection in the Andes of southern Peru. *Tectonics* 30(2):TC2010. <https://doi.org/10.1029/2010TC002725>
- Rubin J, Henry C, Price J (1993) The mobility of zirconium and other “immobile” elements during hydrothermal alteration. *Chem Geol* 110(1–3):29-47. [https://doi.org/10.1016/0009-2541\(93\)90246-F](https://doi.org/10.1016/0009-2541(93)90246-F).
- Rumbo Minero (2023) Macusani Yellowcake: El proyecto de litio Falchani no contiene uranio. <https://www.rumbominero.com/peru/noticias/mineria/proyecto-de-litio-falchani-no-uranio/>. Accessed 2 June 2023
- Rusak AA, Shchekina TI, Zinovyeva NG, Alferyeva YO, Khvostikov VA, Gramenitskiy EN, Kotelnikov AR (2021) The Peculiarities of Crystallization of Lithium-Containing Granite Melt with High Water and Fluorine Contents in the Temperature Range of 800–400 °C and Pressure of 1 Kbar (According to Experimental Data). *Environ Sci Proc* 6(1):9. <https://doi.org/10.3390/iecms2021-09361>
- Ryan J, Beck S, Zandt G, Wagner L, Minaya E, Taverna H (2016) Central Andean crustal structure from receiver function analysis. *Tectonophysics* 682:120–33. <https://doi.org/10.1016/j.tecto.2016.04.048>
- Salazar E (2023a) Ulises Solís Llapa: “La nacionalización del litio en Chile es una oportunidad para el Perú”. <https://larepublica.pe/economia/2023/04/29/minem-ulises-solis-llapa-la-nacionalizacion-del-litio-en-chile-es-una-oportunidad-para-el-peru-macusani-yellowcake-explotacion-litio-puno-1239866>. Accessed 18 Dec. 2023
- Salazar E (2023b) Falchani: admiten a trámite EIASd del proyecto de litio de Macusani Yellowcake en Puno. <https://larepublica.pe/economia/2023/10/31/litio-falchani->

admiten-a-tramite-eiasd-del-proyecto-de-macusani-yellowcake-en-puno-minem-dgaam-2567389. Accessed 18 Dec. 2023

Saldarriaga J (2021a) Proyecto de litio en Puno cambia de manos y pertenece ahora a American Lithium. El Comercio. <https://elcomercio.pe/economia/dia-1/litio-proyecto-de-litio-en-puno-cambia-de-manos-y-pertenece-ahora-a-american-lithium-uranio-noticia/>. Accessed 2 November 2023

Saldarriaga J (2021b) Minem advierte que la explotación de litio generará “serio problema de radiación en Puno. ¿Tiene razón? In: El Comercio. <https://elcomercio.pe/economia/litio-minem-advierte-que-la-explotacion-de-litio-generara-serio-problema-de-radiacion-en-puno-tiene-razon-noticia/?ref=ecr>. Accessed 11 Jul 2022

Salisbury MJ, Jicha BR, de Silva SL, Singer BS, Jimenez NC, Ort MH (2011) $^{40}\text{Ar}/^{39}\text{Ar}$ chronostratigraphy of Altiplano-Puna Volcanic Complex ignimbrites reveals the development of a major magmatic province. *Geol Soc Am Bull* 123(5-6):821–840. <https://doi.org/10.1130/B30280.1>

Salisbury M, Jiménez N, Barfod D (2022) $^{40}\text{Ar}/^{39}\text{Ar}$ ages and geochemistry of the Intersalar Range of the Bolivian Altiplano: A volcanological transect spanning the arc and reararc of the Central Andean Plateau. *Front Earth Sci Sec Geochemistry* 10:23. <https://doi.org/10.3389/feart.2022.917488>

Salters VJ, Stracke A (2004) Composition of the depleted mantle. *Geochem Geophys* 5(5):Q05B07

Sánchez AW, Zapata AA (2003) Memoria descriptiva de la revisión y actualización de los cuadrángulos de Río Picha (25-p), Timpia (25-q), Chuanquiri (26-p), Quillabamba (26-q), Quebrada Honda (26-r), Parobamba (26-s), Pacaypata (27-p), Machupicchu (27-q), Urubamba (27-r), Calca (27-s), Chotachaca (27-t), Quincemil (27-u), Ocongate (28-t), Corani (28-u) y Ayapata (28-v). Instituto Geológico, Minero y Metalúrgico, 51 pp

- Sandeman HA, Clark AH (2003) Glass-rich, cordierite–biotite rhyodacite, Valle Ninahuisa, Puno, SE Peru: Petrological evidence for hybridization of ‘Lachlan S-type’ and potassic mafic magmas. *J Petrol* 44(2):355–385. <https://doi.org/10.1093/petrology/44.2.355>
- Sandeman HA, Clark AH (2004) Commingling and mixing of S-type peraluminous, ultrapotassic and basaltic magmas in the Cayconi volcanic field, Cordillera de Carabaya, SE Peru. *Lithos* 73(1-4):187–213. <https://doi.org/10.1016/j.lithos.2003.12.005>
- Sandeman HA, Clark AH, Farrar E (1995) An integrated tectono-magmatic model for the evolution of the southern Peruvian Andes (13°–20° S) since 55 Ma. *Int Geol Rev* 37(12):1039–1073. <https://doi.org/10.1080/00206819509465439>
- Sandeman HA, Clark AH, Farrar E, Arroyo Pauca G (1996) A critical appraisal of the Cayconi Formation, Crucero Basin, southeastern Peru. *J South Am Earth Sci* 9(5-6):381–392. [https://doi.org/10.1016/S0895-9811\(96\)00021-1](https://doi.org/10.1016/S0895-9811(96)00021-1)
- Sandeman HA, Clark AH, Farrar E, Arroyo-Pauca G (1997) Lithostratigraphy, petrology and ^{40}Ar - ^{39}Ar geochronology of the Crucero Supergroup, Puno Department, SE Peru. *J South Am Earth Sci* 10(3):223–245
- Santos A, Weimin G, Rivera F, Tassarini C, Cerpa L, Kojima S (2019) Early Jurassic arc related magmatism associated with porphyry copper mineralization at Zafranal, Southern Peru unraveled by zircon U-Pb ages. *Andean Geol* 46(3):445-470. <https://doi.org/10.5027/andgeoV46n3-3041>
- Savage D, Walker C, Arthur R, Rochelle C, Oda C, Takase H (2007) Alteration of bentonite by hyperalkaline fluids: A review of the role of secondary minerals. *Phys Chem Earth* 32(1–7):287-297. <https://doi.org/10.1016/j.pce.2005.08.048>.
- Schilling FR, Trumbull RB, Brasse H, Haberland C, Asch G, Bruhn D, Mai K, Haak V, Giese P, Muñoz M, Ramelow J, Rietbrock A, Ricaldi E, Vietor T (2006) Partial melting in the Central Andean crust: a review of geophysical, petrophysical, and petrologic evidence. In: Oncken O, Chong G, Franz G, Giese P, Götze H-J, Ramos V, Strecker M, Wigger P

(eds) The Andes — Active Subduction Orogeny. *Front Earth Sci*:459–474.
https://doi.org/10.1007/978-3-540-48684-8_22

Schneider A (1985) Eruptive processes, mineralization and isotopic evolution of the Los Frailes KariKari region, Boliva. Doctoral dissertation, Imperial College of Science and Technology, University of London

Schurr B, Rietbrock A, Asch G, Kind R, Oncken O (2006) Evidence for lithospheric detachment in the central Andes from local earthquake tomography. *Tectonophysics* 415(1-4):203–223. <https://doi.org/10.1016/j.tecto.2005.12.007>

Segovia-More MK, Torró L, Villanova-de-Benavent C, Ramírez-Briones J, Vallance J, Monnier L, Laurent O, Salvi S, Baby P, Proenza JA, Nieto F (2023). High-resolution mineralogy of Lithium-rich Tuff from the Macusani Volcanic Field, Puno, Peru. *Proceedings of the 17th SGA Biennial Meeting* 1:303-306

Sempere T, Jacay J (2008) Anatomy of the Central Andes: Distinguishing between western, magmatic Andes and eastern, tectonic Andes. *7th International Symposium on Andean Geodynamics*: 504-507

Sempere T, Herail G, Oller J, Bonhomme MG (1990) Late Oligocene-Early Miocene major tectonic crisis and related basins in Bolivia. *Geology* 18(10):946–949, [https://doi.org/10.1130/0091-7613\(1990\)018<0946:LOEMMT>2.3.CO;2](https://doi.org/10.1130/0091-7613(1990)018<0946:LOEMMT>2.3.CO;2)

Sempere T, Carlier G, Soler P, Fornari M, Carlotto V, Jacay J, Arispe O, Néraudeau D, Cárdenas J, Rosas S, Jiménez N (2002) Late Permian-Middle Jurassic lithospheric thinning in Peru and Bolivia, and its bearing on Andean-age tectonics. *Tectonophysics* 345(1-4):153–181. [https://doi.org/10.1016/S0040-1951\(01\)00211-6](https://doi.org/10.1016/S0040-1951(01)00211-6)

Sempere T, Jacay J, Carlotto V, Matínez W, Bedoya C, Fornari M, Roperch P, Acosta H, Acosta J, Cerpa L, Flores A, Ibarra I, Latorre O, Mamani M, Meza P, Odonne F, Orós Y, Pino A, Rodríguez R (2004) Sistemas transcurrentes de escala litosférica en el sur del Peru. *Sociedad Geológica del Peru, Publicación Especial* 5:105-110

Shand SJ (1943) *The eruptive rocks*. Second edition, John Wiley, New York, 444 p

- Shaw R, Goodenough K, Deady E, Nex P, Ruzvidzo B, Rushton J, Pearson M (2022) The Magmatic–Hydrothermal Transition in Lithium Pegmatites: Petrographic and Geochemical Characteristics of Pegmatites from the Kamativi Area, Zimbabwe. *Can Mineral* 60(6):957-987. <https://doi.org/10.3749/canmin.2100032>
- SIDEMCAT (2023) Consulta al Sistema de Derechos Mineros y Catastro. In: Instituto Geológico, Minero y Metalúrgico. <https://portal.ingemmet.gob.pe/web/guest/sidemcat>. Accessed 10 Jul 2022
- Siebel W, Schnurr WBW, Hahne K, Kraemer B, Trumbull RB, Bogaard P, Emmermann R (2001) Geochemistry and isotope systematics of small- to medium-volume Neogene-Quaternary ignimbrites in the southern central Andes: evidence for derivation from andesitic magma sources. *Chem Geol* 171(3-4):213-237. [https://doi.org/10.1016/S0009-2541\(00\)00249-7](https://doi.org/10.1016/S0009-2541(00)00249-7)
- Sillitoe R, Lehmann B (2021) Copper-rich tin deposits. *Miner Deposita* 57(1):1-11. <https://doi.org/10.1007/s00126-021-01078-9>
- Soberón D, Rodríguez R, Choquehuanca S, Gómez W (2022) Geología del cuadrángulo de Corani (hojas 28u1, 28u2, 28u3, 28u4). Instituto Geológico, Minero y Metalúrgico, Boletín Serie L: Actualización Carta Geológica Nacional (Escala 1:50 000) N° 47, 113 pp
- Soler MM (2005) Caldera Vilama (Mioceno Superior): Su Estratigrafía, Evolución Magmática y Relación con Eventos Ignimbríticos Tempranos. Puna Argentina – Altiplano Boliviano. Doctoral dissertation. Universidad Nacional de Salta, Argentina
- Somoza R, Ghidella ME (2005) Convergence in the western margin of South America during the Cenozoic: Subduction of Nazca, Farallon and Aluk plates. *Rev Asoc Geol Argent* 60(4):797-809
- Spikings R, Reitsma MJ, Boekhout F, Mišković A, Ulianov A, Chiaradia M, Gerde A, Schaltegger U (2016) Characterization of Triassic rifting in Peru and implications for

the early disassembly of western Pangaea. *Gondwana Res* 35:124–143.
<https://doi.org/10.1016/j.gr.2016.02.008>

Stacey JS, Kramers JD (1975) Approximation of terrestrial lead isotope evolution by a two-stage model. *Earth Planet Sci Lett* 26(2):207-221. [https://doi.org/10.1016/0012-821X\(75\)90088-6](https://doi.org/10.1016/0012-821X(75)90088-6)

Stamatakis MG., VasilatosC, Stamataki IS (2021) Petrology and Genesis of the Italian Zeolite Tuffs Used in the Construction Industry. *Materials Proceedings* 5(1):7.
<https://doi.org/10.3390/materproc2021005007>

Steiger RH, Jager E (1977) Subcommittee on geochronology: Convention of the use of decay constants in geo- and cosmochronology. *Earth Planet Sci Lett* 36(3):359-362.
<https://doi.org/10.1306/St6398C6>

Stepanov A, Hermann J, Rubatto D, Rapp R (2012) Experimental study of monazite/melt partitioning with implications for the REE, Th and U geochemistry of crustal rocks. *Chem Geol* 300–301:200-220. <https://doi.org/10.1016/j.chemgeo.2012.01.007>

Sterba J, Krzemień A, Fernández PR, García-Miranda C E, Valverde GF (2019) Lithium mining: Accelerating the transition to sustainable energy. *Resour Policy* 62:416–426.
<https://doi.org/10.1016/j.resourpol.2019.05.002>

Stilling A, Čern P, Vanstone PJ (2006) The Tanco pegmatite at Bernic Lake, Manitoba. XVI. zonal and bulk composition and their petrogenetic significance. *Can Mineral* 44(3):599-623. <https://doi.org/10.2113/gscanmin.44.3.599>

Stuani PLA, Candido AM, Nakasuga WM, Figueroa P, Tello SCA (2020) Fission-track evolution in Macusanite volcanic glass. *Radiat Phys Chem* 176(17):109076.
<https://doi.org/10.1016/j.radphyschem.2020.109076>

Sundell K, Saylor J, Lapen T, Styron R, Villarreal D, Usnayo P, Cárdenas J (2019) Peruvian Altiplano stratigraphy highlights along-strike variability in foreland basin evolution of the Cenozoic Central Andes. *Tectonics* 37(6):1876-1904.
<https://doi.org/10.1029/2017TC004775>

- Swarthout A, Leduc M, Rios C (2010) The Discovery History and Geology of Corani: A Significant New Ag-Pb-Zn Epithermal Deposit, Puno Department, Peru. In: Richard J, Erin M, Thomas M (eds) *The Challenge of Finding New Mineral Resources: Global Metallogeny, Innovative Exploration, and New Discoveries* 15(1). <https://doi.org/10.5382/SP.15.1.10>
- Sylvester PJ (1998) Post-collisional strongly peraluminous granites. *Lithos* 45(1-4):29-44. [https://doi.org/10.1016/S0024-4937\(98\)00024-3](https://doi.org/10.1016/S0024-4937(98)00024-3)
- Tamayo J, Salvador J, Vásquez A, Vilches C (2016) *La industria de la electricidad en el Perú: 25 años de aportes al crecimiento económico del país*, Primera ed. Organismo Supervisor de la Inversión en Energía y Minería, Lima
- Tankard AJ, Uliana MA, Welsink HJ, Ramos VA, Turic M, Franca AB, Milani EJ, Brito-Neves B.B., Eyles N, Skarmeta J, Santa Ana H, Wiens F, Cirbián M, López-Paulsen O, Germs CGB, De Wit MJ, Machacha T, Miller RM (1995) Structural and tectonic controls of basin evolution in southwestern Gondwana during the Phanerozoic. In: Tankard A, Suárez R, Welsink HJ (eds) *Petroleum Basins of South America*. *Am Assoc Pet Geol Bull* 62:5–52
- Taylor SR, McLennan SM (1981) The composition and evolution of the continental crust: Rare earth element evidence from sedimentary rocks. *Philos Trans R Soc London, Ser A* 301(1461):381–399. <https://doi.org/10.1098/rsta.1981.0119>
- Thomas R, Davidson P (2012) Water in granite and pegmatite-forming melts. *Ore Geol Rev* 46:32–46. <https://doi.org/10.1016/j.oregeorev.2012.02.006>
- Thomas R, Davidson P, Badanina E (2012) Water- and boron-rich melt inclusions in quartz from the Malkhan pegmatite, Transbaikalia, Russia. *Minerals* 2(4):435–458. <https://doi.org/10.3390/min2040435>
- Thomas R, Davidson P (2013) The missing link between granites and granitic pegmatites. *J Geosci* 58(2):183–200. <https://doi.org/10.3190/jgeosci.135>

- Thomas R, Davidson P (2016) Revisiting complete miscibility between silicate melts and hydrous fluids, and the extreme enrichment of some elements in the supercritical state — Consequences for the formation of pegmatites and ore deposits. *Ore Geol Rev* 72(1):1088-1101. <https://doi.org/10.1016/j.oregeorev.2015.10.004>
- Thouret J-C, Wörner G, Gunnell Y, Singer B, Zhang X, and Souriot T (2007) Geochronologic and stratigraphic constraints on canyon incision and Miocene uplift of the Central Andes in Peru. *Earth Planet Sci Lett* 263(3-4):151–166. <https://doi.org/10.1016/j.epsl.2007.07.023>
- Torró L, Villanova-de-Benavent C, Monnier L, Laurent O, Segovia-More MK, Sanandres-Flores M, Ramírez-Briones J, Vallance J, Salvi S, Baby P, Proenza JA, Nieto F (2023) Lepidolite and zinnwaldite mineralization in ‘lithium-rich tuffs’ from the Macusani Volcanic Field, Puno, Peru. *Proceedings of the 17th SGA Biennial Meeting* 1:319-322.
- Townsend M, Huber C, Degruyter W, Bachmann O (2019) Magma chamber growth during intercaldera periods: Insights from thermo-mechanical modeling with applications to Laguna del Maule, Campi Flegrei, Santorini, and Aso. *Geochem, Geophys* 20(3):1574–1591. <https://doi.org/10.1029/2018GC008103>
- Transport & Environment (2018) Cars are retired on average after close to 15 years. How to decarbonise European transport by 2050.
- Transport & Environment (2021) From dirty oil to clean batteries
- Trading Economics (2023) Lithium. <https://tradingeconomics.com/commodity/lithium>. Accessed 18 Dec 2023
- Troch J, Huber C, Bachmann O (2022) The physical and chemical evolution of magmatic fluids in near-solidus silicic magma reservoirs: Implications for the formation of pegmatites. *Am Min* 107(2):190–205. <https://doi.org/10.2138/am-2021-7915>
- Trumbull R, Riller U, Oncken O, Scheuber E, Munier K, Hongn F (2006) The time-space distribution of Cenozoic volcanism in the south-central Andes: A new data compilation and some tectonic implications. In: Oncken O, Chong G, Franz G, Giese P, Götze H-J,

- Ramos V, Strecker M, Wigger P (eds) *The Andes — Active Subduction Orogeny*. Springer, Berlin, Heidelberg, pp 29-43. https://doi.org/10.1007/978-3-540-48684-8_2
- Ullrich TD (2006) Report on $^{40}\text{Ar}/^{39}\text{Ar}$ geochronological analysis: Unpublished report to Bear Creek Mining, 12 pp
- United States Geological Survey (2023) *Mineral Commodity Summaries 2023*. <https://doi.org/10.3133/mcs2023>
- Valencia J, Arroyo G (1985) Geochemical aspects of the uranium occurrences of Macusani, Puno (Peru). International Atomic Energy Agency, *Uranium Deposits in Volcanic Rocks, Proceedings of a Technical Committee Meeting*, pp 275–288
- Valencia M, Paico D, Rivera R (2010) Geoquímica y mineralización de los depósitos syn-rift Permotriásicos del sureste del Perú. XV Congreso Peruano de Geología, Resúmenes Extendidos, Sociedad Geológica del Perú, *Publicación Especial 9*:656-659
- van Zalinge, ME, Mark DF, Sparks RSJ, Tremblay MM, Keller CB, Cooper FJ, Rust A (2022) Timescales for pluton growth, magma-chamber formation and super-eruptions. *Nature* 608:87–92. <https://doi.org/10.1038/s41586-022-04921-9>
- Victor P, Oncken O, Glodny J (2004) Uplift of the western Altiplano plateau: Evidence from the Precordillera between 20° and 21°S (northern Chile). *Tectonics* 23(4):TC4004. <https://doi.org/10.1029/2003TC001519>
- Vilca Arpasi PC (2020) *El proyecto de explotación de litio en Puno*. Asociación Servicios Educativos Rurales, Lima
- Viramonte JG, Petrinovic IA (1990) Calderas asociadas a megafacturas transcurrentes en los Andes Centrales del Sur. XI Congreso Geológico Argentino, *Actas II*:369-372
- Viramonte JG, Galliski MA, Saavedra G, Aparicio A, Garcia Cacho L, and Escorza MC (1984) El fin del vulcanismo básico de la Depresión de Arizaro, Provincia de Salta, República Argentina. IX Congreso Geológico Argentino, *Actas III*:234-254

- Wagner LS, Beck S, Zandt G (2005) Upper mantle structure in the south central Chilean subduction zone (30° to 36°S). *J Geophys Res* 110:B01308. <https://doi.org/10.1029/2004JB003238>
- Wagner LS, Beck S, Zandt G, Ducea MN (2006) Depleted lithosphere, cold, trapped asthenosphere, and frozen melt puddles above the flat slab in central Chile and Argentina. *Earth Planet Sci Lett* 245(1-2):289–301. <https://doi.org/10.1016/j.epsl.2006.02.014>
- Wang W, Wei H-Z, Jiang S-Y, Tan H-B, Eastoe J, Williams-Jones A, Hohl S, Wu H-P (2019) The origin of rare alkali metals in geothermal fluids of southern Tibet, China: A silicon isotope perspective. *Sci Rep* 9:7918. <https://doi.org/10.1038/s41598-019-44249-5>
- Wasserburg GJ, Jacobsen SB, DePaolo DJ, McCulloch MT, Wen J (1981) Precise determinations of Sm/Nd ratios, Sm and Nd isotopic abundances in standard solutions. *Geochim Cosmochim Acta* 45(12):2311-2323. [https://doi.org/10.1016/0016-7037\(81\)90085-5](https://doi.org/10.1016/0016-7037(81)90085-5)
- Watson EB, Harrison TM (1983) Zircon saturation revisited: temperature and composition effects in a variety of crustal magma types. *Earth Planet Sci Lett* 64(2):295–304. [https://doi.org/10.1016/0012-821X\(83\)90211-X](https://doi.org/10.1016/0012-821X(83)90211-X)
- Ward KM, Zandt G, Beck SL, Wagner LS, Tavera H (2016) Lithospheric structure beneath the northern Central Andean Plateau from the joint inversion of ambient noise and earthquake-generated surface waves. *J Geophys Res Solid Earth* 121(11):8217–8238. <https://doi.org/10.1002/2016JB013237>
- Ward KM, Delph JR, Zandt G, Beck SL, Ducea MN (2017) Magmatic evolution of a Cordilleran flare-up and its role in the creation of silicic crust. *Sci Rep* 7:9047. <https://doi.org/10.1038/s41598-017-09015-5>
- Wasteneys HAHP (1990) Epithermal silver mineralization with a mid-Tertiary diatreme: Santa Bárbara, Santa Lucía District, Puno, Peru. Ph.D. thesis, Kingston, Ontario, Canada, Queen's University

- Webster JD, Duffield WA (1994) Extreme halogen abundances in tin-rich magma of the Taylor Creek Rhyolite, New Mexico. *Econ Geol* 89(4):840–850. <https://doi.org/10.2113/gsecongeo.89.4.840>
- White D (1957) Thermal waters of volcanic origin. *Geol Soc Am Bull* 68:1637-1658
- Wilde P, Quinby-Hunt M, Erdtmann B-D (1995) The whole-rock cerium anomaly: a potential indicator of eustatic sea-level changes in shales of the anoxic facies. *Sediment Geol* 101(1-2):43-53. [https://doi.org/10.1016/0037-0738\(95\)00020-8](https://doi.org/10.1016/0037-0738(95)00020-8)
- Winter JD (2014) *Principles of Igneous and Metamorphic Petrology*. Pearson New International Edition. Pearson Education Limited, Harlow, UK
- Wölbern I, Heit B, Yuan X, Asch G, Kind R (2009) Receiver function images from the Moho and the slab below the Altiplano and Puna plateaus in the Central Andes. *Geophys J Int* 177(1):296–308. <https://doi.org/10.1111/j.1365-246X.2008.04075.x>
- Wolf MB, Romer RL, Glodny J (2019) Isotope disequilibrium during partial melting of metasedimentary rocks. *Geochim Cosmochim Acta* 257:163–183. <https://doi.org/10.1016/j.gca.2019.05.008>
- Wörner G, Schildgen TF, Reich M (2018) The Central Andes: Elements of an extreme land. *Elements* 14(4):225–230. <https://doi.org/10.2138/gselements.14.4.225>
- Wörner G, Hammerschmidt K, Henjes-Kunst F, Lezaun J, Wilke H (2000) Geochronology ($^{40}\text{Ar}/^{39}\text{Ar}$, K-Ar and He-exposure ages) of Cenozoic magmatic rocks from Northern Chile (18–22°): implications for magmatism and tectonic evolution of the central Andes. *Rev Geol Chile* 27(2):205–240
- Xie L, Wang R-C, Che X-D, Huang F-F, Erdmann S, Zhang W-L (2016) Tracking magmatic and hydrothermal Nb–Ta–W–Sn fractionation using mineral textures and composition: A case study from the late Cretaceous Jiepailing ore district in the Nanling Range in South China. *Ore Geol Rev* 78:300–321. <https://doi.org/10.1016/j.oregeorev.2016.04.003>

- Xu B, Jiang S-Y, Wang R, Ma L, Zhao K, Yan X (2015) Late Cretaceous granites from the giant Dulong Sn-polymetallic ore district in Yunnan Province, South China: Geochronology, geochemistry, mineral chemistry and Nd–Hf isotopic compositions. *Lithos* 218–219:54–72. <https://doi.org/10.1016/j.lithos.2015.01.004>
- Yañéz GA, Ramiro CR, von Huene R, Diaz J (2001) Magnetic anomaly interpretation across the southern Central Andes (32°–34°S): The role of the Juan Fernández Ridge in the late Tertiary evolution of the margin. *J Geophys Res* 106(B4):6325–6345. <https://doi.org/10.1029/2000JB900337>
- Yuan X, Sobolev SV, Kind R (2002) Moho topography in the Central Andes and its geodynamic implications. *Earth Planet Sci Lett* 199(3-4):389–402. [https://doi.org/10.1016/S0012-821X\(02\)00589-7](https://doi.org/10.1016/S0012-821X(02)00589-7)
- Zaraisky GP, Aksyuk AM, Devyatova VN, Udoratina OV, Chevychelov VY (2009) The Zr/Hf ratio as a fractionation indicator of rare-metal granites. *Petrology* (17):25–45. <https://doi.org/10.1134/S0869591109010020>
- Zartman RE, Doe BR (1981) Plumbotectonics—the model. *Tectonophysics* 75(1-2):135–162. [https://doi.org/10.1016/0040-1951\(81\)90213-4](https://doi.org/10.1016/0040-1951(81)90213-4)
- Zhu Z-Y, Wang R-C, Che X-D, Zhu J-C, Wei X-L, Huang X (2015) Magmatic–hydrothermal rare-element mineralization in the Songshugang granite (northeastern Jiangxi, China): Insights from an electron-microprobe study of Nb–Ta–Zr minerals. *Ore Geol Rev* 65(4):749–760. <https://doi.org/10.1016/j.oregeorev.2014.07.021>



APPENDIX A
List of samples

Sample	UTM E ²	UTM N ²	Elevation (m.a.s.l.)	DDH ¹	Depth (m)	Lithotype	Concession	Area ³	Field description
2021-MAC-003	317848	8451426	4872			Quenamari Suite granite	Falchani	Falchani	Fresh stock of granitic composition. Porphyritic, medium grained. Large K feldspar crystals with Carlsbad twinning up to 20 mm in length.
2021-MAC-008A	317880	8451590	4899			Lithium-rich Tuff	Falchani	Falchani	Very fine grained. Bedded and tectonized (fault zone). Fine lamination is strongly deformed. Abundant, partially dissolved concretions.
2021-MAC-008B	317880	8451590	4899			Lithium-rich Tuff	Falchani	Falchani	Very fine grained. Bedded and tectonized (fault zone). Fine lamination is strongly deformed. Dissolved concretion molds.
2021-MAC-011A	319446	8451382	4716			Lithium-rich Tuff	Falchani	Falchani	Very fine grained, white to cream color. Lamination and abundant concretions.
2021-MAC-011B	319446	8451382	4716			Lithium-rich Tuff	Falchani	Falchani	Very fine grained, white to cream color. Lamination and abundant concretions.
2021-MAC-012	319564	8451884	4745			Post-Li-ore ash-flow tuff	Falchani	Falchani	Rhyolitic tuff. Medium-grained.
2021-MAC-016	312300	8451977	4820			Quenamari Suite granite	Huarituña 4	Quelcaya	Dyke. Granularity is variable from contact (fine grained) to core (medium grained). Aphanitic, pale cream groundmass.
2021-MAC-018B	312313	8452026	4846			Post-Li-ore ash-flow tuff	Huarituña 4	Quelcaya	Welded ignimbrite. Fossilizes deformation.
2021-MAC-019A	308594	8451082	4915			White tuff	Sapanuta 3	Quelcaya	8-to-10-m-thick, fine-grained, white, bedded tuff. Subvertical, dipping S.
2021-MAC-020	308600	8451057	4903			Post-Li-ore ash-flow tuff	Sapanuta 3	Quelcaya	Mapped as rhyolite, it hosts rock fragments and therefore it is classified as a crystal-rich tuff of rhyolitic composition. Altered.
2021-MAC-021	308601	8450888	4849			White tuff	Sapanuta 3	Quelcaya	Bedded, crystal-poor, white tuff. Dipping south. Sharp lateral fault contact with rhyolite.
2021-MAC-022A	308738	8450791	4777			White tuff	Sapanuta 3	Quelcaya	White, very fine-grained, bedded tuff. Contains some black crystal clasts.
2021-MAC-022B	308738	8450791	4777			White tuff	Sapanuta 3	Quelcaya	White, fine-grained, bedded tuff. Stibnite and cinnabar are observed in some surfaces of the sample. Stibnite crystals are up to 8 cm in length
2021-MAC-025	318397	8451249	4884			Lithium-rich Tuff	Falchani	Falchani	Massive, crystal-poor, white, fine-grained, bedded tuff.
2021-MAC-026	318247	8451169	4903			Lithium-rich Tuff	Falchani	Falchani	White and apple green, coarsely laminated to anastomosed fine-grained tuff with grayish-green blocky patches.
2021-MAC-031	318003	8451079	4943			Lithium-rich Tuff	Falchani	Falchani	White, fine-grained tuffs in fault zone. Dissemination of small biotite crystal clasts.
2021-MAC-033	319729	8451374		PCHAC 01-TSW(1)	37.05-37.10	Post-Li-ore ash-flow tuff	Falchani	Falchani	Rhyolitic tuff, quartz, K feldspar, and biotite (up to 2 mm in size) crystal clasts.
2021-MAC-034	319729	8451374		PCHAC 01-TSW(1)	42.80-42.90	Post-Li-ore ash-flow tuff	Falchani	Falchani	Crystal- and lithic-rich tuff.

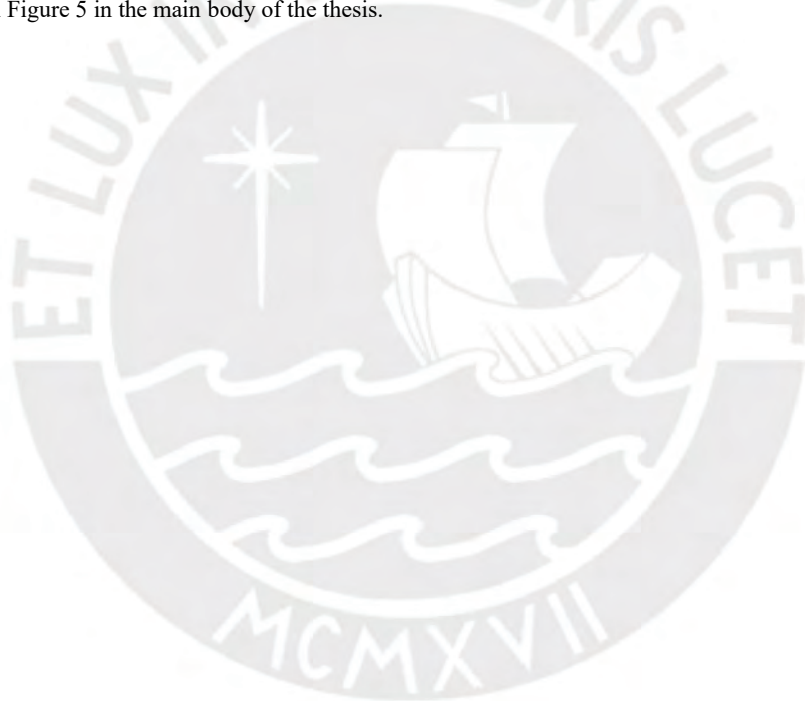
Sample	UTM E ²	UTM N ²	Elevation (m.a.s.l.)	DDH ¹	Depth (m)	Lithotype	Concession	Area ³	Field description
2021-MAC-035	319729	8451374		PCHAC 01-TSW(1)	62.55-62.60	Upper Breccia	Falchani	Falchani	Brecciated, containing angular, mm- to cm-scale white tuff and deep grey lithic fragments.
2021-MAC-038	319729	8451374		PCHAC 01-TSW(1)	80.35-80.45	Lithium-rich Tuff	Falchani	Falchani	White, fine-grained tuff. Bedded. Millimeter-scale lamination is slumped.
2021-MAC-039	319729	8451374		PCHAC 01-TSW(1)	149.00-149.10	Lithium-rich Tuff	Falchani	Falchani	White, fine-grained tuff. Bedded. Millimeter-scale lamination is slumped.
2021-MAC-040	319729	8451374		PCHAC 01-TSW(1)	183.25-183.35	Lithium-rich Tuff	Falchani	Falchani	White, fine-grained tuff. Bedding and strongly folded (slumped) lamination.
2021-MAC-042	319729	8451374		PCHAC 01-TSW(1)	195.80-195.90	Lower Breccia	Falchani	Falchani	Breccia containing tuff rock fragments in dark brown matrix.
2021-MAC-045	319729	8451374		PCHAC 01-TSW(1)	257.10-257.20	Pre-Li-ore ash-flow tuff	Falchani	Falchani	Pyroclastic rock (not intrusive unit, as described in log). Crystal-rich lapilli/breccia tuff. Juvenile rock fragments are angular, show curvilinear outlines, and are often deformed (elongated).
2021-MAC-046	319729	8451374		PCHAC 01-TSW(1)	260.40-260.50	Pre-Li-ore ash-flow tuff	Falchani	Falchani	Crystal-rich tuff. It hosts large K feldspar crystals up to 20 mm in length, showing Carlsbad twinning.
2021-MAC-047	319748	8451643		PCHAC 04-TV	33.00-33.10	Post-Li-ore ash-flow tuff	Ocaca 4	Falchani	Poorly sorted, crystal-rich lapilli-tuff with white aphanitic matrix and variable proportions of lapilli-sized juvenile clasts.
2021-MAC-048	319748	8451643		PCHAC 04-TV	174.40-174.50	Lithium-rich Tuff	Ocaca 4	Falchani	Bedded, white tuff. Very fine lamination (mm-scale) is planar to anastomosed.
2021-MAC-049	319748	8451643		PCHAC 04-TV	226.00-226.10	Lower Breccia	Ocaca 4	Falchani	Altered breccia with abundant tuff fragments. Clayey texture.
2021-MAC-050	318576	8451429		PCHAC 32-TNW	34.50-34.60	Upper Breccia	Falchani	Falchani	Disaggregated material, rich in clay minerals.
2021-MAC-051	318576	8451429		PCHAC 32-TNW	Approx. 43.00	Upper Breccia	Falchani	Falchani	Soft, white material, rich in clay minerals. Brecciated texture.
2021-MAC-052	318576	8451429		PCHAC 32-TNW	Approx. 52.50	Upper Breccia	Falchani	Falchani	Disaggregated material, rich in clay minerals. Brecciated texture.
2021-MAC-053	318576	8451429		PCHAC 32-TNW	Approx. 115.00	Lithium-rich Tuff	Falchani	Falchani	Disaggregated material, rich in clay minerals. Some of the clasts show internal lamination.
2021-MAC-055	321619	8439706	4695			Picotani Suite granite	Colibri LXXIII	La Huaña	Porphyritic granite hosting K feldspar megacrysts up to 15 cm in length (monzonitic texture). Two phenocryst sizes: biotite, quartz, and plagioclase < 2 cm, and K feldspar < 15 cm. Phantoms of cordierite and altered cordierite crystals.
2021-MAC-065A	316951	8440039	5071			White tuff	Antacora seis	La Huaña	Bedded, fine- to medium-grained felsic tuff. It hosts lithic fragments up to 10 cm in diameter.
2021-MAC-065B	316951	8440039	5071			White tuff	Antacora seis	La Huaña	Bedded, fine- to medium-grained felsic tuff. Internal lamination is contorted.
2021-MAC-065C	316951	8440039	5071			White tuff	Antacora seis	La Huaña	Bedded, fine- to medium-grained felsic tuff. It hosts sedimentary and igneous lithic fragments up to 10 cm in diameter. Dissolved mm-scale concretions.

Sample	UTM E ²	UTM N ²	Elevation (m.a.s.l.)	DDH ¹	Depth (m)	Lithotype	Concession	Area ³	Field description
2021-MAC-066	316910	8439957	5170			White tuff	Antacora seis	La Huaña	Bedded, crystal-rich- fine- to medium-grained felsic tuff.
2021-MAC-067A	319344	8437743	5031			White tuff	San Vicente White	La Huaña	Very fine-grained tuff hosting randomly distributed subhedral quartz crystals up to 5 mm in diameter. Verticalized and deformed (fault zone).
2021-MAC-067B	319344	8437743	5031			White tuff	San Vicente White	La Huaña	Very fine-grained tuff hosting randomly distributed subhedral quartz crystals up to 5 mm in diameter. Verticalized and deformed (fault zone).
2021-MAC-067C	319344	8437743	5031			White tuff	San Vicente White	La Huaña	Very fine-grained tuff hosting randomly distributed subhedral quartz crystals up to 5 mm in diameter. Verticalized and deformed (fault zone).

¹In DDH samples, the given coordinates correspond to the location of the DDH collar.

²UTM coordinates are reported in the 19L zone.

³Zones as shown in Figure 5 in the main body of the thesis.





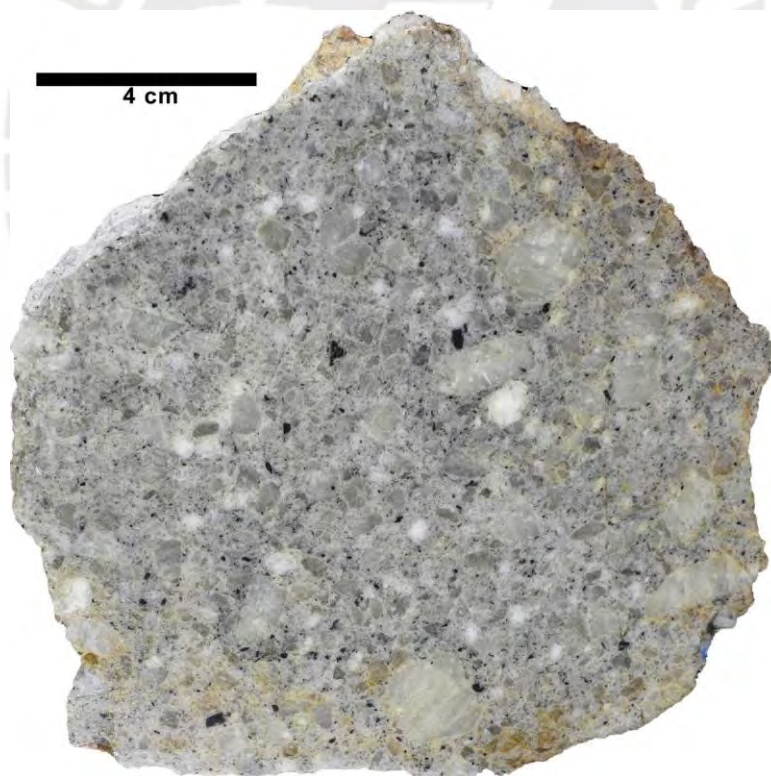
APPENDIX B

Hand sample pictures and description

2021-MAC-003

Leucocratic, medium- to coarse-grained, alkali feldspar-phyric biotite-muscovite-tourmaline-bearing granite with hypidiomorphic texture and fine-grained, isotropic groundmass.

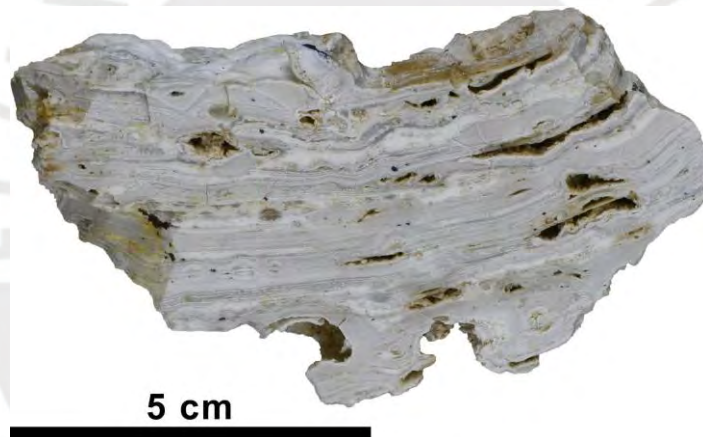
Euhedral prismatic alkali feldspar phenocrysts are translucent and white. Alkali feldspar phenocrysts show a wide range of grain sizes (coarse- to very coarse-grained, up to 20 mm long), common simple Carlsbad twinning, and scarce inclusions of fine- to very fine-grained biotite crystals. Quartz phenocrysts are anhedral, sub-rounded to angular, fine- to medium-grained (up to 5 mm), and have variable sphericity. Subhedral booklets of biotite phenocrysts are evenly distributed and show three distinct size populations: scarce medium- to coarse grained (2.5 to 6 mm), evenly distributed fine- to medium grained (up to 1.2 mm), and ubiquitous very fine-grained (microphenocrysts). The coarser biotite crystals are poikilitic and host very fine- to fine-grained, anhedral, rounded to sub-rounded quartz inclusions. Euhedral tabular muscovite phenocrysts are fine- to medium-grained, up to 1.7 mm, translucent, and exhibit vitreous luster, brownish-pink color, and perfect cleavage on {001}. Euhedral prismatic tourmaline crystals are elongated, 1.2-1.7 mm long, and exhibits striations, ditrigonal basal sections, vitreous luster, brownish-black color, and conchoidal fracture.



2021-MAC-008A

Hard, finely laminated, whitish tuffaceous mudstone with cavities after dissolution of concretions. It is interpreted as a resedimented syn-eruptive felsic volcanoclastic rock that experienced soft-sediment deformation.

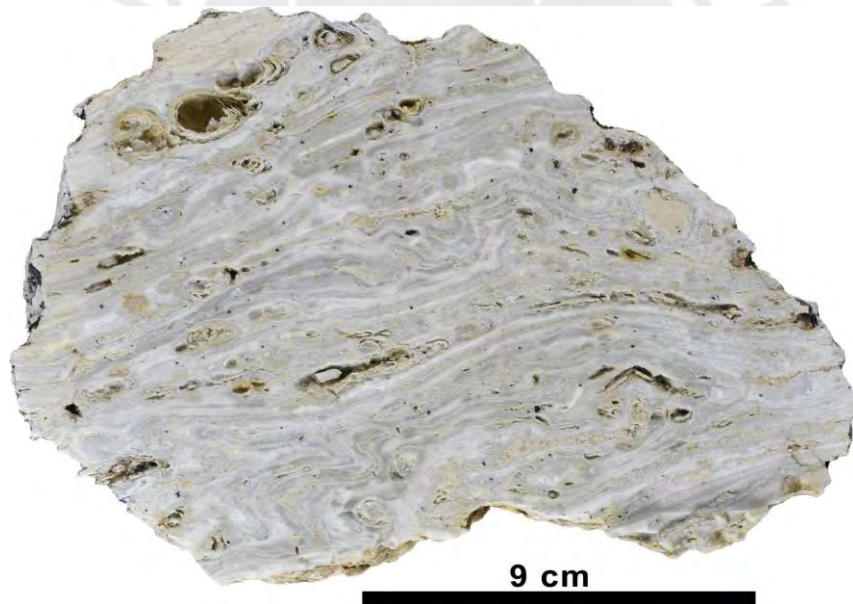
Alternating white/gray laminae are irregularly stacked and make up wavy levels intercalated with undeformed levels. Unevenly distributed, medium ash-sized biotite crystal clasts are bedded within laminae. Cavities exhibit two main morphologies: moderate sphericity (1-2 length/thickness ratios, with 1-16 mm long axes parallel to the laminated microstructure); and flattened, to planar, with elongated to irregular shapes. Adjacent spherical cavities may join within a given sedimentary level. Cavities may host concretion relicts which are composed of fine concentric bands with decreasing cement content from core to edge (cohesive cores). Cavity walls and surfaces of concretion relicts are coated by very fine aggregates composed of euhedral, tabular, brownish-orange crystals with hexagonal basal section, pearly luster, and very good {001} cleavage. Very fine to fine (up to 0.5 mm) acicular radiating crystal aggregates, which are translucent and colorless, and very fine druses (probably quartz) occur coating cavity walls as well.



2021-MAC-008B

Hard, finely laminated, whitish tuffaceous mudstone with cavities and relicts of concretions. Interpreted as a resedimented syn-eruptive felsic volcanoclastic rock that experienced soft-sediment deformation.

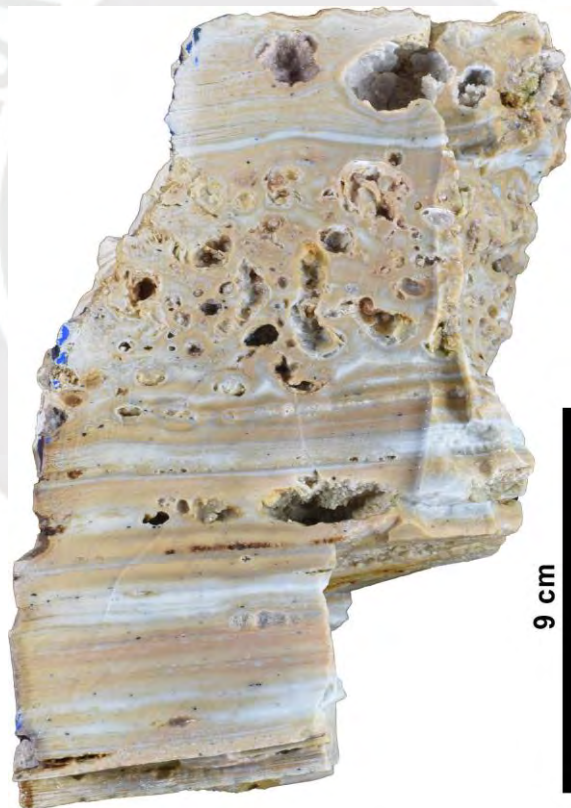
Alternating white/gray laminae are irregularly stacked and make up strongly wrinkled- and convoluted-levels intercalated with gently folded levels. Unevenly distributed medium ash-grained biotite crystal clasts are embedded within laminae. Cavities exhibit two morphologies: concretion molds with high- to moderate-sphericity (1 to 2 length/thickness ratios, with 4 to >20 mm long parallel the laminated microstructure); and flattened ovoid, planar, or irregular. Some adjacent cavities may join within a level. Cavities may host concretion relicts which are scarce and exhibit fine concentric bands with decreasing cement content from core to edge. Some plastically deformed levels exhibit asymmetric folds, whose geometry appears to have been partially controlled by preexisting concretions. Cavity walls and concretion relict surfaces are coated by very fine-grained aggregates of euhedral-tabular brownish-orange crystals with hexagonal basal sections, pearly luster and very good {001} cleavage. Very fine to fine (up to 0.5 mm), acicular, radiating, translucent and colorless, crystal aggregates (probably quartz) form druses in cavities walls.



2021-MAC-011A

Very hard, finely laminated, orange-beige mudstone with relatively abundant cavities. Interpreted as a resedimented syn-eruptive felsic volcanoclastic rock that experienced soft-sediment deformation.

Alternating orange-beige/white laminae are irregularly stacked and make up planar and gently folded levels that host unevenly distributed matrix-supported medium ash-grained biotite crystal clasts. Cavities exhibit two morphologies: high- to moderate-sphericity voids that are 1-7 mm long and appear with long axes parallel to the laminated microstructure; and flattened ovoid-cavities with irregular outline. Adjacent spherical cavities may join within a level (e.g., lateral union of at least 4 spheres of 3-2 mm each). In an extremely convoluted, 4.5 cm-thick level, closed packaged ovoid cavities with high sphericity up to 5 mm of diameter resemble a sponge-like texture. Cavities may host scarce concretion relicts that exhibit fine concentric bands with decreasing cement content from core to edge. Cavity walls are generally coated by very fine-grained aggregates of euhedral-tabular brownish-orange crystals with hexagonal basal sections, pearly luster, and very good {001} cleavage. Very fine druses (probably quartz) also occur in cavity walls.



2021-MAC-011B

Cohesive, finely laminated, whitish tuffaceous mudstone. It is interpreted as a resedimented syn-eruptive felsic volcanoclastic rock that experienced soft-sediment deformation.

Alternating beige/white laminae are evenly stacked and make up wavy- to strongly wrinkled-levels that host matrix-supported ash-sized quartz, feldspar, and biotite crystal clasts. Scarce cavities are tabular and parallel to the rock fabric. Feldspar and quartz crystal clasts are angular to sub-angular. Biotite crystal clasts are unaltered and show two distinct size populations: fine ash-sized, and medium- to coarse ash-sized.



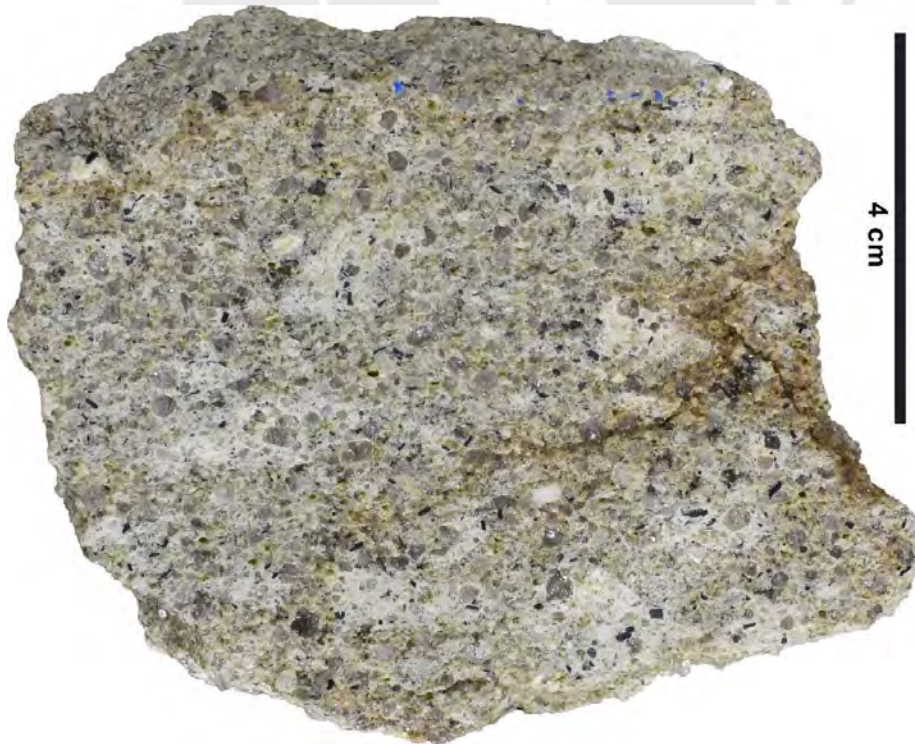
2021-MAC-012

Leucocratic, cohesive, poorly sorted, crystal-rich lapilli- and ash-flow tuff with a white aphanitic matrix and variable proportions of ash- to lapilli-sized juvenile clasts.

Clast-supported crystal clasts are medium-ash- to fine-lapilli-sized and consist mainly of quartz, feldspar, and biotite, and local andalusite. Quartz crystal clasts are gray, translucent, subhedral and anhedral, and exhibit sub angular to -rounded bipyramidal shapes. Alkali feldspar crystal clasts are colorless, angular to sub-angular, euhedral, and prismatic. Biotite crystal clasts are unaltered, euhedral, and show two distinct size populations: ubiquitous fine ash, and coarse ash- to fine lapilli. Both quartz and alkali feldspar occasionally host fine- to very fine-grained tabular biotite crystal inclusions. Scarce translucent brownish-pink andalusite crystal clasts are coarse ash-sized, up to 1.5 mm, and exhibit prismatic shapes. Prismatic plagioclase molds are usually partially filled by a greenish mustard-color, waxy, very fine-grained material.

Juvenile fragments include flattened and slightly flattened lapilli-sized clasts of porphyritic pumice up to 20 mm long, with the same mineralogical and textural characteristics as the surrounding rock except for a lesser proportion of crystals. Pumice and biotite crystal clasts exhibit a common orientation. Lithic fragments are very scarce and include angular clasts of dark gray (up to 5 mm) and black (up to 10 mm) shale, both with low sphericity.

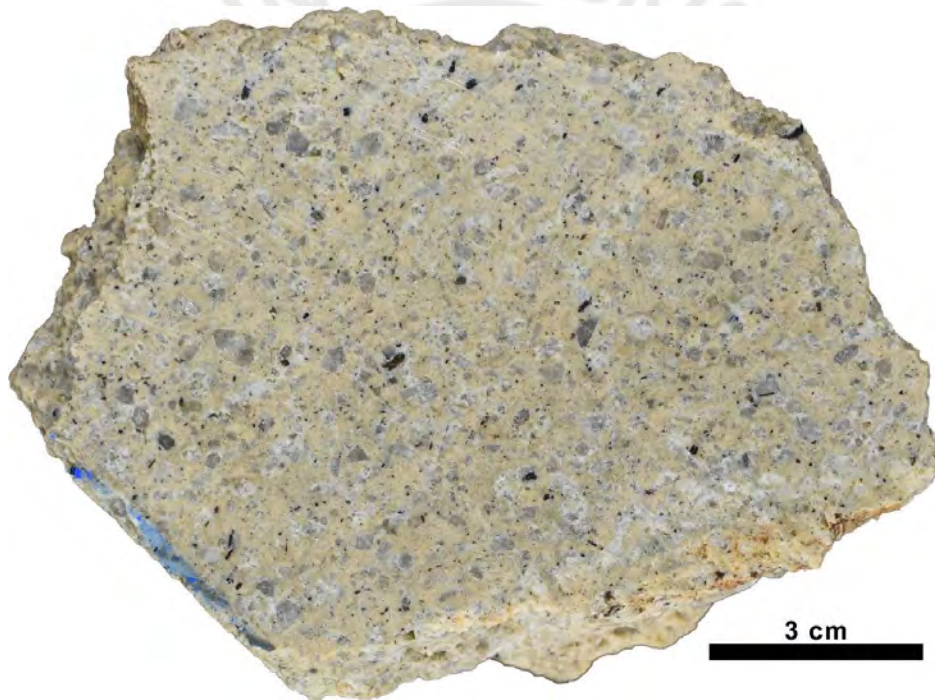
Surface-impregnated ferric oxides and hydroxides exhibit red-orange color.



2021-MAC-016

Leucocratic, medium-grained, quartz-feldspar-biotite-phyric, tourmaline-bearing, granitic dyke with hypidiomorphic texture, and green-beige aphanitic mesostasis representing 40-60% of the rock volume.

Euhedral prismatic alkali feldspar phenocrysts are medium-grained, up to 5 mm long, and translucent. Subhedral to anhedral quartz phenocrysts are subhedral, angular to sub-angular, medium-grained, up to 3 mm in size, translucent, and gray in color. Euhedral to subhedral biotite phenocrysts are reddish brown to brownish red in color and show three distinct size populations: scarce unevenly distributed medium-grained (up to 1.5 mm), evenly distributed fine-grained (up to 0.7 mm), and ubiquitous evenly distributed very fine-grained (microphenocrysts). Euhedral, prismatic, black tourmaline crystals show lengths in range from 1.2 to 1.7 mm, striations parallel to the c axis, ditrigonal basal sections, vitreous luster, and conchoidal fracture. Fine-grained plagioclase phenocryst molds are up to 0.8 mm long and partially filled by a silvery green, very fine-grained material.

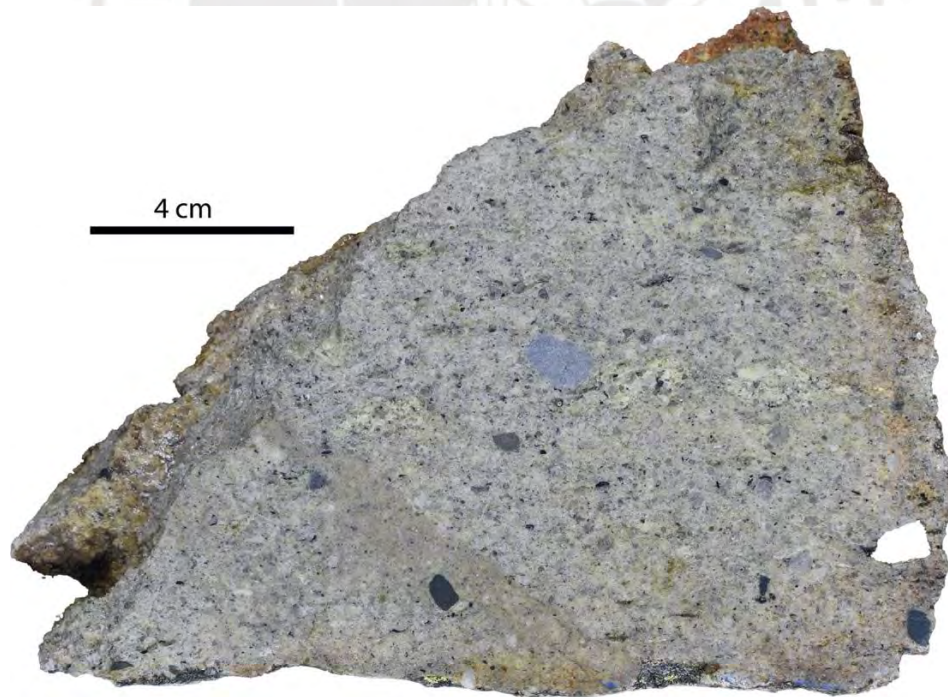


2021-MAC-018B

Leucocratic, cohesive, poorly sorted, crystal-rich lapilli- and ash-flow tuff with white aphanitic matrix and variable proportions of altered ash- to lapilli-sized juvenile and accidental lithic clasts. The rock is cut by 1 to 2 cm-thick veins filled by a very fine-grained white material with cryptic halos and, less frequently, with up to 6 mm-thick pinkish brown halos.

Clast-supported crystal clasts are medium ash- to fine lapilli-sized and consist mainly of quartz, feldspar, and biotite, and local andalusite. Quartz crystal clasts are the most abundant rock component and are translucent, subhedral to anhedral and exhibit sub angular to - rounded bipyramidal shapes. Translucent, colorless alkali feldspar crystal clasts are angular to sub-angular. Biotite crystal clasts show two distinct size populations: ubiquitous fine ash, and coarse ash- to fine lapilli. Both quartz and alkali feldspar locally host fine- to very fine-grained tabular biotite inclusions. Scarce translucent brownish pink andalusite crystal clasts are coarse ash-sized, prismatic, and up to 1.5 mm in length. Prismatic plagioclase molds are usually partially filled by a greenish mustard, waxy, very fine-grained material.

Juvenile fragments include relicts of “flame-like” lenses of porphyritic pumice up to 20 mm long that are altered to a greenish mustard, waxy, very fine-grained material. Relicts of porphyritic pumice have the same mineralogical and textural characteristics as the surrounding rock except for a lesser abundance of crystals. Accidental clasts of porphyritic basalt/andesite and black and gray shale exhibit a wide variety of shapes, sizes. Biotite crystal clasts, pumice fiammes, and some of the lithic clasts exhibit common orientation.



2021-MAC-019A

Massive, hard, slightly gray tuffaceous mudstone interpreted as a resedimented syn-eruptive felsic volcaniclastic rock.

Laterally discontinuous thin (mm-scale) white levels are mud-size grained. Matrix-supported, medium ash-size biotite crystal clasts are scarce and randomly distributed.

Surface-impregnate ferric oxides and hydroxides are brown-orange color and in fresh surfaces occur mostly along fractures.



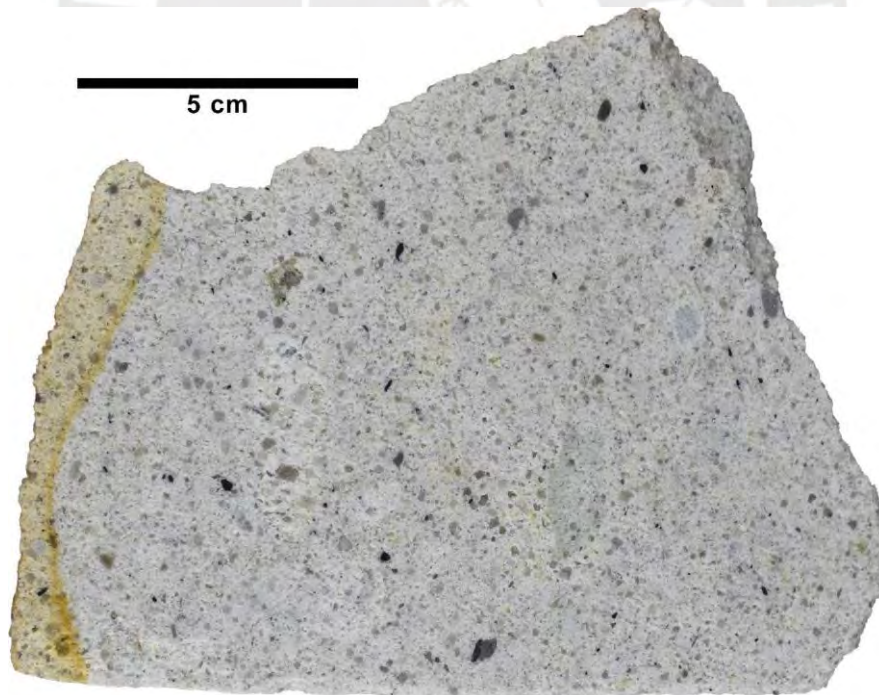
2021-MAC-020

Leucocratic, cohesive, poorly sorted, crystal-rich lapilli- and ash-flow tuff with white aphanitic matrix and variable proportions of lapilli-sized juvenile clasts.

Clast-supported crystal clasts are fine ash- to fine lapilli-sized and consist mainly of quartz, feldspar, biotite, and cordierite. Quartz crystal clasts are translucent, subhedral to anhedral, and exhibit sub-rounded to sub-angular, bipyramidal shapes. Translucent, colorless alkali feldspar crystal clasts are euhedral, and exhibit sub-rounded to sub-angular, prismatic shapes. Biotite crystal clasts are fresh, euhedral, and show two distinct size populations: ubiquitous fine ash and unevenly distributed coarse ash to fine lapilli (up to 5 mm). Both quartz and alkali feldspar generally host variable amounts of very fine-grained biotite inclusions. Scarce prismatic plagioclase molds are coarse ash-sized, up to 1 mm in width, and were filled by a very fine-grained, extremely soft, milky-white material. Very scarce, gray, individual subhedral cordierite crystal clasts host inclusions of a fine-grained, black material.

Juvenile fragments include up to 40 mm-long flattened clasts of porphyritic pumice with 20 to 2.75 length:thickness ratios. Pumice clasts exhibit the same mineralogical and textural characteristics as the surrounding rock except for a lesser abundance of crystals. Lithic fragments are very scarce and include angular to sub-angular accidental clasts of dark shale. Pumice clasts and biotite crystal clasts exhibit a common orientation.

Surface-impregnate ferric oxides and hydroxides exhibit a red-orange color, and are commonly found along cavities walls.



2021-MAC-021

Massive, cohesive, milky white, tuffaceous mudstone interpreted as a resedimented syn-eruptive felsic volcanoclastic rock.

Unevenly distributed, matrix-supported, medium ash-sized biotite crystal clasts are scarce and randomly distributed in a very fine-grained matrix.



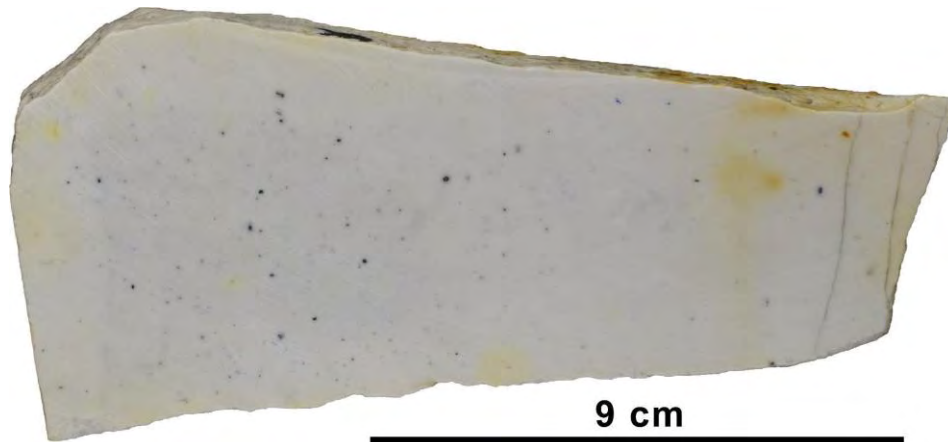
2021-MAC-022A

Massive, hard, whitish, tuffaceous mudstone with secondary, low-temperature Sb-Hg hydrothermal mineralization. The rock is interpreted as a resedimented syn-eruptive felsic volcanoclastic rock.

Matrix-supported medium ash-size biotite crystal clasts are unevenly distributed in the white matrix.

Radiating crystal aggregates of acicular stibnite are scarce and less than 1 mm in size.

Surface-impregnate ferric oxides and hydroxides exhibit brown-orange colors.



2021-MAC-022B

Massive, hard, white to pale gray, tuffaceous mudstone with low-temperature As-Sb-Hg-S hydrothermal mineralization. The rock is interpreted as a resedimented syn-eruptive felsic volcanoclastic rock.

Scarce matrix-supported medium ash-size biotite crystal clasts are unevenly distributed in the white matrix.

Abundant radiating crystal aggregates of acicular stibnite are up to 7 mm long and disseminated, very fine-grained, orange of realgar/orpiment patches with lesser cinnabar are unevenly distributed along planes fracture and bedding.



2021-MAC-025

Massive, cohesive, white to pale gray, tuffaceous mudstone interpreted as a resedimented syn-eruptive felsic volcaniclastic rock.

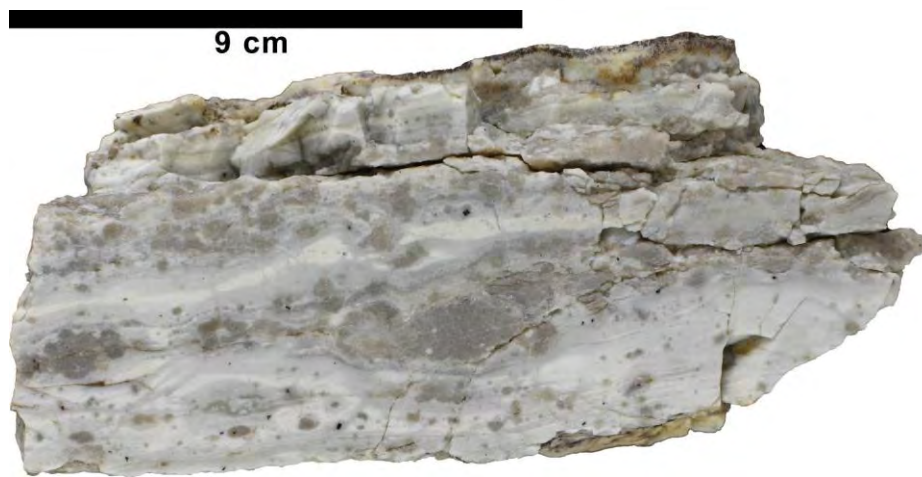
Matrix-supported, medium ash-sized biotite crystal clasts are scarce and randomly distributed in the white matrix.



2021-MAC-026

Very hard, finely laminated, whitish mudstone with brownish gray nodules. It is interpreted as a resedimented syn-eruptive felsic volcanoclastic rock that experienced soft-sediment deformation.

Alternating white/brownish-gray laminae are irregularly stacked and make up gently undulated levels with non-constant thickness that commonly host variable amounts of unevenly scattered nodules with medium sphericity. Nodule aggregates can be concentrated within laterally discontinuous centimetric levels. Laminae are generally curved around nodules, which points to deformation prior to lithification. Sporadic medium ash-grain sized, matrix-supported biotite crystal clasts are unevenly distributed in the nodules or interlayered within laminae.

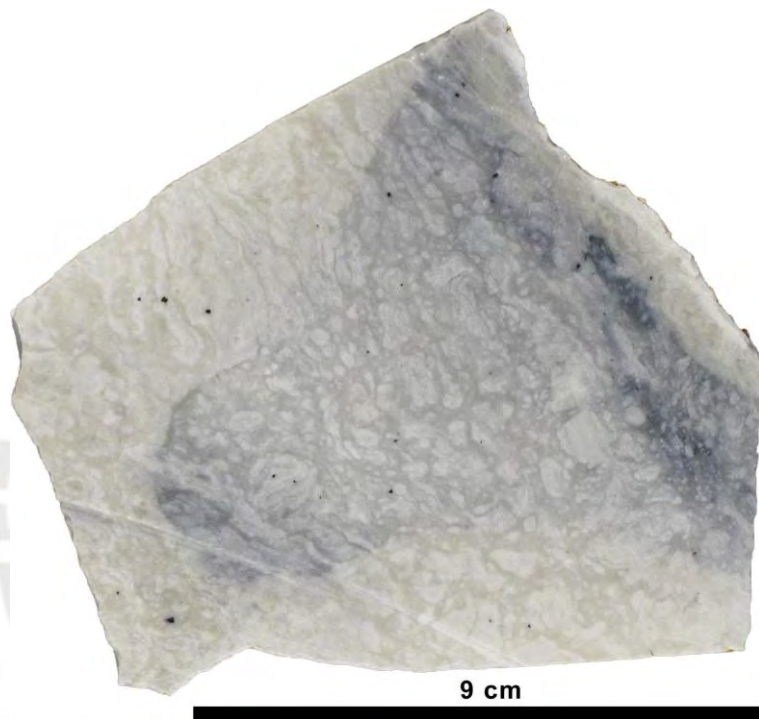


2021-MAC-031

Very hard, oriented oligomictic cemented floatbreccia with dark-gray matrix and light clasts. It is interpreted as a brecciated, re-sedimented, syn-eruptive felsic volcanoclastic rock.

Matrix and sub-rounded and angular clasts are mud-size grained. Unevenly distributed medium ash-sized biotite crystal clasts are present in both the clast and matrix. Clasts exhibit fine internal bedding and have irregular shapes and a wide range of morphologies and sizes (mostly <1 cm).

There are bluish-black and bluish-gray patches that overprinted rock components.

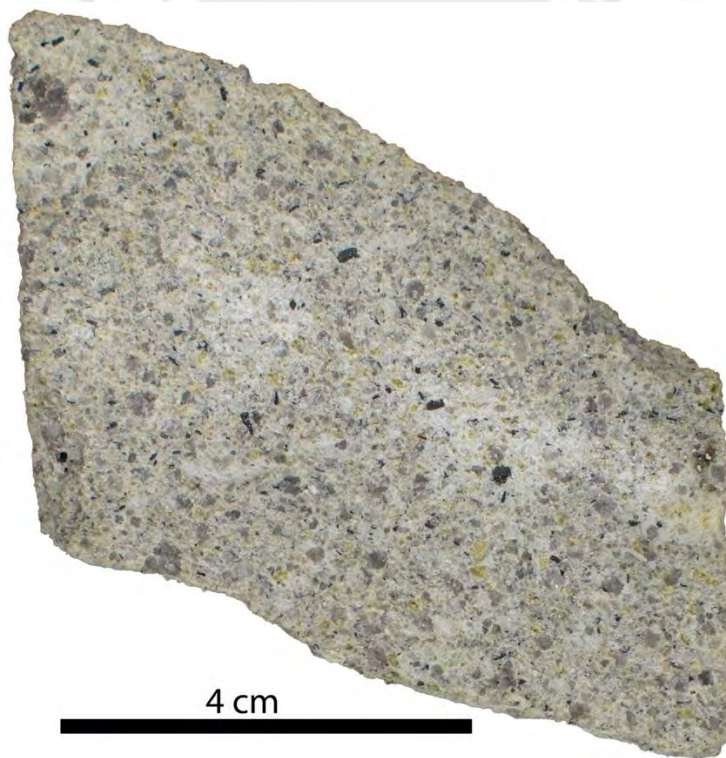


2021-MAC-033

Leucocratic, cohesive, poorly sorted, crystal-rich lapilli- and ash-flow tuff with white aphanitic matrix and variable proportions of lapilli-sized juvenile clasts.

Clast-supported crystal fragments are fine ash- to fine lapilli-sized and consist mainly of quartz, feldspar, and biotite, and local andalusite. Quartz crystal clasts are translucent, euhedral to subhedral bipyramidal. Alkali feldspar crystal clasts are colorless and show euhedral, angular to sub-angular textures. Biotite crystal clasts are fresh, euhedral, and show two distinct size populations: ubiquitous fine ash, and coarse ash. Quartz and alkali feldspar grains locally host very fine-grained biotite crystal inclusions. Scarce, prismatic, translucent, brownish pink andalusite crystal clasts are medium ash-sized (up to 0.5 mm). Prismatic plagioclase molds are up to 1 mm in width and partially filled by a very fine-grained, pale greenish mustard, waxy material.

Juvenile fragments include flattened clast of porphyritic pumice up to 30 mm long. Pumice clasts exhibit the same mineralogical and textural characteristics as the surrounding rock except for a lesser proportion of crystals.

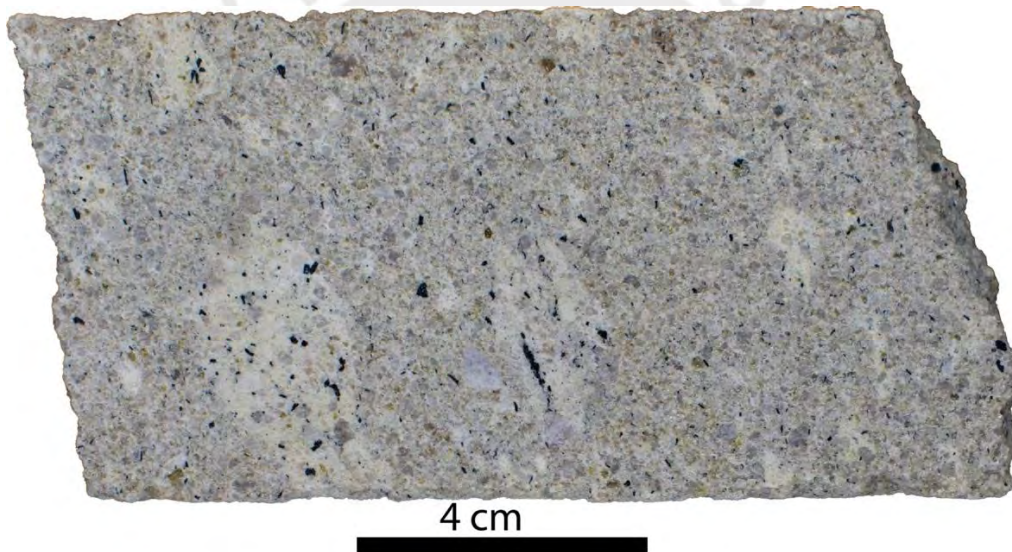


2021-MAC-034

Leucocratic, cohesive, poorly sorted, crystal-rich lapilli-tuff with white aphanitic matrix and variable proportions of lapilli-sized juvenile clasts.

Clast-supported crystal fragments are fine ash- to fine lapilli-sized and consist mainly of quartz, feldspar, and biotite, and local andalusite. Quartz crystal clasts are gray, translucent, euhedral to subhedral, and exhibit angular to sub-rounded, bipyramidal shapes. Alkali feldspar crystal clasts are colorless, euhedral, and angular to sub-angular in shape. Biotite crystal clasts are unaltered and euhedral and show two distinct size populations: ubiquitous fine ash, and coarse ash to fine lapilli (up to 3 mm). Quartz and alkali feldspar grains hosts very fine-grained biotite crystal inclusions locally. Scarce, medium ash-sized, translucent, brownish-pink andalusite crystal clasts are also observed.

Juvenile fragments include variably flattened clasts of porphyritic pumice that are up to >40 mm long. Pumice clasts exhibit the same mineralogical and textural characteristics as the surrounding rock except for a lesser abundance of crystals and slightly paler colors. Pumice clasts and biotite crystal clasts exhibit a common orientation.

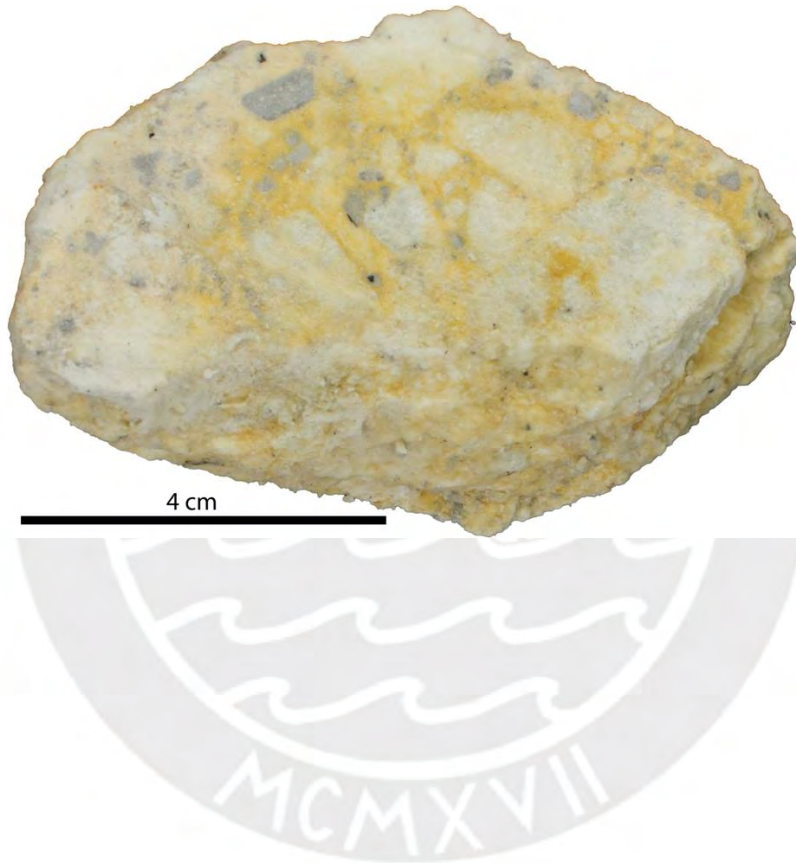


2021-MAC-035

Unconsolidated, chaotic, white and yellow, clayey volcanoclastic breccia. It is interpreted as a strongly altered felsic volcanoclastic rock in which most original textures have been obliterated.

The matrix shows saccharoidal texture and comprises mainly ash-sized feldspar, quartz, and biotite crystal clasts. The matrix-supported rock fabric changes to clast-supported without continuous gradation. Clasts are sub-angular to rounded and include light gray and white clasts with coarse sand- to pebble-size.

Ferric oxides and hydroxides concentrate in matrix and show a yellow to orange color.



2021-MAC-038

Hard, finely laminated, whitish tuffaceous mudstone interpreted as a resedimented syn-eruptive felsic volcanoclastic rock.

Alternating white and gray laminae are irregularly stacked and make up planar- to gently wavy-levels. Greenish-beige laminae are only locally observed. Unevenly distributed, fine ash- to medium ash-grained biotite crystal clasts are up to 1.5 mm. Local cavities are located within laminae and exhibit lenticular morphology with 2.5 to 3.3 length/thickness ratios and up to 10 mm lengths.



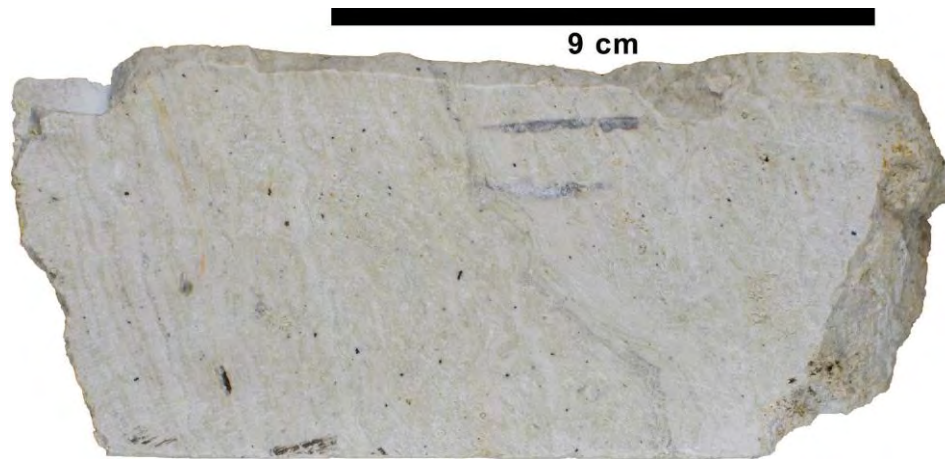
9 cm



2021-MAC-039

Hard, finely laminated, whitish, tuffaceous mudstone. It is interpreted as a resedimented syn-eruptive felsic volcanoclastic rock.

Alternating white/gray laminae are regularly stacked and make up wavy- to strongly wrinkled-levels. Unevenly distributed fine ash- to medium ash-sized biotite crystal clasts are up to 1.3 mm. Coarser-grained biotite tend to be oriented parallel to the lamination. Scarce cavities are restricted to a few bedding levels and exhibit lenticular morphology with 2.3-3.3 length/thickness ratios and 4 to 7 mm in length and their longer axes are parallel to the laminated microstructure.



2021-MAC-040

Hard, finely laminated, whitish, tuffaceous mudstone. It is interpreted as a resedimented syn-eruptive felsic volcanoclastic rock.

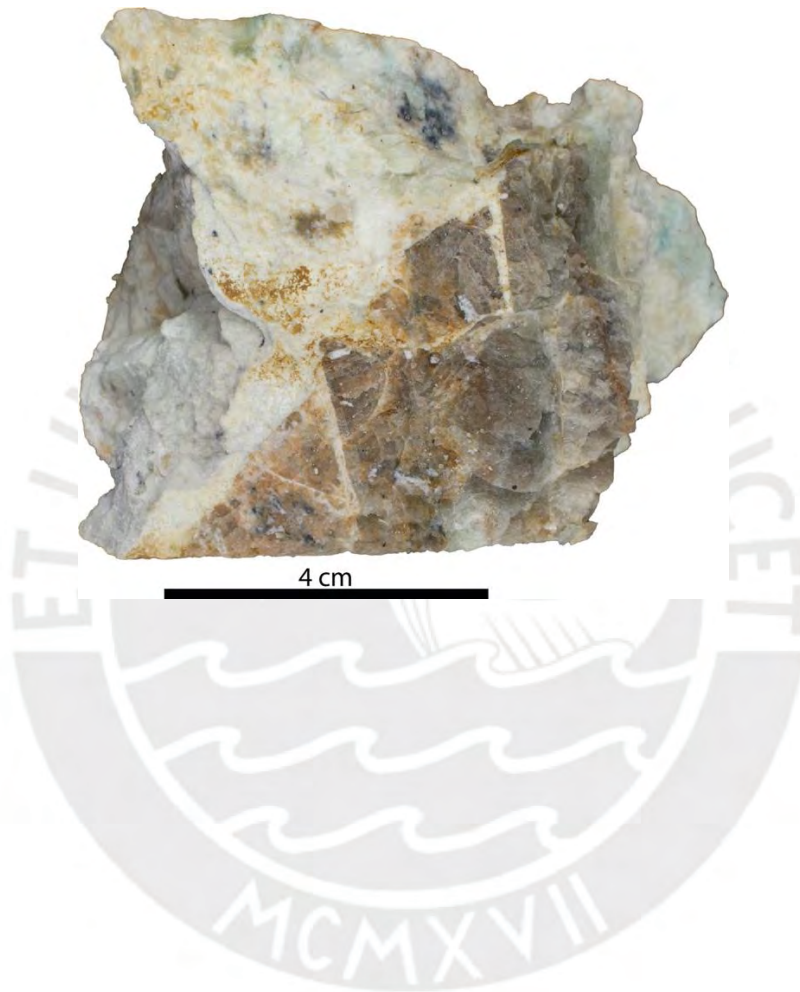
Alternating beige-white to gray laminae are regularly stacked and make up wavy- to wrinkled-levels that host abundant white micronodules. The micronodules exhibit morphologies that range from spherical to extremely elongated, in which case their long axes are aligned parallel to rock lamination; their sizes are in the range between 0.5 and 3 mm. Fine ash- to medium ash-sized (up to 2 mm) biotite crystal clasts are unevenly distributed within laminae. The coarser biotite crystal clasts tend to be oriented parallel to the laminated microstructure.



2021-MAC-042

Unconsolidated, clayey, volcanoclastic breccia with brown clasts and ash-sized white matrix. It is interpreted as a strongly altered felsic volcanoclastic rock in which most original textures have been obliterated.

Matrix-supported medium ash-sized biotite crystal clasts are evenly distributed in both the matrix and clasts. Black and pale-green patches are overprinted over the rock components.



2021-MAC-045

Leucocratic, cohesive, poorly sorted, crystal-rich lapilli- and ash-flow tuff with white aphanitic matrix and variable proportions of lapilli-sized juvenile clasts.

Clast-supported crystal fragments are fine ash- to medium lapilli-sized and consist mainly of quartz, feldspar, and biotite. Broken quartz crystal clasts are translucent, euhedral to subhedral, up to 8 mm in size, and exhibit sub-angular, bipyramidal shapes. Alkali feldspar crystal clasts are colorless and euhedral, up to 12 mm in length, and exhibit angular to sub-angular shapes. Biotite crystal clasts are euhedral and show two distinct size populations: ubiquitous fine ash, and coarse ash- to medium lapilli (up to 5 mm). Quartz and alkali feldspar grains host local, very fine-grained biotite crystal inclusions.

Juvenile fragments include flattened clast of porphyritic pumice that are up to 30 mm long. They are characterized by their very irregular outlines including delicate, acute or spinous terminations. Pumice clasts exhibit the same mineralogical and textural characteristics as the surrounding rock except for a lesser proportion of crystals and a more felsic aspect. Pumice clasts and biotite crystal clasts show roughly parallel orientations.



3 cm

2021-MAC-046

Leucocratic, cohesive, poorly sorted, crystal-rich lapilli- and ash-flow tuff with white aphanitic matrix.

Clast-supported crystal fragments are fine ash- to coarse lapilli-sized and consist mainly of quartz, feldspar, and biotite. Quartz crystal clasts are translucent and euhedral to subhedral, up to 5 mm in size, and exhibit sub-rounded to angular, bipyramidal shapes. Alkali feldspar crystal clasts are colorless and euhedral, up to 24 mm long, and exhibit angular to sub-angular, prismatic shapes. Biotite crystal clasts are fresh and show two distinct size populations: ubiquitous fine ash and coarse ash to fine lapilli (up to 5 mm). Quartz and alkali feldspar grains host scarce, very fine-grained biotite crystal inclusions. Coarse lapilli-sized alkali feldspar and medium lapilli-sized biotite crystal clasts tend to show roughly parallel orientation.



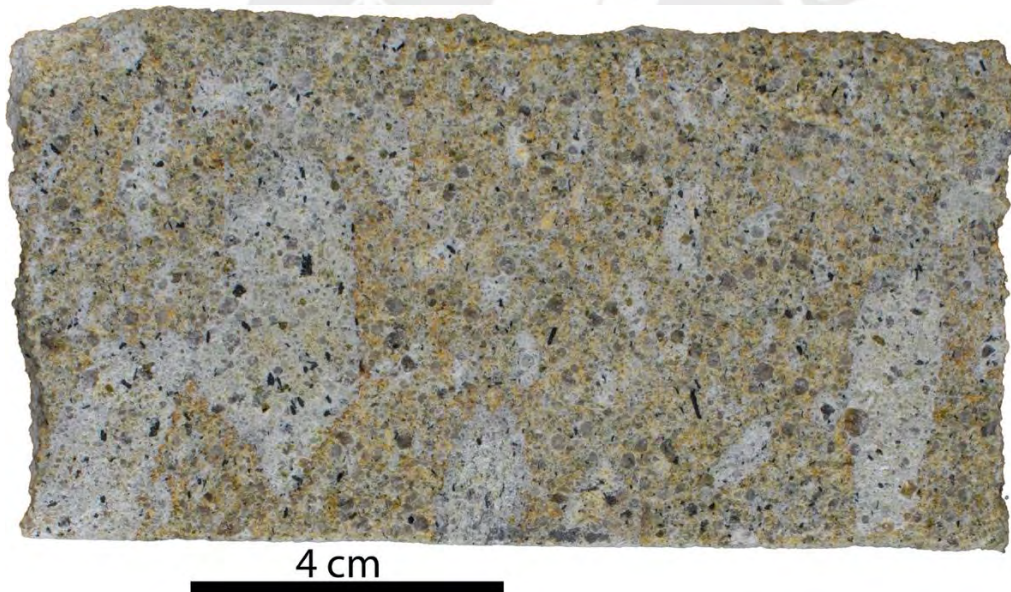
4 cm

2021-MAC-047

Leucocratic, cohesive, poorly sorted, crystal-rich lapilli- and ash-flow tuff with white aphanitic matrix and variable proportions of lapilli-sized juvenile clasts.

Clast-supported crystal fragments are fine ash- to fine lapilli-sized and consist mainly of quartz, feldspar, and biotite, and local andalusite. Quartz crystal clasts are gray, translucent, and euhedral to subhedral, and exhibit sub-rounded to angular, bipyramidal shapes. Alkali feldspar crystal clasts are colorless and show euhedral textures and angular to sub-angular shapes. Biotite crystal clasts are euhedral and show two distinct size populations: ubiquitous fine ash and coarse ash (up to 1.2 mm). Quartz and alkali feldspar grains locally host very fine-grained biotite crystal inclusions. Scarce, translucent, brownish-pink andalusite crystal clasts are medium ash-sized (up to 1.2 mm long) and exhibit prismatic shapes. Prismatic plagioclase molds, up to 1 mm in width, are partially filled by a very fine-grained, waxy, pale greenish mustard material.

Juvenile fragments include flattened clasts of porphyritic pumice up to 6.5 cm in length. Pumice clasts exhibit the same mineralogical and textural characteristics as the surrounding rock except for a lesser proportion of crystals and a more felsic character. The long axes of pumice clasts and biotite crystal clasts show parallel orientation depicting a non-tectonic foliation in this ash-flow tuff.



2021-MAC-048

Cohesive, finely laminated, whitish, tuffaceous mudstone. It is interpreted as a resedimented, syn-eruptive, felsic, volcanoclastic rock.

White, gray, and orange-beige laminae are regularly stacked and make up planar to wavy-levels that occasionally host mm-scale, elongated nodules. Fine ash- to medium ash-sized (up to 1 mm), matrix-supported biotite crystal clasts are unevenly distributed. The elongation of the nodules is parallel to rock lamination.



2021-MAC-049

Unconsolidated, massive, clayey, white volcanoclastic rock with saccharoidal texture. It is interpreted as a strongly altered felsic volcanoclastic rock in which most original textures have been obliterated.

Scarce, medium ash-sized biotite crystal clasts are scattered in a white matrix. A very fine-grained grayish black material with iridescent surface is distributed along line arrays marked by two structural orientations, probably as fracture-infill.

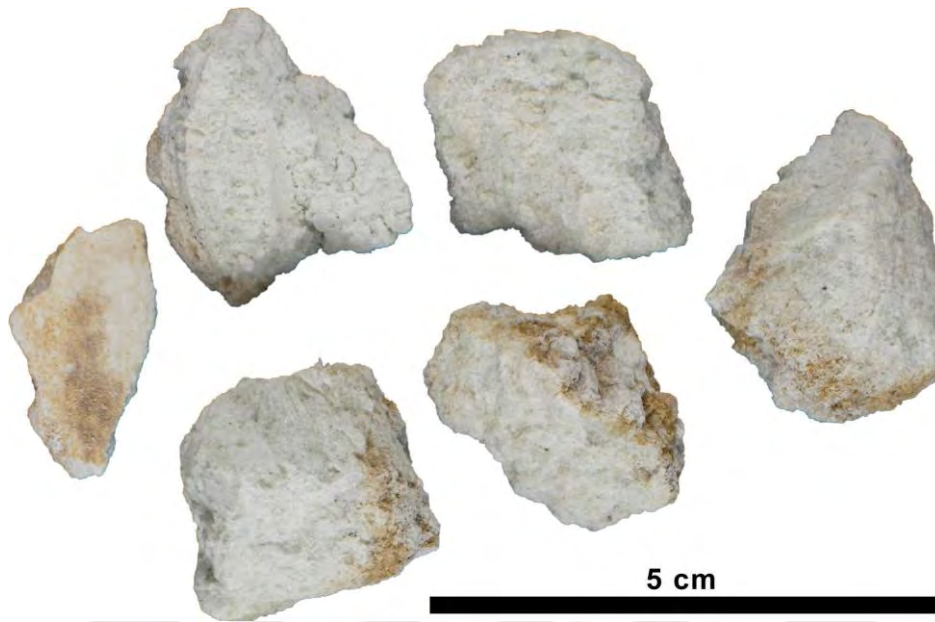


2021-MAC-050

Unconsolidated, massive, clayey, white mudstone. It is interpreted as a strongly altered felsic volcanoclastic rock in which most original textures have been obliterated.

Matrix-supported, sub-rounded to subangular feldspar and quartz crystal clasts are very fine- to medium-grained. Feldspar crystals are strongly altered. Scarce medium ash-sized biotite crystal clasts are evenly distributed.

Some of the surfaces show distinctive brown patinas.



2021-MAC-051

Unconsolidated, massive, clayey, greyish white mudstone. It is interpreted as a strongly altered felsic volcanoclastic rock in which most original textures have been obliterated.

Matrix-supported medium ash- to coarse ash-sized feldspar and quartz crystal clasts are sub-rounded to subangular. Feldspar crystals are strongly altered. Scarce biotite crystal clasts are medium ash- to fine lapilli-sized (up to 3.5 mm). Coarse ash-sized light gray clasts, up to 1.5 mm, are subangular and are distinguished in a slightly darker gray matrix.

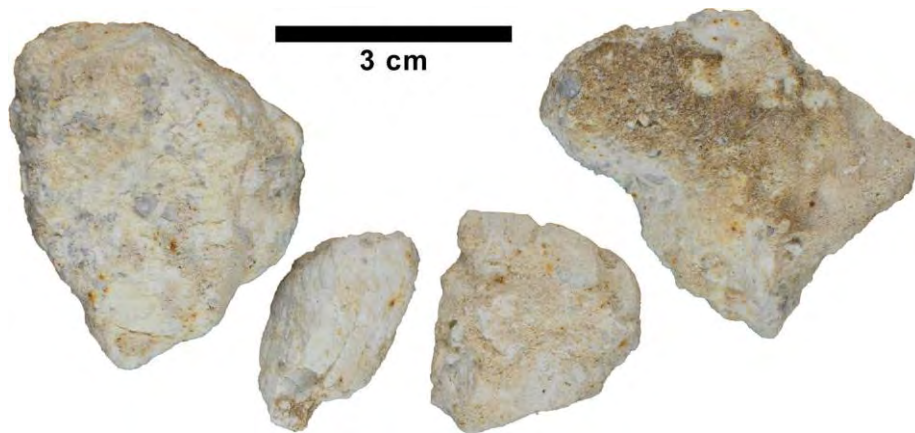


2021-MAC-052

Unconsolidated, massive, clayey, greyish white mudstone. It is interpreted as a strongly altered felsic volcanoclastic rock in which most original textures have been obliterated.

Sub-rounded to subangular feldspar and quartz crystal clasts are fine ash to fine lapilli-sized. Prismatic feldspar crystal clasts have been pseudomorphically replaced by a light gray material, probably clay minerals. Biotite crystal clasts are fine ash- to fine lapilli-sized (up to 4 mm). In most cases, biotite crystal clasts show a reddish-orange halo. Coarse ash-sized light gray clasts, up to 1.5 mm, are subangular and are distinguished in a slightly darker gray matrix.

Some of the surfaces show distinctive brown patinas.

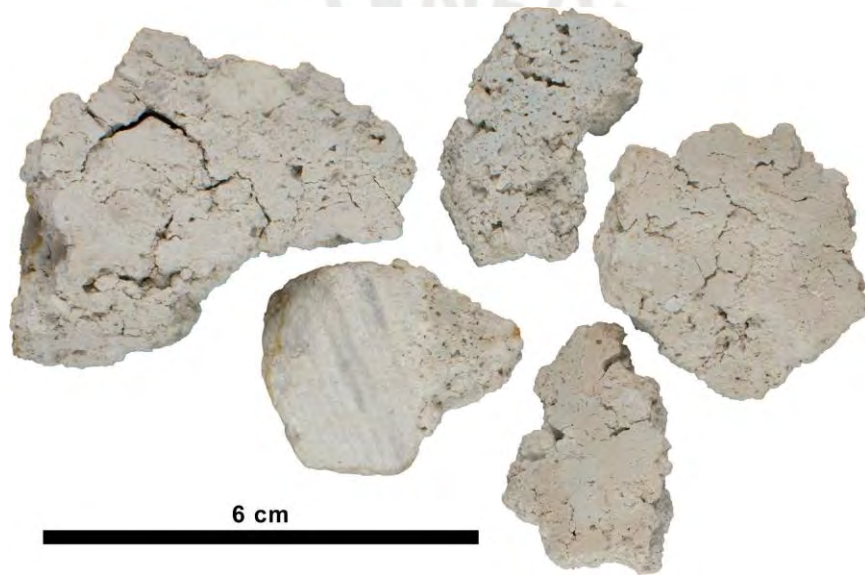


2021-MAC-053

Unconsolidated, laminated, clayey, light cream mudstone. It is interpreted as a strongly altered felsic volcanoclastic rock in which most original mineral features have been obliterated

Relicts of mm-scale gray to pale cream laminae sedimentary figures are visible. Medium ash-size matrix-supported biotite, quartz, feldspar crystal clasts are unevenly distributed. Feldspar crystals clasts are strongly altered and exhibit sub-rounded to sub-angular shapes. Quartz crystal clasts are gray and show sub-rounded to sub-angular. Relicts of biotite crystal clasts are fine ash-sized (up to 0.5 mm). Scarce translucent orange acicular crystals of unknown nature range from 1 to 2.6 mm in length.

A blanket-like beige layer with a waxy appearance and extremely low hardness covers some surfaces of the rock fragments.



2021-MAC-055

Leucocratic, medium-grained, alkali feldspar-phyric, cordierite-biotite-bearing granite with hypidiomorphic texture and pinkish-brown aphanitic mesostasis.

The most conspicuous aspect of this sample is the occurrence of white, euhedral alkali feldspar phenocrysts with two distinct size populations: very coarse-grained alkali feldspar megaphenocrysts up to 15 cm long, and medium- to coarse-grained alkali feldspar, up to 20 mm. Alkali feldspar phenocrysts often show simple Carlsbad twinning and inclusions of fine- to medium-grained biotite crystals. Quartz phenocrysts are anhedral, rounded to sub-angular, and medium- to coarse-grained (up to 7 mm). Quartz host local inclusions of medium-grain (up to 1.2 mm) biotite crystals. Euhedral- and subhedral booklets of biotite phenocrysts have reddish brown color and show three distinct size populations: sporadic medium-grained (up to 3 mm), fine-grained (0.4 to 1 mm), and ubiquitous very fine-grained. Euhedral, prismatic plagioclase phenocrysts are 0.7-10 mm in length, eventually host fine-grained biotite inclusions up to 0.5 mm long, and have been pseudomorphically replaced by a soft, pale green material. Medium- to very coarse-grained (up to 20 mm), subrounded cordierite has been largely pseudomorphically replaced by a greenish brown material; some of these pseudomorphically altered cordierite exhibit pseudo-rhombic sections.



2021-MAC-065A, B and C

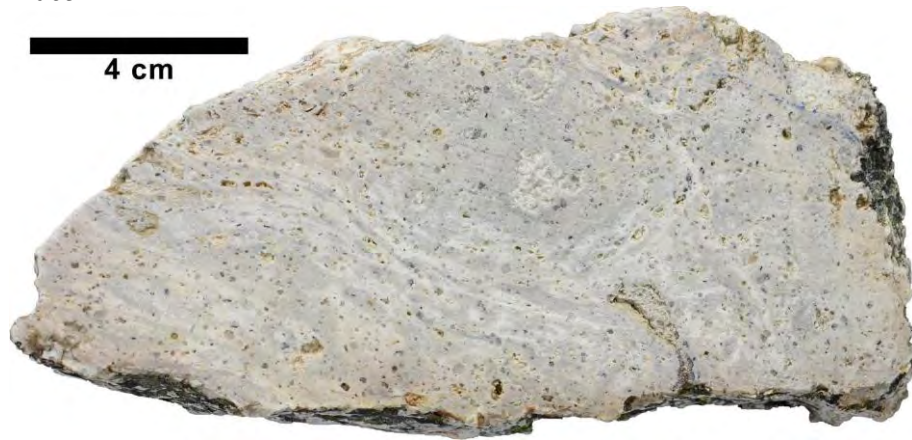
Cohesive, finely laminated, whitish, tuffaceous mudstone with abundant porosity after concretion dissolution. It is interpreted as a resedimented syn-eruptive felsic volcanoclastic rock that experienced soft-sediment deformation.

Alternating, dark gray/light laminae are discontinuous, unevenly stacked, and make up wavy-levels. Matrix-supported, ash-sized quartz, feldspar, and biotite crystal clasts are observed. Cavities may host concretion relicts which are composed of fine concentric bands with decreasing cement content from core to edge, and high to moderate sphericity. Also, concretion cores have preserved the pre-existing fine lamination sedimentary figures. Feldspar and quartz crystal clasts are angular to sub-angular. Plagioclase crystal clasts are coarse ash-sized and have been completely replaced by a pseudomorphic very fine-grained beige-white material of extremely low hardness. Biotite crystal clasts are fresh and show two distinct size populations: fine ash, and medium- to coarse ash (up to 2 mm).

2021-MAC-065A



2021-MAC-065B



2021-MAC-065C



2021-MAC-066

Leucocratic, massive, cohesive, crystal-rich, pale pink tuff.

Matrix-supported crystal clasts are medium ash- to fine lapilli-sized and consist mainly of broken translucent euhedral to subhedral bipyramidal quartz grains, translucent euhedral feldspar grains, and less abundant euhedral biotite grains.



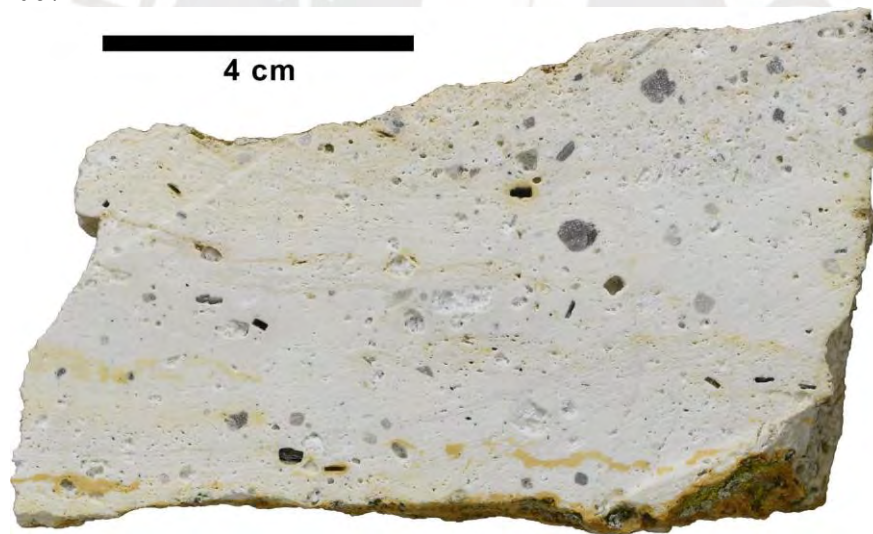
2021-MAC-067

Hard, massive, crystal-rich, pinkish white tuff.

Matrix-supported crystal fragments are unevenly distributed in a white matrix, and exhibit coarse ash- to medium lapilli-sizes. They include quartz, feldspar, and biotite, and local muscovite and tourmaline. Quartz crystal clasts are gray, translucent, and euhedral to subhedral, show sub-angular to rounded, bipyramidal shapes, up to 4.5 mm in size, and host local inclusions of very fine-grained biotite crystals. Alkali feldspar grains are white, euhedral, tabular, and show two distinct size populations: medium lapilli (up to 7.5 mm in length; some with visible Carlsbad twins), and fine lapilli. Booklets of biotite crystal clasts are partially or totally oxidized and show two distinct size populations: fine ash, and medium ash (up to 1.6 mm). Some feldspar crystals have been totally or partially dissolved. Prismatic-shape molds after plagioclase are coarse ash-sized, up to 1 mm long, and have been pseudomorphically replaced by a soft, greenish-beige very fine-grained material. Scarce subhedral, tabular, pinkish, pearly muscovite crystals are fine- to medium ash-sized (up to 1 mm). Rare euhedral, prismatic tourmaline crystals are fine to medium ash-grained (up to <0.1 mm) and exhibit black color, vitreous luster, and ditrigonal-shape basal section.

Pale brown patinas are common in some weathered surfaces and around some biotite booklets.

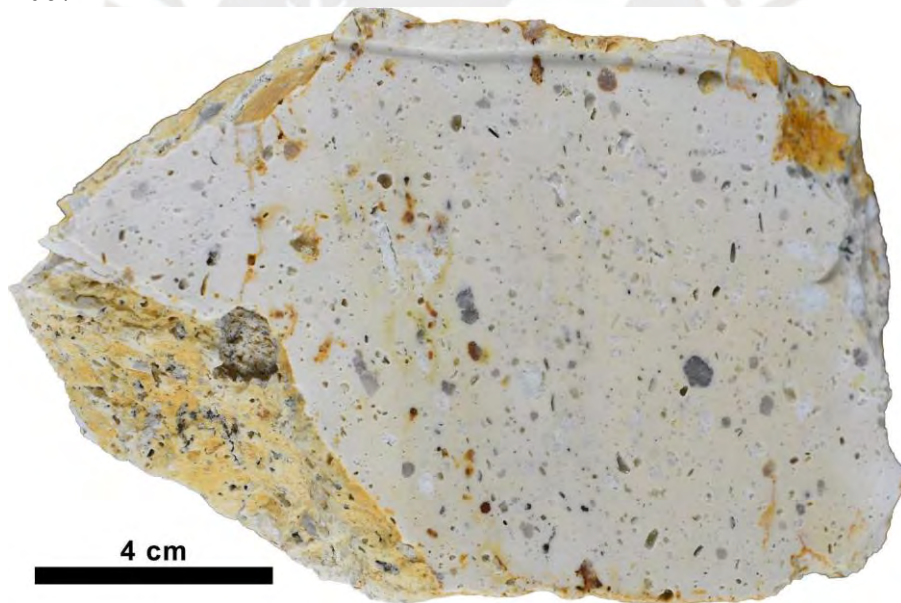
2021-MAC-067A



2021-MAC-067B



2021-MAC-067C





APPENDIX C

Major and trace element contents

Unit	Quenamari Suite granite	Lithium-rich Tuff	Lithium-rich Tuff	Lithium-rich Tuff	Lithium-rich Tuff	Post-LRT ash-flow tuff	Quenamari Suite granite	Post-LRT ash-flow tuff	White tuff	Post-LRT ash-flow tuff
Sample	2021-MAC-003	2021-MAC-008A	2021-MAC-008B	2021-MAC-011A	2021-MAC-011B	2021-MAC-012	2021-MAC-016	2021-MAC-018B	2021-MAC-019A	2021-MAC-020
A=Al-(K+Na+2Ca)	96.6	136.7	141.6	112.4	126.2	56.8	82.5	30.5	166.9	141.0
B=Fe+Mg+Ti	19.2	8.3	8.4	8.8	8.2	19.7	8.2	31.3	9.4	17.3
Q=Si/3-(K+Na+2Ca/3)	215	197	200	187	193	204	188	173	348	276
P=K-(Na+Ca)	-17.6	-24.8	-28.2	-56.4	-45.7	-17.8	-25.4	-29.4	38.7	83.2

Unit	White tuff	White tuff	White tuff	Lithium-rich Tuff	Lithium-rich Tuff	Lithium-rich Tuff	Post-LRT ash-flow tuff	Post-LRT ash-flow tuff	Upper Breccia	Lithium-rich Tuff
Sample	2021-MAC-021	2021-MAC-022A	2021-MAC-022B	2021-MAC-025	2021-MAC-026	2021-MAC-031	2021-MAC-033	2021-MAC-034	2021-MAC-035	2021-MAC-038
Alteration ¹	W	W	W	W	S	W	W	W	S	W
Major elements (wt%)										
SiO ₂	74.3	75.2	80.8	70.8	65.0	71.8	72.7	74.2	n.a.	73.9
TiO ₂	0.07	0.04	0.05	0.05	0.05	0.05	0.23	0.23	n.a.	0.03
Al ₂ O ₃	16.4	14.2	11.7	17.6	15.2	16.4	13.8	13.5	n.a.	14.0
Fe ₂ O ₃	0.68	0.62	0.56	0.67	0.54	0.61	0.99	0.99	n.a.	0.50
MnO	0.07	0.06	0.05	0.09	0.11	0.07	0.04	0.04	n.a.	0.06
MgO	0.04	0.08	0.08	b.d.l.	0.04	b.d.l.	0.50	0.48	n.a.	b.d.l.
CaO	0.17	0.33	0.19	0.21	0.53	0.13	0.91	0.91	n.a.	0.07
Na ₂ O	0.71	0.65	0.61	2.06	3.38	3.91	2.98	3.16	n.a.	1.25
K ₂ O	4.43	4.68	2.54	3.66	3.67	3.57	4.66	4.67	n.a.	6.80
P ₂ O ₅	0.16	0.25	0.16	0.19	0.61	0.57	0.26	0.27	n.a.	0.25
H ₂ O(-)	0.33	0.33	0.67	1.67	3.67	0.67	n.a.	n.a.	n.a.	0.33
H ₂ O(+)	3.34	2.68	2.01	2.37	5.54	1.01	n.a.	n.a.	n.a.	1.67
LOI	3.68	3.01	2.68	4.04	9.20	1.67	2.67	1.67	n.a.	2.01
Total	100.7	99.1	99.4	99.4	98.3	98.8	99.7	100.1		98.9
Trace elements (ppm)										
Li ³	1490	n.a.	n.a.	2920	n.a.	n.a.	420	370	780	3630
Be	129.1	16.4	33.4	82.2	172.0	270.7	21.1	23.5	n.a.	54.2
B	500	n.a.	n.a.	400	n.a.	n.a.	n.a.	n.a.	1900	900
Mg	437	625	620	237	357	178	1248	1093	n.a.	127
Sc	2.08	2.15	1.90	2.11	1.60	1.80	3.04	2.97	n.a.	1.82
V	1.23	0.25	0.44	b.d.l.	b.d.l.	0.29	5.68	5.66	n.a.	0.96
Cr	15.4	9.96	11.1	10.1	4.69	16.6	11.4	7.4	n.a.	10.9
Mn	523	428	413	726	829	566	110	98.1	n.a.	460
Ni	b.d.l.	2.20	b.d.l.	b.d.l.	b.d.l.	b.d.l.	4.44	2.25	n.a.	b.d.l.
Co	b.d.l.	b.d.l.	b.d.l.	b.d.l.	b.d.l.	b.d.l.	b.d.l.	b.d.l.	n.a.	b.d.l.
Cu	13.0	26.2	24.1	27.6	12.0	28.0	16.4	17.4	n.a.	18.0
Zn	63.0	49.9	42.4	93.0	117	84.7	53.3	57.9	n.a.	59.5
Ga	26.9	22.5	21.4	32.4	28.9	32.6	21.9	21.1	n.a.	24.5
Ge	1.13	1.55	1.43	1.81	3.09	5.03	1.95	1.49	n.a.	5.63
As	16.8	270	809	6.21	45.5	71.5	7.69	8.20	n.a.	23.6
Rb	898	834	622	1139	1363	1506	375	360	n.a.	2177
Sr	42.9	58.6	35.5	18.2	197	10.4	142	141	n.a.	17.6
Y	3.88	4.47	7.84	5.22	5.20	6.34	9.34	9.34	n.a.	12.2
Zr	36.7	47.8	93.1	35.1	40.4	45.1	87.7	80.8	n.a.	181
Nb	32.8	28.2	24.1	49.6	47.6	51.2	13.5	13.2	n.a.	34.9
Mo	b.d.l.	b.d.l.	1.45	b.d.l.	1.97	1.37	b.d.l.	b.d.l.	n.a.	1.76
Ti	405	329	276	309	285	334	1068	1060	n.a.	218
Sn	178	146	130	237	221	226	16.4	15.6	n.a.	175
Sb	2.38	120	2083	b.d.l.	1.84	b.d.l.	b.d.l.	b.d.l.	n.a.	8.11
Se	b.d.l.	4.37	9.45	b.d.l.	2.39	4.25	1.35	1.24	n.a.	2.57
Te	0.25	0.36	b.d.l.	0.45	0.40	1.43	b.d.l.	b.d.l.	n.a.	0.24
Cs	350	369	361	287	6238	566	57.8	56.3	n.a.	210
Ba	102	135	37.6	26.0	122	27.4	438	438	n.a.	239
La	5.24	4.87	4.28	3.63	3.29	3.31	20.2	20.1	n.a.	2.35
Ce	10.3	9.92	8.53	7.65	7.05	7.51	41.0	41.1	n.a.	5.38
Pr	1.09	1.07	0.92	0.87	0.82	0.82	4.66	4.76	n.a.	0.53
Nd	3.57	4.23	3.60	3.10	2.84	2.98	16.7	17.1	n.a.	2.14
Sm	0.65	0.90	0.74	0.80	0.69	0.86	3.81	3.73	n.a.	0.43
Eu	0.11	0.20	0.21	0.03	0.02	0.05	0.76	0.73	n.a.	0.02
Gd	0.57	0.75	0.71	0.71	0.52	0.92	2.84	3.01	n.a.	0.31
Tb	0.12	0.15	0.10	0.13	0.12	0.15	0.39	0.38	n.a.	0.09
Dy	0.63	0.64	0.56	0.80	0.85	0.87	1.97	1.96	n.a.	0.44
Ho	0.13	0.10	0.11	0.15	0.13	0.17	0.30	0.30	n.a.	0.06
Er	0.31	0.32	0.29	0.39	0.35	0.57	0.77	0.80	n.a.	0.26
Tm	0.07	0.05	0.06	0.06	0.06	0.07	0.11	0.11	n.a.	0.02
Yb	0.44	0.36	0.44	0.57	0.60	0.58	0.70	0.72	n.a.	0.23
Lu	0.07	0.04	0.04	0.06	0.05	0.07	0.10	0.09	n.a.	0.05
Hf	1.58	1.66	2.74	1.62	1.67	1.74	2.72	2.47	n.a.	4.97
Ta	25.6	21.0	18.2	31.9	29.0	30.8	2.33	2.28	n.a.	22.5
W	11.0	11.8	12.9	21.6	61.1	76.6	b.d.l.	b.d.l.	n.a.	39.2
Tl	0.06	0.03	0.02	0.10	0.13	0.12	0.02	0.01	n.a.	0.08
Pb	12.3	21.0	57.9	35.0	20.7	21.1	199	122	n.a.	30.8
Bi	1.18	1.76	0.83	1.25	1.54	1.34	0.23	0.14	n.a.	0.40

Er	0.39	0.44	n.a.	0.57	0.42	0.73	0.43	0.40	0.36	0.42
Tm	0.07	0.06	n.a.	0.09	0.06	0.11	0.07	0.06	0.07	0.08
Yb	0.45	0.43	n.a.	0.58	0.48	0.57	0.50	0.54	0.48	0.55
Lu	0.07	0.06	n.a.	0.09	0.07	0.09	0.07	0.08	0.06	0.07
Hf	1.84	1.95	n.a.	2.04	1.57	2.68	1.87	2.18	1.69	17.3
Ta	30.7	33.3	n.a.	4.99	4.12	2.71	34.0	39.2	31.4	33.0
W	72.0	66.9	n.a.	14.5	8.26	b.d.l.	70.7	38.9	74.5	36.9
Tl	0.11	0.13	n.a.	0.02	0.04	0.09	0.15	0.22	0.90	0.74
Pb	17.0	35.4	n.a.	71.2	83.9	61.3	26.4	28.3	28.3	26.3
Bi	0.64	0.26	n.a.	28.7	30.4	0.31	0.29	1.92	1.79	5.74
Th	2.89	3.04	n.a.	6.37	5.09	10.5	3.26	3.45	2.95	3.14
U	11.0	24.2	n.a.	15.4	12.6	15.9	15.9	27.9	21.0	20.7
F	18650	18400	10600	2860	2240	1590	19400	10500	13750	13800
Cl	b.d.l.	b.d.l.	600	100	110	140	90	290	700	390
Σ REE	19	19		54	45	94	20	21.6	18.0	21
(La/Yb) _N	5.37	5.44		13.37	13.91	23.39	4.99	5.21	4.91	4.53
(Eu/Eu*) _N	0.20	0.18		0.80	1.04	0.62	0.18	0.17	0.13	0.16
Nb/Ta	1.41	1.49		3.48	3.45	5.42	1.4	1.49	1.57	1.66
Zr/Hf	23.0	22.7		31.1	32.3	32.6	23.4	20.1	21.7	41.3
Mineral-chemical parameters										
A/NK	1.67	1.71		1.49	1.42	1.38	1.77	3.13	1.45	2.76
A/CNK	1.61	1.67		1.36	1.30	1.19	1.71	2.82	1.35	2.04
A=Al- (K+Na+2Ca)	126.3	133.9		79.3	66.2	45.2	140.1	253.9	80.7	163.8
B=Fe+Mg+Ti	8.6	8.4		21.5	16.5	27.5	8.8	9.0	8.3	11.3
Q=Si3/ (K+Na+2Ca/3)	186	204		188	202	193	195	205	135	211
P=K-(Na+Ca)	-48.1	-44.4		-16.2	-13.4	-24.6	-35.5	-79.2	-87.6	-48.4

Unit	Upper Breccia	Lithium-rich Tuff	Picotani Suite granite	White tuff	White tuff	White tuff	White tuff	White tuff	White tuff	White tuff
Sample	2021-MAC-052	2021-MAC-053	2021-MAC-055	2021-MAC-065A	2021-MAC-065B	2021-MAC-065C	2021-MAC-066	2021-MAC-067A	2021-MAC-067B	2021-MAC-067C
Alteration ¹	S	S	U	W	W	W	W	W	W	W
Major elements (wt%)										
SiO ₂	69.0	64.3	67.0	71.2	72.5	71.7	73.8	72.0	71.8	73.7
TiO ₂	0.05	0.05	0.44	0.09	0.08	0.08	0.16	0.07	0.08	0.07
Al ₂ O ₃	16.1	14.7	14.6	16.1	15.5	15.0	14.5	15.9	15.8	15.8
Fe ₂ O ₃	0.70	0.61	2.60	1.22	1.07	1.10	1.03	0.68	0.73	0.69
MnO	0.08	0.06	0.05	0.03	0.02	0.02	0.03	0.09	0.09	0.09
MgO	0.03	0.03	1.99	0.05	0.05	0.05	0.09	0.04	0.06	0.05
CaO	0.23	1.50	1.04	0.22	0.31	0.33	0.55	0.47	0.40	0.43
Na ₂ O	2.82	1.58	3.52	2.74	3.20	2.93	2.34	2.90	3.25	0.90
K ₂ O	3.61	3.61	4.92	5.61	5.28	5.25	4.62	3.64	3.96	5.08
P ₂ O ₅	0.45	0.56	0.35	0.23	0.27	0.26	0.34	0.37	0.32	0.38
H ₂ O(-)	2.33	4.00	0.67	1.00	0.67	0.67	1.67	0.00	0.33	0.33
H ₂ O(+)	2.05	6.60	1.68	2.02	1.68	2.35	2.03	3.33	2.68	3.34
LOI	4.38	10.60	2.34	3.02	2.34	3.02	3.70	3.33	3.01	3.68
Total	97.5	97.6	98.9	100.5	100.6	99.7	101.2	99.5	99.5	100.9
Trace elements (ppm)										
Li ³	2890	3620	310	n.a.	n.a.	420	n.a.	1670	n.a.	n.a.
Be	84.3	216.1	20.1	15.4	14.5	14.4	25.5	115.5	97.0	89.5
B	600	1800	n.a.	n.a.	n.a.	300	n.a.	300	n.a.	n.a.
Mg	227	339	11727	466	436	444	691	450	532	536
Sc	1.55	1.88	7.77	3.58	3.49	3.23	3.39	2.11	2.14	2.22
V	0.18	b.d.l.	32.1	b.d.l.	b.d.l.	b.d.l.	2.15	0.57	0.36	0.51
Cr	9.66	9.14	111	b.d.l.	b.d.l.	b.d.l.	b.d.l.	b.d.l.	b.d.l.	b.d.l.
Mn	651	460	372	204	174	173	187	680	680	676
Ni	1.38	6.15	5.73	b.d.l.	b.d.l.	b.d.l.	b.d.l.	b.d.l.	b.d.l.	b.d.l.
Co	b.d.l.	b.d.l.	5.82	0.40	0.20	0.31	0.50	b.d.l.	b.d.l.	b.d.l.
Cu	35.1	45.8	33.2	13.1	25.6	15.7	16.3	52.7	23.3	18.4
Zn	85.0	85.4	56.1	93.1	89.8	86.9	95.4	54.3	54.5	45.0
Ga	31.2	28.0	24.4	28.8	27.4	28.2	23.8	27.2	27.6	26.5
Ge	3.70	2.09	1.39	0.82	1.59	1.91	1.40	0.74	1.32	1.36
As	59.4	51.1	54.0	32.1	32.7	73.7	5.74	45.8	23.1	13.3
Rb	1447	1284	417	853	813	828	638	894	861	1017
Sr	17.7	125	198	20.2	19.8	20.4	46.0	44.6	37.3	45.2
Y	4.26	8.76	20.6	4.77	6.49	5.97	8.39	4.37	5.35	6.09
Zr	46.2	48.9	272	49.9	64.9	60.0	90.6	40.4	53.5	53.3
Nb	58.3	45.9	15.8	27.6	25.8	24.9	23.7	34.1	29.4	32.4
Mo	0.51	1.51	0.84	0.79	0.52	b.d.l.	0.85	1.37	0.78	b.d.l.
Ti	316	278	2907	526	510	495	984	403	440	463
Sn	211	222	18.5	68.7	65.0	66.2	41.0	154	122	118
Sb	0.72	3.86	b.d.l.	b.d.l.	b.d.l.	b.d.l.	b.d.l.	b.d.l.	b.d.l.	b.d.l.
Se	3.86	b.d.l.	b.d.l.	b.d.l.	4.23	b.d.l.	b.d.l.	b.d.l.	3.12	3.34
Te	0.23	b.d.l.	b.d.l.	b.d.l.	b.d.l.	b.d.l.	0.27	b.d.l.	b.d.l.	b.d.l.
Cs	656	8993	29.2	92.6	95.9	98.5	51.6	513	444	590
Ba	23.7	63.7	1429	130	101	103	168	69.8	77.7	110
La	3.60	3.32	34.1	4.67	4.68	4.49	14.2	4.62	4.93	7.16
Ce	7.69	6.99	78.5	10.0	10.0	9.48	30.8	10.0	11.2	14.9
Pr	0.87	0.86	10.3	1.21	1.18	1.15	3.76	1.19	1.30	1.81
Nd	3.33	3.03	43.9	4.22	3.79	3.58	13.4	3.84	4.67	6.35
Sm	0.77	0.81	9.10	1.08	1.08	0.84	3.10	0.93	1.00	1.34
Eu	0.03	0.03	1.61	0.06	0.08	0.07	0.25	0.11	0.13	0.17

Gd	0.56	0.90	5.81	0.83	0.84	0.80	2.23	0.87	0.80	1.12
Tb	0.11	0.16	0.67	0.13	0.13	0.15	0.30	0.14	0.14	0.15
Dy	0.70	1.17	3.16	0.67	0.84	0.86	1.61	0.70	0.75	0.89
Ho	0.09	0.18	0.53	0.11	0.14	0.13	0.24	0.10	0.13	0.16
Er	0.31	0.57	1.40	0.35	0.42	0.40	0.58	0.29	0.41	0.50
Tm	0.05	0.11	0.15	0.02	0.03	0.02	0.05	0.03	0.04	0.03
Yb	0.39	0.72	1.27	0.38	0.39	0.40	0.43	0.43	0.50	0.41
Lu	0.05	0.09	0.18	0.05	0.06	0.06	0.08	0.05	0.07	0.05
Hf	1.88	2.13	7.37	1.97	2.43	2.23	3.02	1.52	1.97	1.92
Ta	34.0	30.2	2.25	6.13	5.99	5.82	4.64	20.5	16.9	18.1
W	58.6	74.7	7.37	10.3	9.84	10.3	6.10	22.2	19.5	19.6
Ti	0.21	0.03	0.06	0.09	0.06	0.15	0.03	0.12	0.03	0.09
Pb	41.6	29.3	70.8	31.9	31.0	47.8	53.9	42.2	24.1	48.0
Bi	1.31	1.69	1.39	1.12	1.01	0.66	0.40	1.22	0.52	0.15
Th	3.03	2.82	34.1	6.20	5.91	5.81	11.7	3.48	4.52	4.52
U	17.4	23.9	15.6	13.8	15.8	15.7	11.7	13.1	17.1	16.8
F	14700	15350	2080	n.a.	n.a.	n.a.	n.a.	n.a.	n.a.	n.a.
Cl	130	80	200	n.a.	n.a.	n.a.	n.a.	n.a.	n.a.	n.a.
ΣREE	19	19	191	24	24	22.4	71.1	23.3	26	35
(La/Yb) _N	6.32	3.13	18.2	8.30	8.2	7.71	22.4	7.33	6.73	11.8
(Eu/Eu*) _N	0.13	0.11	0.67	0.20	0.26	0.26	0.29	0.38	0.46	0.43
Nb/Ta	1.71	1.5	7.0	4.50	4.3	4.27	5.12	1.66	1.74	1.79
Zr/Hf	24.5	23.0	36.9	25.3	26.7	26.9	30.0	26.6	27.2	27.8
Mineral-chemical parameters										
A/NK	1.89	2.26	1.32	1.52	1.41	1.43	1.64	1.83	1.64	2.26
A/CNK	1.80	1.59	1.12	1.46	1.34	1.35	1.48	1.67	1.53	2.03
A=Al-(K+Na+2Ca)	140.9	107.6	31.9	100.2	78.0	77.1	92.0	125.2	106.8	157.5
B=Fe+Mg+Ti	10.1	9.1	87.4	17.7	15.6	15.9	17.0	10.3	11.7	10.8
Q=Si/3-(K+Na+2Ca/3)	212	211	141	185	183	188	229	223	205	267
P=K-(Na+Ca)	-18.4	-1.0	-27.9	26.6	3.2	11.0	12.6	-24.5	-28.0	71.1

¹Abbreviations for alteration: U = unaltered, W = weakly altered, M = moderately altered, S = strongly altered

²Lithium contents for samples 2021-MAC-038, 2021-MAC-039, 2021-MAC-040, 2021-MAC-048, 2021-MAC-049, 2021-MAC-050, 2021-MAC-051, 2021-MAC-052, and 2021-MAC-053 originally reported by [Segovia-More et al. \(2023\)](#)

³Average value of two duplicate analyses of sample 2021-MAC-003

b.d.l. = below detection limits, n.a. = not analyzed



APPENDIX D

Normative mineralogy

Sample	Lithotype	Apatite (wt.%)	Ilmenite (wt.%)	Orthoclase (wt.%)	Albite (wt.%)	Anorthite (wt.%)*	Corundum (wt.%)	Hypersthene (wt.%)	Quartz (wt.%)	Total (wt.%)
2021-MAC-003	Quenamari Suite granite	0.6	0.2	25.0	26.2	0.6	5.7	2.1	39.6	100.0
2021-MAC-008A	Lithium-rich Tuff	1.3	0.1	24.1	29.2	-3.2	8.8	1.1	38.7	100.0
2021-MAC-008B	Lithium-rich Tuff	1.3	0.1	23.4	29.5	-3.1	8.9	1.1	38.9	100.0
2021-MAC-011A	Lithium-rich Tuff	1.9	0.1	21.5	34.3	-4.0	8.0	1.1	36.9	100.0
2021-MAC-011B	Lithium-rich Tuff	1.3	0.1	22.5	32.9	-2.9	8.0	1.1	37.0	100.0
2021-MAC-012	Post-lithium-ore ash-flow tuff	0.5	0.3	27.1	26.7	2.5	3.5	2.0	37.3	100.0
2021-MAC-016	Quenamari Suite granite	0.7	0.1	27.3	31.6	-1.1	5.1	0.9	35.2	100.0
2021-MAC-018B	Post-lithium-ore ash-flow tuff	0.6	0.5	28.4	29.6	3.7	2.3	3.1	31.7	100.0
2021-MAC-019A	White tuff	0.6	0.1	18.3	5.9	-0.9	9.5	1.2	65.3	100.0
2021-MAC-020	Post-lithium-ore ash-flow tuff	0.2	0.4	32.3	7.7	-0.2	7.6	1.5	50.7	100.0
2021-MAC-021	White tuff	0.4	0.1	27.0	6.2	-0.2	10.8	1.3	54.4	100.0
2021-MAC-022A	White tuff	0.6	0.1	28.8	5.7	0.0	8.4	1.3	55.1	100.0
2021-MAC-022B	White tuff	0.4	0.1	15.5	5.3	-0.1	8.2	1.2	69.4	100.0
2021-MAC-025	Lithium-rich Tuff	0.5	0.1	22.7	18.3	-0.2	10.8	1.2	46.6	100.0
2021-MAC-026	Lithium-rich Tuff	1.6	0.1	24.4	32.1	-1.5	6.9	1.2	35.1	100.0
2021-MAC-031	Lithium-rich Tuff	1.3	0.1	21.7	34.1	-3.1	7.4	1.1	37.3	100.0
2021-MAC-033	Post-lithium-ore ash-flow tuff	0.6	0.4	28.4	26.0	3.0	2.9	2.7	36.0	100.0
2021-MAC-034	Post-lithium-ore ash-flow tuff	0.6	0.4	28.0	27.2	2.9	2.2	2.6	36.0	100.0
2021-MAC-038	Lithium-rich Tuff	0.6	0.1	41.5	11.0	-1.3	5.2	0.9	42.0	100.0
2021-MAC-039	Lithium-rich Tuff	1.3	0.1	22.5	33.4	-2.5	8.0	1.2	36.0	100.0
2021-MAC-040	Lithium-rich Tuff	1.3	0.1	21.7	31.8	-2.9	8.3	1.1	38.6	100.0
2021-MAC-045	Pre-lithium-ore ash-flow tuff	0.7	0.3	28.1	28.2	1.0	4.9	2.1	34.7	100.0
2021-MAC-046	Pre-lithium-ore ash-flow tuff	0.6	0.3	28.1	27.5	1.0	4.1	1.5	37.0	100.0
2021-MAC-047	Post-lithium-ore ash-flow tuff	0.7	0.4	27.4	28.3	2.5	3.1	2.7	35.0	100.0
2021-MAC-048	Lithium-rich Tuff	1.1	0.1	23.0	30.6	-2.3	8.6	1.1	37.7	100.0
2021-MAC-049	Lower Breccia	0.7	0.1	8.7	30.1	0.3	15.7	1.3	43.0	100.0
2021-MAC-050	Upper Breccia	1.4	0.1	21.0	43.1	-1.4	6.1	1.2	28.5	100.0
2021-MAC-051	Upper Breccia	1.2	0.1	14.5	22.3	3.4	11.1	1.7	45.6	100.0
2021-MAC-052	Upper Breccia	1.1	0.1	22.9	25.6	-1.9	8.9	1.4	41.9	100.0
2021-MAC-053	Lithium-rich Tuff	1.5	0.1	24.5	15.4	4.4	7.8	1.3	45.0	100.0
2021-MAC-055	Picotani Suite granite	0.8	0.9	30.2	31.0	3.0	2.6	9.0	22.6	100.0
2021-MAC-065A	White tuff	0.5	0.2	34.0	23.8	-0.4	5.8	2.1	33.9	100.0
2021-MAC-065B	White tuff	0.6	0.2	31.8	27.6	-0.2	4.7	1.8	33.5	100.0
2021-MAC-065C	White tuff	0.6	0.2	32.1	25.6	0.0	4.7	1.9	34.9	100.0
2021-MAC-066	White tuff	0.8	0.3	28.0	20.3	0.6	5.6	1.7	42.6	100.0
2021-MAC-067A	White tuff	0.9	0.1	22.4	25.5	-0.1	7.6	1.3	42.2	100.0
2021-MAC-067B	White tuff	0.8	0.2	24.3	28.5	-0.1	6.5	1.4	38.5	100.0
2021-MAC-067C	White tuff	0.9	0.1	30.9	7.9	-0.3	9.2	1.3	49.9	100.0

*Negative values for anorthite are a numerical artifact due to the low contents of CaO and high contents of P₂O₅ in the studied rocks.